Allosteric contributions of muscle nicotinic acetylcholine receptor residues in small-molecule interactions, disease and subunit assembly

Max Epstein

Green Templeton College

University of Oxford

A thesis submitted for the degree of

Doctor of Philosophy

Michaelmas 2020

Statement of figure contributions

All figures that have been adapted or reproduced within this thesis have been properly attributed in the figure legends. Chapter 4 of this thesis was a collaborative effort, with all wet-lab experiments performed by Dr. Hakan Cetin under the supervision of Professor David Beeson. ^{125}I-α-BuTx binding assays in figure 5.5c were performed by the author with assistance from Susan Maxwell (Beeson group). All other figures were generated by the author.

Acknowledgements

First and foremost, a huge thanks to my supervisor, Professor Phil Biggin for being so supportive over the duration of my DPhil and for giving me the freedom to explore my own interests and experimental approaches. I don't think I could have asked for a better supervisor.

Thanks to Professor Isabel Bermudez for allowing a computational chemist such as myself to moonlight as an electrophysiologist in your lab and also for your continued support over these last few years. A big thank you to Professor David Beeson for a fruitful collaboration and welcoming me in to your group to perform some of my own experiments. I would also like to thank Hakan, who's boundless patience with the long duration of my data collection and also for your overall encouragement really made this collaboration so enjoyable. Also, thanks to Susan for teaching and assisting me in some of the experimental work. Thank you to Dr Thomas Piggot for your mentorship and collaboration. I'd also like to thank the rest of the guys at DSTL, namely John, Chris and Chris, who have been so great to work with.

Massive thank you to the entirety of the SBCB and the rest of the Biggin group in particular. To Maria, Tere and Afroditi, thank you for putting up with my obnoxiously loud typing and for being available to explain things or help me out whenever I've needed it. Also a big thanks to Irfan and Marc for so much technical assistance over the years. Thanks to Will G, Harold, Joe and Shad for not only being great lab-mates but also great friends. To my students Karan, Tom and Ian, it was an absolute pleasure teaching you fellas and I know that I probably ended up learning about as much from you all. Thanks to Joe and Andy for all your help with molecular biology and for just being great people to work and chat with.

I would also like to thank my friends and house mates in Oxford over the last few years including Harvey, Sam, Linus, Alex, Dom, Jon, Alice, Brad and Sev.

Finally, I want to thank my dad, step-mum and brother. Thank you for everything.

Max Epstein
October 2020, University of Oxford

Published Works Arising From This Thesis

H.Cetin, M. Epstein *et al.* Muscle acetylcholine receptor conversion into chloride conductance at positive potentials by a single mutation. *Proc. Natl. Acad. Sci. U.S.A.* 2019, 116(42), 21228-21235

M. Epstein *et al.* Structural correlates of human muscle nicotinic acetylcholine receptor subunit assembly mediated by $\delta(+)$ interface residues. *bioRxiv.* 2020, https://doi.org/10.1101/2020.06.11.145466. (Reviewer corrections being implemented for publication in *JBC.*)

M. Epstein *et al.* Molecular determinants of non-oxime bispyridinium compounds at the adult muscle nAChR. (Manuscript in preperation for submission to *Toxicology Letters.*)

Abstract

The nicotinic acetylcholine receptor (nAChR) is a member of the Cys-loop receptor superfamily of heteropentameric ligand-gated ion channels. The nAChR subfamily has 17 different possible subunits in vertebrates that are found in multiple stoichiometric combinations. Compared to other nAChRs, muscle type nAChRs possess a large subunit repertoire with respect to other nAChRs being comprised of four different subunits- namely α, β, δ and either ϵ or γ in adult or foetal varieties respectively.

The endogenous neurotransmitter of nAChRs, acetylcholine (ACh), binds at the interfaces of $\alpha(+)\delta(-)$ and $\alpha(+)\epsilon(-)$ or $\alpha(+)\gamma(-)$ subunits. By controlling the safety margin of neuromuscular transmission, nAChRs maintain high-fidelity muscle contraction under a range of physiological conditions. The interference of this process as a result of organophosphorus nerve agent (OPNA) exposure or from genetic disorders such as congenital myasthenic syndrome (CMS) can therefore have deleterious consequences.

OPNAs work by covalent modification of acetylcholinesterase, preventing the breakdown of acetylcholine leading to desensitising block of nAChRs. No antidotes that interact with nAChRs currently exist, however a class of non-oxime bispyridinium compounds (BPDs) have been shown to be efficacious in this regard. In the first part of this project, we sought to rationalise the structure activity relationship data of a series of congeneric BPDs using molecular dynamics (MD) simulations, followed by mutagenesis and electrophysiology to elucidate molecular determinants for their interactions.

In part II of this thesis we identify a novel CMS mutation located at the muscle nAChR alpha subunit transmembrane domain and use enhanced sampling MD simulations and patch-clamp electrophysiology to reveal a new CMS pathomechanism caused by a swap in charge selectivity from cationic to anionic.

In the final part of this thesis, we sought to further explore observations from part I regarding functional differences between orthosteric interfaces as well as discern

the structural correlates responsible for the fixed stoichiometric assembly of muscle nAChRs. In the first instance, by integrating MD simulation, evolutionary data and electrophysiology we determine the structural correlates for muscle nAChR subunit assembly and show functional differences between WT and 'double δ' human muscle nAChR subtypes . Further to this, we explore the relative importance of individual domains of the nAChR δ subunit in contributing to this fixed stoichiometric assembly by generating a range of chimeric ϵ and δ subunits and assessing their cell-surface expression with I^{125}-α-BuTx binding assays.

Contents

List of Figures

"Hello Steven. It's Clem Fandango.
Can you hear me?"

— Clem H. Fandango

1 Introduction

1.1 Nicotinic acetylcholine receptors

The identification of a 'receptive-substance' by Jonathan Newport Langley marked the keystone moment in the fields of structural biology, pharmacology and biophysics [1] and the birth of drug receptor theory as a concept. This receptive-substance as it would turn out was the nicotinic acetylcholine receptor (nAChR) – the prototypical ion channel receptor.

Early experiments pioneered by Katz and Miledi using voltage clamp electrophysiology allowed for the biophysical investigation of these ion channels in a macroscopic context [2, 3]. This coupled with molecular biology, cloning [4, 5] and heterologous expression [6] of channels further improved the detailed molecular dissection of these elusive proteins.

From the development of fluctuation analysis [7] and then single-channel patch clamp recordings [8], the biophysical properties and conformational changes of individual channels could be probed for the first time and in conjunction with the Monod-Wyman-Changeux (MWC) model of allostery, the complex conformational landscape of this protein could be understood with huge implications for future drug

discovery efforts [9]. It was just over a decade after the discovery of the giga-Ω seal patch clamp configuration and with the advent of pioneering work on Cryo-Electron Microscopy (Cryo-EM) from Richard Henderson [10] that the tools became available to determine the pentameric structure of the nAChR [11].

Since then, structural biology efforts have revealed much about pentameric ligand gated ion channels (pLGICs) in general and with over 4435 published membrane protein coordinate files as of 15/12/20 ('mpstruc' database) and a resolution revolution in cryo-EM currently underway [12] sure to further reveal the secrets of these proteins. Other equally important efforts have focused on elucidating the complex conformational landscape and allosteric nature of this protein [13] (see [14, 15] for reviews on conformational change and allostery in pLGICs and other membrane proteins) .

Given the length of time since the nAChRs discovery and the corresponding intense efforts to understand and characterise this receptor protein it is surprising that plenty of questions still remain about their fundamental properties including ion selectivity, gating and assembly. Despite this, the nAChR remains relevant with it being implicated in newly discovered mechanisms of disease such as congenital myasthenic syndrome (CMS) [16–18] or as a therapeutic target in the ever evolving threat of organophosphorus nerve-agent use [19].

As such, this thesis seeks to identify and link the specific structural components responsible for contributing to allosteric mechanisms of gating/charge selectivity as well as small-molecule binding in the context of the pathological processes of CMS and nerve agent exposure to their functional outcomes. Additionally- it identifies and explores the previously overlooked contributions of the nAChR δ subunit assembly signature.

1.2 nAChR overview

The nicotinic acetylcholine receptor encompasses a class of pLGIC cys-loop receptor accordingly named due to the widely conserved disulphide bond signature sequence residing at the extracellular domain [20]. Other ion channels of this class include the Glycine receptor (GlyR), serotonin receptor (5HT3AR), gamma-aminobutyric acid receptors (GABAa and GABAc) and also bacterial and invertebrate channels such as GLIC, ELIC, GLUCl [21], as well as chloride channels gated by ACh and tyramine in *C. elegans* [22, 23] and histamine in *Drosophila melanogaster* [24].

Cys-loop receptors all possess a similar topological fold, with a β-sheet extracellular domain, α-helical transmembrane domain and much less highly conserved intracellular domain for vertebrate channels. The nAChR is widely expressed in vertebrate nervous systems, regulating autonomic, central and neuromuscular processes [25]. As such, a plethora of functions are implicated in nAChR function. These include but are not limited to breathing, reward processing [26, 27], learning and memory [28], movement [18] and pain regulation [29].

NAChRs are cooperative allosteric proteins insofar that they are comprised of multiple homologous subunits, possess a pseudosymmetrical quaternary structure and are cooperative with respect to the binding of their endogenous ligand, acetylcholine (ACh). Typically, nAChRs require two molecules of ACh to bind. This occurs after vesicles of ACh fuse to the presynaptic membrane after receiving an electrical stimulus, whereby ACh molecules can diffuse across the synaptic cleft and bind to the nAChR.

This causes a conformational change is induced in the nAChR whereby they quickly isomerise on the millisecond time scale from a closed to open configuration. This open state allows for the influx of cations with preference for specific cations being in part determined by subunit makeup. For example, α7 homomeric nAChRs benefit from being highly calcium permeable as this allows for the regulation of

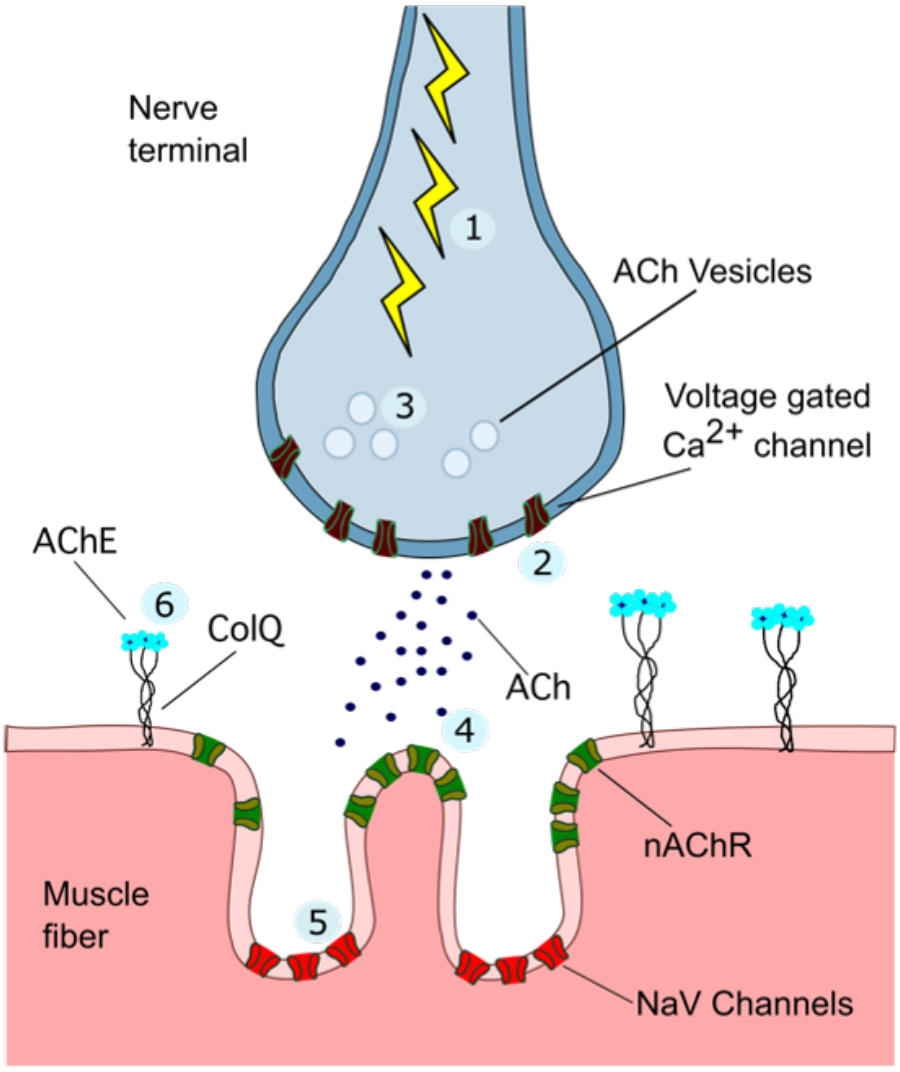

Figure 1.1: Neuromuscular Junction (NMJ) schematic. (**1**) An electrical stimulus reaches the nerve terminal. (**2**) Voltage-gated Ca^{2+} channels are activated and cause an influx of Ca^{2+} into the nerve terminal. This Ca^{2+} enables vesicles of ACh to bind to the postsynaptic membrane and exocytose their contents into the synaptic cleft (**3**). Molecules of ACh diffuse across the synaptic cleft and bind to nAChRs present postsynaptically (**4**), activating them to cause an end-plate potential (EPP). Once this EPP has reached the V_m required to activate voltage-gated Na^+ channels (NaV) present at the depths of the junctional folds of the muscle cell, an action potential is elicited by NaV channels (**5**) allowing for the muscle fibre to contract. This response is terminated (**6**) by Acetylcholinesterase (AChE) that is anchored to the muscle fibre, breaking down ACh into choline and acetic acid, where choline is recycled back into the nerve terminal.

downstream signalling processes on the immune cells of which they can reside [30]. In other heteromeric nAChRs, in skeletal muscle for example, cation influx excites the membrane leading to depolarisation and generation of action potentials through the activation of voltage gated NaV 1.4 channels [31].

Skeletal muscle morphology helps to ensure efficient neuromuscular transmission via junctional folds that allow for nAChRs to be positioned in active zones close to the site of ACh release (figure 1.1). NaV channels located at the depths of these folds allow for high local concentrations of channels in these regions and the quick and efficient generation of action potentials through the additive charge contributions from individual channels [32], (see [33] for a review of neuromuscular transmission).

The fast-catalytic breakdown of ACh by acetylcholinesterase helps to ensure that temporal and spatial aspects of nAChR mediated signalling are well regulated and the breakdown product choline can then be recycled during ACh synthesis by choline acetyltransferase after it is shuttled back into the presynaptic terminal via the choline transporter (CHT).

1.3 nAChR subunit diversity

There are 16 identified nAChR subunits in vertebrates with an additional subunit ($\alpha 8$) for avian species [34]. These subunits assemble via a multitude of mechanisms and with various stringencies allowing for specific fixed stoichiometries in the case of muscle nAChR's or variable stoichiometries for $\alpha 4\beta 2$ for example which can exist in either high and low sensitivity forms with $2(\alpha 4)3(\beta 2)$ or $3(\alpha 4)2(\beta 2)$ arrangements.

All functional nAChRs possess at least 2 α subunits of a possible 10 ($\alpha 1$-$\alpha 10$) that are characterised by the additional disulfide bond located on loop-C of the agonist binding site. The $\alpha 7$ and $\alpha 8$ nAChR subunits are capable of forming homomeric receptors whilst all other α subunits require the co-expression of β subunits ($\beta 1$-$\beta 4$)

for the formation of functional receptors. The $\alpha3\beta4$ or $\alpha3\beta4\alpha5$ nAChR subtypes are expressed in autonomic ganglia whereas $\alpha4\beta2$ heteromers are expressed centrally predominantly.

1.3.1 Extracellular domain

The extracellular domain of nAChRs is comprised of a β-sandwich fold of 10 individual β strands. The main immunogenic region (MIR) resides in the N-terminal region of this domain formed by the close association of α-1 helix and β-2-β-3 loop components [36]. The MIR is a solvent exposed, predominantly α helical accessible target to antibodies and as such, explains its role in the autoimmune disease myasthenia gravis [37]. It has also been implicated in shaping agonist sensitivity and is involved in expression efficiency [38].

The α type nAChR subunits also bind with high affinity to snake venoms such as α-BuTx via interactions predominantly mediated by loop-C [39], explaining their toxicity and also providing useful biochemical probes for assessing nAChR cell surface expression [35, 36]. An additional structural identifier of α type nAChR subunits is the presence of a disulphide bond located at the cap of loop C and occuring across both vertebrate and invertebrate species [40]. The characteristic Cys-loop is located between β-strands 6 and 7 where the signature disulfide bond connects these two strands and is conserved across cys-loop receptors [41, 42]. Mutation of these residues greatly reduces expression and α-BuTx binding [43]. Post agonist binding, the pore facing inner β-sheet undergoes a 15-16 degree rotation thought to be a key structural reorganisation in the closed to open gating isomerisation [44, 45].

The orthosteric binding site for acetylcholine also resides in the extracellular domain and is comprised of residues from two neighbouring subunits with the binding site itself situated between the interface of these two participating subunits as suggested

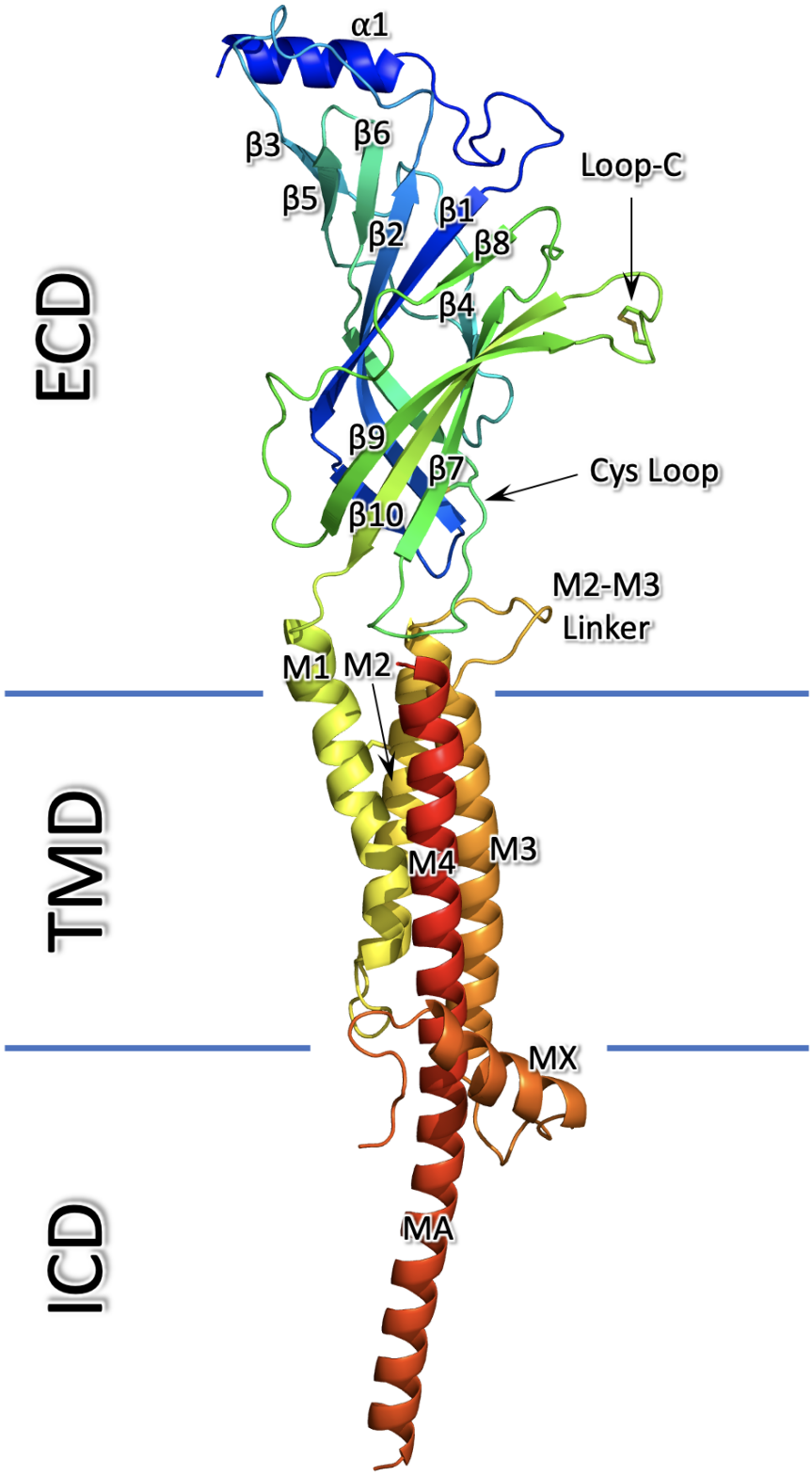

Figure 1.2: Cartoon representation of human α1 nAChR subunit homology model based on α3 subunit cryo-EM structure [35]. Subunit is coloured according to a rainbow colour scheme with N-terminal in blue and C-terminal in red. individual structural motifs are individually labelled with each ECD β sheet strand labelled from β1-β10. TMD helices are labelled M1-M4 as well as intracellular MA and periplasmic MX helices.

by various biochemical studies and later confirmed by the 3-dimensonal structure of numerous acetylcholine binding proteins[46–48]. More specifically, the agonist binding site is comprised of loops A,B and C from the principal subunit (designated as the (+) face)- which for nAChRs is always an α subunit- and loops D, E and F from the complementary subunit (designated as the (-) face). Loops A,B,C and D collectively contribute 5 aromatic side chains that make up the aromatic box as first shown from the x-ray crystal structure of acetylcholine binding protein (AChBP) [49, 50], with 4 aromatics from the principal face and a single conserved tryptophan residue form complementary face ACh binding sites. This agonist recognition motif is highly hospitable to quaternary charged amines which the endogenous neurotransmitter acetylcholine possesses.

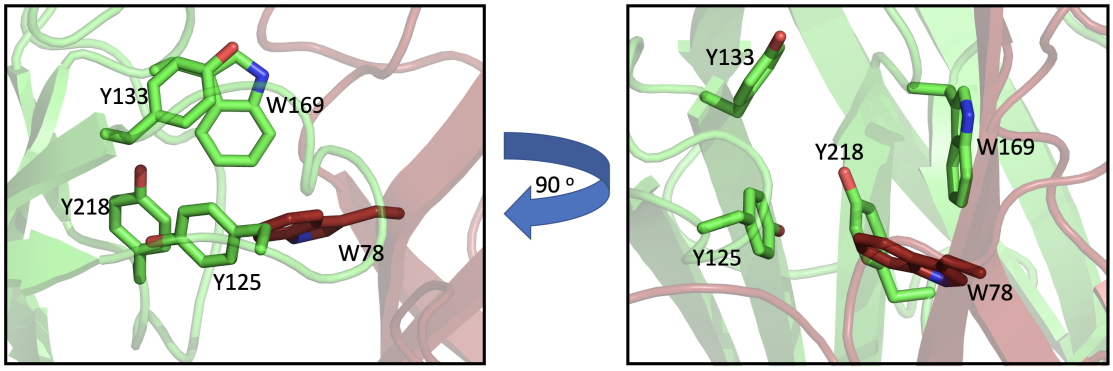

Figure 1.3: Snapshots of the α-δ interface orthosteric site. The five aromatic box residues are represented as sticks with α subunit residues in green and δ in red. Residues are labelled according to uniprot numbering.

Successive fluoridation of mouse α1W149 decreased sensitivity to agonist witch each individual fluoridation but not for other tryptophan residues located at this aromatic box. The small size and electron withdrawing nature of the fluorine atoms used here demonstrate that the reduction in agonist binding is the result of the perturbation of the π-orbital present on the benzene ring of tryptophan and not as a result of steric interactions with other side chains [51]. In another study, mutation of additional aromatic amino acid residues that comprise the binding site demonstrate that residues αY190 and αY198 (as well as αW149) also contribute substantially to

agonist binding at the adult mouse muscle nAChR [52]. Whilst this was shown in part to be mediated via hydrogen bond interactions as demonstrated by the change in ACh binding free energy by +2 kcal/mol after Y198F mutation, the additional 2 kcal/mol change after Y198A and Y190A respectively are probably too large for a simple van der Waals interaction and point to other steric and conformational effects that shape the overall binding site.

1.3.2 Transmembrane domain

Four α helices comprise the TMD of each nAChR subunit with an extended M4 helix that protrudes into the cytoplasm of the cell and an MX helix that resides in the juxta-membrane region between the transmembrane and intracellular domains. The interdomain M2-M3 loop residing between the ECD and TMD interacts with residues from the Cys-loop and β1-β2 loop to propagate the global conformational change after agonist binding and enable the pore lining M2 helix to rotate [53]. Upon M2 helix rotation, hydrophobic residues move into hydrophobic pockets located at the interfaces of transmembrane domain subunits [54].

Helix M4 is exposed to the plasma-membrane and is involved in lipid and neurosteroid sensing [55] as also demonstrated for the same strctural motif in the GABAR [56] suggesting a conserved pLGIC wide lipid and neurosteroid sensing mechanism. Modulation of the lipidic content of the bilayer can induce various degrees of M4 coupling and decoupling of M1 and M3 helices with effects on agonist binding and kinetic properties of the receptor [57, 58]. This has been further shown by how alanine mutations of the aromatic residues of the hydrophobic core between M1, M3 and M4 helices, thereby disrupting interhelical packing, lead to gain-of-function effects [59]. This lipid exposed region also contains a cholesterol recognition motif that further modulates nAChR function [60].

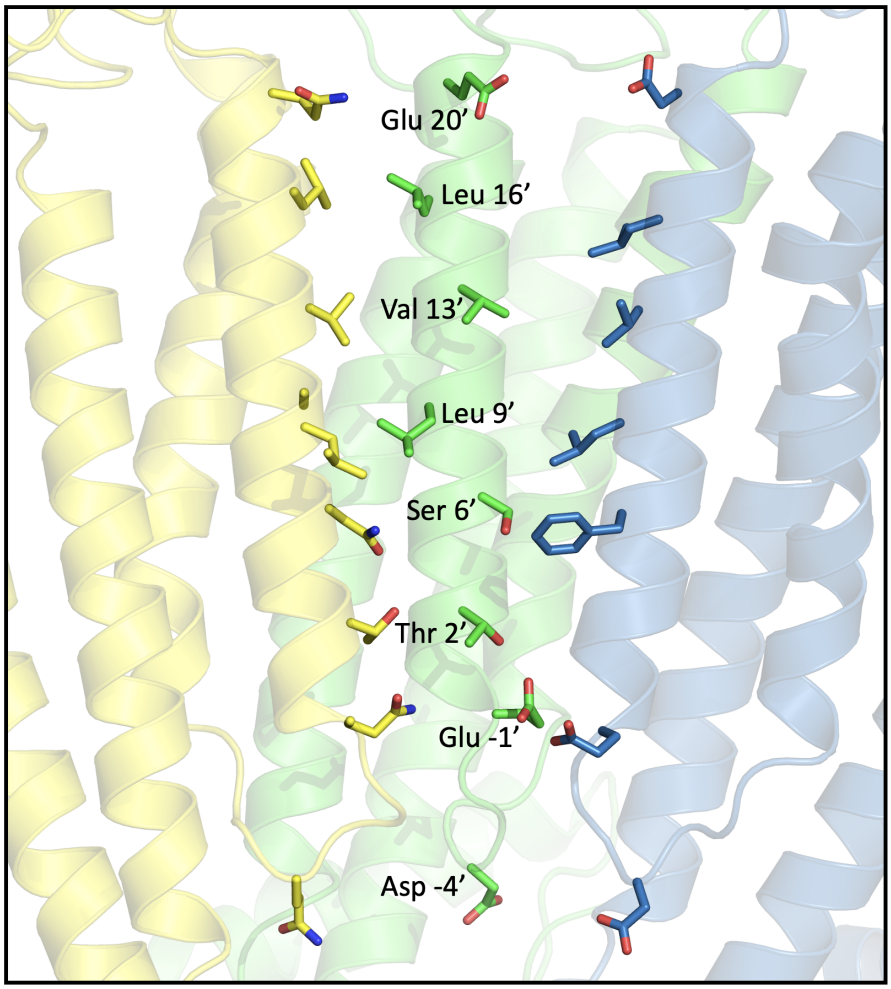

Figure 1.4: M2 pore lining helices of ϵ (yellow), $\alpha 1$ (green) and β (blue) transmembrane domains. Additional α and δ subunit have been removed for clarity. Pore lining residues are represented in a stick representation and labelled according to the prime numbering system [61].

The Golgi retention motif is thought to reside on MX helices, with perturbations in MX helices of δ, β and ϵ subunits all increasing golgi retention [62, 63]. Similarly, in GFP tagged ϵ subunits, deletion of C-terminal M4 helix residues caused a reduction in cell surface expression and retention of subunits in the endoplasmic reticulum [64]. Further to this and explained in more detail in chapter 4, the M1 helices of all muscle nAChR subunits have a PL(Y/F)(F/Y)xxN ER retention motif [65] that prevents cell-surface expression of receptors that are not fully assembled.

The M2 helices of each of the 5 subunits that line the pore of the ion channel contain

many of the structural components required for selectivity and gating. Equivalent levels of each helix are numbered according to the prime numbering system, with positive prime residues located toward the ECD and negative prime residues toward the ICD. Mutations of charged residues at three associated anionic rings located at the -1', 20' and 27' positions cause substantial changes in the rate of ion flow [66] and selectivity [67]. The existence of oppositely charged positive residues at equivalent positions in anion channels further supports these distinct rings as determinants of charge selectivity and conductivity [68]. The narrowest position of the pore is located at the 9' region, which is thought to be the position of the gate, a near totally conserved residue across the cys-loop receptor family.

Previous computational work has also suggested that 13' valine residue is the predominant energetic barrier to ions [69], however recent structural data [39, 70] coupled with computational work contained within this thesis suggest that the 9' residues are likely to be the main gating barrier to ion translocation. Indeed, the recently published p-torpedo nAChR bound to α-BuTx shows that a constriction of around 3Å occurs at the 9' region- corresponding to the narrowest position in the pore. The inability for a 1Å diameter sodium ion to permeate the 3Å diameter pore demonstrates that ions traverse the channel in a hydrated state and that gating residues impart their effects via a hydrophobic gating mechanism [71].

1.4 The nAChR as an allosteric protein and its conformational transitions

With the development of the Monod-Wyman-Changeux (MWC) model of allostery [72], the nAChR was seen to exist initially in one of two states, either an open agonist bound state or closed agonist unbound state. This model was eventually expanded on to include a desensitised state [73]; a closed state bound to an agonist with high affinity. More recently however, these conformational states have been expanded upon further to include 'flipped' and 'primed' states [74, 75] and with the advent of

increasing computational power, molecular dynamics studies have demonstrated that all these states in fact represent points in a large overall conformational ensemble as part of a sprawling energetic landscape [13, 76].

An allosteric protein is defined as being comprised of multiple homologous subunits arranged in such a way as to possess at least one axis of symmetry and exhibit cooperativity between the subunits [9]. In the context of drug-protein interactions, allostery is asserted as a drug which is capable of binding at a site that is sterically distinct from the orthosteric endogenous ligand, typically exhibiting so-called heterotropic effects [72]. With nAChRs and pLGICs in general possessing a 5-fold rotational axis of symmetry along the central ion conducting pore as well as demonstrating cooperativity between subunits, these proteins are indeed allosteric. Here we will first examine the conformational transitions of the nAChR and how it relates to the concept of an allosteric protein.

From structural insights of several pLGICs in complex with different ligands/ in different states, a detailed description of how allosteric transitions are communicated through the nAChR have been determined. For example, cryo-EM structures of the GlyR pLGIC in 3 different states demonstrate that the global quaternary changes that occur after agonist binding are an anti-clockwise twisiting of the ECD with a concomitant clockwise twist of the TMD. This is also coupled with outward movements of the M2 pore lining helices allowing for ions to flow through the channel. Although the exact diameters of the open channel may differ between pLGICs, the underlying mechanism is likely to be the same [77]. Additionally, X-ray crystal structures of a pLGIC bacterial homolog in a liganded and unligand state also show the same quaternary conformational change where ECD subunits twist and ‘bloom’ by moving towards the extracellular vestibule [78].

In a meta-analysis of over 100 experimentally solved AChBP structures – a soluble ECD homologue of pLGICs that lack a TMD or ICD- each complexed with different

ligands, it was determined that the ability of a competitive ligand to open loop C such that it is less tightly associated with the ECD correlates well with each ligands' pharmacological profile. Smaller ligands with a tightly associated loop C were more likely to be full or partial agonists, whereas large ligands that caused loop C opening were more likely to be antagonists [79]. This demonstrates that as well as being involved in direct contact with the competitive ligand, loop C is also critically involved as one of the early steps in the conformational wave between agonist binding and gating.

The earlier hypothesis of pLGIC conformations suggested the existence of two states, open and closed [80] and that the efficacy of an agonist was determined by their ability to change the equilibrium constants between those conformations. More recently however, through analysis of kinetic rate constants derived from single channel recordings at both muscle nAChR and GlyR in the presence of either full or partial agonists, it has been shown that an intermediary stage exists between open and shut states denoted as the 'flipped' configuration [74]. Partial or full agonists have a different affinity for this state that determines their respective efficacies inasmuch that the resting closed receptor must overcome a larger energy barrier to reach the flipped state in the presence of a partial agonist than compared to full agonist but that once in the flipped state, receptors bound to either full or partial agonists both have the same propensity to isomerise to an open state [74].

Additionally, using single channel recordings and disulphide cross linking of the agonist binding loop C, in order to fix each binding site individually into an agonist bound conformation, the presence of multiple unique and distinct kinetic rates from closed to open was shown. This indicated the existence of pre-open 'primed' conformations. In this case, channels exhibited either quick openings or longer openings arising from the ability of both binding sites to activate either separately or simultaneously [75]. This single channel work demonstrates how nAChRs and pLGICs undergo a complex wave of multistate conformational isomerisations before

reaching the open state, with intermediary states obtaining different preferences for agonists.

In a combined study using MD simulations and tryptophan fluorescence quenching it was demonstrated that two tryptophan residues each from either the principle and complementary faces of the binding site had a reduction in their Trp fluorescence lifetime as a consequence of ACh binding-induced conformational changes [81]. Acrylamide is capable of quenching fluorescence of Trp residues and as such, application of ACh can prevent acrylamide dependent fluorescence quenching of these two key binding site Trp residues. By simultaneously mutating both of these Trp residues to Phe, acrylamide dependent fluorescence quenching remained the same in the presence or absence of ACh. MD simulations of AChBP in ACh bound or unbound states demonstrated that these Trp residues have a stabilised conformation in the ACh bound state and explains the results of the Trp fluorescence quenching. A conformational change in these two binding site residues are therefore likely the first step in the conformational wave proceeding agonist binding.

In a separate study, K145Q or D200N at the α subunit of the nAChR individually resulted in a reduction in channel opening whilst swapping of these mutants to generate a simultaneous K145D and D200K at the α subunit recovered channel function to WT. This indicated that K145 and D200 form a salt bridge with each other. Taken in conjunction with the structure of AChBP bound to carbamylcholine [82] - in which this salt bridge is disrupted by Y190 of the α subunit which forms a hydrogen bond with K145 and simultaneously interacts with the bound ligand, the first step in the conformational wave elicited post ACh binding is likely to occur via this triad of residues. Further to this, simulations of AChBP with and without ACh show differences in loop C conformations, replicating the bond breaking and formation of these three residues observed in the electrophysiology and structural data [81]. The new contact made by loop C Y190 with β7 strand K145 therefore allows agonist binding to be transduced in the direction of the gate. As this

interaction occurs within the subunit and quaternary motions of the entire receptor are a prerequisite to receptor opening, it is very likely that this represents an early step in the closed to open transition.

Mutant cycle ϕ value analysis is a technique that has been applied to pLGICs to discern the extent of coupling between a pair of residues. By measuring gating isomerisation constants between closed and open states in two single mutants, the corrosponding double mutant and comparing to WT, a free energy change can be derived, the value of which suggestive of coupling if the ΔG of the double mutant exceeds the sum of both single mutants. This is well documented in the GABAaR for example, which shows the existence of a conserved salt bridge between homologous residues [83] suggesting that the conformational waves exhibited across the pLGIC superfamily are largely the same and commensurate with the similar global topology seen in resolved 3-dimensional structures across eukaryotic and prokaryotic homologues of pLGICs. For nAChRs specifically, an extensive mutational analysis by Auerbach and colleagues determined that coupling between loop C and M2-M3 loop residues occurs despite occurring around 3 nm apart [84] and again provides evidence for how signals are propagated within subunit monomers. Computational efforts further support the notion that the general closed to open allosteric transitions across pLGICs are common for the receptor superfamily [85–87].

By combining computational studies and cryo-EM of a prokaryotic homologue of the nAChR, namely GLIC, the activated and resting states were simulated and demonstrate that in submaximal conditions before pH dependent activation, the number of accessible conformational states become more limited. This is consistent with the existence of a primed pre-activation state [88]. This study also provides more evidence that the conformational transition from closed to open proceeds through loops B and C via loop F to the M2-M3 loop and then finally to the M2-helix.

Rate equilibrium free energy relationships (REFER) expand on mutant cycle-ϕ analysis by determining the temporal contributions of individual channel domains and residues to the overall conformational change of the protein [89] as demonstrated for example by single channel recordings showing that R209 and E45 at the base of the α subunit ECD are energetically coupled [90]. By comparing the free energy difference in the gating isomerisation constants for single point mutation constructs to combined point mutations constructs, one can determine the extent of residue coupling by the level of synergy expressed from simultaneous point mutations. E45K or R209Q caused a substantial slowing in rate constants for opening and that simultaneous E45R+R209E mutations reverted rate constants for gating to WT like kinetics with an energetic value in excellent agreement of previously determined salt bridge interactions energies [91].

The neighbouring residue to E45, V46 is in close proximity to proximal M2-M3 linker region residues S269 and P272 and expanding this REFER analysis to include these residues also showed an energetic coupling between E45 to V46 which was couple to S269 and P272 via hydrophobic interactions [90]. By using ϕ-value analysis, the time it takes for individual residues to undergo a conformational change can be measured. To this end, it was shown that ϕ values for M2-M3 linker residues are very similar to that of M2 pore lining helix residues and that conformational changes in this region are therefore concerted and highly coupled with M2 secondary structural changes [92]. The results of individual electrophysiological and kinetic analysis taken together provide a clear picture that stitches together the individual components comprising the conformation wave that characterises the closed to open gating isomerisation after ACh binding.

1.5 Allosteric contributions arising from unique subunit interfaces

As we have seen, pLGICs are allosteric proteins with the ability for cross-communication within and between individual monomers and it is from the ability for subunits to contact each other and transmit signals via these conformational changes that agonist recognition can be transduced. The interfaces between subunits therefore represent a critical point of allosteric control with unique subunits coming together to form unique interfaces and overall receptor subtypes that shape the biophysics and pharmacology of nAChRs.

This is clearly seen for the $\alpha4\beta2$ nAChR which is found in two distinct stoichiometric arrangements [93] of $(\alpha4\beta2)2\alpha4$ and $(\alpha4\beta2)_2\beta_2$ subunits respectively and with a corresponding high and low sensitivity to ACh. Concatenation of low or high sensitivity subunits with an individual mutation introduced selectively in a single α subunit at the $\alpha(+)$ $\alpha(-)$ interface of $(\alpha4\beta2)_2\alpha4$ revealed the presence of a biphasic ACh concentration response curve [94]. This additional low affinity response explains the need for higher ACh concentrations to enable full activation of the receptor.

Another interesting observation from this study was that by introducing the same mutations selectively and individually at either of the two $\alpha4\beta2$ subtypes, two characteristically different concentration response curves were obtained- with one becoming biphasic compared to the other. This demonstrated that identical interfaces could have different responses to agonists depending on their location with respect to other subunits in the receptor [94].

In muscle nAChRs, by exchanging residues between δ and ϵ subunits known to contribute to agonist binding, the affinities for dimethyl d-Tubocurarine (DMT) for $\alpha\delta$ or $\alpha\epsilon$ subunit interfaces could be swapped [95] and this difference in preference for DMT was also demonstrated for foetal nAChR subunit interfaces [96]. Additionally, concatomeric GABAa receptors with selective mutations at individual interfaces also

show differences in agonist sensitivities between binding sites [97] and heteromeric receptors have evolved across the wider pLGIC class of receptors as a means of generating unique and finely tuned responses to agonists.

1.6 Allosteric modulation of nAChRs

With nAChRs being capable of isomerising between multiple states, there is ample opportunity to modulate this energy landscape to stabilise these distinct states as a way of altering receptor function. As well as this, given the large variety of different nAChRs as well as their implications in several commonly occurring diseases, subtype selective allosteric modulation provides a useful therapeutic strategy for treating the many diseases and pathologies that nAChRs may be implicated in whilst reducing off target effects.

A combination of structural biology, computational and biochemical methods have been helpful in elucidating previously unknown allosteric binding pockets in nAChRs. For example, at the $\alpha 7$ nAChR, a combination of site-directed mutagenesis and molecular docking demonstrated that the positive allosteric modulators PNU-120596, LY-2087101 [98] and 4BP-TQS [99] bind to intrasubunit transmembrane sites analogous to allosteric modulators of GlyR [100] and GABAaR [56]. X-ray crystallographic techniques have been helpful in finding the locations of allosteric pockets in addition to the precise binding modes of the corresponding ligands. In the case of the GABAaR- by fusing the readily crystallisable homomeric GLIC extracellular domain to the TMD of the neuronal GABAaR in order to facilitate crystallisation- the interfacial TMD binding sites of neursoteroid hormones tetrahydodeoxycorticosterone and pregnenolone sulfate could be elucidated. [101].

Photoaffinity labelling is another useful technique to elucidate allosteric modulator binding sites. These have the benefit of being able to distinguish between true binding sites and residues that contribute to allosteric transitions between binding

and gating. This circumvents the limitation of site-directed mutagenesis where residues that are implicated in gating or allosteric transitions might be incorrectly attributed to direct protein-ligand binding interactions. Photoaffinity labelling of the *Torpedo californica* nAChR demonstrated that tritiated physotigmine and galanthamine were capable of binding at α-γ and δ-β interfaces. This provided evidence of allosteric sites near the orthosteric binding site (α-γ) (figure 1.5) and at a non-canonical interface (δ-β) in the extracellular domain [102]. Allosteric binding sites at the *Torpedo californica* nAChR transmembrane domain have also been identified with this technique [103, 104].

As well as being identified as a potential allosteric residue capable of being photoaffinity labbeled by physostigmine, in a seperate study- *p. torpedo* mutagenesis of nAChR residue αW86 was found to result in a substantial loss of function for bisquaternary compound Suberyldicholine (SbCh) [105]. SbChs' 18.7Å length corrosponds roughly to the distance between the orthosteric site and that of αW86, providing an example of a bitopic ligand capable of binding to both orthosteric and distinct allosteric subsites simultaneously. This also further demonstrates the potential druggability of residues located N-terminally from the orthosteric site as well as the usefuleness of extended bisquaternary ligands for probing the location of allosteric pockets.

Additional photoaffinity labelling studies with etomidate analogues TFD-etomidate and TDBzl-etomidate show non-selective binding to the pacific electric ray *Torpedo californica* nAChR, 5HT3A and GABAa receptor transmembrane domains [106], [107]. This provides evidence for widely conserved allosteric binding pockets between several pLGICs.

Neuropsychiatric disorders and nicotine addiction are mediated in part by $\alpha4\beta2$ neuronal nAChRs [108] and due to their common occurrence there have been substantial efforts to develop subtype selective allosteric pharmacological probes

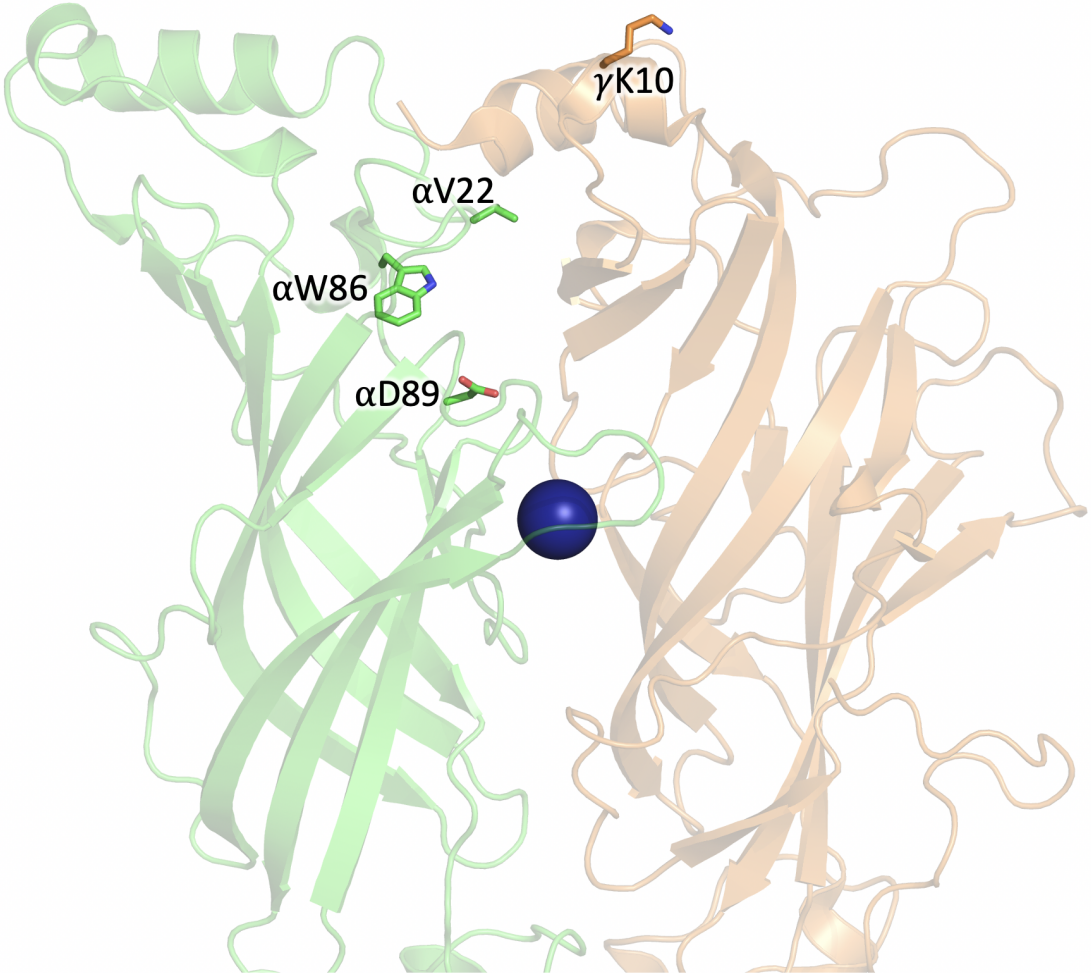

Figure 1.5: Image adapted from [102]. α and γ subunits of *p. torpedo* nAChR (PDB accession code 6UWZ [39]) represented as green and orange cartoon ribbons. The center of geometry of the aromatic box is shown as a blue sphere with allosteric residues identified from photoaffinity labeling studies with physostigmine shown as sticks.

for this nAChR subtype [109, 110]. Site-directed mutagenesis of the $\alpha4\beta2$ nAChR combined with docking studies identified an allosteric region residing at the complementary face of the $\alpha4\beta2$ nAChR binding site for the negative allosteric modulator KAB-18 [110, 111] which occurs in a similar position to physostigmine at the *Torpedo californica* nAChR. The complementary face of nAChRs may therefore provide an opportunity for allosteric modulation in addition to non-canonical ECD binding sites. In conjunction with this, chemical elaboration of orthosteric binding ligands have demonstrated success in probing potential allosteric binding interfaces. Through C-H functionalization of (-)-cytisine, an $\alpha7$ agonist, a series of enhanced

subtype selective compounds were generated which, through a combination of MD simulation and electrophysiology was shown to occur as a result of interactions with non-conserved amino acid residues located on the complementary face of the orthosteric binding sites [112] of a series of neuronal nAChR subtypes.

1.7 Molecular determinants of expression and stoichiometry in pLGICs

Different subunits effect biophysical and pharmacological properties of pLGICs in different ways and to different extents. The $\alpha4\beta2$ nAChR for example can exist in either high or low sensitivity stoichiometries being $(\alpha4\beta2)2\alpha4$ or $(\alpha4\beta2)2\beta2$ and whilst two of the original binding sites between those subtypes are the same, the presence of an interchangeable auxillary subunit that does not participate directly in agonist binding can have profound effects on receptor biophysics and pharmacology [94]. Expanding on this, comparison between foetal and adult muscle nAChRs also show substantial differences regarding ACh sensitivity, pharmacology, calcium permeability and kinetic properties [113–115]. Given the different functional consequences that result from the overall subunit makeup and arrangement of those subunits within a given pLGIC subtype, there should be specific molecular determinants/mechanisms that govern the correct assembly and trafficking of subunits.

Although not necessarily a determinant for enabling specific unique interface formation, the presence of an intrahelical aromatic network between TMD helices M1, M3 and M4 enables the packing of helices in such a way that generates the core underlying monomer conformation that gives rise to the overall pentameric quaternary structure of pLGICs [116]. In essence, these intrahelical interactions allow for multiple subunits to form interfaces with each other of which inter-subunit determinants then dictate the specific stoichiometries allowed in heteromeric pLGICS. The formation of these intrahelical interactions and their subsequent interhelical

associations also allows for the masking of the PL(Y/F)(F/Y)xxN ER retention motif present on the M1 helices of all subunits [65] preventing degradation of individual subunits and enabling the cell surface expression of fully formed pentamers.

Whilst the presence of a specific molecular determinant for assembly may not be necessary for homomeric subunits where instead, mechanisms of simple gene expression/ repression could dominate, for heteromeric receptors of specific arrangement, it is not feasible that their canonical arrangements occur by chance and specific molecular determinants will dictate these arrangements that arise by spontaneous associations.

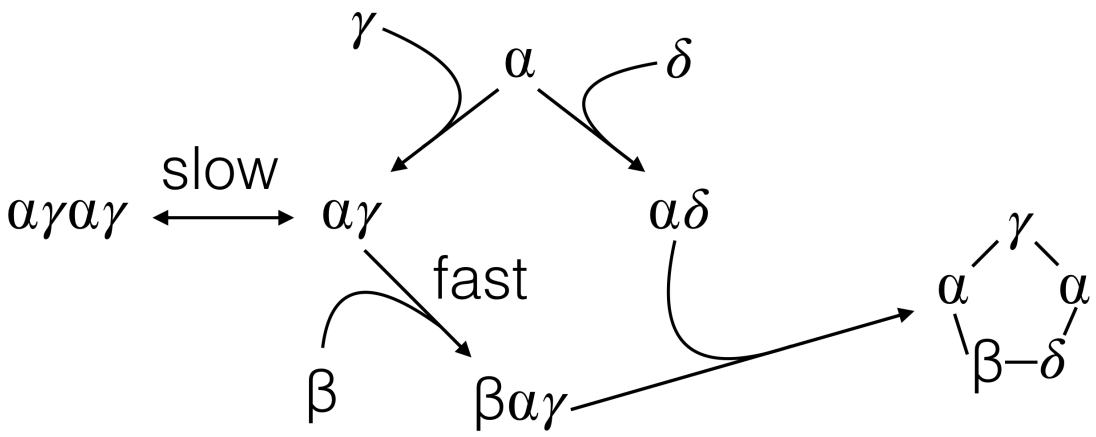

Figure 1.6: Image adapted from [117]. Steps towards the assembly of pentamers begins with the formation of both α-γ and α-δ dimers. The association of the β auxiliary subunit with an α-gamma dimer enables the formation of a pentamer through association of the β-α-γ trimer with the α-δ dimer. In the absence of the β subunit, α-γ tetramers form.

For mouse muscle nAChRs, by progressively mutating regions of the γ subunit to β, a stretch of amino acids in the γ subunit ECD were determined to be essential for forming $\alpha(+)$ $\gamma(-)$ interface associations by measuring the propensity for dimer formation from these subunits [117]. By selectively transfecting HEK293 cells and performing sucrose density gradient analysis on the permeablized cells, an assembly pathway was determined 1.6.

The inability for α-δ tetramers to form showed how the γ subunit resides between both α subunits. Comparison of the amino acid sequences between γ and δ subunits suggest that residues δK150 and δK145 interfere with associations between the $\delta(+)\alpha(-)$ and form favourable interaction with the $\beta(-)$ face instead- although this has not yet been experimentally determined. Point mutations at the β subunit suggest at least one of the many possible interfacial contacts, βR117, to be important in forming (-) contacts with the δ subunit although this positively charged residue would be expected to repel δK150 and δK145 residues. Additionally, since this study, the presence of pentamers containing two δ subunits have been identified, suggesting that the strength K150 and K145 in interfering with tetramer formation may be overstated. This also would expand on the previously determined set of steps in subunit associations [117] (figure 1.6).

Mutational analysis of the homomeric α1GlyR has also shown determinants of subunit assembly to be located at the ECD [118, 119] although the precise location of these determinants are not in homologous locations to δ and γ mouse nAChR subunits [119]. Clearly the full set of molecular determinants for muscle nAChR have yet to be completely explored.

1.8 Congenital Myasthenic Syndrome

One way to understand the complex structure-function relationship and specific determinants of correct stoichiometric assembly of muscle nAChRs is by analysis of genetically occurring pathologies and their resulting effects on channel function and physiology. One such disease for which a multitude of different genetically occurring pathomechanisms arises from is Congenital myasthenic syndrome (CMS). This disease of compromised muscle function can occur from over 24 different abbarent NMJ related genes [120] with over 50% of recorded mutations between 1988 and 2018 at the Mayo clinic occurring at endplate nAChRs [121]. Furthermore, a plurality of these mutations ouccur at the ϵ subunit as a result of a partial compensatory

mechanism from the γ subunit that rescues nAChR expression [122].

For CMS mutations at the nAChR that are penetrant and do not exhibit γ subunit compensation, several specific changes in nAChR biophysics caan be observed, not limited to but including slow-channel CMSs, fast-channel CMSs and also changes in levels of cell surface expression that can effect normal physiology.

1.8.1 Slow channel CMSs

Slow channel CMSs (SCCMS) are typically characterised by increased nAChR open durations, ACh sensitivity and also calcium permeability (predominantly for ϵ subunit containing nAChRs)- with a resulting muscular excitotoxicity that results in morphological damage [123] and non-responsiveness to pharmacological interventions. In three different kinships Croxen and colleagues identified two specific ϵ mutations [124] in which patients were homozygous. ϵL78P is located in the ECD towards the N-terminal region whilst ϵL221F is located at the M1 helix- both causing increased open durations in the presence of ACh.

Other SCCMSs include the TM2 ϵL269F & null mutation delQ267E heteroallelic SCCMS, TM2 βV266M SCCMS [125] and TM1 αN217K SCCMS [126], all of which not only had prolonged channel openings but also a commensurate increase in ACh affinity. The M2 helix located αV249F CMS causing mutation points towards the M1, M2, M3 helical bundle and results in constitutive activity as well as increased open duration in the presence of ACh [127]. The increase in ACh affinity resulting from a sterically distant residue demonstrates how distant structural elements are allosterically connected, in this case the binding site and gate.

Other TMD residing CMS mutations such as βV229F [128] or αN217K [126] located on the M1 TMD helix increased channel opening durations and with 10-fold decrease in ACh EC50 [128] at βV229F and 20-fold decrease for or αN217K [126]. Interestingly, lysine mutation of residues homologous to αN127 at other

muscle nAChR subunits had no effect on ACh binding or channel kinetics. Similar effects are again seen for δS268F residing on the M2 helix [129], which also had a decreased rate of transition from closed to open states as well as prolonged openings.

1.8.2 Fast channel CMSs

Most Fast channel CMSs (FCCMS) being recessive, occur as a result of heteroallelic mutations in which one mutant prevents the folding or expression of full subunits and the other mutation is incorporated successfully into pentamers therefore being the proximal origin of the CMS phenotype [121]. Heterozygous carriers of FCCMS mutations exhibit normal phenotypes due to expression of WT subunits. In two different patients, heteroallelic mutations of ϵP121L (common to both patients) and either an ϵS143L or ϵG-8R mutation in the signal sequence of the subunit were discovered [130]. The exhibition of a biphasic ACh binding affinity curve for this mutation compared to WT in which one part of this curve was WT like and another with greatly increased Kd suggested that this mutation participated in the binding site located at the α-ϵ interface and this impeded ACh binding caused a reduction in the open probability of these channels. Another example of a heteroallelic located FCCMS is the co-expressed δE59K and del756ins2 null mutation [131] that also resulted in short channel open durations and is located in the ECD. As the δ subunit is expressed in both foetal and adult nAChRs, it is unsurprising that this patient exhibits CMS symptoms from birth.

The αV132L mutation is located at the TMD-ECD interface of the cys-loop. [132]. This mutation caused a large decrease in ACh affinity and gating efficiency. The equivalent mutation of valine to leucine at the δ subunit caused an even larger change in gating efficiency but had a negligible impact on ACh binding affinity. Additionally, these same mutations introduced into β and ϵ subunits had no effect on either ACh binding or gating. This demonstrates the unique contributions of seemingly identical regions/residues of individual subunits and highlights the

potential importance of distant allosteric mechanisms acting upon and stemming from these regions as a consequence of the nAChRs pseudo-symmetrical topology.

Whilst one would expect mutations in the ECD and orthosteric site to have effects on ACh binding and efficacy, it might be expected that TMD related mutations should affect gating more directly. Indeed, the αF256L mutation located on the M2 pore lining helix hydrophobic girdle gate leads to a decreased number of openings with shorter durations. Its location is consistent with the observed kinetic effects and is further supported by how the mutation of the homologous βF267L, which also contributes to this same hydrophobic girdle effects nAChR kinetics in a similar manner [133].

The homozygous ϵW55R mutation represents an FCCMS ϵ subunit mutation that is not compensated for by a γ subunit and is expressed robustly at the surface of the cell [123] . The inability for WT nAChR rescue and expression of a kinetically altered receptor explains this particular CMSs lethality. This residue typically participates in the aromatic box orthosteric site and its mutation to a positively charged residue would have substantial chemically repulsive effects on the choline containing ACh. Patch-clamp recordings showed that this mutant construct possessed a 30-fold decrease in ACh binding affinity and an even greater reduction in gating efficiency and open probability [123] .

Typically, FCCMSs respond well to pharmacological interventions such as the AChE inhibitor pyrodostigmine- as the lack of sustained excitotoxic calcium usually seen in SCCMSs preserves neuromuscular morphology and therefore the number of available nAChRs. Therefore, this patient's inability to respond to treatment despite preservation of neuromuscular morphology further stresses the functional importance of ϵW55 and the need for two functional binding sites to maintain a normal safety margin for neuromuscular transmission. The ability of this mutant subunit to be incorporated into functional nAChRs also suggests that it is not important in the

determination of the specific stoichiometric arrangement of nAChRs.

1.8.3 nAChR deficiency syndromes

As well as CMSs that result from kinetic perturbations of nAChRs, a range of mutations have been identified that effect the ability of nAChRs to assemble properly or reach the cell surface in sufficient numbers. Due to the compensatory mechanism of alternative subunits to substitute for deficiently expressed ϵ subunits, these nAChR deficiency mutations are especially prevalent for ϵ subunits. Consistent with this, ϵ knockout mice have similar life spans to WT mice [122]. This also means that patients with CMS mutations that effect ϵ expression efficiency are usually heterozygous for the mutation or possess heteroallelic null mutations. One such example is the heteroallelic null mutation ϵC128S which prevents the formation of the Cys-loop and therefore assembly [134].

The ϵA411P mutation present on the amphipathic MX helix [135] possesses a duel pathomechanism where cell surface expression is reduced to around 31% of WT in 293HEK transfected cells but also with increases in the range of channel open probabilities. The cell-surface expression of nAChRs for this example is close to the threshold level for compromising the safety factor, with the additional kinetic effect essentially moving transmission into the pathological margins of the neuromuscular safety factor [135]. Equivalent engineered mutations at β and δ subunits did not have an effect demonstrating the specific importance of the ϵ MX helix in stabilising channel kinetics and enabling efficient expression of cell surface receptors. The difference between determinants for expression efficiency and allowable interfaces should be noted here, with the preservation of WT-like stoichiometry meaning that the MX helix is unlikely to be important in the determination of specific interfaces. In chapter 5 we explore the effects of the αL251R mutation, which also possesses this duel effect of reducing cell-surface expression alongside an additional active mechanism that could explain the transient CMS phenotype exhibited by

the identified patient [16].

The δE381K CMS mutation located on the intracellular loop is a rare CMS genotype that does not benefit from compensatory mechanisms often seen for ϵ deficient CMS patients and as such results in severe phenotypes [136]. In transfected HEK cells, this mutant construct displayed reduced rapsyn-nAChR co-clustering compared to WT whilst the homologous mutation in the ϵ subunit did not exhibit any effect showing the importance of the δ subunit ICD in enabling nAChRs to reach the correct position of the junctional folds of muscle tissue and at sufficient concentrations.

Other null ϵ mutations include ϵ1267delG located on the cytoplasmic ICD loop [137] and the missense mutations ϵR147, ϵP245L and ϵR311W found in three different patients [138]. *In vitro* analysis of ϵ1267delG demonstrated that α-BuTx binding levels were the same for both $\alpha 2\delta 2\beta$ and $\alpha 2\beta\delta\epsilon$1267delG with a large reduction in α-BuTx binding compared to WT and is another example of a mutation with a 'backup' compensatory mechanism.

1.9 Organophosphorus nerve agent exposure and AChE activity

NAChR function can also be perturbed through other exogenous means not to do with aberrant congenital mutations of proteins involved in neuromuscular transmission. For instance, organophosphate nerve agents (OPNAs), pesticide or insecticide exposure is a common and hazardous occurrence with pesticide exposures estimated to cause over 150000 deaths a year [139]. Organophosphorus compounds cause their pathological effects by covalently inhibiting acetylcholinesterase (AChE), thereby preventing the breakdown of ACh with the concomitant loss in spatial and temporal control of neuromuscular transmission.

1.10 ACh hydrolysis and neurotransmission mechanism

Under normal physiological conditions, during synaptic or neuromuscular transmission, quanta of ACh in synaptic vesicles are released from the pre-synaptic nerve terminal after receiving input in the form of an action potential. These quanta of ACh diffuse across the synaptic cleft and bind to receptors present post-synaptically. The amount of ACh released is substantially greater than what is actually required to elicit an end-plate potential and ensures that muscle contraction can still occur during sustained activation or under certain physiological stressors [140]. This phenomenon is known as the 'safety factor' of neuromuscular function.

In neuronal synapses, this usually consists of muscarinic receptors (a class of GPCR) or a number of different nAChRs - such as $\alpha4\beta2$ in the brain or $\alpha3\beta4$ in ganglionic nerve terminals. At neuromuscular synapses and specifically on muscle cells, muscle nicotinic acetylcholine receptors consisting of either an $\alpha2\delta\epsilon\beta$ subunit stoichiometry in adults or $\alpha2\delta\gamma\beta$ in the foetus and respond to ACh release by undergoing a conformation change that enables cations to permeate them. These nAChRs are present on protruding junctional folds with this deliberate morphology designed to facilitate efficient neuromuscular transmission. Voltage dependent sodium channels (NaV 1.4) present in high number at the depths of these junctional folds react to the threshold potential generated by activated muscle nAChRs, enabling a knock-on effect where muscle nAChR activation leads to NaV1.4 activation causing an action potential and the subsequent contraction of muscle tissue. To maintain the tight spatial and temporal control of muscle and neuronal firing, acetylcholinesterase, a serine hydrolase, catalyses the breakdown of ACh into acetic acid and choline which are then taken back up into the pre-synaptic nerve terminal to be recycled.

Acetylcholine hydrolysis is a two-step mechanism [143] mediated by the so-called catalytic triad comprised of residues S203, H447 and E334 [144]. This catalytic triad resides in the esteratic site, located within a narrow 20 Å deep gorge lined with

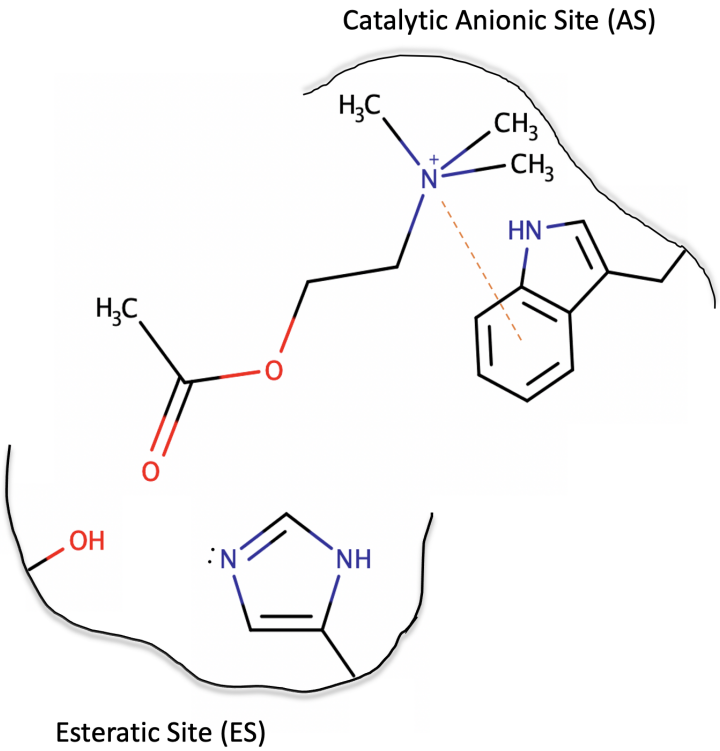

Figure 1.7: Figure adapted from [141]. Schematic representation of the AChE binding site. ACh occupies two main distinct pockets- the Esteratic Site (ES) and Catalytic Anionic Site (AS)

14 hydrophobic aromatic amino acid residues [145] (figure 1.8). ACh is stabilised in its binding site in part by the catalytic anionic site (AS), a site which is in fact not anionic but hydrophobic, stabilising the ACh choline moeity via cation-π interactions [146] as depicted in figure 1.7.

The large number of structural features described herein help to speed up ACh catalysis to a a rate close to the diffusion-controlled limit [147] and interfering with this process would have substantial deleterious effects.

Organophosphorus nerve agents (OPNAs) elicit their lethal effects by phosphylating the active site serine residue of AChE, rendering it inactive. This causes a subsequent increase in ACh at the synaptic cleft which can repeatedly bind in an uncontrolled fashion to downstream receptors. The wide symptomatology shown in patients who have been exposed to a nerve agent is indicative of the expression profile of

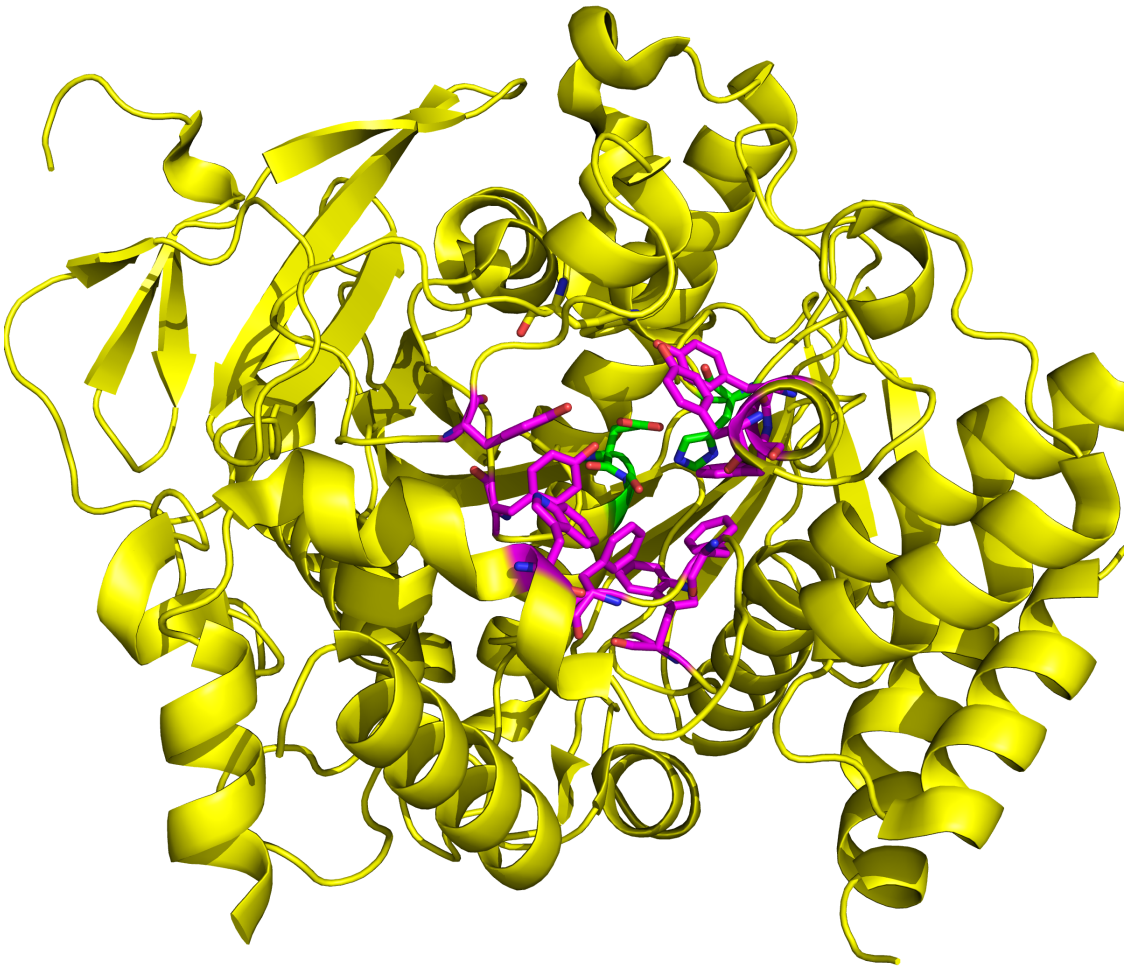

Figure 1.8: Crystal structure of mouse AChE [142]. The original structure is covalently inhibited by fenamiphos. Here, the phosphorylated serine has been manually remodelled in Pymol with the phosphate adduct removed. Hydrophobic tunnel residues are represented as magenta sticks and the catalytic triad residues as green sticks. The rest of the enzyme is shown in a yellow cartoon representation.

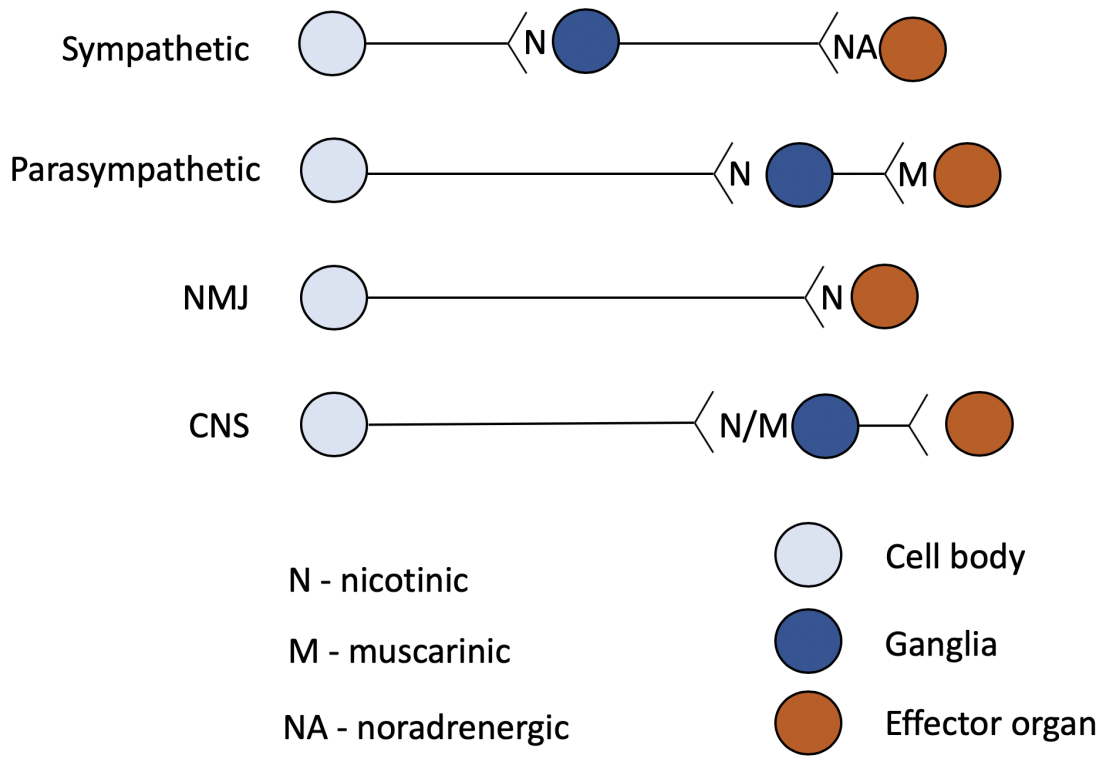

Figure 1.9: Branches of sympathetic and parasympethetic nervous systems and their innervation by neurotransmitters. Adapted from [25].

ACh receptors which are present parasympathetically, sympathetically, centrally and in neuromuscular synapses (figure 1.9) [25]. Death occurs via a combination of respiratory effects namely centrally mediated apnoea, bronchoconstriction and bronchodilation and paralysis of skeletal muscle tissue controlling breathing [25].

1.11 Mechanism of nerve agent actions

Figure 1.10 depicts the mechanism of AChE phosphorylation by Soman. This reaction proceeds as an associative addition-elimination reaction via the formation of a metastable pentacovalent intermediate transition state of the phospho-serine adduct which is thought to resemble the tetrahedral transition state of ACh during breakdown. For soman and sarin, fluorine acts as a leaving group in part through its stabilisation by the neighbouring Y121 hydroxyl group. This specific stabilisation might indicate that different nerve agents could proceed mechanistically via different

means although ultimately leading to the formation of a serine(S200)-phosphate adduct [148].

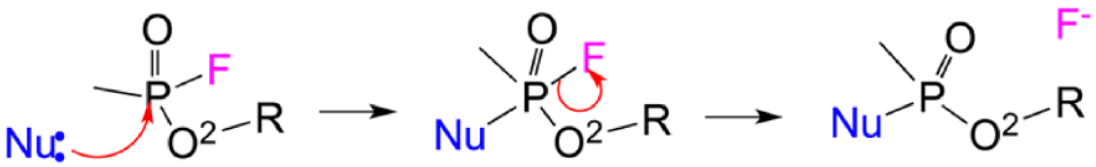

Figure 1.10: General reaction mechanism for G-agent phosphorylation. Figure taken from [148]

1.12 Organophosphorus nerve agents

Modern nerve agents were first synthesised in the 1930s by German chemist Gherard Schrader and initially intended for use on the battlefield. These 'G series' nerve agents include Tabun, Sarin and Soman.

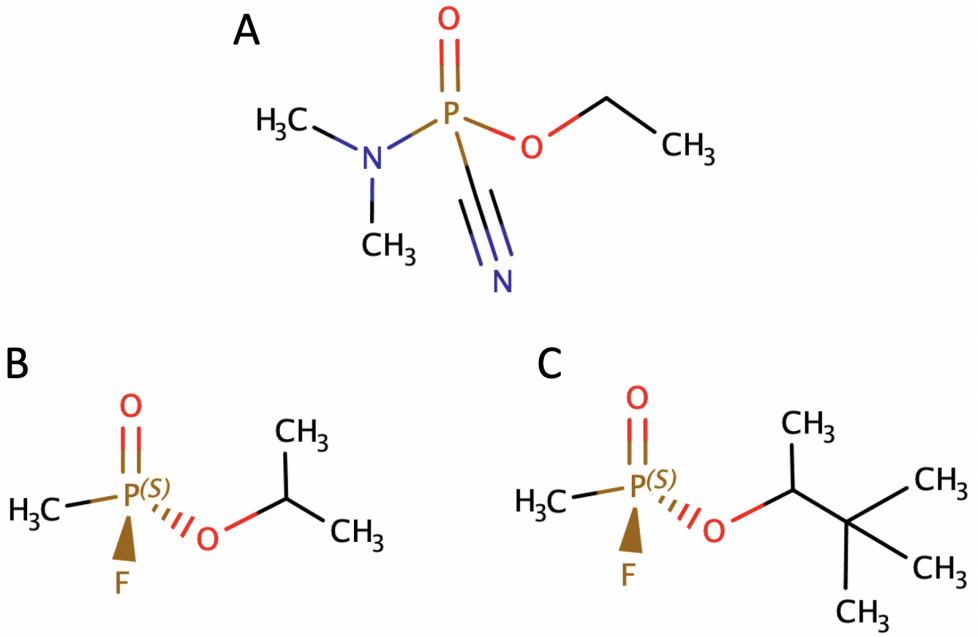

Figure 1.11: Tabun (A), sarin (B) and soman (C) chemical structures

Expanding on the toxicity of previously synthesised g-series nerve agents, VX was synthesised by scientists in the UK in the 1950s. This highly toxic and persistent

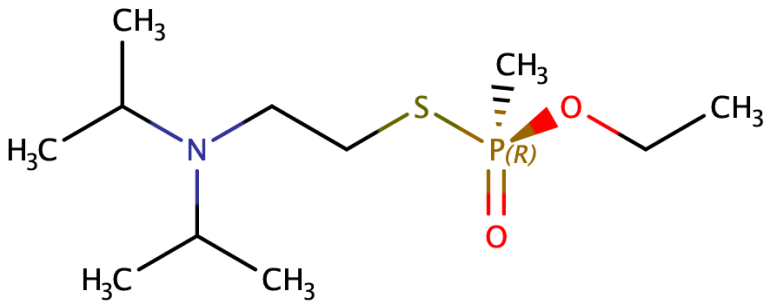

Figure 1.12: VX chemical structure

nerve agent mimics the transition state of ACh undergoing hydrolysis by ACh, thereby increasing VXs potency with respect to previous iterations of OPNAs [149].

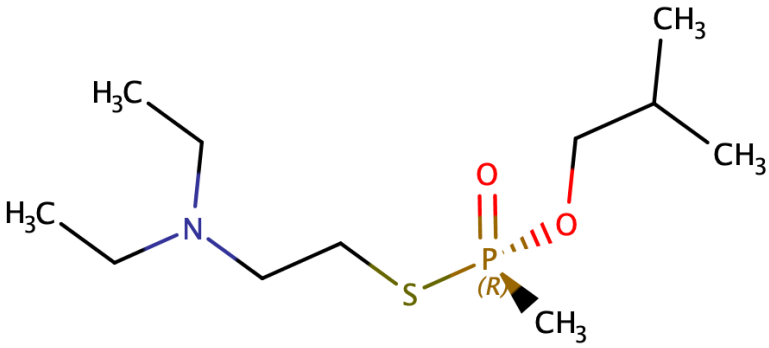

Figure 1.13: VR chemical structure

The next generation of nerve agents were developed by Russian Soviet scientists seeking to increase nerve agent potency and circumvent the chemical weapons convention (CWC) by developing a novel class of weapon, chemically related to common pesticides and insecticides. Initial iterations of these chemical agents were however shown to be impractical from a military standpoint as modern militaries are suitably equipped to deal with nerve agents on a battlefield setting, rendering their use in warfare to be limited. Historically, this has tended to lead to civilian populations being at the greatest risk of nerve agent exposure, be it from targeted attacks, terrorism [150–152] or from asymmetric warfare practices [153, 154].

Whilst all possessing the same overall pathomechanism, the physicochemical parameters of nerve agents are arguably the most important components to their lethality and how they are used. Low degradation times make for 'area-denial' weapons that may persist for long periods of time. These will tend to lack volatility compared to agents such as sarin which despite having a lower potency than viscous substances such as VX, are readily aerosilised. This has resulted in their pervasive use in events reporting mass casualties where their ability to spread quickly can cause indiscriminate damage to civilian populations, consequently overwhelming healthcare services. Conversely, viscous agents have been used recently in targeted attacks [155, 156] where the physicochemical nature of the nerve agent is exploited ostensibly to avoid collateral damage.

1.13 AChE Ageing

A critical component to nerve agent lethality is their ability to be reactivated. A study by [157] demonstrated a relationship between the Connolly surface area of VX, sarin, VR and cyclosarin nerve agents alkylmethylphosphonate moiety and the effectiveness of a series of Oxime reactivators. For oximes 2-PAM and obidoxime, a clear relationship can be seen, whereby nerve agents with larger alkylmethylphosphonate groups are less amenable to reactivation, with a corresponding decrease in both protective ratios and K_{r2} values. This indicates that a steric hindrance of the electrophilic reactive phosphorus of the nerve agent adduct by its alkylmethylphosphonate moiety physically prevents oxime reactivator approach. Interestingly, no such relationship could be observed for oximes HI-6 and ICD585 suggesting a different mechanism of approach to the enzyme-nerve agent adduct.

Despite this, alkylmethylphosphonate size is not the only determinant of a nerve agents amenability to oxime reactivation as can be seen for tabun which possesses a comparatively small ethoxy moiety and is not readily cleaved by a range of oxime therapies [158]. In this case, the CN group of tabun is believed to reduce

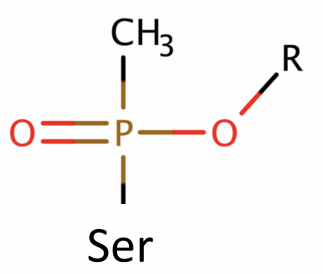

Figure 1.14: General structure of AChE-nerve agent adduct of VX, VR, sarin and cyclosarin

proximal phosphorus electrophilicity thereby preventing 'attack' by an oxime. A comprehensive analysis of 11 different organophosphorus insecticides, pesticides and nerve agents tested against 4 different oxime therapies shows large variations in oxime efficacy between different combinations [159]. Clearly, the large chemical diversity of organophosphorus nerve agents and their concomitant reactivation amenability by specific oxime therapeutics further complicates how first responders should act in the event of nerve agent exposure.

As well as the requirement of a specific oxime reactivator, AChE-OPNA adducts undergo a spontaneous dealkylation process after initial enzyme phosphylation in a process known as 'ageing'. This is where the aforementioned alkyl group undergoes a dealkylation resulting in a negatively charged AChE-OPNA adduct which is thought to increase enzyme stability and prevent reactivation. OPNA ageing propensity is generally dictated by the ability to form a stable carbocation, with increasingly branched alkyl groups acting as better leaving groups, facilitating this ageing process [160]. Indeed, soman, with its branched pinacolyl alkyl chain- has a τ 1/2 of 6.3 min [161].

Mutagenesis studies have demonstrated that this dealkylation reaction is primarily facilitated by W86, which participates in cation-π interactions with the cleaved carbonium[162]. Indeed, mutation of this residue to alanine reduced ageing rate by between 1850-3300 fold [163]. Mutations of other AChE binding site residues E202 and F338 to alanine also show marked decreases in ageing and taken with

associated molecular modelling, point to these residues' involvement in stabilisation of the imidazolium of H447 which participates in charge-charge interactions of the remaining oxonium nerve agent adduct (figure 1.15).

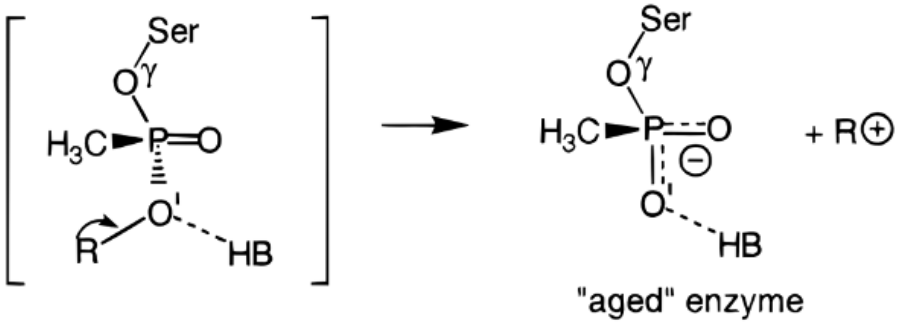

Figure 1.15: Ageing mechanism (figure taken from [143])

1.14 Oximes and their mechanism of reactivation

Whilst oxime therapeutics are theoretically a cure for nerve-agent exposure, when considering the potential for fast ageing and their non-degeneracy with respect to the large number of OPNAs, these antidotes are insufficient on their own. Further to this, due to their quaternary charged amine group- blood brain barrier penetrance is a problem, limiting efficacy for centrally mediated effects [164]. Despite this, oxime bispyridinium compounds have displayed success in reactivation of nerve agent phosphorylated AChE that is worth examining. The genesis of modern oxime therapies occurred over 60 years ago where it was found that methylation of 2-pyridine aldoxime (figure 1.16) to 2-pyridine aldoxime methiodide (figure 1.17) was capable of improving reactivation of organophosphate inhibited crude *Electrophorus electricus* enzyme solution, containing high concentrations of AChE [165]. This quaternary amine oxime reactivator was rationalised to interact with the AChE anionic site resulting in the million-fold improvement in non-methylated uncharged oxime. This 2-pyridine aldoxime methiodide (2-PAM) has been used as part of a combination therapy since.

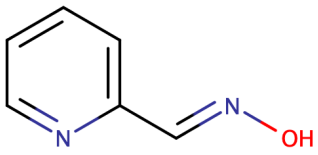

Figure 1.16: Structure of 2-pyridine aldoxime. The 2-PAM progenitor.

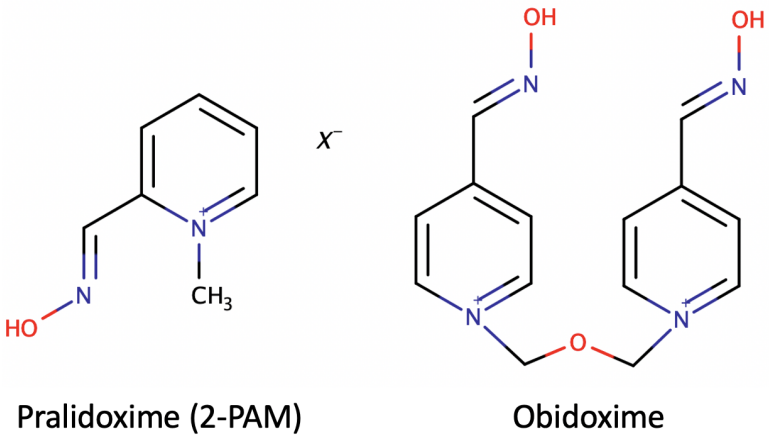

Figure 1.17: Two oxime therapeutics currently in use (image adapted from [166])

Later, bis-quaternary derivatives with good sarin reactivation properties were synthesised- with the additional quaternary site believed to interact with an additional anionic region [167]. This was later confirmed with x-ray crystallographic studies [168, 169] in which phosphorylated AChE with oximes HI-6, Ortho-7 and HLö-7.

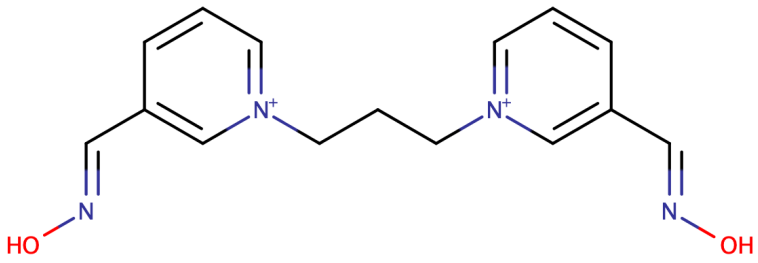

Figure 1.18: Structure of Trimedoxime (TMB-4), the first bis-quaternary oxime.

More recent attempts to improve the structure-activity relationship data has confirmed that a linker length between pyridinium groups of oxime BPD compounds of 3 or 4 is the most optimal [171] and should be a consideration if attempting to

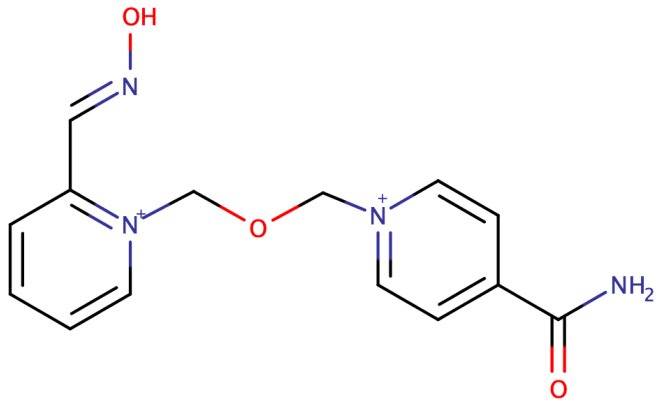

Figure 1.19: Structure of HI-6 adapted from [170]

improve selectivity over AChE for OPNA therapeutics focused on other targets. QM/MM studies of bispyridinium oxime HI-6 have demonstrated that this occurs via a concerted mechanism by which H447 activates the oxime in a manner that is analogous to serine activation under normal ACh catalysis by deprotonating its hydroxyimino group. The resulting activated bispyridinium oxime is able to cleave the phosphate adduct via nucleophilic addition where it forms a pentacovalent transition state analogue. The serine oxygen of the serine-oxime adduct then reforms its bond with the originally sequestered oxime bispyridinium proton at H447 allowing for the release of the oxime-OPNA adduct and resulting reactivation of AChE [170].

1.15 Efficacy of atropine sulphate

Atropine sulfate is a competitive muscarinic receptor antagonist and has been shown to reduce nerve agent lethality primarily by improving the response of anticonvulsant treatments such as midazolam while also possessing its own intrinsic anticonvulsant activity probably mediated by its interaction with centrally located muscarinic receptors. This is critically important due to the high association between the length of nerve-agent induced epileptic seizures and nerve-agent lethality [172, 173].

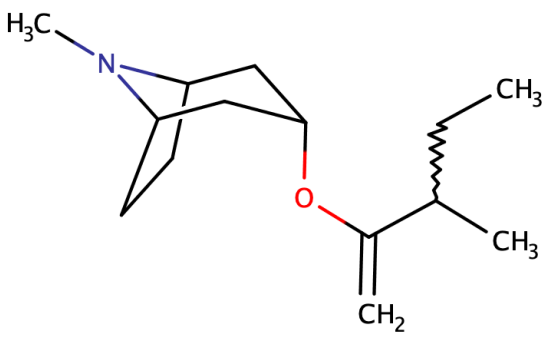

Figure 1.20: Structure of atropine

Additional effects include the cessation of peripheral systems such as bronchorrhea, bronchospasm and miosis where muscarinic receptors are present in smooth muscle tissue. Studies in rats show that large doses of atropine were capable of preventing cholinergic effects after sub cutaneous soman injection [174].

1.16 Bioscavengers

Animal studies have demonstrated that bioscavangers – proteins that react with OPNAs, either sequestering them or catalysing their breakdown and thereby preventing further reaction with AChE, could protect against nerve agent exposure [175]. Rats that had been given a carboxylesterase inhibitor prior to nerve agent administration exhibited decreased LD_{50} values for soman, sarin, tabun and paraoxon compared to control. By comparing the ratio of inhibition rate constants of CaE and AChE with in-vivo effects it was shown that CaE provided greater protection against organophosphates selective for AChE over CaE. This was not the case for VX however where its selectivity for AChE over CaE was found to be substantially greater than soman, sarin, tabun and paraoxon. It's negligible interactions with CaE compared to soman, sarin, tabun and paraoxon provide further evidence for the efficacy of bioscavengers for low doses of OPNA [175]. CaE knockout mice studies also provide further evidence as to the efficacy of bioscavengers in treating OPNA exposure [176]. Indeed, human studies in the 1950's demonstrated that butyrylcholinesterase (BuChE) – another AChE related serine hydrolase- could also

be inhibited by intravenous nerve agent administration [177] and that people who do not possess functional BChE lead normal lives [178].

Guinea pigs injected prophylactically with human BuChE, displayed substantial protection against soman and VX with corresponding increases in LD_{50} values of 5.5 and 8-fold respectively [179]. BuChE injection alone was well tolerated in this study, consistent with the lack of psychological and behavioural effects seen in BuChE injected mice [180]. This indicates that BChE and bioscavangers in general could in future be a useful therapeutic route to treat OPNA exposure. Despite this, concerns remain as to the potential immunogenicity [181, 182] and pharmacokinetic [183] challenges that limit current therapeutic use.

1.17 Non-oxime bispyridinium compounds

Despite the range of therapeutic OPNA exposure treatments, only muscarinic and AChE sources of pathology have been addressed and the downstream nAChR mediated effects of OPNA pathology is not currently treated in emergency settings. Early work in isolated animal tissue preparations and also from single-channel recordings demonstrated that oxime therapies could work in part via direct action with nAChRs [184]. Indeed, by removing the reactive oxime group from non-oxime BPD molecules the ability to recover some response in soman challenged guinea pig phrenic nerve-hemidiaphragm preparations could be seen.

Tetanic contractions of diaphragm preparations were measured and then challenged with 100 nM soman causing a near complete ablation of response. By applying a non-oxime bispyridinium molecule such as SAD-128, diaphragm response recovered to near 40% of maximal response. A subsequent reduction in response was observed post washout, with additional applications of soman having no effect on the residual diaphragm response. The lack of further reductions in diaphragm response after additional soman application demonstrates that all AChE in the sample preparation

had already been phosphorylated and that recovery post oxime or non-oxime BPD application was due partially to factors not associated with reactivation of AChE. Single channel recordings further indicated pore block as the mechanism for this recovery. This provided the first evidence that OPNA exposure could be treated via negative allosteric modulation of nAChRs. As large excesses of ACh is to be expected post OPNA exposure, a competitive antagonist of nAChRs would not be suitable due to the large amount of antagonist required and could paradoxically result in block of neuromuscular transmission. Indeed in more recent studies, non-oxime BPD molecule MB327 was able to restore neuromuscular activity in human intercostal muscle and rat diaphragm preparations challenged with soman in a concentration dependent manner, the effect of which was reversable on washout [185]. This is again indicative of direct action at nAChRS.

In vivo studies of MB327 [186] demonstrated that this non-oxime BPD molecule was capable of increasing the LD_{50} value of sarin in mice when used in conjunction with existing standard antidotal treatments compared to standard treatment regiments alone. Statistically significant changes could not be observed for tabun or soman however which is difficult to reconcile given the downstream mechanism of nAChR mediated effects of OPNA exposure being conserved for all OPNAs.

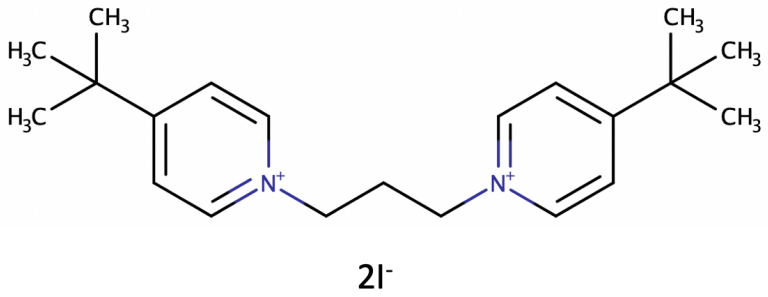

Figure 1.21: Structure of MB327 adapted from [186].

Although the principal of negative allosteric modulation for nerve agent exposure treatment has been suggested- other groups have pursued the potential of non-oxime

BPD compounds as positive allosteric modulators to treat OPNA exposure. MB327 and its two regioisomers were examined for their potential to act as 'resensitizers' of the nAChR by SSM-based electrophysiology and whilst currents could be obtained, very large concentrations of MB327 were required to elicit these effects [187]. Whole-cell patch clamp recordings have shown that carbamoylcholine and epibatidine responses at α7 nAChRs could be potentiated by MB327 and several additional congeneric short-linker non-oxime bispyridinium compounds [188]. It should be noted that whilst early work has pointed to pore-block as the principal mechanism of action of non-oxime BPDs, the non-specific chemical structure of these compounds suggests multiple potential mechanisms of action. MB327 has in fact been shown to relax smooth muscle via muscarinic receptors in rat preparations [189].

Further contrary to the concept of MB327 as a resensitizer- single channel recordings have shown pore block of the nAChR of this compound that is linked to recovery of soman challenged guinea-pig diaphragm preparations [190]. In the same study it was demonstrated that survival outcomes were improved in tabun challenged guinea-pigs treated with the water soluble dimethanesulphonate formulation of MB327 (MB399) and also for guinea-pigs challenged with soman when used as part of a combination therapy of pyridostigmine and hyoscine [191]. Additional *in vivo* work with analogous non-oxime BPD compounds structurally related to MB327 with either 3, 4 or 5 methyl linkers was shown to improve outcomes for sarin or cyclosarin poisoned mice when used as part of a combination therapy of HI-6 or obidoxime and atropine compared to HI-6 or obidoxime and atropine alone [192].

Radioligand binding studies have also shown that MB327 is able to increase the binding of orthosteric agonist epibatidine to nAChR [187]. Further to this, additional radioligand binding assays have demonstrated that epibatidine displacement is increased progressively with increasing linker length between the pyridinium moieties of BPD compounds at *Torpedo californica* and α7 nAChRs [193, 194]. Commensurate with structure-activity relationship data for non-oxime BPDs with

extended alkyl linkers- calcium fluorescence data also shows inhibition of nAChRs in muscle and neuronal derived cell lines with a relationship between linker length and inhibitory potency [195]. These SAR studies taken with the allosteric mode of action of the short linker-length BPD MB327 suggest that the allosteric component of non-oxime BPD activity occurs reasonably close to the orthosteric site. Unbiased docking of MB327 to *Torpedo marmorata* nAChR detected several potential binding sites located near the pore and also at subunit interfaces of the extracellular domain, however this study was not unsupported by experimental data [196] and should be taken with caution due to the low accuracy of the docking scoring algorithm used [197] and additionally the model used has been shown to possess inaccuracies in the M2 helical register [198].

Given the low therapeutic index of competitive antagonists for treating nAChR mediated OPNA pathology [199] and the toxicity of current lead non-oxime BPD compound MB327 [200], the elucidation of an allosteric binding mode for a non-oxime BPD compound would be useful in enabling further structure-based design efforts and improvement of existing compounds.

1.18 Aims of this thesis

1.18.1 Binding modes and bitopic interactions of variable alkyl-linker length non-oxime bispyridinium molecules at the human adult muscle nAChR

Structure-activity relationship data of non-oxime bispyridinium compounds demonstrates incremental improvements in antagonist potency with increasing alkyl-linker length at both muscular and neuronal subtypes. Substantial changes in *Hill slope* are observed between the range of 5-8 methyl groups, indicative of a change in the mechanism of action for this congeneric series. A structural and mechanistic explanation for this observation is however lacking.

In chapter 3 of this thesis, molecular dynamics simulations are performed on non-oxime bispyridinium molecules MB442 and MB505, bearing 5 or 8 methyl group containing linkers respectively, to discern the binding mode and mechanistic differences responsible for the changing pharmacological profile between short (CH3 <= 5) and long length (CH3 >=8) non-oxime bispyridinium molecules. These particular compounds are selected to improve the chance of observing a distinct mechanistic difference between variable length non-oxime BPD compounds.

Further to this, site-directed mutagenesis and two-electrode voltage-clamp electrophysiology of allosteric pocket residues as identified from MD simulations will be performed to discern whether there are specific molecular determinants responsible for interacting with and stabilizing the bitopic face of MB505, the pharmacologically active non-oxime BPD of the two selected molecules under investigation.

1.18.2 Delineating the structure-function relationship of a novel CMS mutation

Recent genetic screening by collaborators of a patient presenting with a mild CMS phenotype has identified a novel heterozygous de-novo CMS causing mutation (αL251R) located in the pore lining M2 helix of the α subunit of the muscle nAChR. Due to the heterozygous nature of this mutation, the possibility of various stoichiometric combinations is likely, however the inability to obtain single-channel electrophysiological traces preclude the studying of these individual stoichiometries.

In chapter 4 of this thesis, umbrella sampling molecular dynamics simulations are performed on a range of aberrant L251R stoichiometries in order to determine the mechanistic underpinnings of this CMS and inform the design of additional experiments to test the basis of charge selectivity in these mutant channels.

Additionally, the solvation of ions as a function of their position along WT and mutant channels as well as the corrosponding behaviour of key pore lining mutant residues are examined to further understand the detailed behaviour of permeation in pathological channels. Electrophysiological experiments from collaborators further validated the observation herein and reveal a new pathomechanism for CMS whereby mutant channels act in an inhibitory fashion to offset the end-plate potential.

1.18.3 $\delta(+)$ face amino acid residues responsible for enabling intransigent WT muscle nAChR stoichiometry

Previous experimental work has demonstrated that the existence of an auxiliary $\beta 2$ subunit for neuronal nAChRs has the potential to modulate the overall biophysical properties of the receptor. And whilst this change in biophysical properties as a result of swapping $\alpha 4$ and $\beta 2$ subunits (sequence identity 55.49%) is unsurprising, the extent of effect on biophysical characteristics as a result of subunit position in isolation is not understood. Due to the large subunit repertoire of muscle nAChRs with respect to other nAChR subtypes, the effect of subunit position on receptor biophysics can be studied in isolation of other mutagenic related effects as the swapping of δ and ϵ subunits would preserve both orthosteric interfaces. As this subtype's stoichiometry is fixed in nature, this further suggests that subunit position with respect to all other subunits is important in shaping biophysical characteristics of the receptor.

In chapter 5 of this thesis, the expression of non-canonical stoichiometries of human muscle nAChRs are assessed by heterologous expression of differing ratios of cDNA.

A combination of MD simulations and evolutionary data from a multiple sequence alignment of mammalian nAChR subunits is used to discern specific molecular signatures at the key assembly determining interface $\delta(+)\beta(-)$, as identified from

heterologous expression studies in this thesis.

Further to this, ^{125}-α-BuTx assays of chimeric $\delta\epsilon$ subunits are performed to determine the extent of Individual domains in contributing to $\delta(+)\beta(-)$ interface formation and validate observations from MD simulations and MSA integration.

"Ludwig Boltzmann, who spent much of his life studying statistical mechanics, died in 1906, by his own hand. Paul Ehrenfest, carrying on the work, died similarly in 1933. Now it is our turn to study statistical mechanics."

— D.L. Goodstein in his book *States of Matter*

2 Theory and Methods

2.1 Introduction

Several techniques exist for probing the structure-function relationships of ion-channel receptor proteins. In relation to the studies outlined in this thesis, a multidisciplinary approach combining molecular dynamics (MD) simulations, two-electrode voltage clamp electrophysiology (TEVC) and I^{125}-α-Bungarotoxin (I^{125}-α-BuTx) binding assays have been utilised to link molecular and atomistic level events to their causative macroscopic effects at the human muscle nAChR.
What follows is a description of the theory, limitations and detailed protocols of these individual methods.

2.2 Molecular Dynamics Simulations

Computer simulations of condensed, soft or biological matter may be conducted with various levels of detail in terms of the energetic description used to describe inter and intramolecular interaction terms and depending on the physical size of the system or timescale of the problem in question, certain levels of detail may be more or less appropriate.

For example, in the context of a large macroscopic system of upwards of a few million particles where questions of large-scale particle diffusion are under regard, a coarse-grained approach may be necessary where entire amino acid residues are modelled as just a few particles. This allows for a substantial reduction in computational expense at the loss of a certain level of detail that may not be as important for the problem under consideration.

At the other end of the scale, where questions of bond breaking or formation are being assessed, a quantum mechanical level of detail is typically required. At this level of detail where individual electrons are considered, these techniques are impractical for applications to systems of more than around a hundred particles and are limited to timescales on the picosecond regime.

All-atom molecular dynamics simulations provide an intermediate level of detail between both quantum mechanical and coarse-grained descriptions of a system. Fortuitously, due to the Born-Oppenheimer approximation, classical MD simulation approaches do a good job (when applied correctly) of recreating experimentally observed phenomenon and replication of associated thermodynamic ensembles.

The Born-Oppenheimer approximation describes how as a result of the light weight of electrons with respect to their associated atomic nuclei, they may adiabatically adjust their positions according to nuclear motions. To this end, atoms can be modelled as single point charges or 'classically' as spherical balls of charge attached to springs (bonds).

2.2.1 Classical Mechanics and the equations of motion

In order to effectively simulate the trajectory of particles in a given system, the energetic description of intra and inter-atomic interactions must be repetitively integrated and updated according to a specific dynamical law. For simulations using

classical force-fields, this usually consists of a Monte Carlo simulation or some form of Newtonian mechanics. For the purposes and scope of this thesis, a Newtonian approach is used and described herein.

Newtons equation of motion states that:

$$\vec{f} = m_i a_i \tag{2.1}$$

In the context of a molecular simulation however, the following formalism is more helpful:

$$X(t+1) \ = at^2 \ + \ v0.t \ + \ x0 \tag{2.2}$$

This states that given a set of initial conditions, namely the positions ($x0$), velocities ($v0$) and acceleration (a) we can calculate the Cartesian positions of all atoms at the next time step X(t+1).

The initial positions of the system are usually derived from an experimentally determined structure typically from X-ray crystallography, cryo-electron Microscopy or NMR techniques but can also be given by a comparative model or predicted structure from *ab initio* type methods.

Initial velocities can be determined from a Maxwell-Boltzmann distribution defined as:

$$f\left(v\right) = \left(\frac{m}{2\pi kT}\right)^{\frac{1}{2}} e^{-\frac{mv^2}{2kT}} \tag{2.3}$$

This equation is applied to each individual particle of the system with a mass = m and the desired temperature T. k represents the Boltzmann constant and v the velocity.

In order to derive the specific components of acceleration and velocity described in equation 2.2, we must initially obtain the potential energy at a specific time-step as shown in the following equation:

$$\vec{f} = \frac{-dE}{dr} \tag{2.4}$$

Where force is equal to the inverse derivative of the potential energy with respect to particle position. Expanding this out we obtain:

$$\vec{f} = m\left(-\frac{1}{m}\frac{dE}{dr}\right) \tag{2.5}$$

from which we can obtain the acceleration:

$$a = \frac{-1}{m}\frac{dE}{dr} \tag{2.6}$$

By using a suitable integration algorithm, we can then obtain velocities and particle positions from the acceleration.

2.2.2 Integration algorithms

In practice, equation 2.2 can be implemented in several ways and typically, updated positions are obtained by integration of the equations of motion using an integration algorithm. One way that this is achieved is through the Leap-frog algorithm, which is implement in two stages, firstly:

$$v_i\left(t+\frac{1}{2}\delta t\right) = v_i\left(t-\frac{1}{2}\delta t\right) + a_i\left(t\right)\delta\ t \tag{2.7}$$

Where the $a_i(t)\delta\ t$ (obtained by dividing the negative derivative of the potential energy with respect to said particles position by its mass) is added to the velocity from 1/2 δt prior to t, i.e $v_i(t-1/2\delta\ t)$. This new term is then added to the position of the particle at time t to obtain the updated positions one time-step along:

$$r_i\left(t+\delta t\right) = r_i\left(t\right) + v_i\left(t+\frac{1}{2}\delta t\right) \tag{2.8}$$

Given that at $t0$ velocities cannot be obtained from half a time-step in the past, for the initial generation of $v_i(t+1/2\delta\ t)$ we can simply divide $v(t)$ (as calculated by the integration of acceleration with respect to time) by 1/2 .

2.2.3 Time steps and ergodicity

Conservation of energy is a fundamental property in molecular mechanics. As such, the incremental timesteps used to obtain numeral solutions to the equations of motion must be smaller than the fastest vibrational motion in the system. With too short a timestep, the computational cost of a simulation will increase without any appreciable increase in accuracy beyond a certain timestep. With too long a time-step, there is a risk that particles may travel far enough between timesteps so as to be effectively superimposed in a non-physical manner. In such a case the energetic value of the system would increase to an extent causing it to 'blow up'. Typical MD simulation timesteps are 1 or 2 femtoseconds given constraints, although with

approximations such as those used for hydrogen mass repartitioning a 4 fs timesteps are not uncommon. From sufficiently long or multiple independent trajectories, we can obtain ensemble averages of the phase space that equate to the macroscopic or true thermodynamic time averages one would expect from experimental data:

$$< A > = \frac{1}{M} \sum_{i=1}^{M} A \left(p^N,\ r^N \right) \tag{2.9}$$

p and r represent the momentum and positions of N particles for a property of interest A. By dividing the summed value of A by the total number of observations, which in the case of a molecular simulation would be the timestep M, we can obtain the thermodynamic average of that property. In such conditions- these simulations are said to be ergodic, insofar that they sufficiently sample the available phase space and replicate the property of interest. Molecular simulations therefore harness statistical mechanics to predict macroscopic properties allowing us to obtain useful atomic or molecular level descriptions of experimental observables at time scales and resolutions inaccessible to those experimental techniques.

2.2.4 Force fields

To realistically model the chemical properties of a given system using finite computational resources – an additive set of approximate functions known collectively as the potential energy function is used. In molecular mechanics (MM) simulations these are comprised of intermolecular and intramolecular terms that balance detail and complexity with efficiency depending on the specific problem of interest. As such, a number of MM forcefields exist with varying complexity but with the same or a similar functional form defined as:

$$U = \sum_{bonds} \frac{k_i}{2}(l_i - l_{i,0})^2 \tag{2.10}$$

$$+ \sum_{angles} \frac{k_i}{2}(\theta_i - \theta_{i,0})^2 \tag{2.11}$$

$$+ \sum_{torsions} \frac{V_n}{2}(1 + cos(n\omega - \gamma)) \tag{2.12}$$

$$+ \sum_{i=1}^{N} \sum_{j=i+1}^{N} \left(4\epsilon_i j \left[(\frac{\sigma_{ij}}{r_{ij}})^{12} - (\frac{\sigma_{ij}}{r_{ij}})^{6} \right] + \frac{q_i q_j}{4\pi\epsilon_0 r_{ij}} \right) \tag{2.13}$$

The first three terms in this equation describe the bonded interactions with both bonds and angles terms being accurately described by simple harmonic potentials. Both terms are described energetically as a quadratic function in which deviation away from an equilibrium value of $l_{i,0}$ for bonds or $\theta_{i,0}$ for angles causes an increase in energy proportional to the respective force constants k_i. For classical MD simulations, as we are usually measuring properties that occur at equilibrium, large deviations from these values are not expected to occur, partly explaining how such simple mathematical descriptions of these processes successfully reproduce thermodynamic ensembles. The *torsions* term is typically described using the trigonometric cosine series expansion which describes dihedral angles between sets of 4 bonded atoms and outlined in more detail in figure (2.1).

Figure (2.1) describes a torsional potential for a molecule with a multiplicity of 3 and maximal torsional energy V_n of 8 (arbitrary units). γ represents the positions of the multiple energy minima and ω the torsional angle. Terms 2.12 and 2.13 denote the Lennard-Jones potential used to model van der Waals interactions and a coulombic term for the long range electrostatic interactions.

The Lennard-Jones term contains a collision diameter σ term describing the distance between the centres of two respective particles i and j at which their energy is 0. ϵ

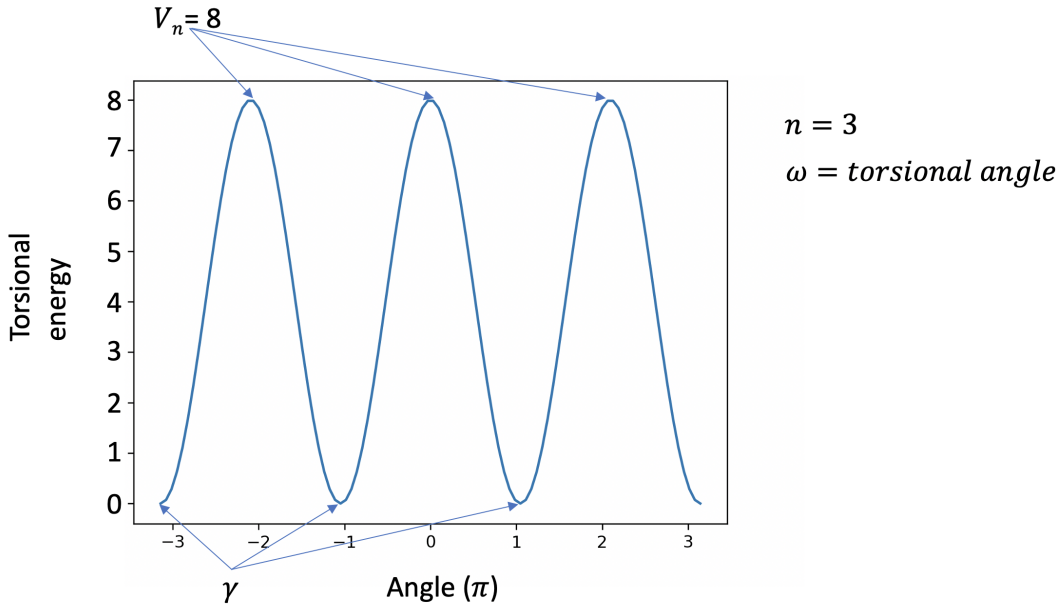

Figure 2.1: A graphical representation of torsional component of the potential energy function (equation 2.12). V_n denotes the barrier height of a single term in the cosine series expansion. n gives the multiplicity of the function, i.e. the number of minimum energy saddle points. γ denotes the phase of the curve or specifically at what torsional angle the respective energy minima reside. Image adapted from Andrew R. Leach – Molecular Modelling, Principles and Applications, second edition.

describes the well depth, which at increasing distances changes at a rate equal to r^6, modelling attractive longer-ranged London dispersion forces and van der Waals interactions, whilst distances $r =< r_m$ change at a rate equal to r^{12}, corresponding to the short ranged repulsive term describing steric hindrance.

The coulombic term contains parameters for ϵ_0 (permittivity of free space), the partial charges q of respective atoms i and j as well as the distance between them r. As mentioned previously, several different variations of this potential energy function exist, with the most commonly used protein forcefield being AMBER [202], CHARMM [203] and OPLS [204]. These force fields are all parametrised using a combination of experimental and quantum chemical information and as such are said to be semi-empirical.

When selecting a particular protein forcefield, it is important to consider what kind

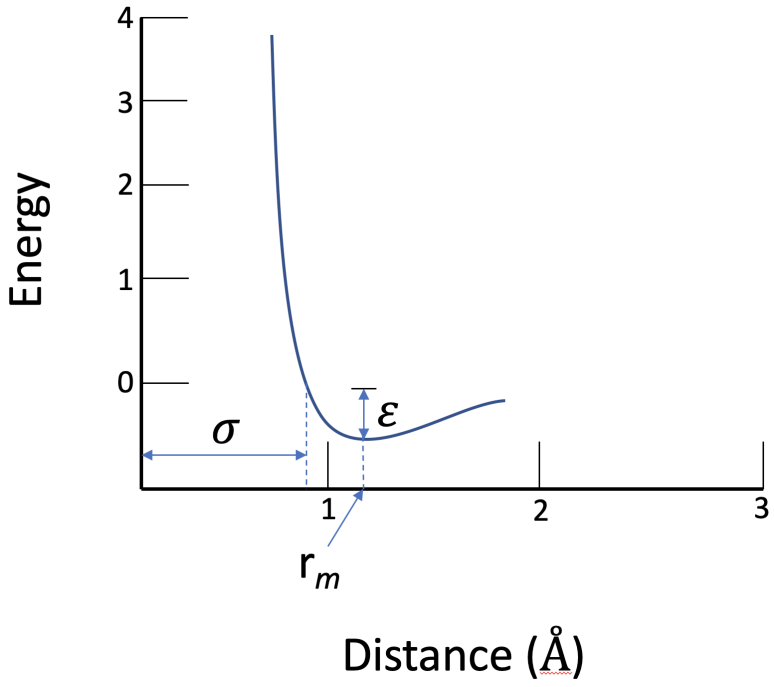

Figure 2.2:
A graphical representation of the Lennard-Jones component of the potential energy function (equation 2.13). ϵ denotes the depth of the energetic well, r_{m} the position of the energy well minimum and σ the seperation distance where the potential energy is equal to 0 kcal/mol. Image adapted from Andrew R. Leach – Molecular Modelling: principles and applications, 2nd edition [201].

of question you wish to address. For example, it might be more suitable to use one forcefield over another if looking at intrinsically disordered proteins over ones with high secondary structural content. Perhaps, your protein of interest is soluble in water or membrane bound, in which case consideration should be given as to the interoperability of different molecule parameters.

AMBER99SSB-ILDN is an iteration of the AMBER forcefield that has excellent agreement with experimental observables for the preservation of protein secondary structural elements, outperforming many other commonly used forcefields [205]. In addition to this, AMBER99SSB-ILDN has been assessed to work in conjunction with the Slipids forcefield for the simulation of bilayers [206]. As such, these two forcefields were selected to be used for the molecular simulation studies described herein. In addition to this, the General AMBER Force Field (GAFF) was used

to parameterise small molecules [207, 208], as this small-molecule forcefield can be used with both these parameter sets.

2.2.5 Constraints

Fortuitously, by constraining the vibrational motions of hydrogen atoms bonded to another heavy atom, a better description of these bonds ground state can be obtained then without constraints [209]. This also allows for the applied time step to be increased, thereby reducing the computational expense of the simulation. As the molecular simulation engine used in this thesis, GROMACS, utilises domain decomposition to parallelise MD calculations, the P-LINCS constraint algorithm was selected to account for bonds that cross different decomposition domains [209].

2.2.6 Neighbour lists and update groups

As LJ type non-bonded interaction energies fall off at a rate of r^6 with distance, these energetic contributions are low enough to be neglected at sufficiently long distances. Practically, this is achieved through the application of a non-bonded cut-off distance and implementation of an associated neighbour-list. This allows for atoms within a specified cut-off distance to be grouped into an associated array for a length of time in which only negligible movements beyond this cut-off distance occur (typically below 20 MD steps). This allows for LJ parameters to be calculated for a specific atom with respect to its neighbouring atoms while substantially reducing the overall cost of the MD simulation by circumventing the calculation of Euclidean distances between all particles to check if cut-off distances are satisfied at each MD timestep.

2.2.7 Particle Mesh Ewald Summation

As long ranged electrostatic interactions fall off very slowly at a rate of r^{-1} with distance, the total number of pairwise interactions required quickly becomes prohibitively expensive and due to the larger energetic contributions at further distances compared to those seen for the LJ potential- simply truncating longer

ranged forces would lead to non-trivial errors. Shorter ranged electrostatic particle-particle interactions can still be calculated in the same way as LJ interactions, however longer ranged interactions typically utilise the Particle Mesh Ewald algorithm to reduce the complexity of the calculation from O(N2) to O(N log N). This involves 'smearing' particle charges on a predetermined mesh at longer ranges and using a Fast Fourier Transformation, which is back-converted to obtain a potential that is applied to a specific particle associated with that particular point on the mesh [210].

2.2.8 Periodic Boundary Conditions

As molecular simulations of biological matter must be scaled to microscopic quantities of finite size, periodic boundary conditions (PBC) are implemented to enable the system of interest to be studied as if in bulk conditions. Simply, this means that if one particle leaves one side of the simulation box boundary, it reappears on the parallel opposite boundary preventing artefacts arising from particle-boundary collision interactions.

2.2.9 Statistical and thermodynamic ensembles

MD simulations harness statistical mechanics to elucidate the molecular underpinnings of macroscopic observables and to obtain their corresponding thermodynamic quantities. For questions of a biochemical nature, these processes happen and are measured under conditions of constant pressure, temperature and particle number, or are said to be in an NpT statistical ensemble. In order to faithfully represent these experimental conditions, MD simulations can be coupled to an external virtual heat bath and pressure piston.

2.2.10 Temperature and pressure coupling

Data acquisition for MD simulations in this thesis utilised both Nosé-Hoover [211] [212] and V-rescale [213] temperature coupling and Parinello-Rahman pressure coupling [214]. Nosé-Hoover temperature coupling allows the system under investigation

to be coupled to an external heat bath in which the equations of motion are modified to include an additional degree of freedom in the form of a frictional heat bath term p_ζ that is calculated by obtaining the difference between the instantaneous temperature of the system (T) and the set heat bath temperature (T_0):

$$\frac{(dp_\zeta)}{dt} = (T - T_0) \tag{2.14}$$

This heat bath term is then subsequently incorporated into the equations of motion as:

$$\frac{(d^2 r_i)}{(dt^2)} = \frac{F_i}{m_i} - \frac{p_\zeta}{Q}\frac{dr_i}{dt} \tag{2.15}$$

As the first derivative of position with respect to time equals velocity, it can be seen from the above equation that the velocities of the system are scaled with respect to the coupling constant Q, where Q determines the sensitivity to which velocities are scaled by the heat bath parameter.

The Parrinello-Rahman barostat has been shown to work well in conjunction with the Nosé-hoover thermostat and couples the system pressure in a similar oscillatory manner to the Nosé-Hoover thermostat with a strength associated to a coupling constant multiplied by the difference between the instantaneous system pressure and set piston pressure. The box vectors are then be modified according to these terms to offset pressure fluctuations.

Both Nosé-Hoover heat bath and Parrinello-Rahman pressure coupling have an advantage over other methods in that it provides a gentler oscillatory coupling that better represents the correct statistical ensemble. The downfall of this is the time it takes to relax the system of interest towards the desired temperature during equilibration stages. As such, during equilibration stages, a Berendsen barostat [215] was used, which relaxes the pressure of the system in an exponential fashion

defined as:

$$\frac{dP}{dt} = \frac{P_0}{\tau_P}\frac{-P}{\tau_P} \tag{2.16}$$

Precisely how the box vectors are scaled in pressure coupling should be given extra consideration when studying biological systems that contain a membrane. To this end, box vectors are scaled in a semi-isotropic fashion where the x and y planes are independent of the z-plane to preserve the integrity of the phospholipid bilayer.

2.3 Additional computational methods

2.3.1 Energy minimization

As part of the process in generating an initial set of coordinates X_0 we may artificially add water molecules, lipids and ions that might clash with the experimentally determined protein structure. indeed, the experimentally determined structure itself may possess inaccuracies that would cause a simulation to immediately fail due to steric violations. To relax this system down to a stable state amenable to simulation we may want to use energy minimization techniques. For the work contained in this thesis, a steepest descents energy minimization algorithm was used in the setting up of all MD simulation systems under investigation. This is performed by the following general procedure:

$$x_{i+1} = x_i - \gamma \nabla E(x_i) \tag{2.17}$$

Where if we consider the potential energy E of a particle x_i, by obtaining the negative gradient -∇ of $E(x_i)$ and iteratively displacing particle x_i by a certain value γ to obtain x_{i+1} until the change in $-\nabla E(x)$, γ and E are ≈ 0 we can arrive at a local minimum.

2.3.2 Homology Modelling

In the event that we do not have an experimentally determined set of initial coordinates X_0 for a given protein structure of interest, we can use comparative or homology modelling techniques to obtain one by using an evolutionarily related previously determined protein structure of which to base our model on. As proteins that are evolutionarily related are unlikely to deviate substantially in terms of their overall topological fold or tertiary and quaternary structure, we can arrive at a reliable computationally derived approximation of the structure given that our template structure is resolved to sufficiently high resolution and does not possesses a too low (below around 30%) sequence similarity [216] compared to our target structure that we wish to model. The software used to obtain the structures studied in this thesis was MODELLER [217] which uses obtain the structure through satisfaction of spatial restraints by implementing a pseudo-energy function that consists of empirical and statistical potential terms [218].

2.3.3 Docking and small-molecule parameterisation

Docking calculations were performed with Vina 1.1.2 [219]. Molecules were generated in Schrodinger Maestro (Schrodinger LLC, New York, 2020) with Gasteiger charges [220] added and non-polar H atoms merged in autodock tools 1.5.6 [221]. For each docking calculation, exhaustiveness was set to 8 with a grid box spacing of 1.0 Å used. The centre of the box was placed towards the centre of geometry of all aromatic box participating residues. Charges and bond types were then reassigned for the molecular mechanics simulations by applying AM1-BCC definitions to the selected docked poses with mol2 output files generated in the antechamber package [207, 222, 223]. Additional bonded, nonbonded or missing General Amber Force Field (GAFF) specific parameters [207] as well as atomic masses were generated with the 'parmchk2' command. Topology and coordinate files were generated using tleap and converted into GROMACS suitable filetypes with acpype [224].

2.4 Enhanced sampling

2.4.1 Calculating the PMF

As eluded to earlier, MD simulation techniques are often used to directly calculate thermodynamic values such as free energies or more specifically free energy differences between processes. Due to the large number of degrees of freedom in a biological system, inaccuracies in force field parameters, and lack of computational resources - the sampling of the rare states or events inherent to obtaining an accurate thermodynamic description of a process makes classical MD simulation incapable of obtaining such values. In order to circumvent this issue, a number of enhanced sampling techniques have been developed that allow non-physical perturbations to the system under study in order to recapitulate a free energy landscape and obtain reliable estimates of the free energies of specific processes.

Free energy calculations are a common method amongst computational chemists to obtain binding free energies of drug molecules to proteins. One example of such a method termed alchemical free energy perturbations successively transforms a ligands potential energy to determine an exact value for ΔG. Another method which utilises transformations in physical space rather than chemical space is umbrella sampling MD simulations (USMD) [225] and allows us to determine the free energy change of a process along a pre-determined physical coordinate ζ known as the potential of mean force W(ζ) (PMF) and is described by following equation [226]:

$$W(\zeta) = W(\zeta^*) - k_B T ln\left[\frac{< p(\zeta) >}{< p(\zeta^*) >}\right] \tag{2.18}$$

Where $W(\zeta^*)$ represents the distribution function obtained from the Boltzmann weighted average of the coordinate under investigation. Due to inadequate sampling, this average and therefore W(ξ) cannot be obtained using traditional methods and therefore the potential energy function must be biased along this reaction coordinate.

This is typically achieved by the implementation of a harmonic potential applied to a specific point along progressive intervals of the reaction coordinate:

$$w_i(\zeta) = \frac{1}{2}K(\zeta - \zeta_i)^2 \tag{2.19}$$

ζ_i is defined as the central position of the biasing potential and ζ as its instantaneous position in the simulation. Therefore, with deviations from ζ_i a potential is applied with the square of this distance to enable ζ to stay within the confines of our predefined window thereby increasing the sampling of this region. By 'stitching together' neighbouring windows along ζ and unbiasing this PMF using a technique known as the weighted histogram analysis method (WHAM) [227] we can obtain the free energy along the physical coordinate ζ. The WHAM equations are as follows:

$$P(\zeta) = \frac{\sum_{i=1}^{N_{sims}} n_i(\zeta)}{\sum_{i=1}^{N_{sims}} N_i \frac{(F_i - w_i(\zeta))}{k_B T}} \tag{2.20}$$

N_{sims} is the total number of simulations, $n_i(x)$ the number of counts in the histogram associated to a given umbrella window, $w_i\ (\zeta)$ the biasing potential, F_i the free energy shift, k_B the Boltzmann constant and T temperature of the system. This gives us the unbiased ensemble average or probability distribution for the reaction coordinate. The free energy shift of umbrella potential window F_i is calculated separately as:

$$F_i = k_B T.ln\left(\sum_{X_{bins}} P(\zeta)^{[\frac{w_i(\zeta)}{k_B T}]}\right) \tag{2.21}$$

2.5 Experimental methods

2.5.1 Reagents

ACh and Type IA Collagenase was purchased from Sigma-Aldrich and of analytical grade quality. MB505 was a gift from DSTL (UK).

2.5.2 Site directed mutagenesis and associated PCR

The QuickChangeTM Site-Directed Mutagenesis Kit (Stratgene) was used to make single point mutations. Oligonucleotides were purchased from Sigma-Aldrich (UK). After transformation and overnight culture in *e.coli*, constructs were extracted and purified using a Promega PCR (polymerase chain reaction) clean up kit before verification by Sanger sequencing (Source Bioscience, UK).
Oligonucleotide primers were purchased (Sigma UK) and optimised to have salt adjusted T_m between 70-80^{o}c and a GC content of around 50% to prevent the formation of secondary structures. Primer lengths were between 30 and 45 nucleotides in length with the mutation residing towards the centre of the primer.
The full PCR protocol for chapter 1 of this thesis is outlined in Table 2.1 with the reagents used listed below:

- H_2O 22 μl
- Pfu enzyme (High Fidelity) (2 mM stock solution) 1 μl
- DMSO 3 μl
- dNTPs (20 μM stock solution) 5 μl
- Forward primer (125 ng/μl) 1 μl
- Reverse primer (125 ng/μl) 1 μl
- Pfu reaction buffer 10X 5 μl
- Template DNA (50 ng/μl)

Thermocycler parameters:

Step	Cycles	Temperature (°C)	Time (minutes)
1	1	95	1
2	16	96 55 68	0.5 1 1/kbp
3	1	68	1/kbp

Table 2.1: PCR parameters for SDM

2.5.3 Chimera PCR protocol

For the chimeric constructs under investigation in Chapter 3, the PCR protocol outined in table 2.2 was used with the following reagents placed in 50 μl microcentrifugre tubes:

- Q5 (High Fidelity) 2X Master Mix 25 μl
- Forward primer (125 ng/μl) 1 μl
- Reverse primer (125 ng/μl) 1 μl
- Template DNA (50 ng/μl) 1 μl
- Nuclease free water 19 μl

Step	Cycles	Temperature (°C)	Time (Seconds)
1	1	98	40
2	35	72	30
3	1	72	30/kbp
4	1	72	120
5	1	4	Overnight

Table 2.2: PCR parameters for overlap extension

2.5.4 Chimera generation

Chimeric construct $\delta\epsilon\epsilon$ was generated using gene splicing by PCR-driven overlap extension [228]. Standard forward and reverse primers were generated for the N and C termini of the subunits to be included in the chimera. Overlap primers with approximately 50% δ and 50% ϵ nucleotide content at the point of overlap were also generated to enable truncated genomic DNA of one subunit to anneal to another subunit at the point of inflection. The primers used to generate the $\delta\epsilon\epsilon$ construct are shown in table 2.3.

Name	Sequence
Forward epsilon 5' δ overlap	ATCATCAACATCCTGGTGCCCTGTGTGCTCATCTCG
Reverse epsilon 5' δ overlap	CGAGATGAGCACACAGGGCACCAGGATGTTGATGAT
BamHI restriction Kozak seq. δ fwd	TATGGATCCGCCACCATGGCTGAAATGGAGGGG
Reverse ϵ XbaI	AGCTCTAGACTAAGGCTGGATACACGGCGC

Table 2.3: Primers used in PCR-driven by overlap extension

2.5.5 Ligation protocol

Restriction sites for BamHI and XBaI were incorporated into all constructs and genomic DNA was isolated using the cognate restriction enzymes. Ligation mixtures were made up to 20 μL volumes in a 1.5 mL microcentrifuge tube. 40.2 ng of construct DNA with a volume of between 1.56-2.67 μL depending on the specific construct was mixed with 2 μL T4 10X ligase buffer, 50 ng linear pcDNA3.1 and nuclease free water up to 19 μL. 1 μL of T4 ligase was then added last. The ligation mixture was gently mixed and incubated at room temperature for 10 minutes before heat inactivation at 65°C for 10 minutes. The resulting mixture was chilled on ice.

2.5.6 Transformation protocol

DH5α *e.coli* competent cells were taken from -80°c storage and 50 μL (100 μL if using ligated constructs) placed in a 1.5 mL Eppendorf tube. These tubes were then placed on ice before the addition of 50 ng DNA allowing for an incubation period of 10 minutes to thaw the cells. The tube mixture was then placed into a

42°C water bath for 35 seconds and then placed back on ice for 2 minutes. 950 μL LB medium was pipetted into the Eppendorf and incubated for 1 hour at 37°C and 220 RPM before spreading of 50-100 μL of the solution per selection plate. Plates were incubated overnight at 37°C for 18 hours.

2.5.7 Animals and oocyte preparation

Xenopus laevis were bought from Xenopus One (USA) and maintained at the John Radcliffe hospital animal house. Dissection of *Xenopus laevis* ovaries was performed in accordance with UK home office regulations and in compliance with the UK 1986 Animals (Scientific Procedures) Act. Ovaries were stored in pH 7.6 OR2 solution (2mM KCl, 82mM NaCl, 2.5 mM HEPES (N-2-hydroxyethlpiperzine-n'-2-ethansulphonic acid), 2mM MgCl). Mature oocytes were isolated with removal of epithelial layers through enzymatic degradation in 2mg/ml Type IA collagenase containing OR2 solution for 2 hours at room temperature on a slowly rotating platform. After this 2-hour incubation period, oocytes were washed in non-collagenase containing OR2 solution and placed in Barth's solution (88mM NaCl, 2.4mM NaHCO3, 1mM KCl, 0.3mM Ca(NO3)2, 0.82mM MgSO4, 15mM HEPES, 0.41mM CaCl2) with 5 mg/l neomycin at 18°C and pH 7.6.

2.5.8 cDNA microinjection

Drummond glass capillaries (Sartorius UK) were used to prepare needles with 3 mm lengths for microinjection, using a microelectrode puller (Campden Instruments). The tips of pulled needles were then manually broken using a pair of surgical forceps in order to create a 1 μm perforation. Needles were filled with mineral oil and attached to a Nanoject II microinjector (Drummond, USA). 1.5 μl cDNA was pipetted on to a drop of mineral oil where it was then extracted into the needle. cDNA injections were set to a volume of 50.6 nl per injection and the gene of interest in a cDNA 3.1 hygro (+) vector was injected directly into the oocytes' germinal vesicle. Injected oocytes were placed into individual wells containing Barth's solution. Oocytes were incubated at 18°C for no more than 5 days.

2.5.9 Electrophysiology

Oocytes were carried forward for experiment based on their health after 2-5 days post injection. Electrodes were pulled from borosilicate capillaries with 1-2μm tips using the same apparatus described in the previous paragraph and filled with 3 M KCl. The KCl filled microelectrodes were topped with light mineral oil to prevent evaporation of the solution. Electrodes with resistances of over 1 MΩ were discarded. The perfusion rate of the system was set at 15ml/min of Ringers solution and oocytes were clamped at a voltage of -60 mV in the two-electrode voltage clamp configuration. Recordings were facilitated with the HiClamp automated electrophysiology system (Multi Channel Systems).

2.5.10 Concentration response curves

All concentration response curves were plotted with a minimum of 6 data points and modelled with a four-parameter Hill equation of the form:

$$Y = Bottom + \frac{(Top - Bottom)}{(1 + 10^{((LogEC_{50} - X)HillSlope)})} \tag{2.22}$$

For inhibition curves, the $LogEC_{50}$ term is simply replaced by $LogIC_{50}$. EC_{50} and IC_{50} terms represent the concentrations required to elicit 50% of the maximal response of agonist and 50% maximal inhibition of antagonist on ACh respectively. Top and Bottom are the lowest and highest points on the concentration response curve respectively and *HillSlope* describes how steep the curve is and is a measure of cooperativity between subunits.

Individual data points were normalised according to the average of the two temporally closest EC_{100} control applications of ACh as demonstrated by the electrophysiology procedure outlined in figures 2.3 and 2.4. A ninety-second interval was used for drug applications for data reported in Chapter 1 and a two-minute interval for data reported in Chapter 3.

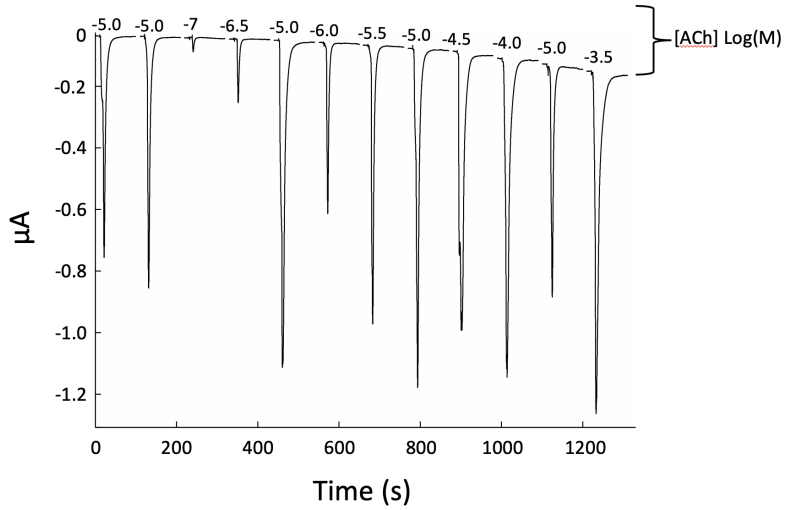

Figure 2.3: Representative continuous TEVC trace from a $2\alpha2\delta\beta$ concentration response curve. Data points were normalised with respect to the average value of the two EC_{100} ACh applications occurring on either side of the data point ACh application. In the above example, the EC_{100} [ACh] used was -5 Log(M).

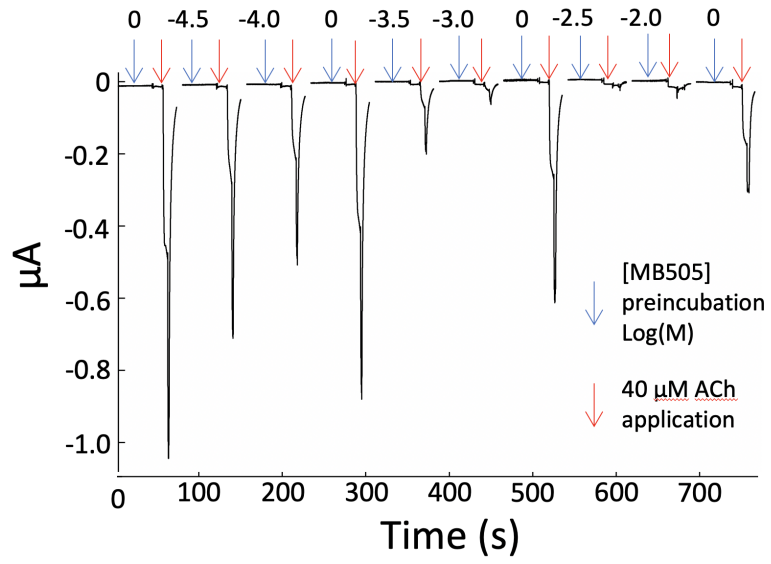

Figure 2.4: Representative continuous TEVC trace for increasing concentrations of MB505 in the presence of 40 μM ACh (EC_{50} [ACh]). MB505 data points were normalised with respect to the two the average of the neighbouring control ACh applications.

2.5.11 HEK293 cell culture and transfection procedure

1% PSA and 10% FCS was added to HEK293 cells bathed in DMEM and maintained at 5 CO_2 at 37°C. Prior to transfection, HEK293 cells were centrifuged and resuspended so that batches were not overconfluent and viability was checked. Transfections were done on batches of cells with over 95% viability with 10^6 cells plated per well. 6-well plates were used with three wells per conditions and wells were pre-coated with poly L Lysine (10 μg/ml) to help cell adhesion. Cells were left overnight at 37°C before transfection. If between 60-80% confluent the following day- a mixture of 3 μg of total cDNA with 20% glucose and PEI in 2ml of growth medium was added per well. To enable WT nAChR stoichiometries to be expressed, α, β, δ and ϵ/γ cDNA subunits were mixed and transfected in a 2:1:1:1 ratio. For chimeric stoichiometries, α, $\delta/\epsilon_{\text{chim}}$ and β cDNA subunits were mixed and transfected in a 2:2:1 ratio.

2.5.12 AChR ^{125}I-BuTx surface expression assay protocol

Relative cell surface expression of nAChR subtypes were determined by a ^{125}I-alpha-bungarotoxin (^{125}I-BuTx) binding assay. ^{125}I-BuTx solutions were made up to a strength of 1 million counts/ml diluted in DMEM solution with 1% BSA and 20 mM HEPES. 1 ml of the ^{125}I-BuTx solution was added per well condition with three wells per condition to ensure reproducibility. Before addition of ^{125}I-BuTx, cells were washed with PBS three times. After addition of ^{125}I-BuTx, cells were incubated at room temperature for 1 hour and gently rocked. Before measuring surface expression, excess ^{125}I-BuTx was removed by three washes performed in 5-minute intervals with 1 ml of PBS. Cells were then removed and placed into an Eppendorf tube by adding protein extraction buffer to each well. Measurements were obtained with a gamma-counter. Background radiation waas accounted for by deducting gamma values obtained from an untransfected HEK293 control cell group.

2.5.13 Statistical analysis

All experimental statistical analysis was performed in GraphPAD-Prism version 5. Concentration response curves were obtained from at least two separate batches of oocytes. Regressions were performed on each CRC individually, obtaining separate EC_{50} / IC_{50} values per experiment. These separate EC_{50}/IC_{50} values were then plotted in a scatter plot so that the obtained EC_{50} and IC_{50} values and their associated p-values were not biased by the curve fitting procedure. For the data obtained in chapter 1 of this thesis, all conditions were analysed with a one-way ANOVA with Dunnett post-hoc test For the data obtained in Chapter 3 of this thesis, an unpaired two-tailed t-test was used to compare two-conditions.

For the ^{125}I-BuTx binding assays, three data points per condition were obtained to ensure reproducibility and then normalized to WT values obtained from the same HEK293 cell batch and performed at the same time. A one-way ANOVA with Tukey's post-hoc test was used to determine statistical significance between all possible comparisons for all conditions for the ^{125}I-BuTx binding assays.

"There's a famous cathedral there, the Salisbury Cathedral. It's famous not just in all of Europe—it's famous all over the world, I think. It's famous for its hundred-and-twenty-three-metre spire. It's famous for its clock, the first clock made in the world that still runs."

— Ruslan Boshirov

3

Molecular determinants of non-oxime bispyridinium activity at the adult muscle nAChR

3.1 Introduction

Organophosphorus nerve agents (OPNAs) are a congeneric class of chemical weapon that work by irreversibly inactivating the enzyme acetylcholinesterase (AChE) [229]. This occurs as a result of the phosphonylation of the active site serine residue of AChE by the OPNA phosphonate group [230, 231]. As the breakdown of ACh is catalysed by AChE at a rate approaching the diffusion controlled limit [232], any perturbation of AChE function can have profound impacts on wider cellular function. Indeed, inactivation of AChE by OPNAs causes a large increase in ACh at the synaptic cleft and concomitant loss of the tightly controlled spatial and temporal signalling of neuromuscular transmission. This is the result of repeated binding of ACh to synaptic receptors without the clearance necessary to terminate the response to nerve impulses and clinically manifests itself in a number of ways. One of the first symptoms is fasciculation or tetanus of muscle tissue and is mediated by the fast excitatory response of endplate nicotinic acetylcholine receptors (nAChRs) [199]. Paralysis of muscle tissue due to depolarising block of nAChRs quickly follows

[233] ultimately leading to death. ACh is also capable of binding to muscarinic acetylcholine receptors (mAChRs) and as such, other tissue specific symptoms are commonly observed, including increased secretions and bronchoconstriction. Centrally mediated effects that lead to seizures and apnoea are also caused by brain expression of neuronal nAChRs and mAChRs [234].

Atropine, oximes and benzodiazepines are currently used medical interventions for OPNA exposure [235] with atropine acting as a competitive antagonist of mAChRs and benzodiazepines working to decrease the excessive brain excitability leading to seizures. Oxime therapies work by hydrolysing the OPNA- AChE phosphonate bond [236] thereby reactivating AChE and inactivating the expelled phosphonate adduct. Oxime therapies are therefore ostensibly a true antidote, however their use is hampered by the occurrence of chemical ageing effects instigated by a spontaneous dealkylation or deamidation of the AChE-nerve agent adduct [237, 238]. The resulting 'aged' enzyme adduct is homologous to the stabilised transition state deacylation analogue seen under normal physiological activity with a conformation that is inhospitable to nucleophillic attack via an oxime re-activator [142, 239]. Additionally, as individual oximes are not universal for all OPNAs, in an emergency scenario it would be very difficult to determine the correct oxime therapy to administer in time [240]. Despite this varied therapeutic arsenal, no small-molecule is currently in use to treat the nAChR mediated component of OPNA pathology.

Previous experimental work has demonstrated that removal of the oxime reactive group responsible for the hydrolysis of the AChE-phosphate adduct still retains the ability to recover skeletal muscle tissue activity in OPNA exposed muscle preparations [241]. This study also demonstrated via single channel recordings that these non-oxime bispyridinium compounds (BPDs) work by antagonising nAChRs in a non-competitive fashion. The use of a nAChR negative allosteric modulator could therefore prove to be a useful strategy in negating OPNA toxicity especially when considering the large concentrations of an orthosteric antagonist that would

be required to out-compete the substantially increased synaptic ACh concentrations post OPNA exposure.

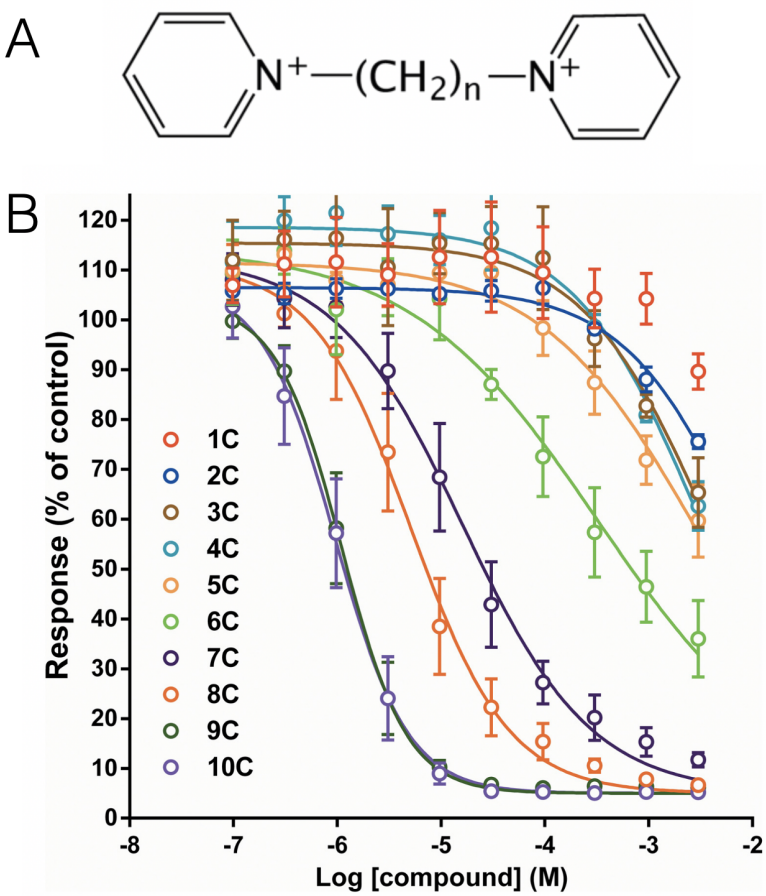

Figure 3.1: (A) General BPD skeletal formula. (B) Effect of linker length of BPD compounds on Ca^{2+} response to 10 μM ACh at CN21 cells (Reproduced from A. Ring 2016 et al).

More recently it has been shown that a series of related non-oxime BPDs antagonise nAChRs and the effectiveness of this antagonism is correlated with the length of the alkane linker that connects both pyridinium substituents [195] (figure 3.1). An important observation contained within this data is that their exists a substantial change in the observed *Hill-slope* at endplate nAChRs for BPDs with 6 or more methyl groups. This is indicative of the emergence of a similar binding mechanism for longer chain BPDs. As BPDs are also capable of displacing orthosteric agonist $[^3H]$epibatidine from *Torpedo californica* nAChRs with increasing methyl group

length, this suggests that this mechanism of action is in part, orthosterically mediated [242].

Additionally, as cation-π interactions are important in orthosteric binding of ligands with Cys-loop receptors [243–246], it is plausible that the presence of the quaternary charged nitrogen contained in each pyridinium ring, would be able to satisfy this criteria of orthosteric nAChR binding. Indeed, an analogous compound to BPDs, the bis-quaternary ammonium suberyldicholine dichloride, interacts in a bitopic fashion at *Torpedo californica* nAChRs with both the orthosteric site and a more distant extracellular domain residue αW86 [105].

So that key BPD-nAChR interactions and differences in binding modes between small and long length analogues could be determined so as to account for experimentally observed changes in *Hill-slope*, a homology model of the adult muscle nAChR based on the $\alpha 3\beta 4$ cryo-EM structure [247] was built, with BPDs containing either 5 or 8 carbon atom linkers docked into both binding interfaces and subjected to unbiased MD simulations. Pentyl and octyl BPDs were selected as they occurred at the extremes of the observed *Hill-slope* changes exhibited from calcium florescence data obtained in previous work [195]. From the simulations, we identified a single amino acid residue located on the ϵ complimentary face, namely ϵY131, that appeared to participate as part of a potential allosteric component to bitopic BPD interactions. Alanine substitution of this tyrosine residue and an additional conserved tyrosine on the δ complimentary face was performed. Concentration response curves were obtained for the 8-methylene linker, BPD 8 (MB505) at wild type (WT) and both mutant receptors ϵY131A, and δY134A respectively.

It was found that residue ϵY131, located on loop E of the complementary face of the α-ϵ subunit interface was able to participate as part of a bitopic component of long methylene linker BPD interactions but that the equivalent residue, δY134, could not.

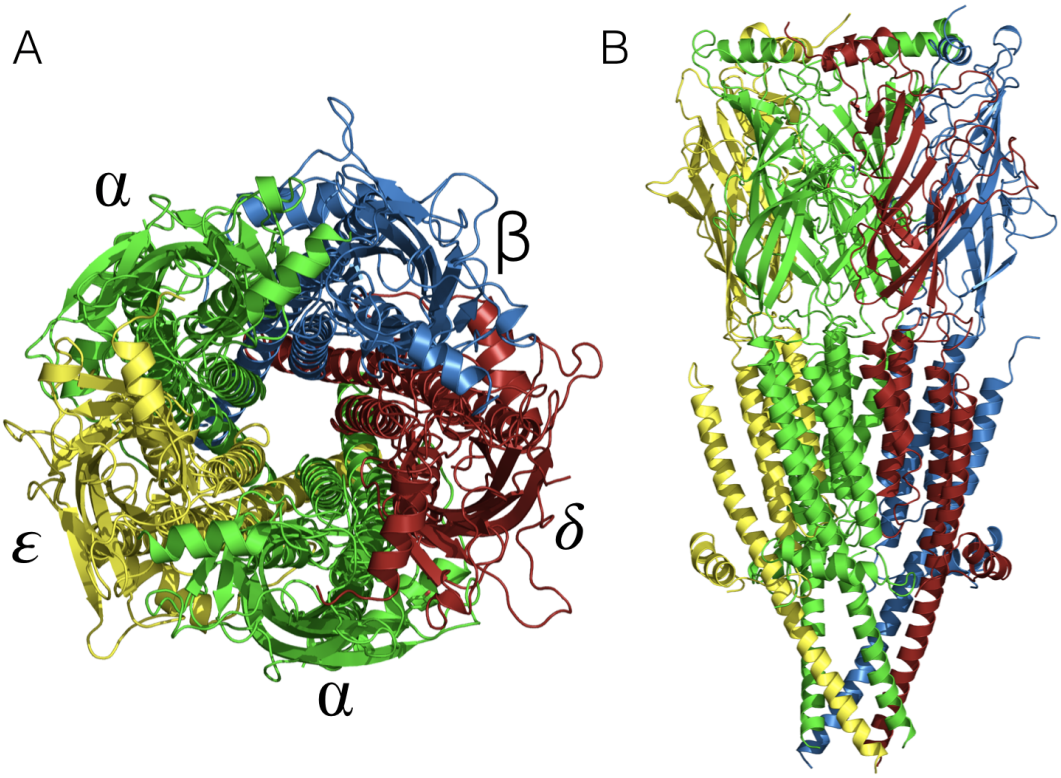

Figure 3.2: Resulting adult muscle nAChR model based on $\alpha 3\beta 4$ (6pv7) template. Panel is shows a top down view, with individual subunits labelled accordingly. Panel B is a side on view. The α helical region resides in the plane of the membrane with the M4 helix extending into the cytoplasm.

Additional observations from the simulations show the existence of two metastable states for MB442 denoted as 'up' or 'down' conformations, with each state effecting loop C dynamics uniquely. The down-state was associated with a more closely associated loop C with the orthosteric site and up-state with a more open extracellular solution exposed loop C [248]. The ablation of this down-state for MB505 offers a partial mechanistic explanation for the structure-activity-relationship data observed in previous experimental data. These dynamical differences coupled with the identification of a specific molecular determinant at the α-ϵ interface highlight the potential importance of the complementary face orthosteric subunit for enabling the design of selective inhibitors at the muscle nAChR and the usefulness of bitopic ligands in treating OPNA exposure.

3.2 Methods

3.2.1 Homology modeling

Human $\alpha 3$ and $\beta 4$ nAChR sequences to be used as the template structures were aligned with human muscle nAChr subunits, α_1,β_1,δ and ϵ along with additional genetically related sequences to improve accuracy of the final alignment. Isoform 2 of the α_1 subunit was used in the multiple sequence alignment (MSA) but with the removal of isoform 2 specific amino acids numbered 122-145 in B.4 and B.4 so that the final model contained the isoform 1 α_1 subunit.

As a template for which to base the homology model off, the $\alpha 3\beta 4$ nAChR (6pv7) cryo-electron microscopy structure [247] was used. The software, MODELLER v 9.12 [249] was used to build a single initial structure with additional loop modelling performed on three separate regions containing flexible loops of low conservation at the Loop-F regions of β, δ and ϵ subunits, with 10 models built per loop. This led to a total of 30 loop refined models for which at each individual loop, the lowest DOPE score model conformation of the 10 conformations per loop was carried forward for sequential modelling of the next loop F. Intracellular domain (ICD) residues were not included in the final model as this region could not be resolved in the experimentally determined template structure. Signal peptide sequences are incorporated into the numbering of residues, with residues labelled as according to uniprot numbering.

3.2.2 Docking and parametrisation

Vina 1.1.2 [219] was used to dock ACh, MB505 and MB442 into orthosteric binding sites using a grid box spacing of 1.0 Å positioned manually at the approximate centre of geometry of aromatic box residues αY113, αW169, αY218 and either δW78 or ϵW72. Exhaustiveness of the docking calculations were set to 8. Autodock 1.5.6 [250] was used to merge non-polar H atoms and add gasteiger charges [220].

Poses with the lowest distance between a pyridinium ring and center of geometry of αY113, αW169, αY218 and δW78 or ϵW72 residues were selected as the final pose. No consideration was given to the non-orthosteric pyrdinium moiety in selecting the final docking poses.

3.2.3 Simulation set-up and parameters

The infaltegro.pl script [251] was used to place the resulting model in a pure 1-palmitoyl-2-oleoyl-sn-glycero-3-phosphocholine (POPC) bilayer and then solvated with the TIP3P water model [252]. Neutralising concentrations of Na^+ and Cl^- ions were added before additional ions placed in the simulation box to make a final NaCl concentration of 0.15 M.

The steepest descents algorithm was used to energy minimised the system until convergence was achieved (step size 0.01 nm). The Particle mesh Ewald (PME) algorithm was used to calculated electrostatics [253]. H-bond constraints were applied using the LINCS algorithm [254], allowing for a 2 fs time-step. The protein forcefield used was Amber ff99SB-ILDN [255].

The Berendsen barostat was used to equilibrate each system in the NPT ensemble for 1 ns [256] (τ = 1.0). Temperature coupling was achieved with the V-rescale thermostat [213] (tau = 0.1) at 310 K. Backbone restraints of 1000 KJ/mol/Å^2 force constant were used as part of the equilibration step in order to let lipid molecules properly equilibrate. Z-axis expansions post equilibration left an excessively large buffer. Water molecules were therefore removed and periodic boundary conditions reduced along this axis before re adding solvent and ions to the system to decrease buffer size and improve sampling. The system was then equilibrated for 5 ns with position restraints removed to allow for protein equilibration. Production runs were carried out with the Nosé-Hoover thermostat [257] (τ t=0.5) and Parrinello-Rahman barostat [258] (tau p=1.0) for 100 ns each. Independent simulations were generated

by the use a random seed for velocity generation at the start of each production run.

3.2.4 Molecular biology and oocyte preparation

Human muscle subunit cDNAs were provided by Prof David Beeson and subcloned into pcDNA3.1 (Invitrogen). Site directed mutagensis (SDM) was performed using the QuikChange Mutagenesis Kit (Stratagene, Europe) and cloned constructs were verified by Sanger-sequencing (Source Bioscience).*Xenopus laevis* oocytes were purchased from Xenopus One (Michigan USA). Dissection of toad ovaries was done in accordance with UK Home Office regulations. Oocytes were placed in OR2 solution (2.5 mM HEPES (2-[4-(2-hydroxyethyl)piperazin-1-yl]ethanesulfonic acid), 2mM MgCl, 2mM KCl, 82mM NaCl). Manual titration of NaOH or HCl was done to adjust pH to 7.6.

Enzymatic digestion of mature isolated oocytes' theca folliculi and epithelial layers was done in a 2 mg/ml type IA collagenase OR2 solution at room temperature for 2 hours on a rotating platform. Oocytes were then bathed in Barth's medium (1mM KCl, 88 NaCl, 2.4 mM NaHCO3, 0.3 mm Ca(NO3)2, 0.82 mM MgSO4, 0.41 mM CaCl2, 15 mM HEPES)) at 18 °C with 1 μg/ml penicillin-streptomycin-amphoterecin b solution supplied by Sigma-Aldrich and 5 % horse serum at pH 7.6. Equal ratios of WT or mutant human nAChR α1, β1, δ or ϵ subunit cDNAs were co-injected into oocyte nuclei at a 50.6 nl/oocyte volume using a Nanoject Automatic Oocyte Injector (Drummond, Broomall, PA, USA). 2 ng of total cDNA was injected per oocyte. Oocytes were incubated for 2-5 days at 18 °C in modified Barth's solution with previously the specified antibiotic/antimycotic mixture post injection.

Microinjection needles were prepared with glass capillaries (Sartorius, UK) pulled using a horizontal microelectrode puller (Campden Instruments). A 1-1.5 μm wide

opening was introduced into electrode tips manually with surgical forceps. Needles were filled with mineral oil before cDNA aspiration with a Nanoject II microinjector (Drummond, USA). Oocytes were placed individually in respective wells of a 96 well plate and incubated for up to 5 days at 18 °C.

3.2.5 Electrophysiology

Recordings were performed within 2 to 5 days post injection. Oocytes were placed in a recording chamber of 0.1 ml and perfused at 15 ml/min with Ringer's solution of composition: KCl 2.8 mM, NaCl 150 mM, CaCl2 1.8 mM, HEPES 10 mM ; pH 7.4 adjusted with NaOH and HCl to obtain the desired pH. Two-electrode voltage-clamp (TEVC) was used to obtain current traces and holding potential set to -60 mV. The automated HiClamp setup (Multi Channel Systems) was used to obtain recordings. 3 M KCl was used as the electrode solution with an aliquot of mineral oil at the entrance of each electrode to stop evaporation and salt crystal formation. Electrode resistances did not exceed 1 MΩ. Serial dilutions of ACh in Ringer's solution was done from frozen stock of 10 mM on the day of the experiments. 6 to 8 point log concentration-response curve (CRC) were obtained for all constructs. All currents were normalised relative to maximal WT ACh response (1 mM).

MB505 concentrations were applied in half-log unit increases and applied in the presence of 40 μM ACh which corresponds to an approximate EC_{50} concentration to obtain inhibitory concentration response curves. Washes were 3 minutes in duration between drug applications. Two EC_{100} ACh applications were performed at the start of each experiment and also after every two incremental half-log increases in MB505 applications to reduce run-up or run-down of responses to reduce noise in the data and assess oocyte stability.

3.2.6 Data analysis

All data points were normalised to the average of the two EC_{100} control applications occurring immediately before and after the data point concentration in consideration. Prism 5 software (Graph Pad, CA, USA) was used to fit CRCs to a logistic regression four-parameter Hill equation as shown below:

$$Y = Bottom + \frac{(Top - Bottom)}{(1 + 10^{((LogEC_{50} - X)HillSlope)})} \tag{3.1}$$

Top presents the maximal values of each curve whilst *Bottom* was fixed to a value of 0. EC_{50} represents the concentration of ACh eliciting 50% of nAChR maximum response (I_{max}). *HillSlope* corresponds to the linear portion of the IC_{50} curve and is a measure of cooperativity. X is ACh concentration. IC_{50}s were also plotted with a four-parameter Hill equation which takes the same form as the above equation but with EC_{50} replaced with IC_{50} values. This is the concentration of antagonist required to inhibit 50% of receptor response. EC_{50} and IC_{50} values for each experiment were obtained from single experiments, plotted individually and all values analysed together by one-way analysis of variance (ANOVA) and Dunnett post Hoc test. A P value of less than 0.05 was considered to be significantly different.

3.3 Results

3.3.1 BPD-nAChR interactions as determined by conventional MD simulation

In order to obtain a mechanistic explanation for the changing *Hill-slope* observed by Ring et al. [195] and to explore specific ligand-protein interactions of BPDs with the adult muscle nAChR, we first constructed a comparative model based on the recent $\alpha 3\beta 4$ nAChR cryo-EM structure [247] as a template (figure 3.2).

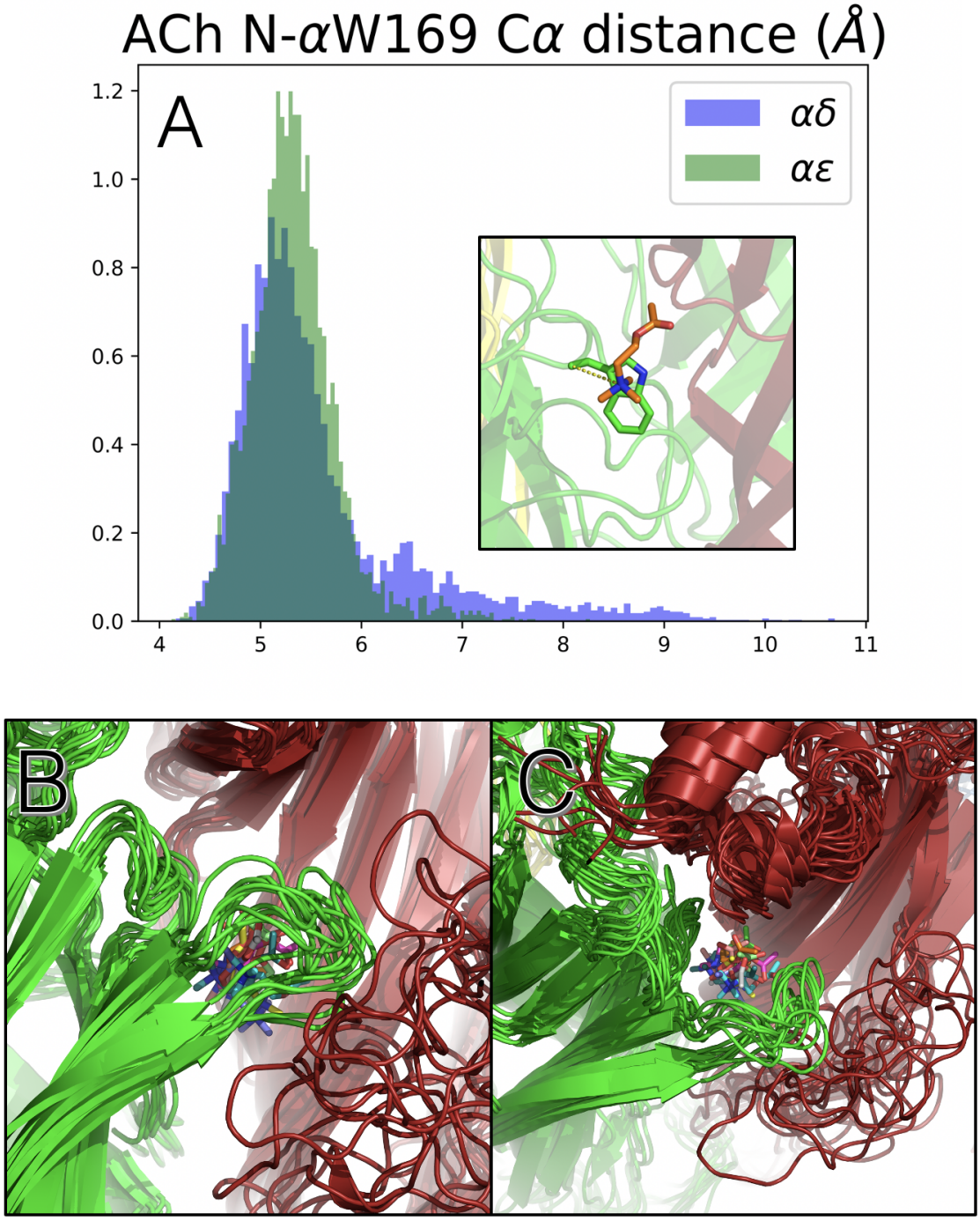

Figure 3.3: Distribution of ACh choline nitrogen atom and αW169 Cα atom distance (A). Histograms are comprised of 1 μS of aggregate simulation time with 5000 frames. The representative binding mode of ACh is shown in the insert (ACh is shown as an orange stick representation and αW169 in a green stick representation; Oxygen and nitrogen are coloured red and blue respectively). The collective variable measured is shown as a dashed yellow line. The presence of a large rightward skew for the $\alpha\delta$ prompted us to analyse individual simulations to determine if unbinding occurred. Two perspectives of the final frames from every replica are superimposed (B and C) and ACh was shown to be stable in all runs.

Model quality was then assessed by examining the behaviour of ACh docked into the resulting model. In these control simulations, ACh was found to bind in stable manner, remaining in the aromatic box with no unbinding events for all 10 repeated simulations (figure 3.3).

Whilst simulated ACh binding modes at human adult muscle nAChRs have not been previously explored for the $\alpha\epsilon$ subunit interface, the key conserved pharmacophoric-protein interactions determined for other pLGICs [245] are preserved in this model and occur at both binding sites. Additionally, key residue interactions determined in a previous study [259] were replicated for the $\alpha\delta$ interface, with the addition of a 2 orders of magnitude increase in sampling and improved template for the generation of the homology model, further improving the accuracy of the observations obtained in this study.

The distance between the nitrogen atom of ACh and the backbone carbonyl oxygen of αW169 has a peak around 5 Å, slightly longer than the 3 Å observed in the AChBP-carbamylcholine structure [243] or the 3.4 Å observed for the nicotine-$\alpha4\beta2$ structure [260]. Whilst these distances are different, binding modes are not expected to be identical for different ligands and receptors and we are therefore confident in the quality of this heuristic for determining nAChR binding site quality.

System	**n (total time in ns)**
ACh	10 (1000)
BPD5	10 (1000)
BPD8	10 (1000)

Table 3.1: Table 1: List of production simulations

We subsequently assessed the stability of BPDs within the orthosteric binding site. BPDs with 5 or 8 methyl groups in the alkyl linker (figure 3.1 A) were docked at both orthosteric sites. Both docked ligands were subjected to 10 100 ns unbiased MD simulations (table 3.1) all starting from the same initial pose but with differently

seeded initial velocites.

The orthosteric pyridinium rings of both MB442 and MB505 was stable at both interfaces as determined by their peak densities of between 5 and 6 Å for the Euclidean distance of between the αW169 R-group and pyridinium nitrogen (figure 3.4). No substantial differences were observed between ligands or interfaces.

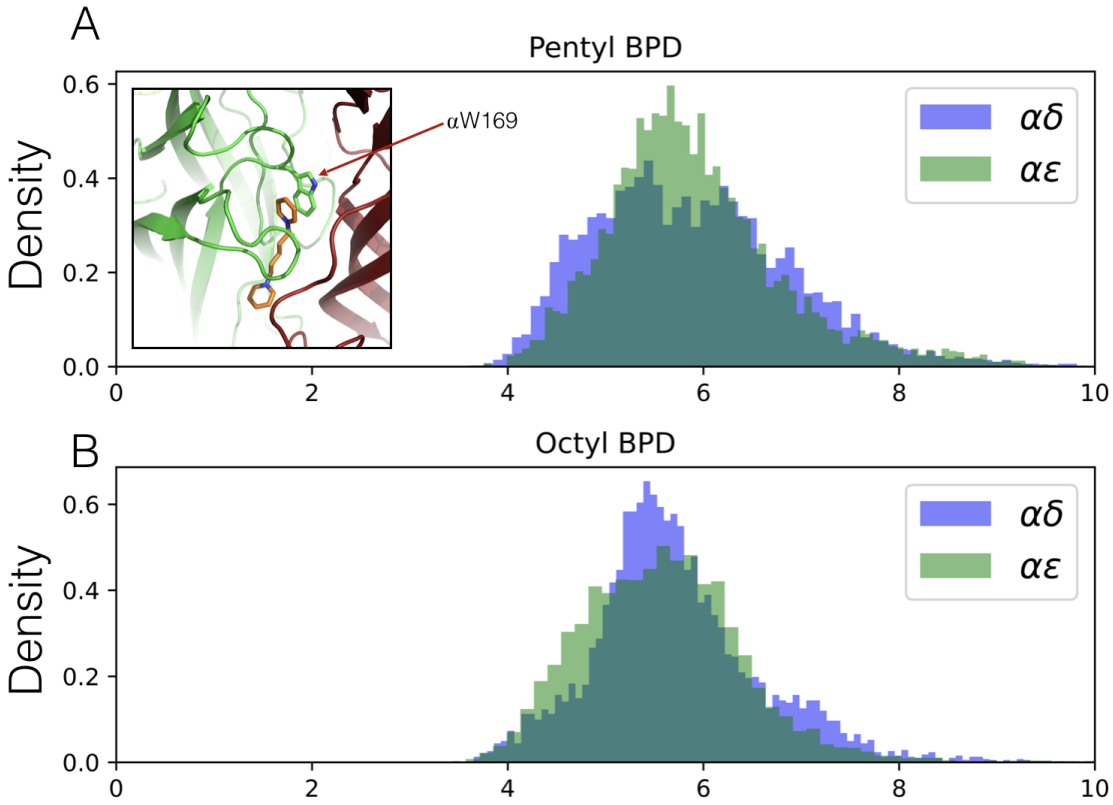

Figure 3.4: Density plots of the distance between BPD orthosteric pyridinium nitrogen atom and center of geometry of αW169 at both orthosteric interfaces. Panel A corresponds to pentyl BPD and panel B to octyl bpd. Panel A insert is a representative snapshot of pentyl BPD (orange) in the down state at the α δ interface with conserved αW169 shown in a green stick representation .

Distinct loop C conformations are known to be associated with either agonist or antagonist binding modes [261, 262] and an agonist's ability to elicit effects has been shown to be associated with loop C conformations that are closely associated with the aromatic box. Antagonists are thought to disrupt this loop C conformation.

Two MB442 binding conformations could be identified from initial 'eyeballing' of individual trajectories wherein the non-orthosteric pyridinium ring was located either towards the TMD or the N-terminus. The distance between the center of geometry of loop C disulphide sulphur residues and the αW169-Cα atom for both BPD molecules with respect to these conformations was therefore analysed to obtain a detailed description of these binding modes and the relative preferences of MB442 and MB505 to adopt them.

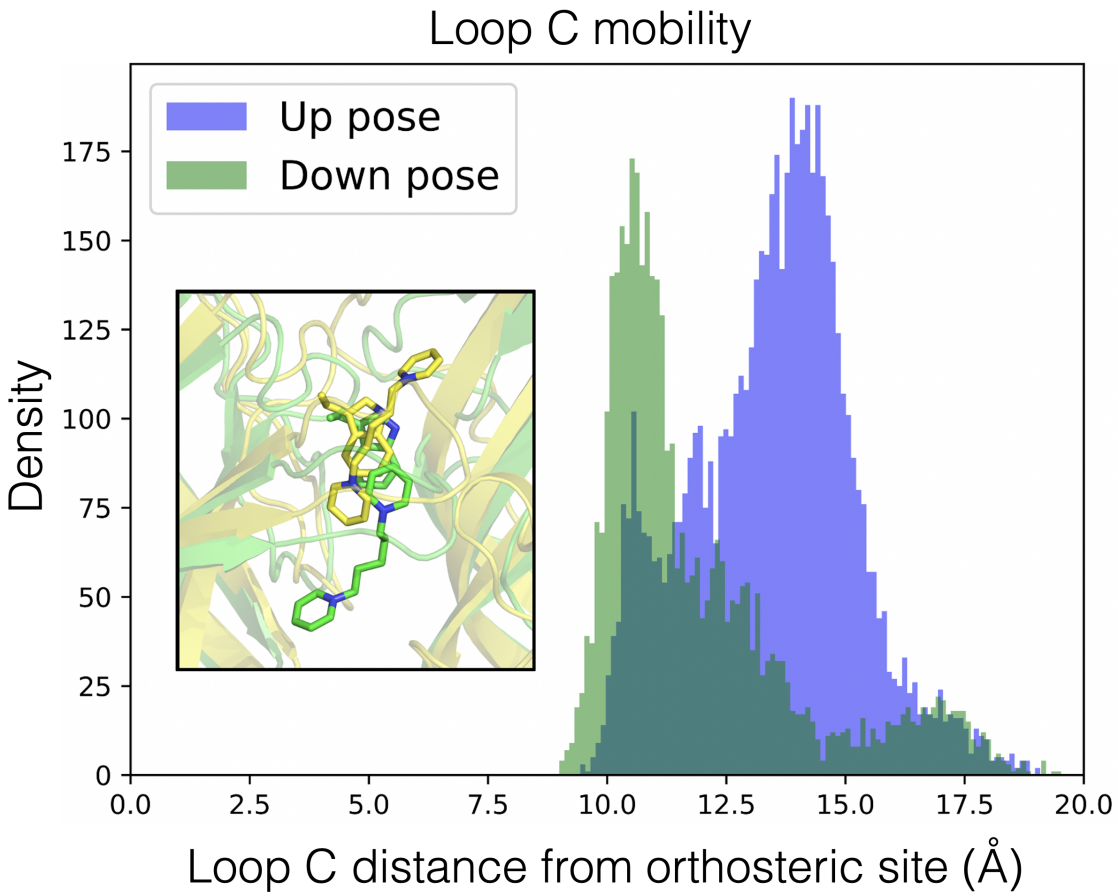

Figure 3.5: Plot of densities for distance between the loop C disulphide sulphur atoms center of geometry and αW169 backbone carbonyl as it purports to MB442 'up' or 'down' binding modes. Binding poses are shown in yellow or green stick representations for 'up' and 'down modes respectively in the insert. At each frame of the trajectory, up or down poses were delineated by whether the non-orthosteric pyridinium rings' z-dimension position in cartesian space was greater or less than the orthosteric pyridinium ring.

Two distinct meta-stable states could be identified for pentyl-BPD that were

associated with an ability to access distinct loop C conformations. The more closed loop C conformation at around 11 Å was associated with a 'down-pose' where the allosteric pyridinium moiety was located towards the TMD (figure 3.5). An upward facing conformation where the allosteric pyridinium moiety was located extracellularly with respect to the orthosteric component could be identified at around 14 Å.

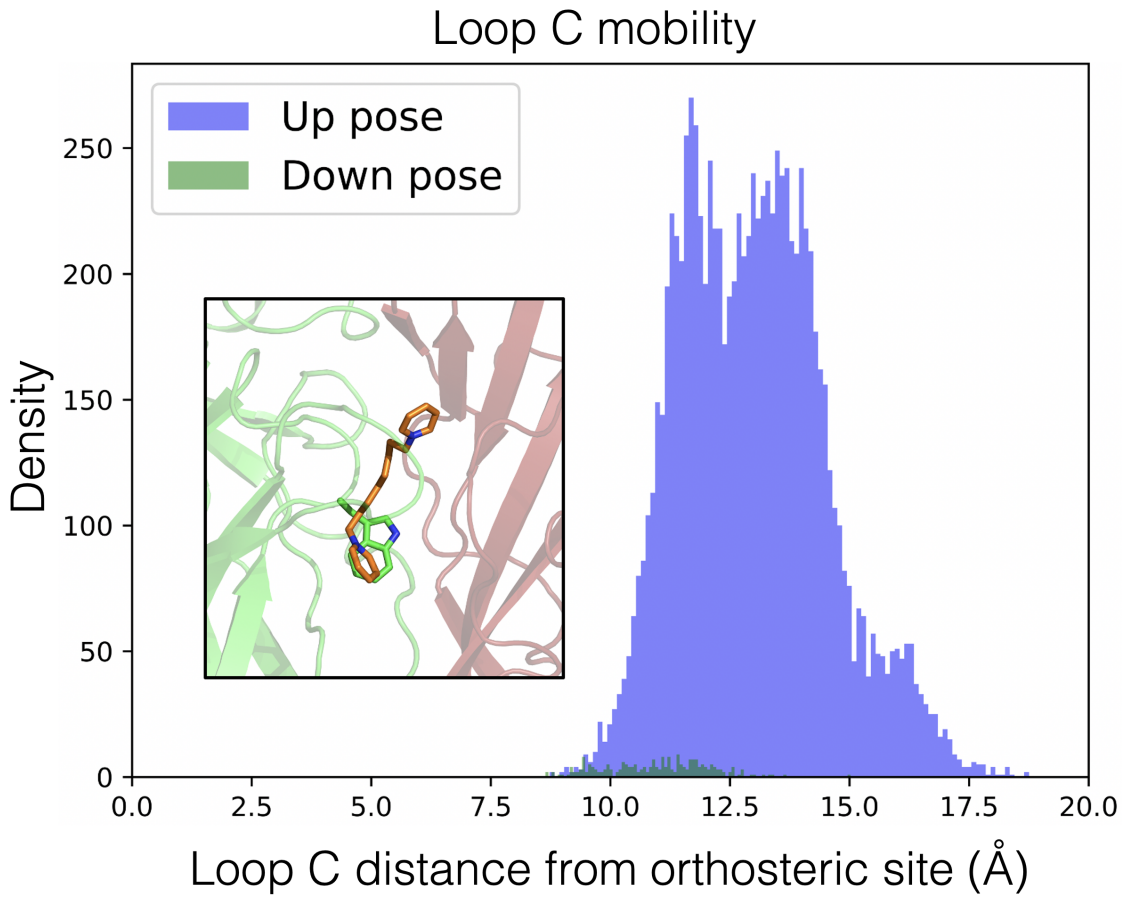

Figure 3.6:
Plot of densities for distance between the loop C disulphide sulphur atoms center of geometry and αW169 backbone carbonyl as it purports to MB505 'up' or 'down' binding modes. A singe representative binding pose is shown in an orange stick representation for the 'up' binding mode in the insert. At each frame of the trajectory, up or down poses were delineated by whether the non-orthosteric pyridinium rings' z-dimension position in cartesian space was greater or less than the orthosteric pyridinium ring.

The larger MB505 molecule accessed this down-state conformation for a negligible amount of all the independent simulations, with only closely associated loop C

receptor configurations obtainable for all simulations with average distances of near to 13 Å (figure 3.6).

As antagonist potency is improved with increasing methylene linker length [195], the up-pose conformation of the pharmacologically active BPD molecule, MB505, was analysed more closely to determine if specific amino acid residues were involved in a bitopic manner to stabilise long chain BPDs at muscle nAChRs. Residues δY134, δY136, δF138 and δY140 were identified on the δ(-) face of the nAChR that were within reach of the non-orthosteric pyridnium ring from an extended conformation of MB505. A conserved tyrosine residue at ϵY131 was also identified, located at an equivalent position to δY134 on the ϵ(-) face. The percentage of time for which a pyridinium nitrogen atom was within 7 Å of the center of geometry of residues δY134, δY136 and δF138 and also for ϵY131 was calculated and plotted for each independent simulation, with this cut-off distance selected so as to incorporate all the aromatic-aromatic interactions possible between the pyridinium ring and tyrosine or phenylalanine.

MB505 possessed a greater % contact than MB442 for both ϵ and δ faces. MB505 % contact at ϵY131 was greater than that of the δ(-) face residue cluster on average with % contact for ϵY131 over 60 % for all independent simulation and over 90 % for 7 of 10 simulations (figure 3.7). As multiple residues were analysed for the δ face, an additional analysis was performed for the ϵY131 equivalent δ face residue, δY134, on its own which did not change this observation 3.8.

Given that ϵY131 is conserved at the δ interface, we analysed % contacts again at the α δ interface, focusing exclusively on δY134. While % contact values were increased with respect to the aggregated δ residue analysis, this was still lower than ϵY131 interactions overall with 5 out of 10 simulations falling below 60% contact (figure 3.8).

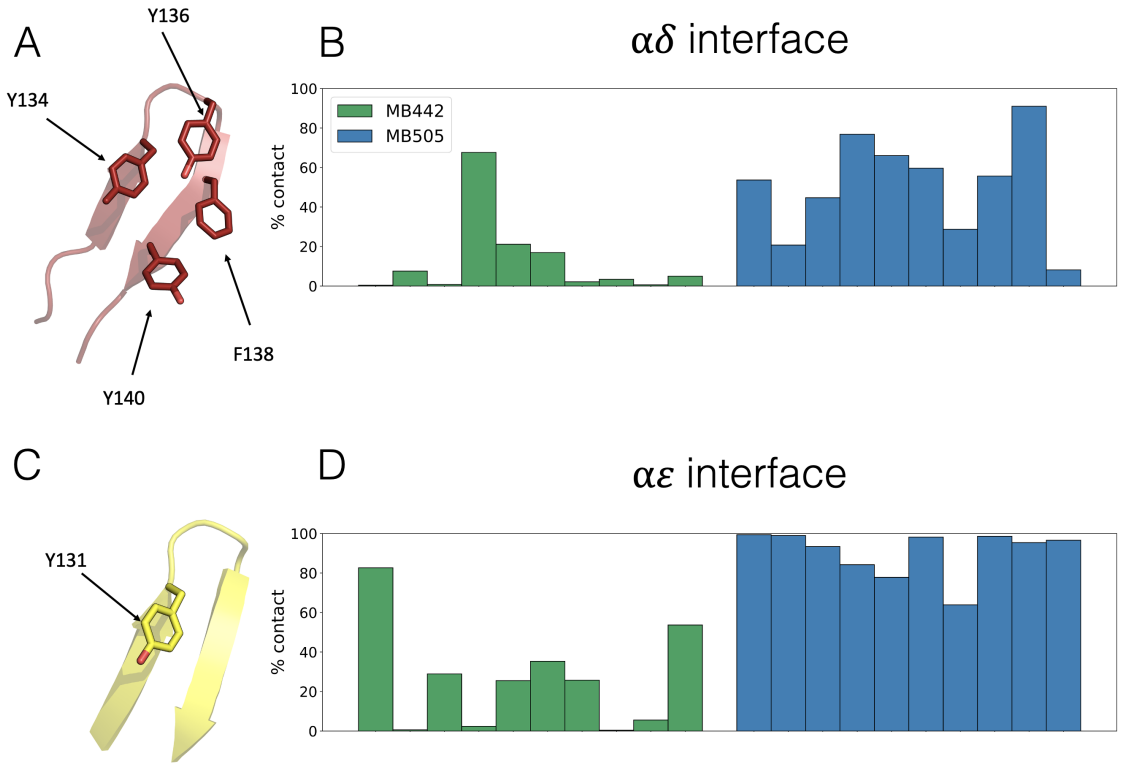

Figure 3.7: The δ(-) face aromatic cluster is depicted in panel A. The % contact time for each simulation in which the non-orthosteric pyridinium nitrogen atom is less than 7Å from (B) δY134, δ136 and δF138 or (D) ϵY131 center of geometry. The ϵ(-) face residue Y131 is shown in panel C. MB442 and MB505 % contact is shown in green and blue respectively.

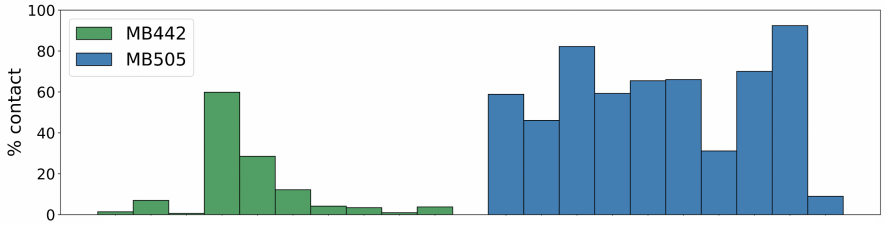

Figure 3.8: % of each independent simulation where a pyrdinium nitrogen falls within 7Å of δY134. Pentyl and octyl BPD molecules are shown as green and blue bars respectively.

3.3.2 Electrophysiological validation

To validate the observations from the MD simulations, δY134A and ϵY131A constructs were generated and expressed heterologously in *Xenopus* oocytes so that concentration-response curves of MB505 could be obtained and compared across mutant and wild-type constructs.

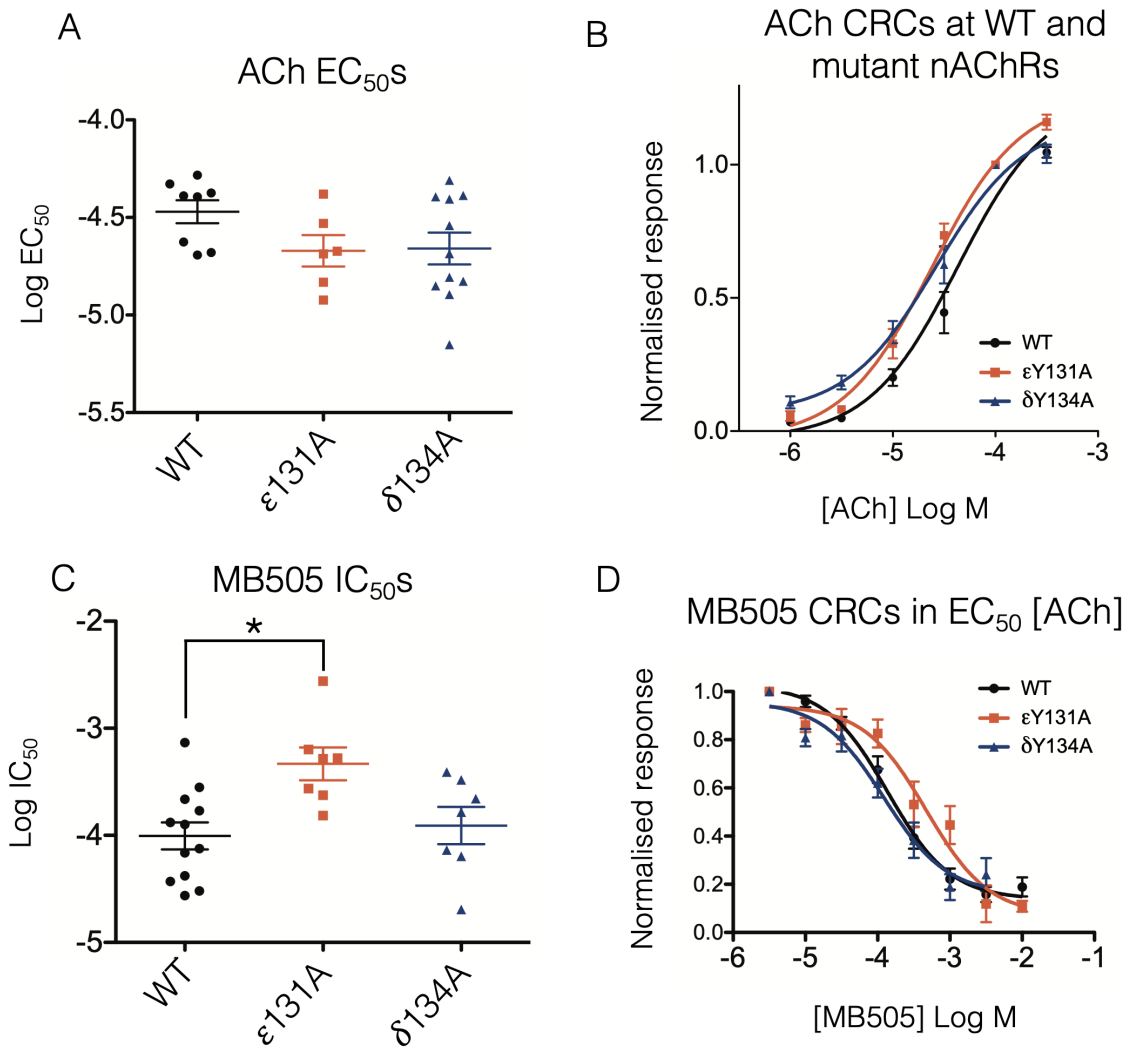

Figure 3.9: EC50s of ACh (A) from obtained from individual CRCs, with associated mean and 95% CIs. Corresponding aggregated CRCs at WT, ϵY131A and δY134A constructs (B). IC_{50}s of MB505 from individual CRCs with mean and 95% CIs (C). Corresponding aggregated CRCs for M505 at WT ϵY131A and δY134A constructs (D). Ooctyes were obtained from a minimum of two seperate *Xenopus*.

The response to increasing ACh concentrations was measured as a control. The observed concentration response curves (CRCs) showed no statistically significant

change between WT and mutant receptors (figure 3.9).

Construct	**Log IC_{50}(M)**
WT	-3.86
δY134	-3.91
ϵY131	-3.33

Table 3.2: Summary of TEVC Octyl-BPD IC50 values

IC_{50} values for MB505 were derived from the fit of each independent inhibtory CRC (table 3.2) from increasing concentrations of MB505 in the presence of 40 μM ACh, which corresponds to an approximate EC_{50} ACh concentration. A statistically significant rightward shift in CRC could be observed for ϵY131A compared to WT ($p < 0.05$) with a 3.42 fold change in log IC_{50} of -3.33 M to -3.86 M (table 3.2) in sensitivity to ACh.

3.4 Discussion

In this chapter, the binding modes of BPD molecules MB442 and MB505 at the adult human muscle nAChR were explored with MD simulations and compared so that a molecular explanation for their different pharmacological profiles [195] could be obtained. Furthermore, mutagenesis and electrophysiology was used to validate observations from these simulations to identify a specific molecular determinant involved in stabilising longer-length BPD compounds via a bitopic interaction. As the blood-brain barrier would theoretically prevent highly charged molecules such as BPDs from reaching neuronal nAChR subtypes and also, due to how more pronounced changes in *Hill-slope* are observed in muscle nAChRs over neuronal nAChRs [195], BPD binding modes were explored exclusively at the adult muscle subtype in this chapter. A substantial part of OPNA lethality is known to be contributed by skeletal muscle components [263, 264] that depress diaphragm

function, making human muscle nAChRs important in a pathophysiological context.

Observations from MD simulations suggested that residues δY134 and ϵY131 located on the δ(-) and ϵ(-) faces of the receptor could be specific molecular determinants that interact bitopically with longer length BPD molecules such as MB505.

Percentage contact of total independent simulation time for these complementary face residues were obtained on the basis that the charged pyridinium moiety might form cation-π interactions with these regions. Whilst previous work focusing on the CHARMM 36 forcefield demonstrated that cation-π interactions are typically underestimated by around 3 kcal/mol, the key geometries encapsulated by cation-π interactions are preserved [265, 266]. Despite the use of a single point charge model for molecular mechanics forcefields, parametrisation of BPDs (figure A.1) show that replication of these cation-π geometries in AMBER should be feasible even if unable to account for correct energies.

In contravention with previous evidence suggesting that ligand size correlates with the degree of loop C occlusion and in turn antagonistic potency, we propose that antagonist response is instead graded in this particular instance by the ability to access 'up' or 'down conformations and that the ability to access the pharmacologically active 'up' state is related to the length of the methylene linker in BPD molecules. EC_{50}s for ACh at WT and mutant receptors demonstrated that these amino acid residues do not effect ACh binding or nAChR gating isomerisation and as such, are potential allosteric sites.

MB505 IC_{50} was statistically significantly different compared to WT for ϵY131 and not for δY134. Despite both residues being conserved and in homologous positions with respect to each other, their surrounding chemical environment differs substantially, with the presence of 3 additional aromatic amino acids clustered around δY134. This could provide a degree of steric occlusion to the allosteric

interacting pyridinium ring of MB505, preventing optimal interactions with δY134 compared to ϵY131 .

Typically, two molecules of ACh are required to elicit a full nAChR response, however it has been shown that muscle nAChRs do exhibit some degree of constitutive activity and may also open (albeit with a lower open probability) with only a single molecule of bound ACh [267, 268]. As a single molecular determinant for BPD binding that was isolated to the ϵ face was identified, it is possible that the small partial agonist profile shown in this chapter and also previously [195] could be explained by occlusion of a single orthosteric site.

At the neuronal $\alpha4\beta2$ nAChR subtype, a series of allosteric compounds have been identified [110, 111] with molecular determinants located in a homologous region to that which has been identified in this chapter. It would thus seem that this region located on or around the $\beta5$ $\beta6$ segments is a potential allosteric site with low sequence conservation between subunits that could be readily exploited in future rational design approaches for subtype selective modulators.

The existence of a specific molecular determinant at only one of two interfaces might explain partial agonist activity. It is unlikely however, to account for the large changes in BPD binding between MB442 and MB505 BPDs [195] as evidenced by the small observed change in IC_{50} shown herein and it is thus more likely that down-state inaccessibility as facilitated by larger BPD molecules is what accounts for previous experimental observations.

3.5 Conclusion and future work

In this chapter, we provide a molecular explanation for previously described structure activity relationship data [195], showing that longer methylene linkers are beneficial for non-oxime BPD compounds in exhibiting antagonistic profiles at muscle nAChRs

as a consequence of stabilising the newly identified 'up' conformation. It was further shown that this stable conformation was associated with a distinct loop C conformation and that this conformation agrees with previous studies on antagonist loop C conformations [243, 261]. Additionally, a specific molecular determinant, ϵY131, has been identified that interacts with MB505 and provides a potential avenue for the design of subunit specific modulators that could pave the way for improved partial agonists.

"Nothing prepares you for this. I cheered. I shouted. I fist pumped the air. I cried. I stood and cheered. It's absolutely everything you hoped it was going to be."

— Richard E. Grant

4

Muscle nAChR conversion into chloride conductance at positive potentials by a single mutation

4.1 Introduction

The essential function of muscle nAChRs is to generate a sufficient endplate potential (EPP), activating voltage-dependent sodium channels and eliciting an action potential with concurrent contraction of muscle tissue. Muscle nAChRs therefore provide the basis for converting chemical signalling by way of ACh release from pre-synaptic neurones into successful neuromuscular transmission.

Improper neuromuscular transmission is associated with both autoimunne or congenital diseases such as myasthenia gravis, or congenital myasthenic syndrome (CMS). The number of different proteins involved directly with neuromuscular transmission and the shaping of neuromuscular junctions results in many potential causes for CMS [17]. To date, over 30 different genes have been implicated in various CMSs [269] with more than half these being nAChR encoding subunits. Of these nAChR specific mutations, identified pathomechanisms have been shown to arise out of conductance decreases [270], changes in kinetic properties [271] and changes

in expression levels [271].

Despite the number of nAChR specific CMS mutations, charge selectivity impairing mutations have not yet been identified as a cause of CMS. These are of particular interest from a biophysical standpoint due to the complicated picture of how charge selectivity is determined amongst cys-loop receptors more widely.

Broadly speaking, ion selectivity is determined by several components primarily residing at the M2 pore lining α helices of each subunit, with a total of 5 M2 helices contributing overall to the pore. Under resting conditions these pore lining helices reside in a closed conformation, whereupon they undergo a conformational change in which they rotate and open after agonist binding to the allosterically coupled binding sites located at the extracellular domains of the receptor [272].

The key step in this allosteric transition is the relief of the so-called hydrophobic girdle [53], known to reside at the highly conserved 9' region of the transmembrane domain, which acts to prevent the hydration of the pore known to be a prerequisite for ion permeation [273]. This 9' region is named according to the Miller consensus numbering system [274] so that clear comparisons across the Cys-loop receptor pore lining helices can be made. The relative positions of these M2 residues and their corresponding prime number label are shown in figure 1.4. During the closed to open state transition it is thought that these pore facing residues rotate to occupy conserved hydrophobic pockets located at the inter-helical bundles between subunit interfaces [54].

Due to the highly conserved overall topology of cys-loop receptors, this mechanism is likely to be shared throughout the cys-loop receptor family and more subtle differences between subtypes will determine ion selectivity. These include the size of the pore [275], rotameric state of pore lining side chains [276, 277] and most

critically, their charge distribution [278].

Specifically, rings of charged residues located at three distinct locations, namely the extracellular, intermediate and cytoplasmic rings of the M2 helices with the intermediate ring being thought to contribute most strongly to cation selectivity [66].

Early evidence for the specific determinants of charge selectivity come from studies where residues from the anion selective glycine receptor where placed in α7 nAChRs, with the smallest number of perturbations inducing a swap in selectivity determined to be the most likely contributors of ion selectivity [67, 279]. Additional experiments on 5-HT3ARs also demonstrated this swap in selectivity for the same regions and again requiring 3 different perturbations per subunit for a total of 15 amino acid substitutions/insertions required [280]. The introduction of 3 α7 mutations into the anionic GlyR was also shown to swap ion selectivity [281].

With such a large number of different biophysical phenomena contributing to ion permeation events, untangling the relative effects of individual motifs or the extent of contributions from particular regions can be challenging. Mutations occurring from diseases therefore provide an opportunity to study the basis for this property whilst simultaneously demonstrating their wider physiological implications. We show for the first time a charge selectivity swapping mutation mediated by significantly reduced perturbations of the M2 region compared to previous work and in a pathophysiological context. This mutation resides at the 9' gating region arising from a αLeu251Arg mutation located at the CHRNA1 gene identified in a CMS patient.

4.2 Results

4.2.1 CMS Patient diagnosis

The patient in question presented with common myasthenia symptoms including dribbling, reduced facial expression and ocular movement. Despite this, overall the patient exhibited a mild phenotype with upper and lower limb weakness only occurring after sustained movement. Presentation of symptoms in infancy is indicative of congenital myasthenic syndrome but to rule out the possibility of the autoimmune version, myasthenia gravis, in which patients display a very similar symptomatology, assays for anti-MuSK and anti-AChR antibodies were performed [282] by collaborators. As these were negative, genetic screening of common CMS implicated genes were performed with identification of a single heterozygous point mutation at CHRNA1. Specifically it was found that c.812T was mutated to guanine manifesting in an αLeu271Arg mutant numbered according to the mature subunit sequence not including the signal sequence. This mutation resides at the 9' region of the α subunit M2 helix.

4.2.2 AChR$_{\alpha\mathbf{L251R}}$ Surface Expression

To determine whether the αL251R mutant was capable of reaching the surface of the cell, experimental collaborators lead by H. Cetin, transfected αL251R mutant cDNA into HEK293 cells along with constituent adult muscle WT subunit cDNA and used ^{125}I-α-bungarotoxin (^{125}I-α-BuTx) binding assays to count radioactivity as a surrogate for nAChR surface expression.

As shown in 4.1A, a reduction of approximately 30.3% for AChR$_{\alpha\mathrm{L251R}}$ compared to WT occurred. Additional immunofluorescent experiments were performed for further conformation of cell surface expression utilising an α1 and δ subunit monoclonal antibodies to infer expression of additional nAChR subunits and therefore a preserved stoichiometry (4.1C and D). Whilst αL251R was capable of reaching the cell surface,

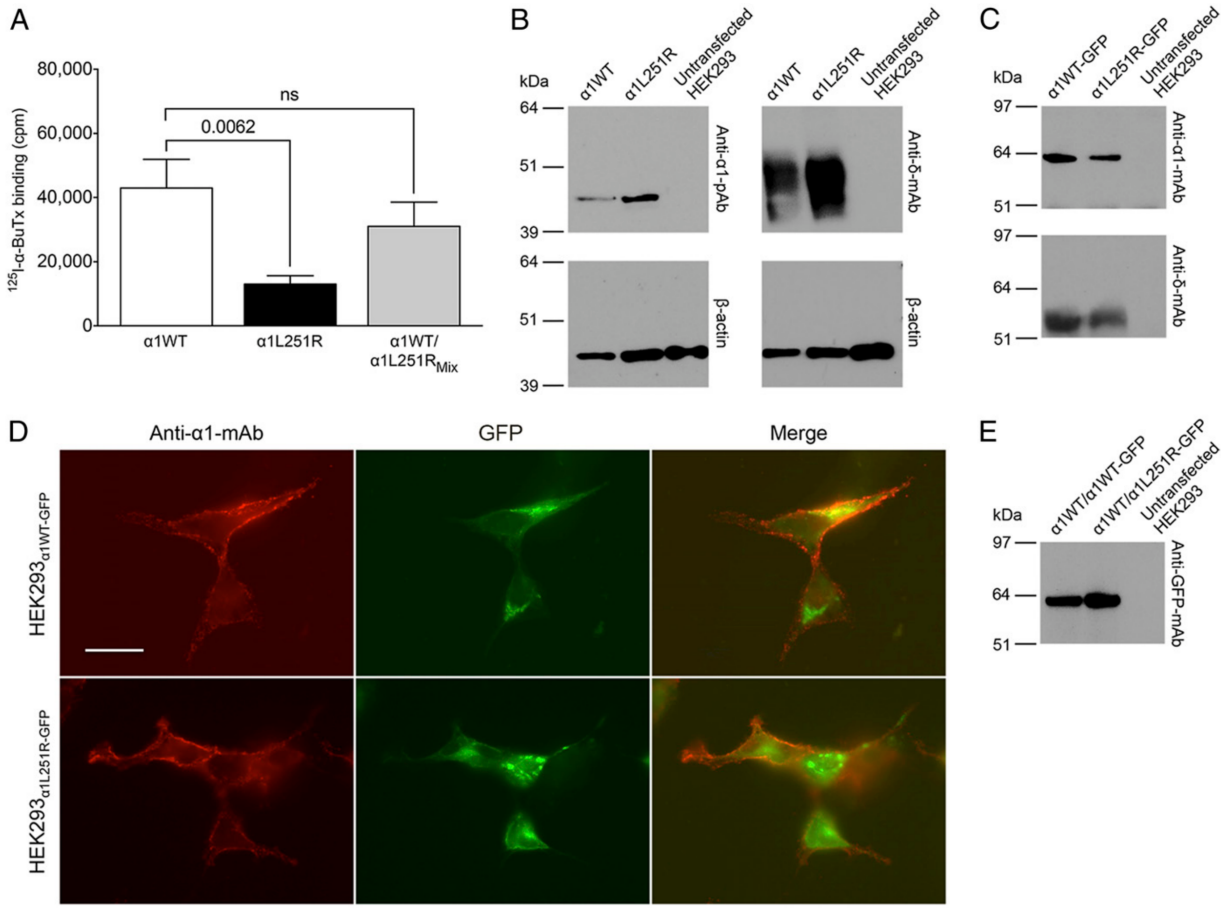

Figure 4.1: (A) ^{125}I-α-BuTx binding assays for WT, α1L251R and WT/α1L251R$_{\text{Mix}}$ (n=8). Bars show mean plus or minus SEM. (B) Western blots of extracts from WT and αL251R mutant transfected whole HEK293 cells precipitated with a polycloncal α1 antibody and monoclonal (mAb) δ antibody with β-Actin binding as a control. (C) Additional western blots were performed with 2:1:1:1 ratios of α1WT-GFP-, β1-, δ-, ϵ-subunits and also separately α1L251R-GFP-, β1-, δ-, ϵ-subunits, immuno-precipitating both with mouse anti-human α1 mAb. (D) Results of immunoflouresence of transfected HEK293 cells with previously mentioned ratios (Scale bar, 20 μm).(E) Western blot of 1:1:1:1:1 ratio of α1WT-, α1WT-GFP, β1-, δ-, ϵ-subunits and α1WT-, α1L251R-GFP, β1-, δ-, δ-subunits. Image taken from *H. Cetin et al, 2019*.

it was also retained in the lysate. Due to the heterozygous nature of the αLeu271Arg point mutation, a WT and αL251R mutant mix was transfected into HEK293 cells. These were not statistically significantly different to WT (figure 4.1A) , with both mutant and WT constructs seemingly co-expressed (figure 4.1E).

4.2.3 Biophysical Properties of Mutant nAChRs determined by Whole-Cell recordings

Patch clamp recordings in the whole-cell configuration were performed on transfected HEK293 cells by experimental collaborators lead by H. Cetin. The kinetic characteristics for WT transfected HEK293 cells show a fast rising peak with a subsequent exponential decay in current. This fast decay in the presence of ACh application indicated substantial desensitization, with little to no additional current over the remaining 3 second ACh application (figure 4.2A). For αL251R mutant transfected HEK293 cells, several different kinetic properties were altered compared to WT.

A 96.7% reduction in current could be observed with a mean current amplitude of -12.1 plus or minus 2.2 nA for WT and -0.4 plus or minus -0.1 nA for αL251R (WT and αL251R, n=18) (figures 4.2 and 4.3A). Desensitization as measured by mean fractional current decay during ACh busrt was determined for WT and αL251R as 95.4 plus or minus 1.0 % and 15.3 plus or minus 1.7 % respectively ($p < 0.0001$) (figure 4.3B). Deactivation was determined through the current decay occurring at ACh washout post ACh application. WT receptors possessed a mean deactivation time constance of 76 plus or minus 13 ms and αL251R 2169 plus or minus 256 ms ($p < 0.0001$) (figure 4.3C).

$HEK293_{\alpha WT\text{-}\alpha L251R}$ displayed reduced current amplitude compared to $HEK293_{\alpha WT}$ with -4.4 plus or minus 1.4 nA and -12.1 plus or minus 2.2 nA respectively ($p=0.0060$) (figure 4.3A). Mean deactivation time constants for $HEK293_{\alpha WT\text{-}\alpha L251R}$ and $HEK293_{\alpha WT}$ were statistically significant different ($p = 0.0097$) at 148 plus or minus 23 ms and 76 plus or minus 13 ms respectively (figure 4.3B).

Analysis of the current-voltage relationships of $HEK293_{\alpha WT\text{-}\alpha L251R}$, $HEK293_{\alpha L251R}$ and $HEK293_{\alpha WT}$ showed a near ohmic relationship for $HEK293_{\alpha WT}$ and $HEK293_{\alpha WT\text{-}\alpha L251R}$ but with outward rectification for $HEK293_{\alpha L251R}$ at positive holding potentials

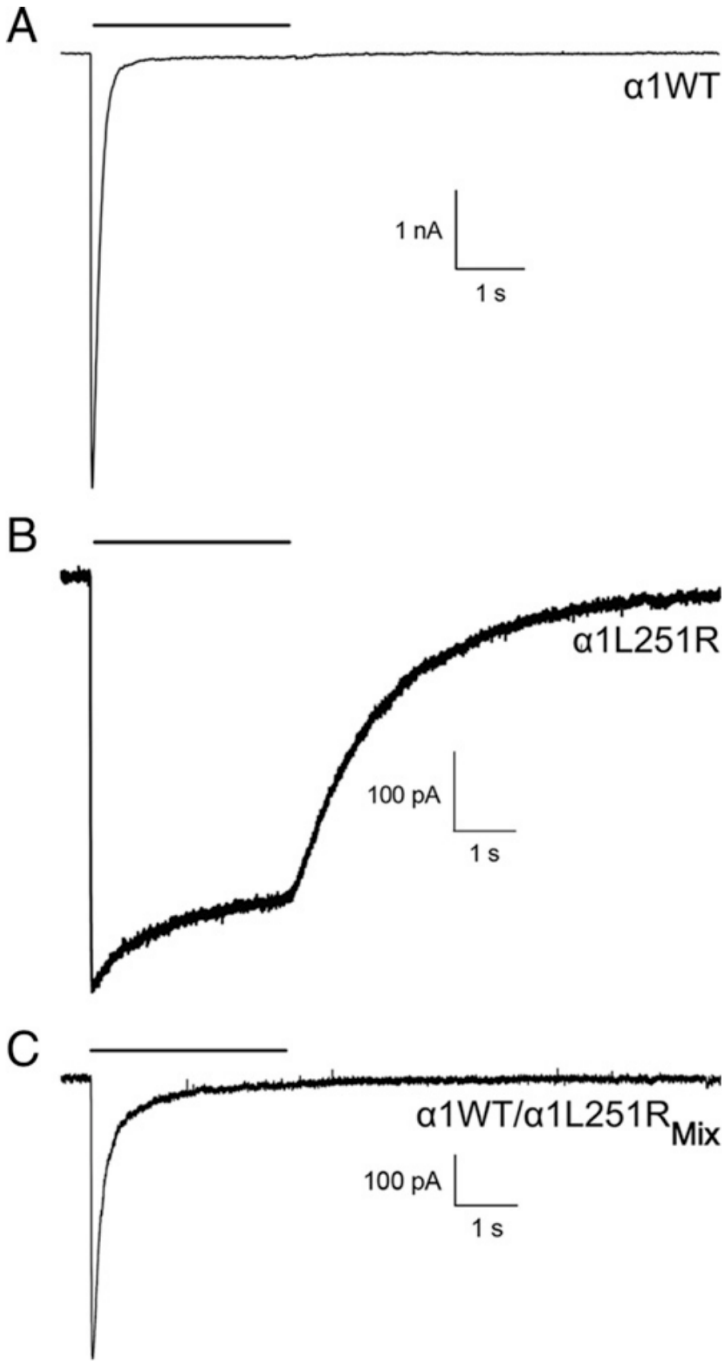

Figure 4.2: Representative current traces from whole-cell patch clamp electrophysiology of transfected HEK293 cells with 2:1:1:1 ratio α1:δ:β:ϵ nAChR subunits, 2:1:1:1 ratio of αL251R:δ:β:ϵ subunits and 1:1:1;1:1 ratio of α1:αL251R:δ:β:ϵ. Image taken from *H. Cetin et al, 2019*.

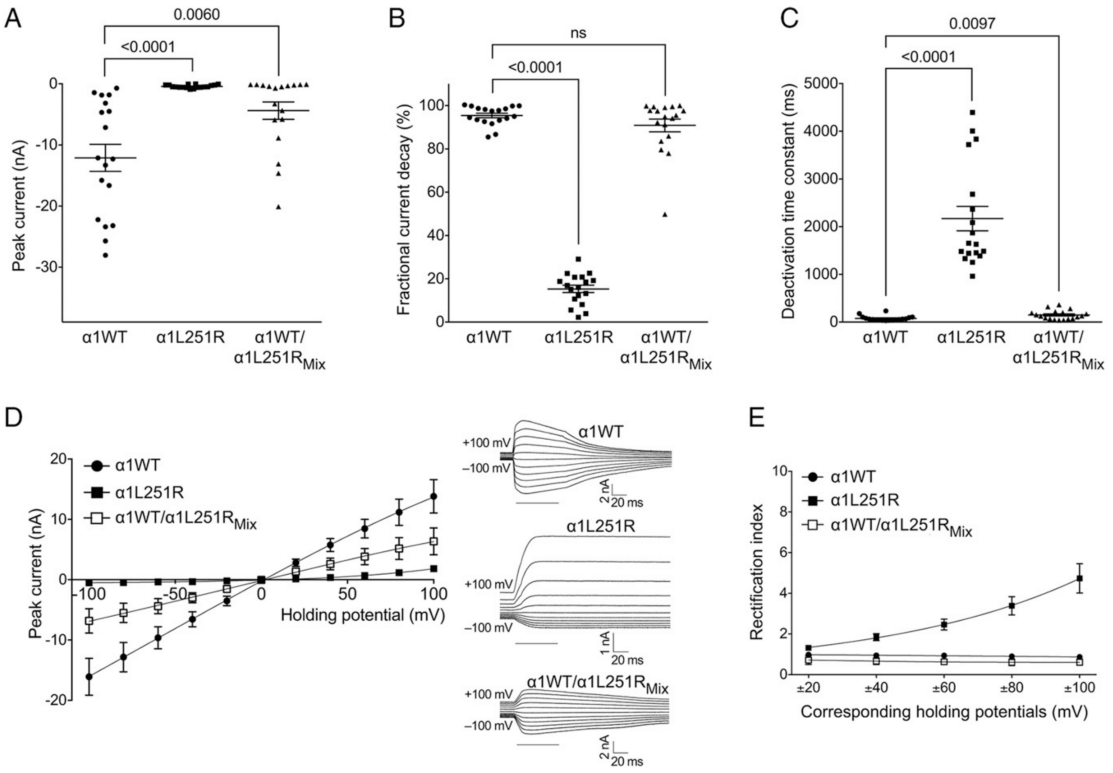

Figure 4.3: Image taken from *H. Cetin et al, 2019*.

without changing the reversal potential (figures 4.3D and E).

4.2.4 Potential of mean force calculations

To discern any potential differences in the biophysical properties between the two possible stoichiometries of HEK293$_{\alpha 1WT/\alpha 1L251R\text{-}Mix}$ and the contribution of HEK293$_{\alpha 1L251R}$ on the overall CMS pathomechanism we performed umbrella sampling molecular dynamics (USMD) simulations for Na^+ and Cl^- ions at each of these systems respectively.

The TMD of the open state *Danio rerio* α1 GlyR (PDB accession code: 3JAE) [283] was used as a template structure for which to build our model on using the protocol outlined in Chapter 2 of this thesis. The final alignment is included in the appendix (B.3). To preserve the open state configuration of the model, protein backbone atoms were restrained with a 1000 kJ/mol/nm^2 harmonic force constant.

The reaction coordinate ζ was projected along the z-axis of the channel, lateral to the phospholipid bilayer with ζ=0 at the center of mass of the protein. Umbrella sampling windows were spaced at 1 Å except at energy barrier regions where a 0.5 Å spacing was used. ζ spanned ± 40 Å to ensure sufficient sampling of bulk water molecules at either end of ζ. Umbrella sampling windows were restrained with a 500 kJ/mol/nm^2 force constant and analysed with GROMACS WHAM [227] to obtain the unbiased PMF. Pore radius profiles were calculated with CHAP [284].

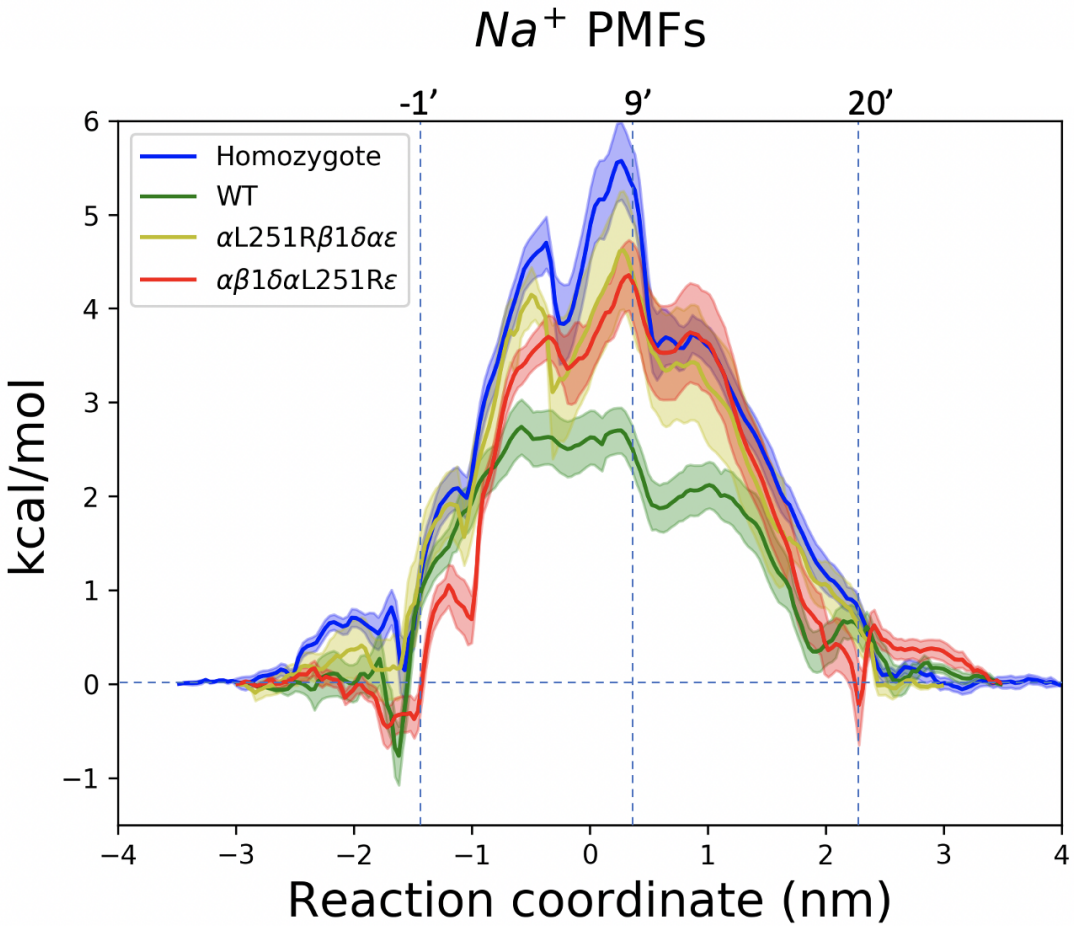

Figure 4.4: Na^+ Potential of mean force calculations at transmembrane pore segment for mutant and WT systems AChRα1WT (green) , AChRα1L251R blue), AChRα1WT/α1L251R(red), AChRα1L251R/α1WT (yellow). Negative position along pore axis denotes intracellular region and positive denotes extracellular region. Dashed vertical lines denote positions of -1', 9' and 20' residue positions for reference. Error bars represent 1 standard deviation. Image adapted from *H. Cetin et al, 2019.*

Control PMFs for Na^+ and Cl^- at WT channels are in agreement with expected physiological observations insofar that this model is in fact selective for Na^+ over Cl^-

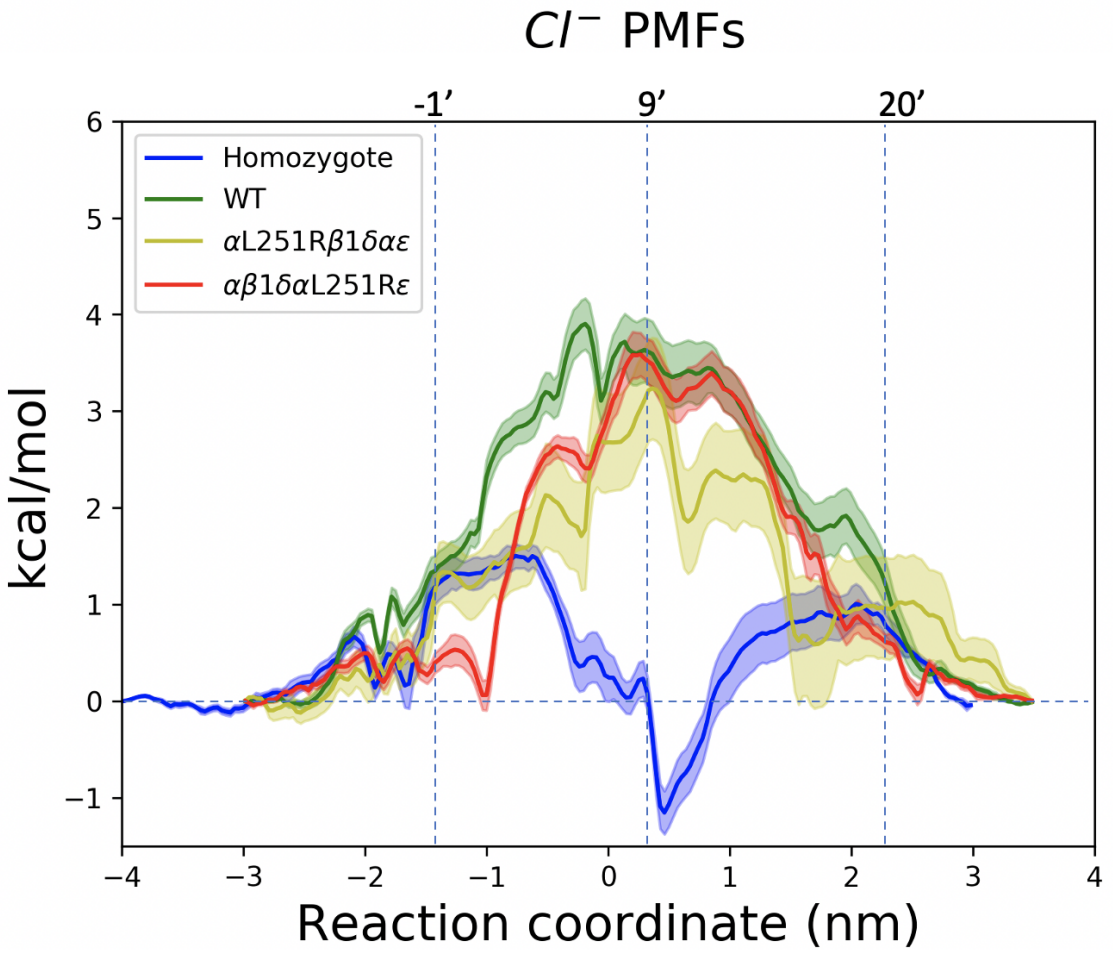

Figure 4.5: Cl^- Potential of mean force calculations at transmembrane pore segment for mutant and WT systems $AChR_{\alpha 1WT}$ (green) , $AChR_{\alpha 1L251R}$ (blue), $AChR_{\alpha 1WT/\alpha 1L251R}$(red), $AChR_{\alpha 1L251R/\alpha 1WT}$ (yellow). Negative position along pore axis denotes intracellular region and positive denotes extracellular region. Dashed vertical lines denote positions of -1', 9' and 20' residue positions for reference. Error bars represent 1 standard deviation. Image taken from *H. Cetin et al, 2019.*

with barrier height values of approximately 2.5 and 4 kcal/mol respectively. Barrier heights for Na^+ at all mutant channels exceeded those for WT Cl^- representing substantial barriers for ion flow and impermeability at holding potentials of 0 mV. Both heterozygous stoichiometries did not differ appreciably from each other with barrier heights for both ions within error of one another.

Cl^- at $AChR_{\alpha 1L251R}$ exhibited a substantial decrease in barrier height to 1.5 kcal/mol at 8Å with an energetic reward of -1.15 kcal.mol at 5Å along the reaction coordinate.

It's constituent counterion Na+ exhibited a large energy barrier at the same position of 5.57 kcal/mol. $AChR_{\alpha 1L251R}$ is therefore strongly Cl^- selective.

4.2.5 L251R conformations and ion interactions

Further analysis of the simulation data showed substantial changes in solvation and L251R conformations that contribute to the overall shape of the observed PMF profiles.

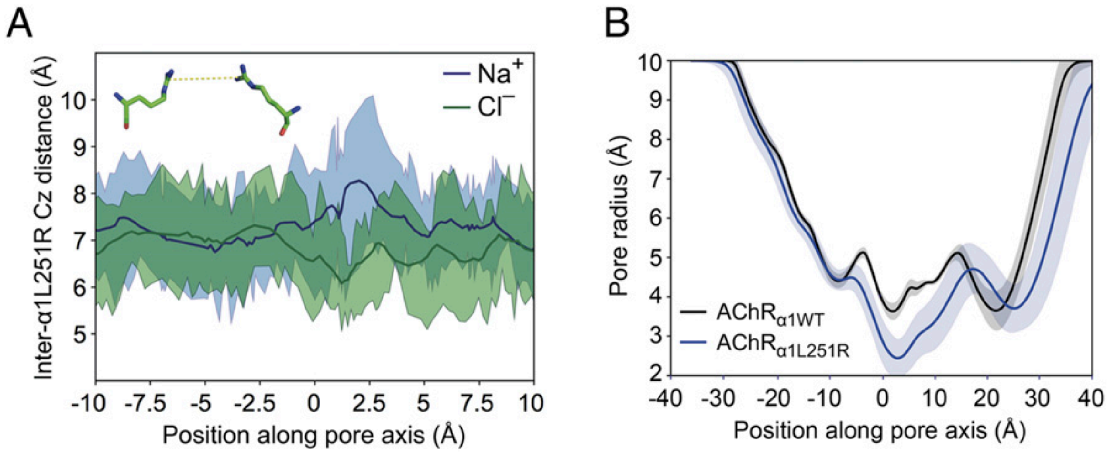

Figure 4.6: Inter-αL251R distance as a function of the position of Na^+ or Cl^- along the z-axis of the channel pore (A). Radius of the channel pore as a function of position with respect to the center of geometry (0 Å) of the TMD (B).
Image taken from *H. Cetin et al, 2019.*

For the WT Na^+ PMF, there are two approximately equal minimum pore radii. Whilst the highest point in the potential energy landscape exists at around 0.4 nm, with a relatively low energy value at the 2.3 nm position constriction. This occurs as the 20' glutamic acid residues favourably compensate for the restriction introduced at this region whilst no such favourable electrostatic interaction exists at the 9' 0.4 nm region.

In correspondence with this- Cl^- possesses a competitively larger peak at the 0.4 nm position of around 1 kcal/mol but an approximately 2 kcal/mol increase at 2.3 nm with respect to Na^+ at the same position. These effects are more pronounced at

$AChR_{\alpha 1L251R}$ where a tight 0.25 nm constriction at around 0.4 nm in conjunction with the electrostatic contributions from both arginine residues raised the Na^+ energy barrier to around 6 kcal/mol whilst introducing a free energy reward of nearly -2 kcal/mol for Cl^-.

Figure 4.6A demonstrates that the wider time averaged density obtained in 4.6 B at the 4 Å position are wider for $AChR_{\alpha 1L251R}$ than WT as a consequence of the torsional flexibility of both mutant arginine residues and their movement in response to ion interactions. Inter-L251R distances increased from their average value of approximately 7 Å up to over 8 Å for Na^+, with a wide standard deviation indicative of this flexibility. A corresponding decrease in the inter-L251R distance could be seen for Cl^- as a result of favourable charge interactions between arginine and Cl^-.

4.2.6 Chloride permeability validation

As the results from the USMD simulations pointed to a strongly chloride selective channel for the $AChR_{\alpha 1L251R}$, additional whole-cell recordings were performed whereby Cl- ions were replaced with AChR impermeable ion SO_4^{2-} to concentrations of 10 mM in either extracellular or intracellular compartments respectively and I-V curves obtained.

The rectification index at various holding potentials was calculated by taking the current value at equivalent opposite sign holding potentials and obtaining a ratio between those two values to determine the deviation from an ohmic relationship as shown in the below equation.

$$RI = \frac{\text{Current at} + Ve(X)}{\text{Current at} - Ve(X)} \tag{4.1}$$

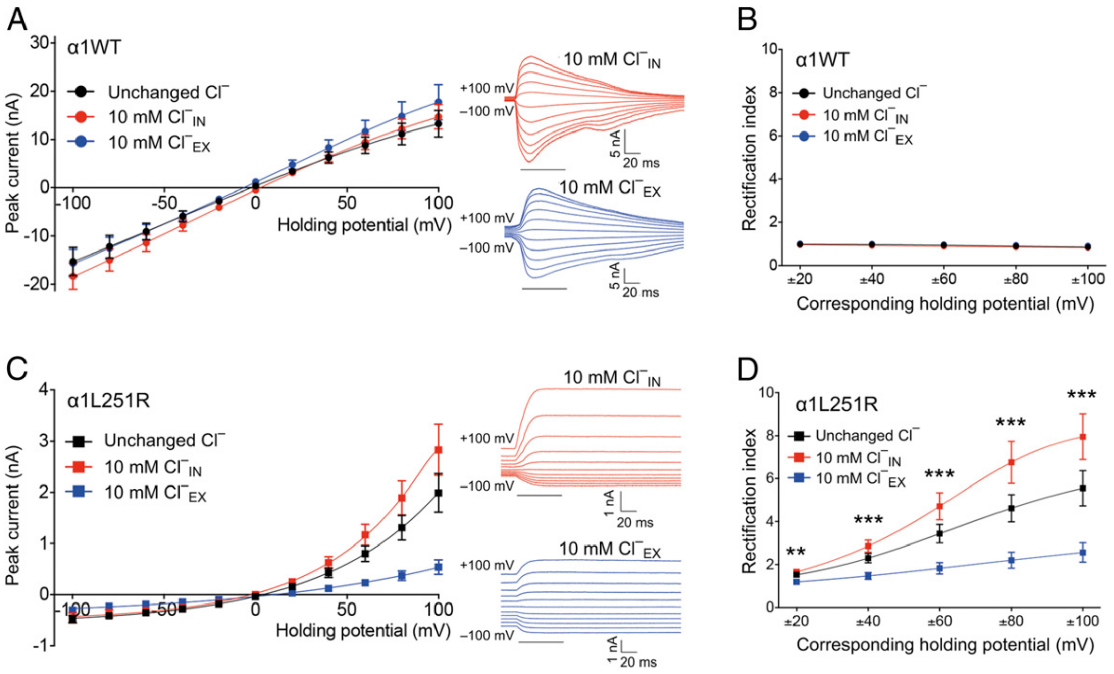

Figure 4.7: Current voltage relationship for changing Cl^- concentration intracellularly and extracellularly at both WT (A) (unchanged Cl. n = 17; 10 mM Cl. IN, n = 11; 10 mM Cl. EX, n = 10) and $AChR_{\alpha 1L251R}$ (C) (unchanged Cl., n = 16; 10mM Cl. IN, n = 11; 10mM Cl. EX,n =12) with corresponding rectification indices at positive holding potentials for WT and $AChR_{\alpha 1L251R}$ (B and D). 10 mM Cl^-_{IN} refers to reduced intracellular Cl- concentration (red) and 10 mM $Cl-_{EX}$ refers to a reduced extracellular Cl^- concentration (blue). One-way ANOVA with Tukey's post hoc test for determining statistical significance with mean ± SEM. **<0.01, ***<0.001. Image taken from *H. Cetin et al, 2019.*

Unsurprisingly, for WT channels, changing the Cl^- concentration did not effect the peak current and rectification index remained constant for all holding potentials and for all chloride concentrations (figure 4.7 A and B). Interestingly, $AChR_{\alpha 1L251R}$ demonstrated inward rectification at positive holding potentials thereby deviating substantially from WT channels.

As shown in figures 4.7 C and D, by changing the driving force for Cl^- such that the intracellular Cl^- concentration with reduced to 10 mM in $AChR_{\alpha 1L251R}$, a change in rectification index to an approximate value of 8 ± 1.1 at a holding potential of ±100 mV indicated substantial inward rectification compared to WT. Indeed,

when the driving force for Cl^- was changed in the opposite way by reducing the extracellular Cl^- concentration to 10 mM, a corresponding decrease in rectification index compared to no change in Cl^- could be observed in which the rectification index was reduced to 2.6 ± 0.4 at ±100 mV.

4.2.7 L251R water interactions

Due to the prerequisite for solvation of cys-loop permeable ions [285, 286] and the wider role of water in ion permeability, we assessed the extent of this mutation on solvation at both Cl^- and Na^+ by comparing WT and $AChR_{\alpha 1L251R}$ channels.
As expected for WT channels, Na^+ permeated the channel with its inner water shell intact, remaining in a fully solvated state. Small but negligable depreciations in outer shell waters can be observed and may provide a small contribution to the energetic barrier seen in figure 4.4. Interestingly, Cl^- seems to pass WT channels with its inner solvation shell intact but with a larger depreciation in outer shell water molecule number. This could in part explain the larger energetic barrier for Cl^- ions and explain how contributions to permeability can arise from removal of water molecules arising from steric compenents determined by overall channel geometry.

Further to this, the Na^+ inner solvation shell at $AChR_{\alpha 1L251R}$ appears to remain intact across the pore and could be as a result of increasing inter L251R distance for Na^+ ions mediated by repulsive electrostatic effects between Na^+ and L251R residues, although substantial shedding of outer shell water molecules were observed. The most pronounced effects on solvation shell occur at Cl^- ions at $AChR_{\alpha 1L251R}$ where both inner and outer shell water molecules are perturbed at the 4 Å position. This partial desolvation of Cl^- is compensated for by L251R residues acting like surrogate water molecules to solvate the passing Cl^- ions as shown by decreasing inter-L215R distance (figure 4.6A).

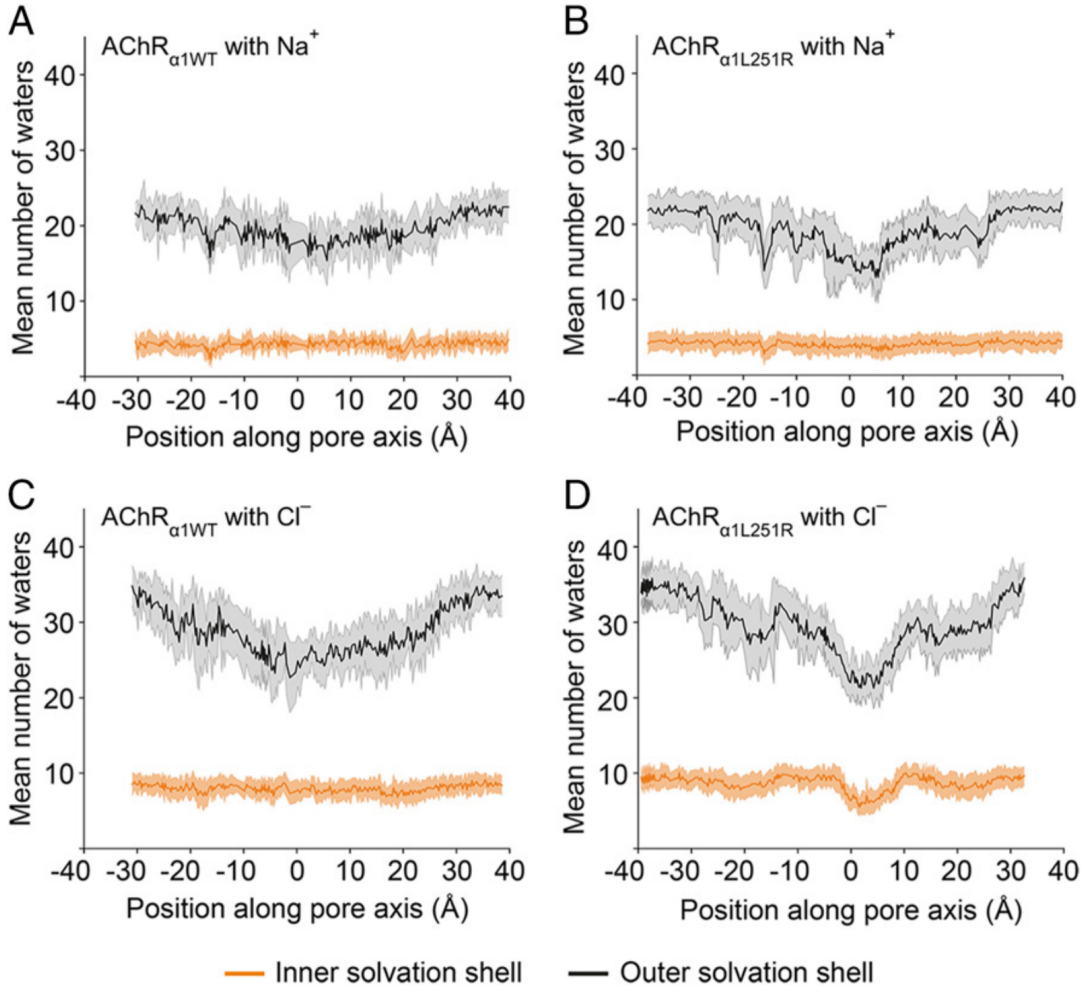

Figure 4.8: Analysis of number of water molecules comprising inner (orange) and outer (black) solvation shells for Cl^- and Na^+ as a function of their position along the z-axis of the channel pore at WT and AChR$_{\alpha 1L251R}$. Error bars show a single standard deviation. The distance used to calculate Inner solvation shell radii was obtained by manually adjusting until previous values [287] in bulk solution could replicated. Image taken from *H. Cetin et al, 2019.*

4.3 Discussion

In this chapter we show how a novel CMS mutation, α1L251R, perturbs normal physiological functions through substantial changes in overall nAChR biophysical properties- arising mainly through prolonged desensitization and deactivation as well as changes to ion selectivity as determined by a combination of whole-cell patch-clamp electrophysiology and enhanced sampling molecular dynamics simulations. Decreases in Na^+ permeability were shown to be responsible for reduced overall

conductances, especially at negative holding potentials for all mutant channels.

$AChR_{\alpha 1L251R}$ channels exhibited a duel voltage dependent permeability in which ion selectivity was swapped from cationic to anionic at positive membrane potentials. Under normal physiological conditions, the highly conserved 9' leucine gate residues at the M2 helix point toward the pore of the channel, forming a hydrophobic occlusion [274]. Post agonist binding, the M2 helices rotate such that these conserved leucine residues relieve this hydrophobic occlusion, opening up a wetted non-occluded path for ion conduction [53].

A previous study where large numbers of simultaneous perturbations to the 9' leucine gate of homomeric $\alpha 7$ neuronal nAChR were performed showed similar changes to desensitization kinetics, along with a change in agonist sensitivity. Additionally a change in rectification index could also be seen here where these mutations caused an ohmic muscle-like current voltage relationship [288]. Similar studies at muscle nAChRs showed that 5 simultaneous 9' leucine to Serine/Threonine ([289],[290]) mutations decreased desensitization rate constants whilst increasing ACh sensitivity.

Other studies that have attempted to swap ion selectivity have required 15 simultaneous mutations for $\alpha 7$ nAChRS ([279],[288]) 5-HT3ARs [280] and glycine receptors [281]. For the $\alpha 7$ nAChR specifically , a proline insertion between the 2' and 3' position located intracellularly alongside simultaneous mutation of 2' glutamic acid to alanine and 13' valine to threonine or the mutation of 9' lecuine to threonine was required.

If proline was inserted, without the additional 2' and 13'/9' mutations, channels were not functional. If proline was not inserted, the 2' and 13' mutations were insufficient to swap selectivity. This provided the first evidence that local conformations around this 2'-3' segment conferred selectivity and that overall helical orientation was less important as a determinant of charge selectivity for cys-loop receptors - work that

has been further expanded on more recently [276].

Our study expands on this previous work by examining a naturally occurring 9' perturbation at a smaller number of mutation sites (up to 2 simultaneous mutations) and which are charged demonstrating that charge selectivity of cys-loop receptors is not only determined by this 2'-3' region and that this can be 'overridden' by the introduction of mutations at the 9' gate.

By utilising enhanced sampling molecular dynamics simulations in the form of umbrella sampling, we could obtain a detailed energetic description of the effects of these mutations, revealing the potential swap in selectivity at homozygotic L251R stoichiometries. Measurement of the time averaged pore radius profiles of WT and AChR$_{\alpha 1L251R}$ showed an approximate 33% reduction in pore radius at AChR$_{\alpha 1L251R}$ channels (figure 4.6B) to 2.4 Å. This is below the typical distance for a hydrated Cl^- ion and therefore required partial desolvation for permeation to occur. Whilst desolvation infers an energetic penalty,positively charged arginine residues compensated for this via favourable electrostatic interactions. The energetic reward seen at around the position of these mutations could also provide an explanation to the reduced overall conductivity of Cl^- with respect to Na^+ at WT channels at positive holding potentials. It should be noted however that the precise open state of Cys-loop receptors is not known and correspondingly how permeation occurs is still unknown. Despite this, the values obtained for the PMF calculation are likely to be accurate- especially considering the ability to obtain ion selectivities in agreement for WT nAChRs.

Differences in rectification occur for both neuronal and muscle nAChRs with neuronal nAChRs displaying inward rectification [291] and muscle nAChRs a more ohmic current voltage relationship [66]. These differences are in part thought to occur as a result of intracellular Mg^{2+} or polyamine block as well as intrinsic voltage-dependent

mechanisms [292–294].

The conformational response of the mutant arginine residues to charged particles shown herein (figure 4.6A) provide an explanation for the rectification of $AChR_{\alpha 1L251R}$ channels at positive holding potentials, whereby different voltages effect these residues ability to interact with permeating ions. In order for the safety threshold for neuromuscular transmission to be met, a minimum of around 25% of WT nAChRs must be functional [295] which corresponds to the % of functional channels in the CMS patient identified herein. This is also in line with the mild phenotype of this patient. The identification of the heterozygous fast channel mutant at CHRNA1 αF256L in previous work also demonstrates how a reduction to 25% of WT channels can compensate for mutant CMS channels [295].

As $AChR_{\alpha 1L251R}$, $AChR_{\alpha 1WT/\alpha 1L251R}$ and $AChR_{\alpha 1L251R/\alpha 1WT}$ channels display very low Na^+ conductance but can successfully reach the cell surface - this CMS pathomechanism is primarily the result of a reduction in functional nAChRs, however the ability of $AChR_{\alpha 1L251R}$ to carry Cl^- at positive holding potentials provides evidence for an additional pathological mechanism. This would occur via a physiological antagonism in which the safety margin of neuromuscular transmission is decreased as a result of the offsetting of depolarising currents from Cl^-. Despite this, the threshold potential needed to elicit an action potential for muscle contraction occurs at around -50 mV [296], not within the range of $AChR_{\alpha 1L251R}$ chloride permeability. It is feasible however that in situations of high input resistance or vesicle release [297–299] the postsynaptic membrane may reach the required potential for Cl^- permeability. Additionally, as action potentials can depolarize the cell by up to 40 mV [295], this could shape the kinetics of an action potential causing them to terminate prematurely and therefore prevent signal propagation.

In conclusion we have shown how a clinically relevant single amino acid mutation in the muscle nAChR causes the conversion of a cation selective channel into a voltage

dependent anion selective channel with corresponding identification of a novel CMS mechanism.

"Let me tell you something about the Titanic: people forget that on the Titanic's maiden voyage there were over 1000 miles of uneventful, very pleasurable cruising before it hit the iceberg."

— Alan Partridge

5

Structural correlates of human muscle nicotinic acetylcholine receptor subunit assembly mediated by $\delta(+)$ interface residues

5.1 Introduction

5.1.1 Determinants of stoichiometric assembly in pLGICs

Pentameric ligand gated ion channels (pLGICs) are a large superfamily of ion channel that participate in a wide range of physiological and cellular functions. The nicotinic acetylcholine receptor (nAChR) represents one such member of this superfamily, with a distinct pharmacological profile and even more varied biophysical properties within its subfamily [300]. These biophysical properties are determined through several factors, with perhaps the most pronounced determinant arising from the large number of possible subunits that the nAChR can be comprised of.

With 17 different vertebrate subunits in the nAChR ion channel family and a total of 5 subunits making up functional channels [301] - the variety of stoichiometries found in nature is large. NAChRs found at the neuromuscular junction are comprised of four different subunits- namely $\alpha 2\delta\beta\epsilon$ for the mature receptor and $\alpha 2\delta\beta\gamma$ for the

foetal or denervated tissue stoichiometry and arranged in a specific fixed orientation (5.1A and B).

Two orthosteric sites located at the interfaces of $\alpha\delta$ and $\alpha\epsilon$ in adult or $\alpha\delta$ and $\alpha\gamma$ in the foetal receptor are typically occupied before the channel can open post Acetylcholine (ACh) binding. ACh binds at the highly conserved aromatic box regions of the orthosteric sites, where the formation cation-π interactions between a conserved tryptophan and the choline moiety of ACh [243, 245, 302] are thought to be a precursor to gating events. The well-preserved ordering of subunits in wild type muscle receptors suggests that allosteric effects arising from the pseudo-symmetrical architecture of the receptor play an important part in shaping its biophysical response and the nAChR has been used to demonstrate this concept in a number of earlier studies [303].

How exactly and to what extent the relative position of particular subunits in the global receptor topology shapes biophysical and pharmacological properties of the receptor is not fully known. By obtaining a detailed breakdown of what specific amino acid residues are involved in determining the fixed ordering of wild type muscle nAChRs, manipulated constructs can be generated with a non-canonical stoichiometric arrangement. These constructs can then be experimentally probed to delineate the importance of arrangement on receptor biophysics.

The molecular determinants of expression efficiency, oligomerization and assembly have been previously studied for GABARs [304], GlyRs [116], 5HT3aRs [305] and also nAChRS [117], [306–312]. Despite this, the full set of assembly determinants for human muscle nAChRs is not known. Work by Kreienkamp and colleagues [117] has shown that in Torpedo muscle nAChRs, a region in the extracellular domain of the γ subunit was essential for determining its position between α subunits. β subunit residues were also identified to play a role in assembly. What δ subunit

residues are important in determining assembly however have not been addressed.

Additionally, limited flexibility in stoichiometric arrangement has been shown in certain non-human heterologous expression systems [313–315], and in vivo [316] with the existence of a 'double-δ' arrangement. Other studies show additional arrangements in rat and mice [317, 318] and pronounced species specific differences within specific subunits have been demonstrated [307]. There is no current evidence of variable human stoichiometries.

Initially, by using Xenopus oocytes injected with specific ratios of human muscle nAChR subunit cDNAs we could determine what stoichiometric combinations could be spontaneously expressed and therefore what interfaces are allowed. The inability to obtain electrophysiological traces for $\alpha 2\epsilon 2\beta$ and $\alpha 2\gamma 2\beta$ arrangements and presence of traces for $\alpha 2\delta 2\beta$ conferred the importance of the δ-β interaction interface for governing WT receptor arrangements. By expanding on these initial results with the use of a human adult muscle nAChR comparative model subjected to conventional molecular dynamics simulations, we could detect potential candidates of specific molecular determinants for this interface. Further to this, integration of evolutionary data by using multiple sequence alignment helped us to further filter this simulation data and obtain a more precise picture of assembly determinants. Observations from the simulation were then validated with I^{125}-α-BuTx assays on chimeric constructs.

Additional MD simulations helped us to obtain a structural and dynamical explanation for the observed shifts in concentration response curve for WT compared to $\alpha 2\delta 2\beta$ assemblies. By comparing ACh bound and apo states of adult human muscle nAChR we could see that substantial dynamical differences for the loop C motif involved in agonist binding and gating occurred between both orthosteric sites and that the $\alpha\delta$ interface loop C was able to access an additional conformation resulting in a non-occluded binding site for the apo-state of the receptor. The $\alpha\epsilon$

interface lacked this conformation and was therefore deemed to be less hospitable to ACh binding during the initial diffusive step of agonist binding. By possessing two maximally hospitable interfaces for the $\alpha 2\delta 2\beta$ receptor stoichiometry, this could explain the increased sensitivity to ACh observed herein.

5.2 Methods

5.2.1 Homology modelling

Human adult muscle nAChR subunits were aligned with template structure (6pv7) subunits $\alpha 3$ and $\beta 4$ [247] with additional evolutionarily related sequences included to improve the accuracy of the alignment. A multiple sequence alignment (MSA) was generated in MUSCLE [319] and manually adjusted to obtain the final MSA (appendix figures B.1 and B.2). A single model was generated before further refinement of three non-conserved loops located on residues 562-572 of the δ subunit, 969-977 on the β subunit and 1768-1776 on the epsilon subunit. The numbers here refer to where they occur chronologically in the comparative model .pdb file. 10 conformations of each of these loops were generated with the best scoring molpdf used to determine what loop conformations to carry forward. The resulting final model was therefore selected from a total of 31 initial structures. Due to failure to resolve the intracellular domain for the template structure, this domain was excluded from modelling.

5.2.2 Docking

The grid box was centered on the aromatic cage region at both binding sites with a grid spacing of 1 Å and exhaustiveness set to 8 in Vina 1.1.2. Gasteiger charges [220] were added with non-polar hydrogen atoms being merged in Autodock 1.5.6. [221]. Poses were selected based on the lowest distance between the centre of geometry of all aromatic cage participating residues and the choline nitrogen atom of ACh

(figure 5.4).

5.2.3 MD Simulation

The comparative model was placed in a pure POPC bilayer with the inflategro.pl script [251]. The system was then solvated with TIP3P water [320] and Na^+ and Cl^- ions added to neutralise the system after which additional ions were added to obtain a 0.15 M Na^+ Cl^- solution. Energy minimisation with the steepest descent algorithm was done with a step size of 0.01 nm. Electrostatic interactions were calculated with Particle mesh Ewald [321] with van der waals and electrostatic cut-offs set to 10 Å and a cubic spline interpolation used. The LINCS algorithm was used [322] to constrain H-bonds enabling the use of a 2 fs tim-step. Amber SLipids [323–325] were used to model POPC and Amber ff99SB-ILDN [326] was used to model the protein. Equilibration steps were perfomed in the NPT ensemble for 1 ns with semi-isotropic pressure coupling using the Berendsen barostat [327]. A coupling constant of 1 was used for the pressure coupling. V-rescale [328] was used as the thermostat with a coupling constant of 0.1 and at 310 K. In this equilibration step, all backbone protein atoms were restrained at 1000 kJ/mol/Å^2 so as to allow lipid and solvent molecules to correctly orientate around the protein.

Expansions in the z dimension post equilibration meant that water and ions were re-added to a reduced box after this initial equilibration step to improve sampling efficiency. This new reduced system was equilibrated using the same parameters as previously described but for an increased length of 5 ns. Production runs were performed in the NPT ensemble using the Nosé-Hoover [257] thermostat with a coupling constant of 0.5. The barostat used was Paririnello-Rahman [329] with a coupling constant of 1.0. Independent simulations were generated by using velocity generation at the start of each simulation with a random seed and simulated for 100 ns each.

5.2.4 Multiple Sequence Alignment and Contact Matrix analysis

An additional MSA was generated using mammalian δ, ϵ and γ subunits to further filter assembly residue candidates detected from the MD simulations. This alignment was performed in accordance with the method described in the previous section. Residue-residue contacts were detected through a pair-wise residue contact matrix where contacts between residue pairs were recorded if they fell below 8 Å between residues Cβ atoms as denoted in the CASP criteria [330]. The contact matrix was coded using the MDanalysis python library [331, 332]. The residues in the contact matrix are numbered without regard to signal peptide sequences.

5.2.5 Molecular Biology

Human muscle nAChR DNA was cloned into pcDNA3.1 vectors (Invitrogen). The δ-ϵ-ϵ chimeric construct was made via PCR with overlap extension [228]. All other chimeras were purchased through GeneArt (Ragensburg, Germany). Cloned constructs were verified by sequencing (Eurofins-MWG, Germany). I^{125}-α-BuTx assays were prepared and performed as described previously [16].

5.2.6 Expression of nAChRs in *Xenopus Oocytes*

Dissection of *Xenopus laevis* for ovary extraction was done in accordance to UK Home Office regulations. Oocyte preparation was done as outlined in chapter 3: Methods. All WT subunits were injected in equivalent ratios at a volume of 50,6 nl per oocyte with an automatic Nanoject Oocyte Injector (Drummond, Broomall, PA, USA).2ng total of $\alpha 2\delta 2\beta$, $\alpha 2\epsilon 2\beta$ and $\alpha 2\gamma 2\beta$ arrangements were injected at a ratio of 2:2:1 for each respective subunit per oocyte. Injected oocytes were kept in Barth's solution at 18°C for a between 2-5 days with 5mg/l of neomycin at pH 7.6.

5.2.7 Electrophysiology and concentration response curves

Electrophysiological traces were obtained with an automated HiClamp system (Multi Channel Systems) using a two-electrode voltage-clamp (TEVC) configuration to obtain macroscopic currents. Oocytes were perfused with Ringer's solution (pH 7.4) at a rate of 15 ml/min with a 3 M KCl solution for the electrodes. Electrodes with resistances over 1 M Ω were discarded. ACh concentrations were diluted with Ringer's solution on the day of the experiments. All recordings were obtained at room temperature. Normalisation of current traces was done by dividing obtained values against the mean of two EC_{100} ACh applications occurring both prior to and post ACh application. EC_{100} ACh concentrations were obtained every two data points.

5.2.8 Data analysis

Concentration response curves were fit according to a four-parameter Hill equation using graphpad Prism 5 (Graph Pad, CA, USA). The EC_{50} values of individual curves were plotted and analysed with an unpaired two-tailed t-test. P was set to 0.05. For I^{125}-α-BuTx assays, statistical significance was determined using a one-way ANOVA and Tukey's post hoc correction.

5.3 Results

5.3.1 Assessment of functional variant stoichiometries by electrophysiology

$\alpha 2\delta 2\beta$, $\alpha 2\gamma 2\beta$ and $\alpha 2\epsilon 2\beta$ stoichiometries were injected in a 2:2:1 ratio for each respective subunit in the construct into *Xenopus* oocytes, with macroscopic currents obtain with TEVC recordings to determine what stoichiometries could be spontaneously expressed in a heterologous expression system and therefore what the allowed and disallowed interfaces were. No current traces were obtained for

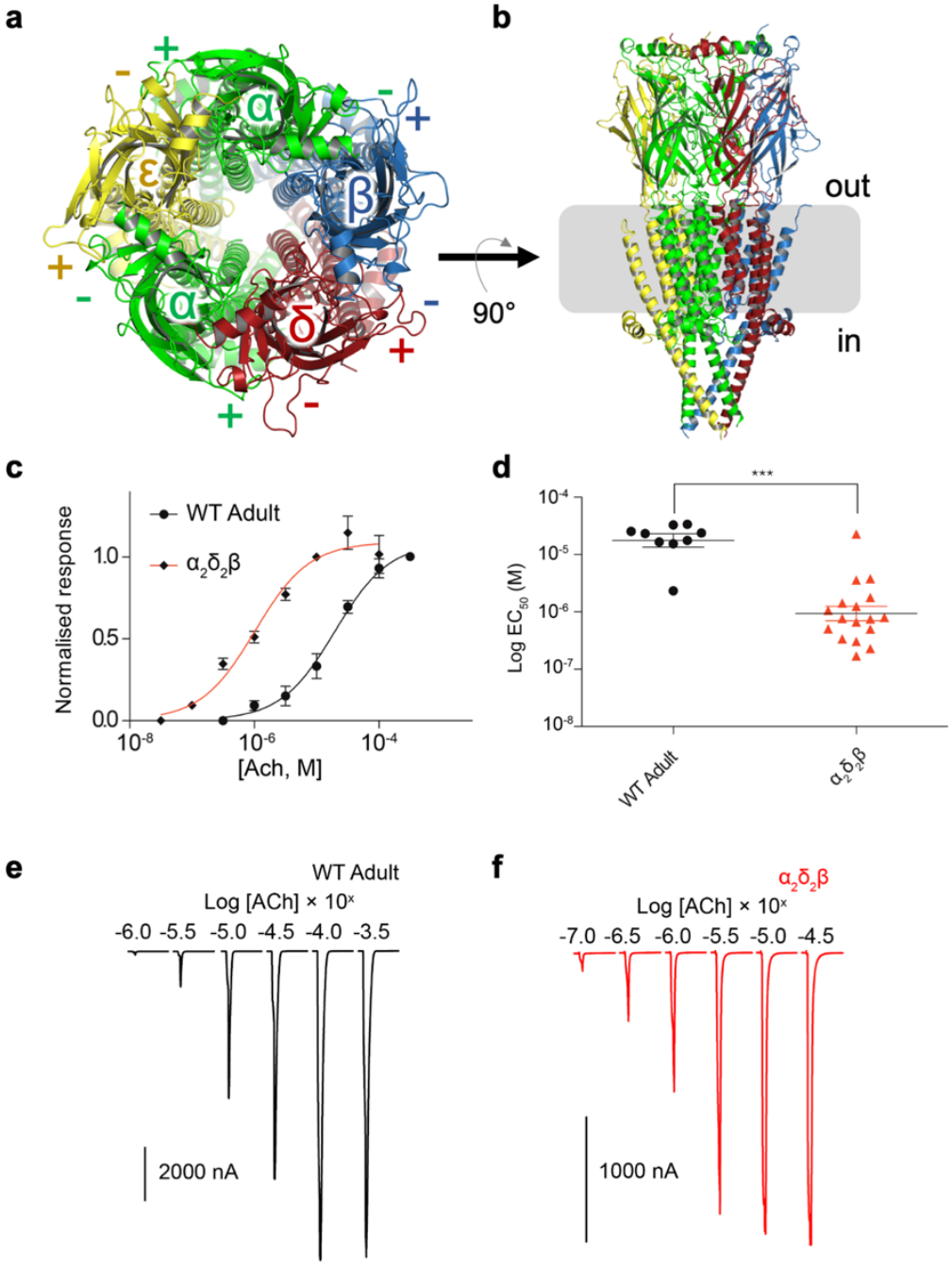

Figure 5.1: Top down view of human adult muscle nAChR (A) and rotated side on view of the same model (B). Individual subunits are labelled accordingly. The grey box depicts the location of the phospholipid bilayer in which the model is situated. WT and $2\alpha2\delta$ β nAChR Log CRCs to ACh (B). EC_{50} values taken from fit data of ACh CRCs and plotted individually with mean and 95% confidence intervals. $p < 0.0001$ = *** (C). Representative current traces of $2\alpha2\delta$ β (red) and WT (black) (C).

$\alpha 2\gamma 2\beta$ and $2\alpha 2\epsilon\beta$ in the first instance and therefore 1:2:1 ratios of each respective subunit were injected. Again, no electrophysiological traces were measured. WT receptors were activated by ACh in a concentration dependent fashion (EC_{50}= 17.58 μM, lower bound CI= 9.46 μM, upper bound CI= 32.7 u M, n=9). The $\alpha 2\delta 2\beta$ stoichiometry responded to ACh in a concentration dependent manner (EC_{50}=0.938 μM, lower bound CI=0.507 μM, upper bound CI= 1.73 μM, n= 17). There was a statistically significant change in EC_{50} value for $\alpha 2\delta 2\beta$ stoichiometry and a resulting leftward shift in CRC denoting increased ACh sensitivity for this stoichiometry with respect to WT. This shift represented an 18.7-fold change in ACh sensitivity for $\alpha 2\delta 2\beta$ constructs. Despite the lack of traces for $\alpha 2\epsilon 2\beta$ and $\alpha 2\gamma 2\beta$ stoichiometries, non-functional receptors could possibly still be expressed at the surface of the cell. To rule out this possibility- I^{125} an α-BuTx assay was done (figure 5.5C). The lack of detectable signal showed that these receptor stoichiometries are not expressed on the surface of the cell. As only $\alpha 2\delta 2\beta$ stoichiometries could be obtained, it appeared that the δ β subunit interactions were the major determinants for functional pentamer formation.

5.3.2 Subunit interactions determined from MD simulations

A per-residue pairwise contact-matrix analysis of 10, 100 ns unbiased MD simulations was employed to determine precise interactions between subunit interfaces where Cβ atom distances below 8 Å were recorded, and densities mapped on to a 2D grid (figure 5.2). All residues that fell below 8 Å for at least 70% of total collective simulation time were determined to be initial assembly candidates and displayed in figure 5.2. Not all of the component residues detected in this initial analysis were likely to be specific assembly determining residues or have a less substantial role in determining assembly and therefore further filtering of the data was required in order to select the major assembly determining residues.

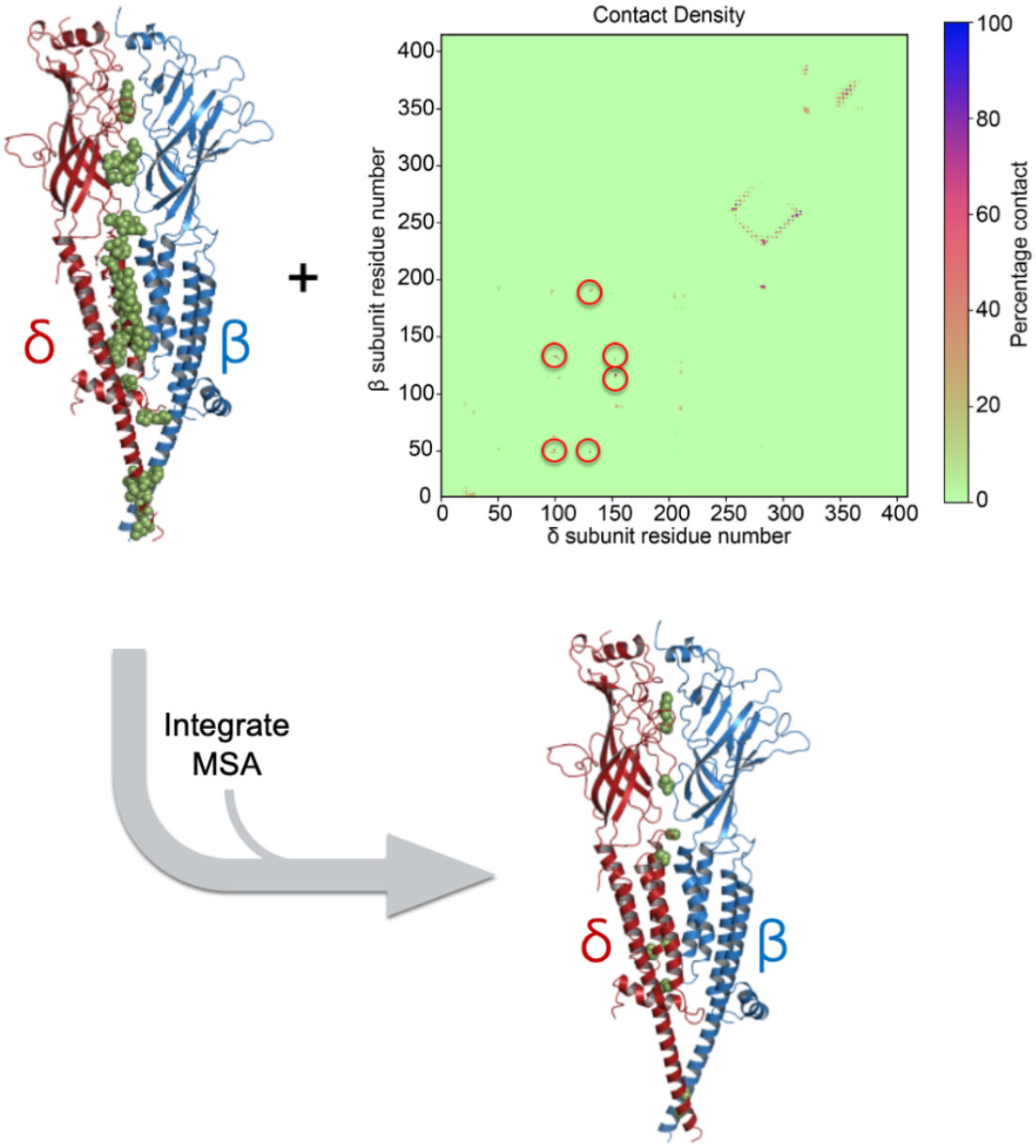

Figure 5.2: Projection of detected residues (green spheres) from the contact matrix on to δ (red) and β (blue) subunits (top left image). % contact of pair-wise Cβ atom contact matrix density for δ and β subunits over all repeated simulations (top right panel). Projection of candidate residues after integration of MSA data (lower panel).

ϵ and γ subunits are both located between the two α subunits and as such should possess the same assembly determining amino acid residues whilst the delta subunit should deviate at those positions. As such, an evolutionary criterion was adopted in which a selection of mammalian δ, ϵ and γ subunits ,with δ residues that deviated from conserved ϵ and γ residues being denoted by a black arrow B.4 and B.5.

Integration of both contact analysis and evolutionary data was able to provide a more precise description of major assembly determinants and those residues that satisfied both criteria are denoted with a red arrow B.4 and B.5. Additionally, these residues are projected onto the comparative model and displayed in figure 5.2.

Residues	**% contact of aggregate simulation time**
N119	287
L172	291
K173	260
E277	120
T279	406
S297	170
A302	365
H335	73
P439	179
G442	365

Table 5.1: Table 1: δ- residues detected in both md simulation contact analysis and MSA integration. % contacts are for respective Cβ atoms below 8 Å. % greater than 100 indicate residues that contact more than 1 β subunit residue.

Each residue determined from this analysis was then analysed specifically to determine the number of frames of the total simulation time that its Cβ atom was below 8 Å of any β subunit Cβ atom (table 5.1). The inability to resolve intracellular domain regions in the template structure of the homology model meant that potential ICD contacts were not determined in this analysis.

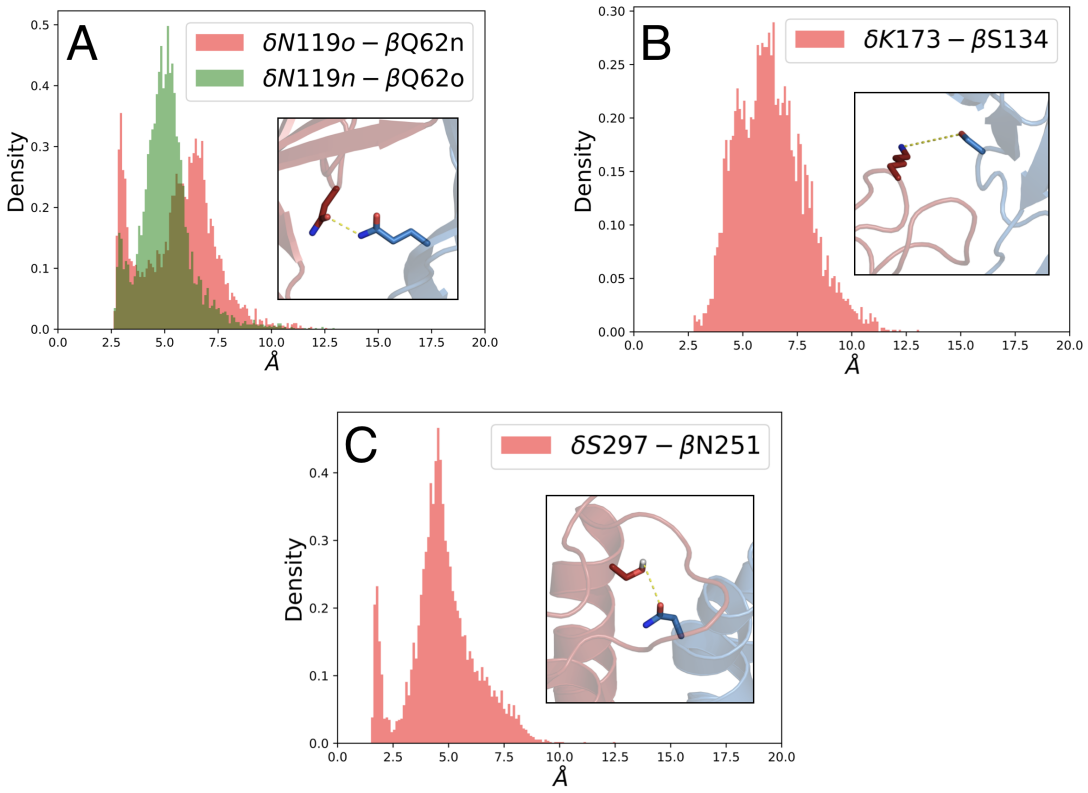

Figure 5.3: Histograms of hydrogen bonding contacts. Both potential H-bond donor and acceptor moieties distances are plotted for δN119 and βQ62 with the dominant mode shown as a representative snapshot in the insert (A). Histograms of δK173-βS134 (B) and δS297-βN251 (C) pairs with representative snapshots of the respective collective variables as inserts. Residues of interest are shown in the stick representation with δ and β residues coloured in red and blue.

5.3.3 Hydrogen bonding dynamics of assembly residues

After determining a set of candidate assembly residues, charged or hydrophilic δ subunit amino acids were specifically analysed for their propensity to form hydrogen bond interactions with the neighbouring β subunit. δ subunit residues K173, N119 and S297 were located proximately to hydrophilic β subunit residues Q62, S134 and N251 respectively. Density plots of each residue pair R-group interactions were performed (figure 5.3).

As δN119 and βQ62 residues each possess an H-bond donor and acceptor moiety N119 carbonyl- Q62 nitrogen and N119 nitrogen-Q62 carbonyl distance distributions were plotted (figure 5.3A). For this residue pair, the N119 carbonyl- Q62 nitrogen

interaction is the dominant hydrogen bond with a sharp, well-defined peak at approximately 3 Å. A representative snapshot of this binding interaction is displayed in the insert of this figure.

Interactions between δK173 and βS134 (figure 5.3B) show a wide bimodal distribution with peaks at around 5 Å and 7 Å. This wide distribution depicts a large conformational flexibility for this residue pair and although hydrogen bond interactions are indeed possible here, they are probably sub-optimal. The δS297 and βN251 residue pair showed clear and well-defined peaks at approximately 2 Å and 5 Å (5.3C). As both residues reside on secondary structural regions, backbone atoms are unlikely to deviate substantially, and the major conformational changes observed will be determined through side chain rotation- likely explaining the clear definition of peaks in this figure.

Non-equivalency of orthosteric sites arising from unique loop C dynamics

To obtain a dynamical and structural explanation for the functional differences in ACh sensitivity demonstrated in figure 5.1, a further 10 100 ns simulations of ACh bound nAChRs were performed. Due to known loop C participation in both agonist binding and gating [333, 334], loop C dynamics at both αδ and αβ interfaces for both ACh bound and apo sates were examined (figure 5.4) by measuring the distance between the centre of geometry of loop C disulphide sulphur atoms and αW149 residue carbonyl backbone oxygen atom. ACh binding modes at both interfaces are largely the same (figure 5.4 A), with loop C mobility also remaining similar between interfaces (figure 5.4 C). A representative snapshot of the ACh binding mode along with the measured collective variable is included as (figure 5.4 B). Comparison of orthosteric site loop C mobility at the apo-state receptor however shows clear differences between binding sites (figure 5.4 D) with the α δ associated loop C possessing a distinct flexible conformational state located at around 15 Å. This peak is suggestive of an open non-occluded binding site and

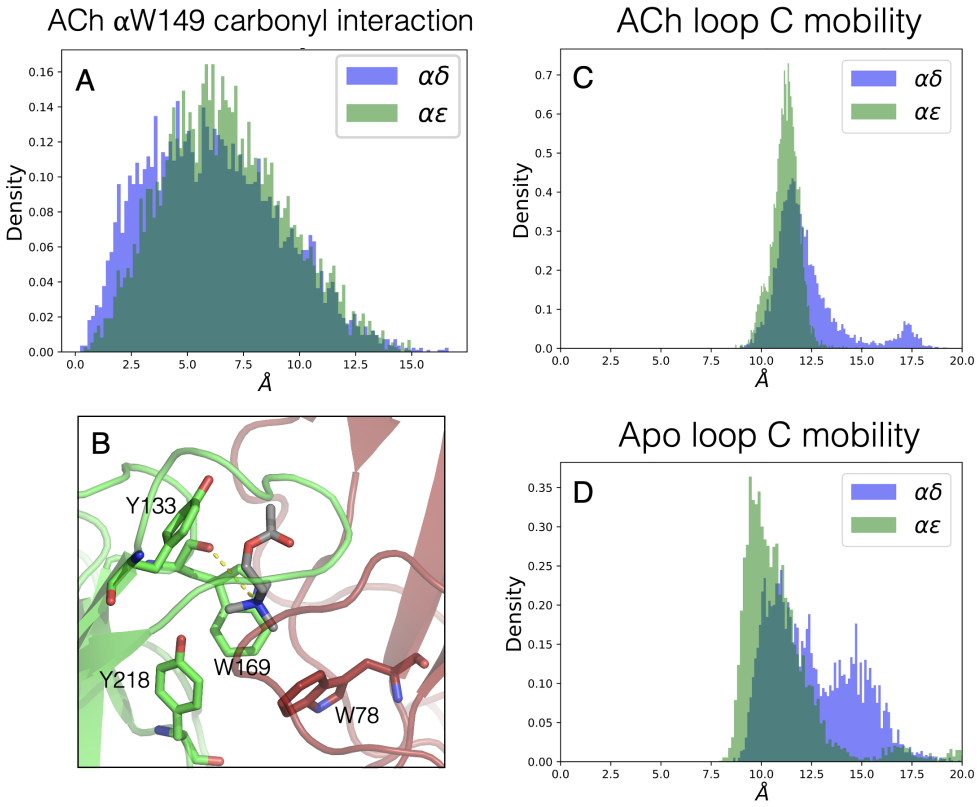

Figure 5.4: Histogram of ACh choline nitrogen and αW169 carbonyl oxygen distance at both binding sites (A) with a representative snapshot at the α δ interface (B). Histograms of loop C motions at ACh bound (C) and apo (D) states at both binding sites. The distance between the centre of geometry of loop C disulphide sulphur atoms and αW169 tryptophan carbonyl oxygen was used to obtain the density plots in C and D.

solution facing loop C.

5.3.4 I^{125}-α-BuTx binding at chimeric constructs

From the combination of electrophysiology, MD simulation and evolutionary analysis, specific assembly determinants were identified and shown to reside across both extracellular and transmembrane domains. As previous experimental work on other pLGICs or nAChRs of different species has only identified extracellular domain residues as being determinants of assembly [118, 335], we sought to confirm the observation shown herein that assembly determinants were not confined to the ECD by generating a series of chimeric nAChR subunits. Specifically, δ subunits with different ϵ components were progressively mutated into the subunit and the ability

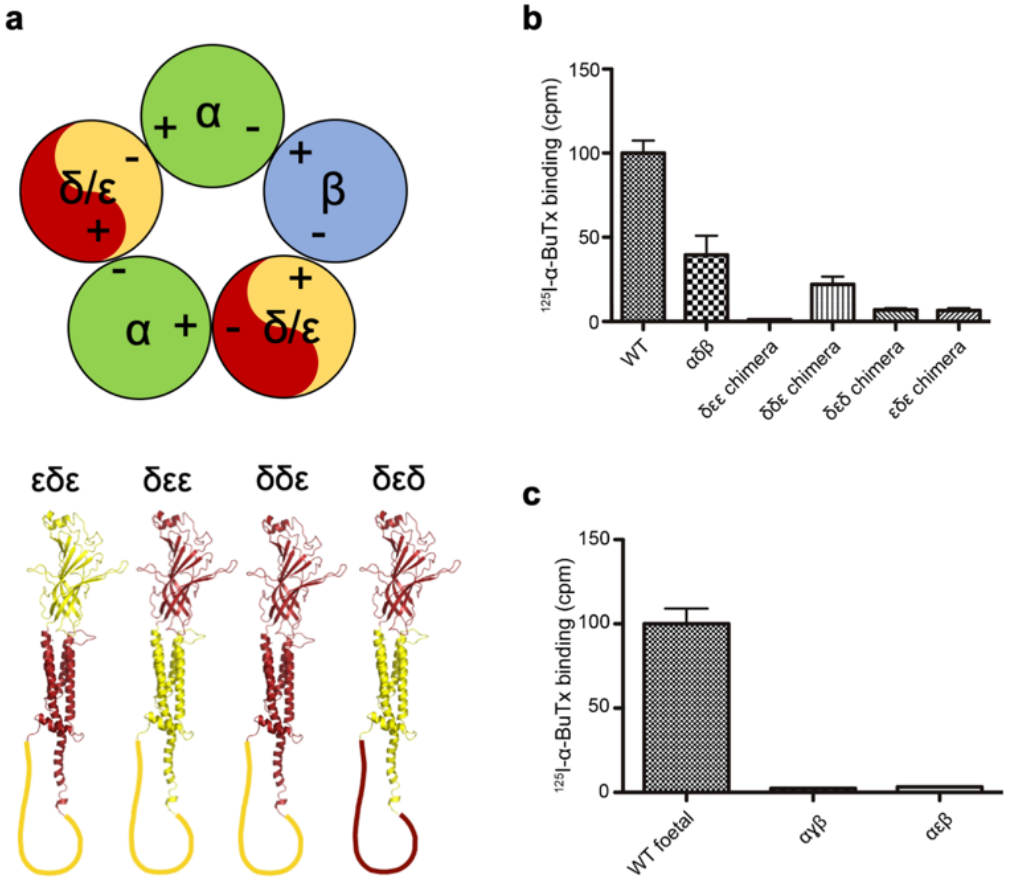

Figure 5.5: Schematic of proposed stoichiometric arrangement of subunits in I^{125}-α-BuTx assay (A) with specific chimeric constructs used depicted in the lower panel. Results of I^{125}-α-BuTx chimera assay. Data normalised with respect to WT counts with mean and 95% confidence intervals.WT n=12, α δ β n=6, δ ϵ ϵ n = 6, δ δ ϵ n = 6, δ ϵ δ n=6, ϵ δ ϵ n=5. I^{125}-α-BuTx data for α γ β (n=3) and α ϵ β (n=3) normalised to WT foetal receptor (n=2). Associated significance table shown for table 5.2

of to form pentameric receptors was determined via I^{125}-α-BuTx binding assays. The associated subunits and overall chimeric receptor stoichiometries are depicted in 5.5A.

The $2\alpha2\delta\beta$ construct show a robust although reduced cell-surface expression compared to WT and is to be expected given the ability to obtain electrophysiological currents for this stoichiometry. The reduced level of expression is commensurate with this non-canonical stoichiometry. Chimeric constructs δ-ϵ-ϵ, δ-ϵ-δ and ϵ-δ-ϵ are not-statistically significant from one another and show radioactive counts indicative of no cell surface expression. The δ-δ-ϵ construct is capable of reaching the surface

Residuess	**Significance**
WT vs $\alpha\delta\beta$	***
WT vs $\delta\epsilon\epsilon$	***
WT vs $\delta\delta\epsilon$	***
WT vs $\delta\epsilon\delta$	***
WT vs $\epsilon\delta\epsilon$	***
$\alpha\delta\beta$ vs $\delta\epsilon\epsilon$	***
$\alpha\delta\beta$ vs $\delta\delta\epsilon$	***
$\alpha\delta\beta$ vs $\delta\epsilon\delta$	***
$\alpha\delta\beta$ vs $\epsilon\delta\epsilon$	***
$\delta\epsilon\epsilon$ vs $\delta\delta\epsilon$	***
$\delta\epsilon\epsilon$ vs $\delta\epsilon\delta$	ns
$\delta\epsilon\epsilon$ vs $\epsilon\delta\epsilon$	ns
$\delta\delta\epsilon$ vs $\delta\epsilon\delta$	*
$\delta\delta\epsilon$ vs$\epsilon\delta\epsilon$	*
$\delta\epsilon\delta$ vs $\epsilon\delta\epsilon$	ns

*** < 0.0001, * < 0.05, ns = not significant

Table 5.2: Table with results of ANOVA with Tukey's multiple comparison tes of I^{125}-α-BuTx binding assay

of the cell albeit with reduced expression compared to WT and $2\alpha2\delta\beta$ constructs and is statistically significantly different to non-expressed chimeric constructs.

The requirement of both δ extracellular and delta transmembrane domain components for cell-surface expression confirms that δ subunit assembly determinants between the $\delta(+)\beta(-)$ interface does indeed occur across domains and that whilst the intracellular domain is not essential in forming pentameric receptors, is important in enabling efficient expression- as seen by the reduced levels of expression compared to $2\alpha2\delta\beta$ stoichiometry.

5.4 Discussion

The plethora of individual nAChR subunits as well as potential for a range of stoichiometric assemblies allows for a range of biophysically and pharmacologically distinct nAChR subtypes capable of performing a large range of different functions

utilized by distinct cell types. End-plate nAChRs are the most structurally diverse nAChRs, consisting of 4 different subunits arranged in a fixed ordering. The emergence of a so-called developmental switch occurring after muscle maturation [336, 337] further increases this functional diversity.

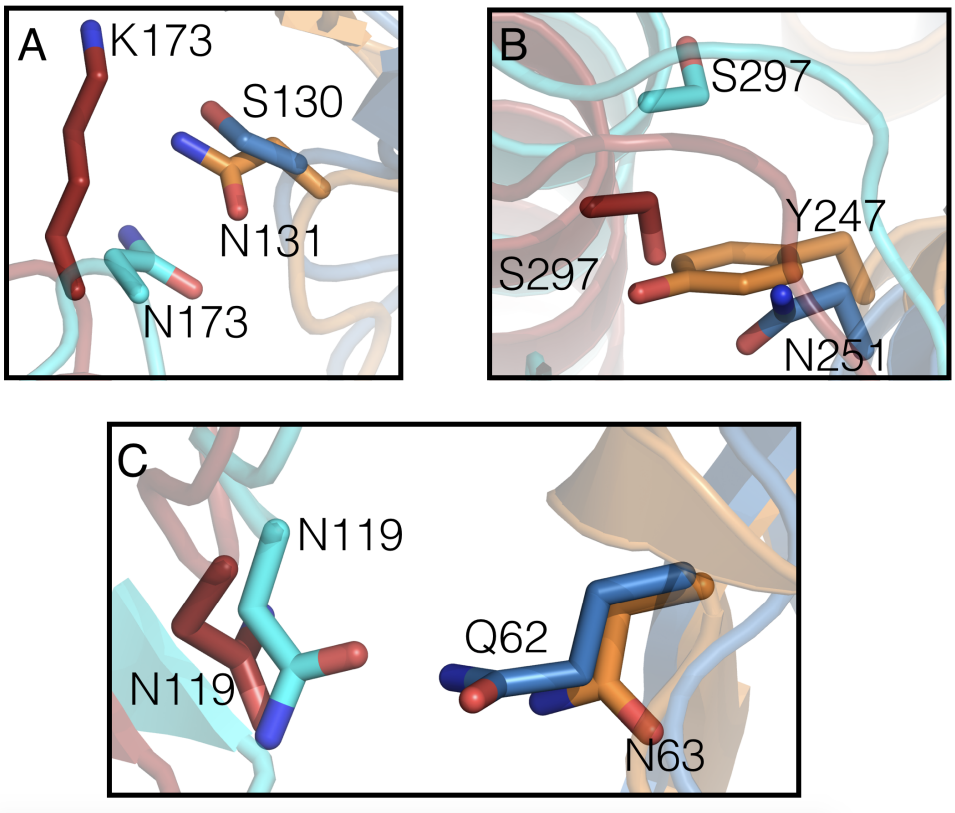

Figure 5.6: Comparison of human adult muscle nAChR δ and β subunits (red and blue) with Torpedo Cryo-EM structure 6UWZ δ and β subunits(cyan and orange). Calculated all-atom RMSD of subunits was 2.43Å)

Hypothetical swapping of ϵ and δ subunits would still retain both orthosteric binding sites, yet this non-canonical arrangement has not been seen in nature. The relative positions of these subunits must therefore play some role in shaping the overall biophysical characteristics of WT nAChRS and that this effect is a consequence of the receptors pseudo-symmetrical geometry. One way to address the question as to what extent subunit position shapes underlying receptor biophysics would therefore be to obtain a construct with swapped δ and ϵ subunits. For a swapped stoichiometry to be obtained however, the full set of molecular determinants that

enable the fixed canonical receptor arrangement must be elucidated so that the appropriate mutations can be made.

Additionally, the large variation in response to ACh observed across species for the same subunit [338–341] in conjunction with how previous studies on nAChr assembly have all been performed on non-human subtypes demonstrate the need to first study human subtypes before appropriate mutations can be made. Previous work on mouse nAChRs indicate that α subunit interfaces possess assembly determinants [117], however the δ subunits role in maintaining canonical receptor stoichiometry specifically has been overlooked as well as the nature of those contacts with the neighbouring beta subunit. Cryo-electron microscopy efforts [342, 343] at *Torpedo* nAChRs have assisted in the understanding of how interfaces are formed, they do not address the relative importance of individual residues in enabling these interfaces. Structural alignment of recently determined *p-torpedo* structure 6UWZ [39] with our human nAChR homology model demonstrate that the assembly residues identified in our analysis deviate between these two species (figure 5.6).

It has been suggested that the δ subunit is an ancestral endplate nAChR subunit of which ϵ and γ subunits later evolved from [344]. Looking at the overlay of p-torpedo and human nAChRs you can see that the identified assembly determinants have evolved since the older p-torpedo variety which do not possess ϵ subunits. Therefore, whilst δ p-torpedo subunits may not possess strong assembly determinants, human subunits could have plausibly evolved to possess strong assembly determinants to allow for the developmental switching of γ and ϵ subunits in a structurally selective and regulated fashion.

By examining the ability for diverse functional stoichiometries of the endplate nAChR to be spontaneously expressed in *Xenopus* oocytes we determined that the $\delta(+)\beta(-)$ interface must play an important role in enabling WT conformations. This was conferred by the inability of 2:2:1 ratio cDNA injection of α, ϵ, β and α, γ, β

subunits to form functional pentamers in contrast to α, δ, β cDNA injections. As the ϵ and δ subunits both share one common interface in the WT conformation, namely with the $\alpha(+)$ face, yet ϵ and γ subunits are not tolerate between $\alpha(+)$ and β(-) interfaces, suggests that the δ subunit is somehow adapted to form a favourable interface with the β(-) interface.

The sigmoidal concentration response curves with approximately uniform hill slope for 2:2:1 injected α, δ, β stoichiometries indicates that this stoichiometry is indeed α-δ-α-δ-β. As β subunits are a requirement for functional expression of WT nAChRS [315, 345], this provides further evidence for this unique stoichiometry. Additionally, the response to ACh of this human $\alpha 2 \delta 2 \beta$ arrangement replicates previous results for bovine nAChRs [314].

The propensity for isolated ICDs for the 5HT3A receptor to assemble independently [305] as well as the ability for currents to be detected at pLGICs lacking ICDs [346] are in line with results obtained by I^{125}-α-BuTx binding assays herein, specifically with regard to the δ-δ-ϵ chimeric construct. The ICD of the δ subunit has been shown to preside in a mostly disordered, unfolded conformation [347] as well as already possessing a role in cytoskeletal protein interactions, further demonstrating its non-involvement in subunit arrangement and importance in expression efficiency.

The lack of expression observed for the δ-ϵ-ϵ chimera when compared to δ-δ-ϵ suggests that transmembrane domain components contribute to canonical subunit assembly and further to this, lack of expression in ϵ-δ-ϵ suggests that both extracellular and transmembrane domains are required simultaneously in enabling $\delta(+)$ face contacts with the β(-) face. As such, molecular determinants for receptor assembly do not in fact reside exclusively in the ECD as previously suggested by the existence of so-called ECD residing 'assembly boxes' [335].

Specific hydrogen bonding interactions between δ and β interfaces were detected from MD simulations with pairs between both δN119 – βQ62 and δK173 – βS134. Interestingly, the δN119-βQ62 pair appeared to interact in a sub optimal fashion, with a single hydrogen bond interaction of two potential hydrogen bonds dominating the observed dynamical ensemble (figure 5.3 A).

The δK173- βS134 pair also formed hydrogen bonding interactions, again in a suboptimal fashion as determined by both residues' high degree of conformational flexibility and solvent exposure. Whilst a notable interaction peak at 5 Å did occur, a denser peak at 7Å was dominant and probably represents weak interactions between the pair (figure 5.3 B). At the equivalent position to δK173 in the mouse γ subunit, this residue was shown to be a key molecular determinant for enabling $\gamma(+)\alpha(-)$ interactions [117] and it is therefore especially interesting that we observe sub optimal interactions for this residue.

By comparing the δ subunit to ϵ with a structural overlay (5.7) we can see that overall assembly may be governed not just by the active favourable contacts between δ and β subunits, but unfavourable ones between ϵ and β. Homologous residues in ϵ to δK173 and δN119 are threonine and isoleucine residues, with a concurrent loss of the hydrogen bonds detected in the simulations outlined here.

δS297 and βN251 were also detected from the simulations as a potential hydrogen bond pair. Examination of the distance between δS297s hydroxyl hydrogen and βN251 oxygen atom shows highly stable interactions (figure 5.3 C). The location of this residue pair at the M2M3 motif is notable due to known involvement in gating transitions [90] [348] for other subunits. Despite this, work by Auerbach and colleagues [349] has shown that the δ subunit M2-M3 linker is unique insofar that mutations to this region do not appreciably effect binding to gating transitions, compared to the same mutations in other subunit M2-M3 linker regions. This leaves open the possibility that the δ M2-M3 linker region participates in other functions

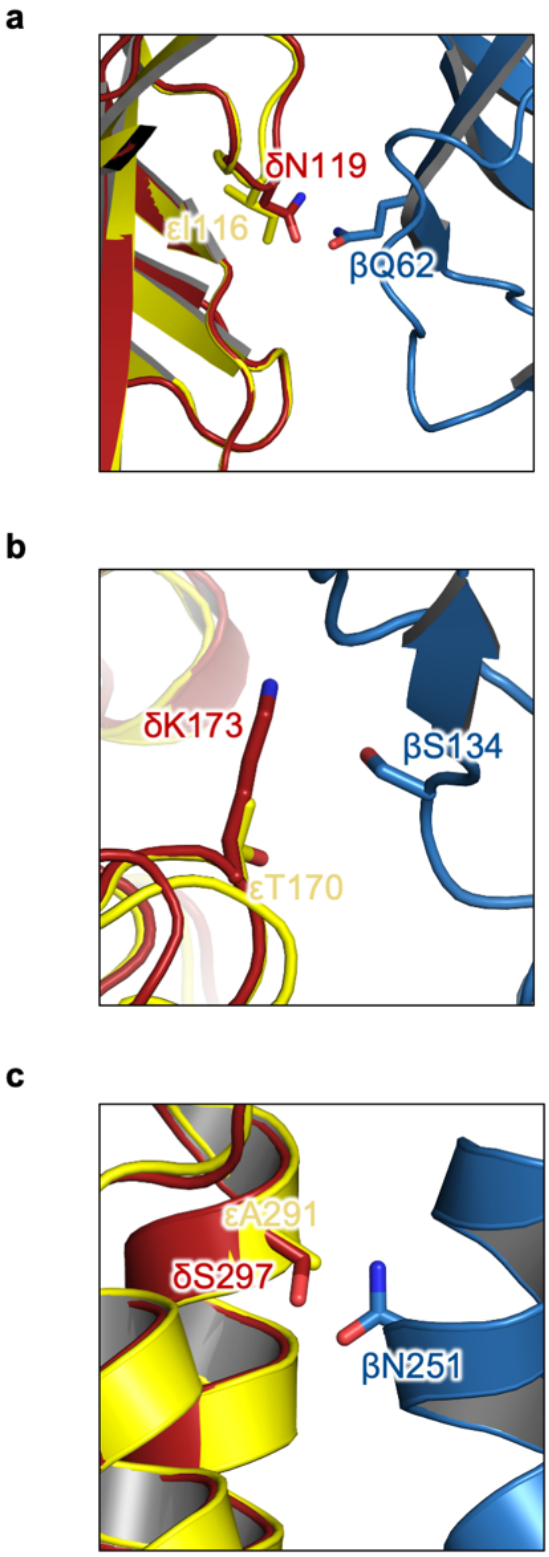

Figure 5.7: Comparison of δ and ϵ assembly determinant positions. δN119 and ϵI116 are located at homologous positions (A). δK173 and ϵT170 are located at homologous positions (B). δS297 and ϵA291 are located at homologous positions. The β subunit and its proposed assembly contributing residue is shown for context.

such as correct subunit assembly.

The hydrophilic amino acid residue δE277 in the -1' region of the TMD was also identified from the contact matrix analyses but is highly unlikely to participate in assembly determination as it is conserved with respect to both β and α subunits. It is also known to contribute to ion selectivity [350]. δH335 was shown to possess contacts with the neighbouring β subunit, however it's protonation state is not known and the percentage contact for this residue was low compared to other detected residues (5.1).

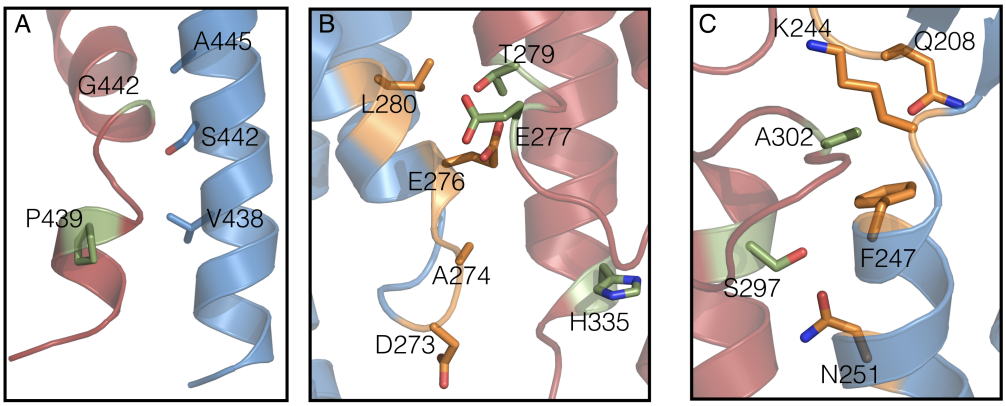

Figure 5.8: Snapshots of potential hydrophobic contributions to δ β interface assembly at the MX helix (A), TMD and M1-M2 loop (B) and M2-M3 loop (C). Candidate residues are displayed as sticks in green (δ subunit) and orange (β subunit).

As well as hydrogen bonding interactions between δ and β subunits, several hydrophobic residues were detected and are outlined in 5.8. Of particular interest is residue δ T279 located at the 1' region at the M1-M2 loop motif (5.8B). This residue is located within the inter-helical bundle of δ and β subunits with inter-helical interactions are not fully known- but have previously been shown to arise as a consequence of intrahelical aromatic packing [116]. Hydrophobic residue δP439 and δG442 are located intracellularly at the M4 helix (5.8 A) in a solvent exposed environment. This solvent exposure would make neighbouring hydrophobic interactions with the β subunit extremely favourable from a thermodynamic

standpoint.

As well as looking at key $\delta(+)\beta(-)$ interaction pairs, we also wanted to obtain a dynamical explanation for the observed changes in CRC between $\alpha 2\delta 2\beta$ and WT receptors. As a well-known structural motif involved in both binding and gating, we examined loop C mobility at α δ and α ϵ orthosteric interfaces in apo and ACh bound models by obtaining density plots of the distance between the centre of geometry of loop C disulphide sulfur atoms and αW149 backbone carbonyl atoms. Loop C dynamics at both interfaces for the ACh bound state were similar (5.4 A) for both interfaces. Comparison between loop C dynamics at apo and ACh bound states however showed marked changes in mobility with a solution facing open loop C conformation at the α-δ interface in the apo state compared to the more closed loop C conformation at the α-ϵ interface (5.4 C and D).

The decreased occlusion at the α-δ interface could plausibly reduce steric occlusion of the binding site to ACh molecules at the diffusive stage of agonist binding. The presence of two $\alpha\delta$ interfaces at the $\alpha 2\delta 2\beta$ stoichiometry would therefore possess maximally hospitable binding sites compared to WT and could explain the increased sensitivity to ACh (5.1). Previous work has suggested that α δ and α ϵ binding sites are functionally equivalent [351], however as these studies were performed in mice and ACh response has shown to deviate across species - it is not necessarily the case that this functional equivalence occurs for human subtypes. Additionally, the δ loop F is poorly conserved between species, residing proximal to the loop C and contributing to signal propagation to the M2M3 linker region from initial loop C contacts [352].

6

Future work and conclusions

6.1 BPD drug discovery

The targeting of nAChRs for the treatment of OPNA exposure remains a sensible therapeutic strategy as no consideration would need to be given to the specific suspected OPNA. The future success of non-oxime BPDs for targeting nAChRs however rests on their optimisation via a rational asymmetric approach allowing for increases in affinity. At present, BPDs bind non-selectively to a range of targets including muscarinic acetylcholine receptors, AChE and of course nAChRs. Whilst all therapeutically relevant, without targeted affinity increases, these compounds are unlikely to be clinically useful.

Removal of a charged quaternary ammonium group from existing symmetric BPDs would prevent the confounding of further structure-based drug design efforts resulting from the swapping of homologous regions of the ligand such that the rationally designed allosteric moiety does not occupy the orthosteric site. These efforts however are likely to prove extremely challenging due to the unburied, solvent exposed nature of the proposed allosteric face thereby decreasing the sites druggability [353]. Further to this, rational drug design approaches on homology models tend to fall off in accuracy with the sequence identity of the model [354]. The accuracy of

predictions for future drug design efforts will therefore depend in part on obtaining an experimentally resolved 3-dimensional structure of the human muscle nAChR.

The highly charged nature of non-oxime bispyridinium compounds would also preclude their use for targeting centrally mediated effects of OPNA exposure due to their low bioavailability resulting from low blood-brain-barrier penetrance and increased consideration should be given to non-oxime BPD pharmacokinetics for future structure-based drug design campaigns.

6.2 Determinations of ion selectivity and permeability in pLGICs

The use of molecular mechanics forcefields are unlikely to correctly predict inductive effects of ions and their associated water molecules and as such may not faithfully represent a complete picture of ion permeation. Recent efforts utilising polarizable water forcefields have shown deviations compared to simple point charge water models where energetic landscapes are more rugged and slightly increased for both cations and anions at the 5HT3A receptor [355]. This likely reflects the increased number of degrees of freedom introduced in the model. Despite this, the validation and implementation of interoperable forcefields for water, ions, proteins and lipids alike needs further study as well as the reconciliation of computational observations with experimental ones.

When it comes to delineating the basis of charge selectivity in pLGICs- a large body of work has already been collected over several decades with recent work by Cymes and Grossman [356] suggesting that complex basis of selectivity may not be clearly explained simply by primary structure of pLGICS. This was further substantiated by molecular simulation studies that suggest the importance of pore lining side-chain conformations on charge selectivity [277].

With regards to the utilisation of molecular simulation for probing structure-function relationships of ion channel proteins, a very careful assessment of model parameters must be considered as small differences between studies may result in drastically different observations [357]. Even subtle changes between forcefield parameters may result in noticeable changes in observed measured values, and in a previous study [358], Na^+ conductance at a *torpedo* nAChR was found to differ substantially between all-atom and united-atom forcefields. To this end, a greater degree of consensus amongst the simulation community as to what underlying parameters should be used for probing ion channel function would greatly assist in enabling reproducible observations and more insightful comparisons.

Computational electrophysiological approaches also offer a way for introducing voltage differences in model systems and could further help to improve the accuracy of computational predictions of ion channel function by replicating physiological phenomena computationally [359].

6.3 Determinants of stoichiometric arrangement in the muscle nAChR

To date, there have been several studies to delineate the structural determinants of the specific stoichiometric arrangement of heteromeric pLGICs. At this point, a complete picture of the muscle nAChR stoichiometry determinants is close. Whilst the study outlined in this thesis focused on validating computational observations by measuring cell-surface binding of chimeric subunits with swapped domains-validation using specific amino acid mutations is ongoing and should help to fully validate the observations contained herein. Additionally, once complete, it should be experimentally feasible to swap δ and ϵ/γ subunits and determine the relative importance of interface location with respect to global receptor topology on the overall biophysical properties of the nAChR.

6.4 Conclusions

Our understanding of nAChR structural biology and allostery has clearly come a long way since John Newport Langley's early observations [360]. Despite this, there is still some way to go before a we have a complete understanding of the nAChR. While neuronal nAChRs remain attractive targets for pharmacological intervention [361] therapeutic drugs targeting the muscle nAChR remain limited and known allosteric sites typically bind lower affinity modulators or non-therapeutic experimental photoaffinity probes [362–366]. The recent 'resolution revolution' in Cryo-EM [12] should help in the determination of heteromeric pLGICs which has thus far been precluded in part by difficulties in subunit assignment as a by-product of low cryo-EM resolution [367]. Also, the increasing number of open-state/ variable state pLGIC structures that have been determined should also help to accelerate structure-based drug design efforts and the discovery of new allosteric modulators. Combining improved experimentally determined 3-dimensional structures of pLGICs with ever improving molecular mechanics force-fields and associated computational hardware should greatly improve our understanding of the various role of allostery in nAChRs and pLGICs more broadly looking into the future.

Appendices

A

Partial charges for MB505 from GAFF parametrisation

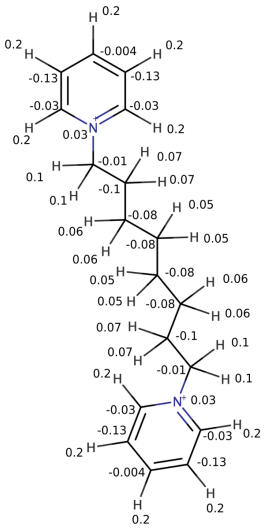

Figure A.1: Skeletal formula of MB505, or 'Octyl-BPD' with associated charges as assigned by parametrisation with the general AMBER forcefield

B

Multiple Sequence Alignments for analysis and model building

Contents

B.1 6UWZ model alignment

B.2 3JAE model alignment

B.3 Chimera contact matrix filter alignment

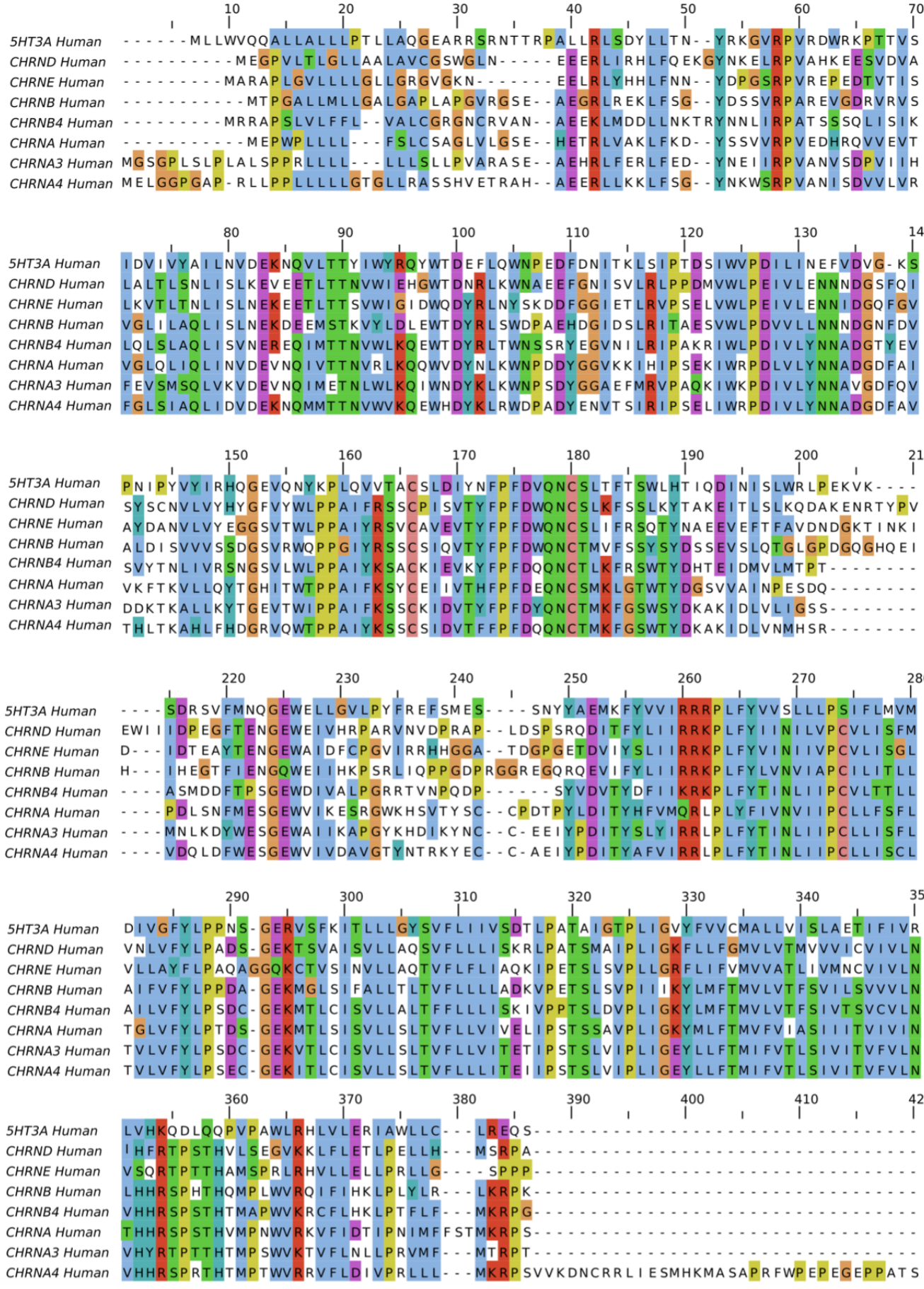

Figure B.1: Homology model MSA

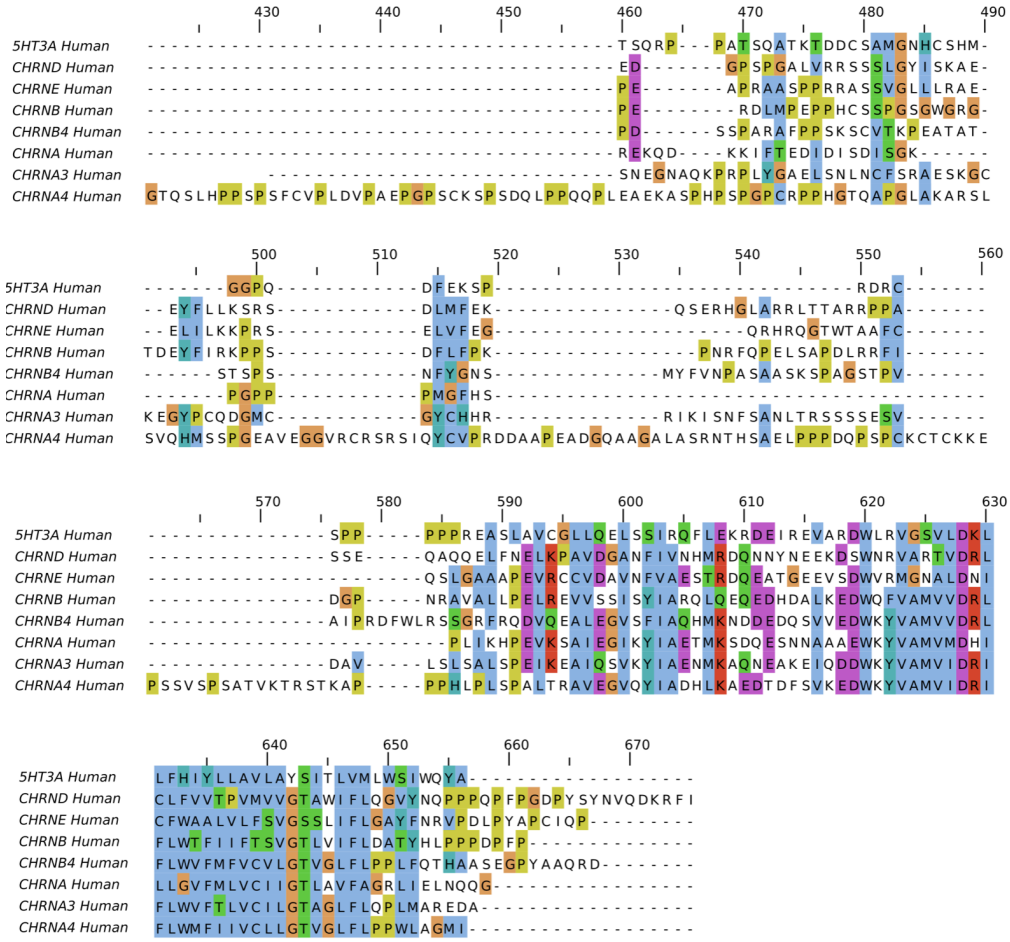

Figure B.2: Homology model MSA

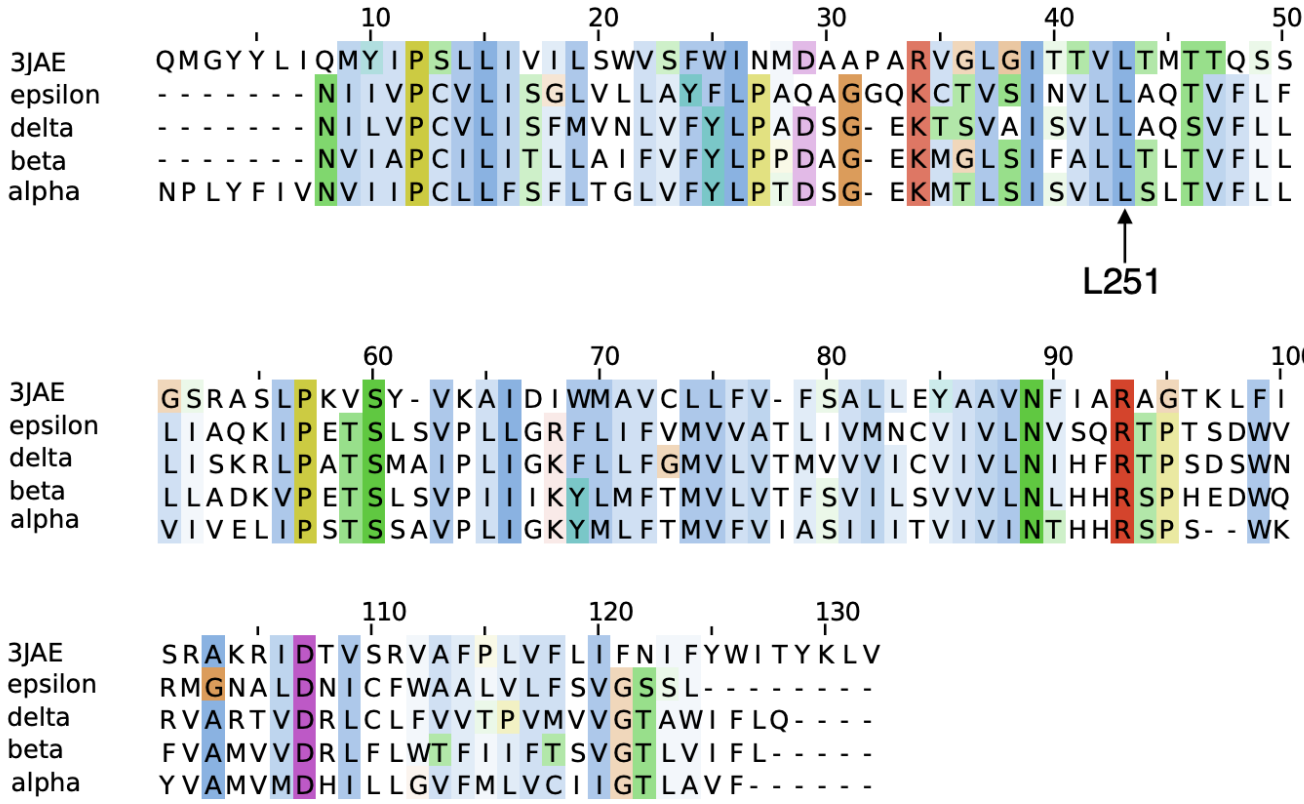

Figure B.3: 3JAE TMD alignment with human muscle TMD regions. Residue conservation is indicated with the ClustalX colouring scheme in Jalview. Image reproduced from [16]

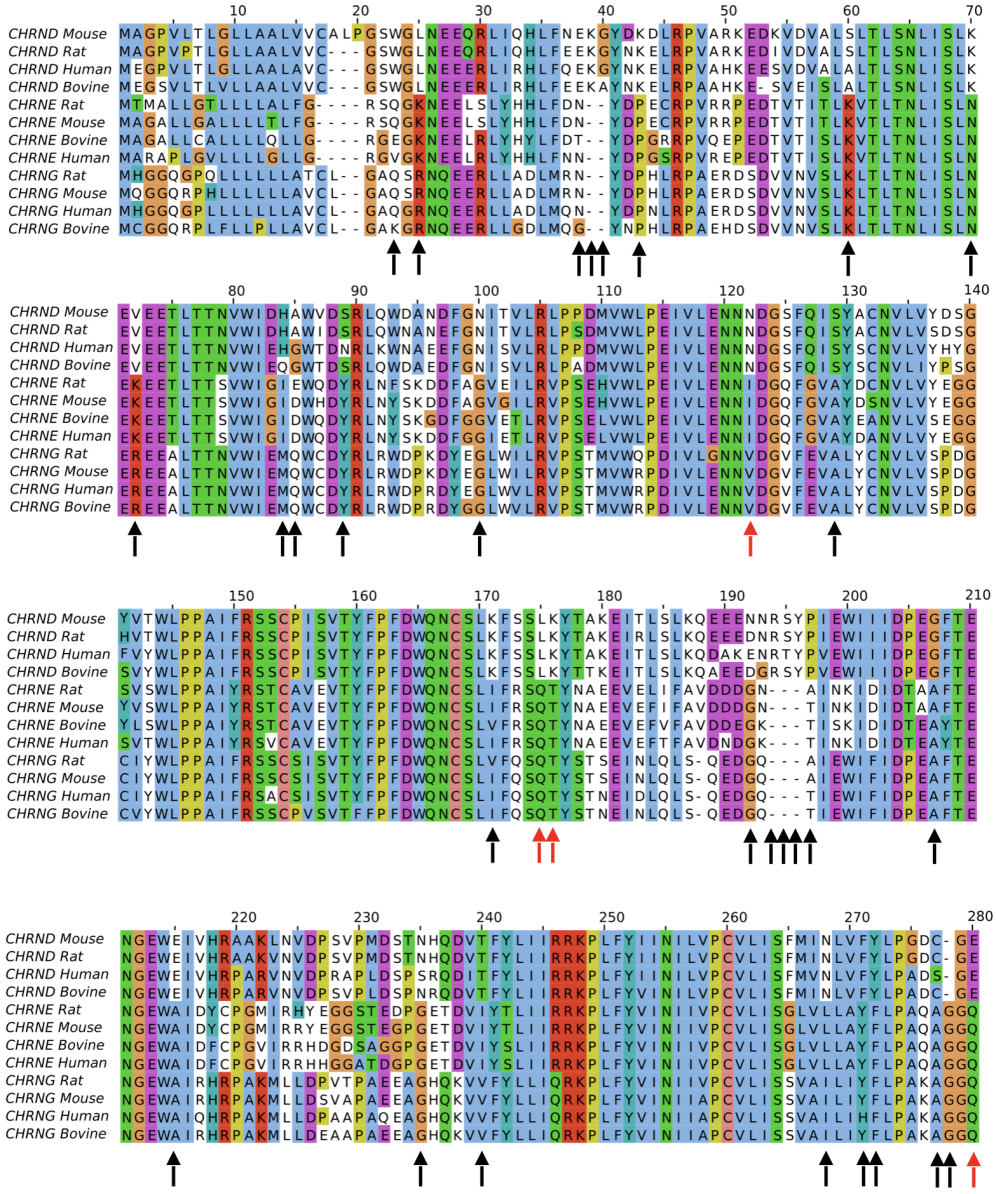

Figure B.4: Contact matrix alignment part 1

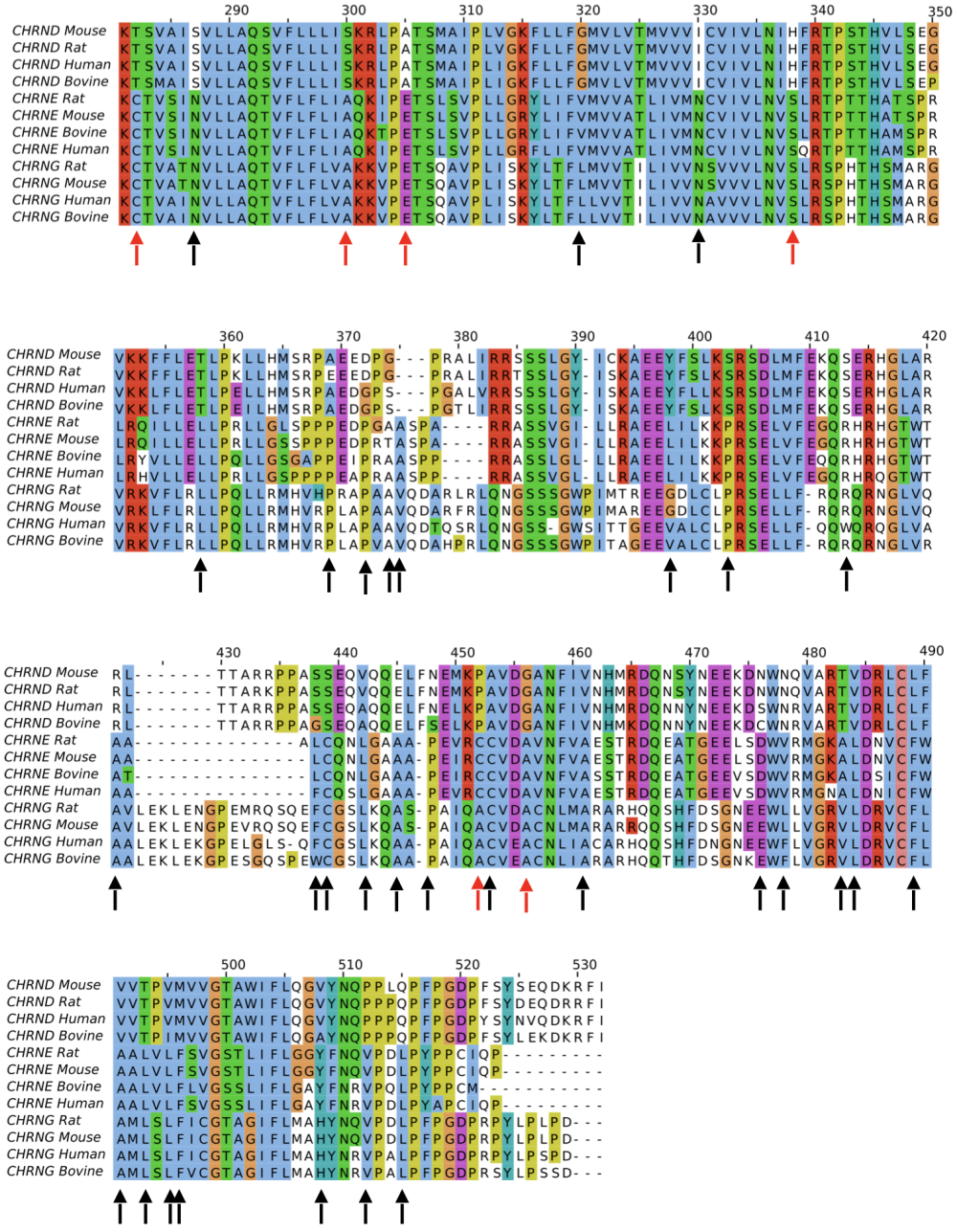

Figure B.5: Contact matrix alignment part 2

C
PMF convergence

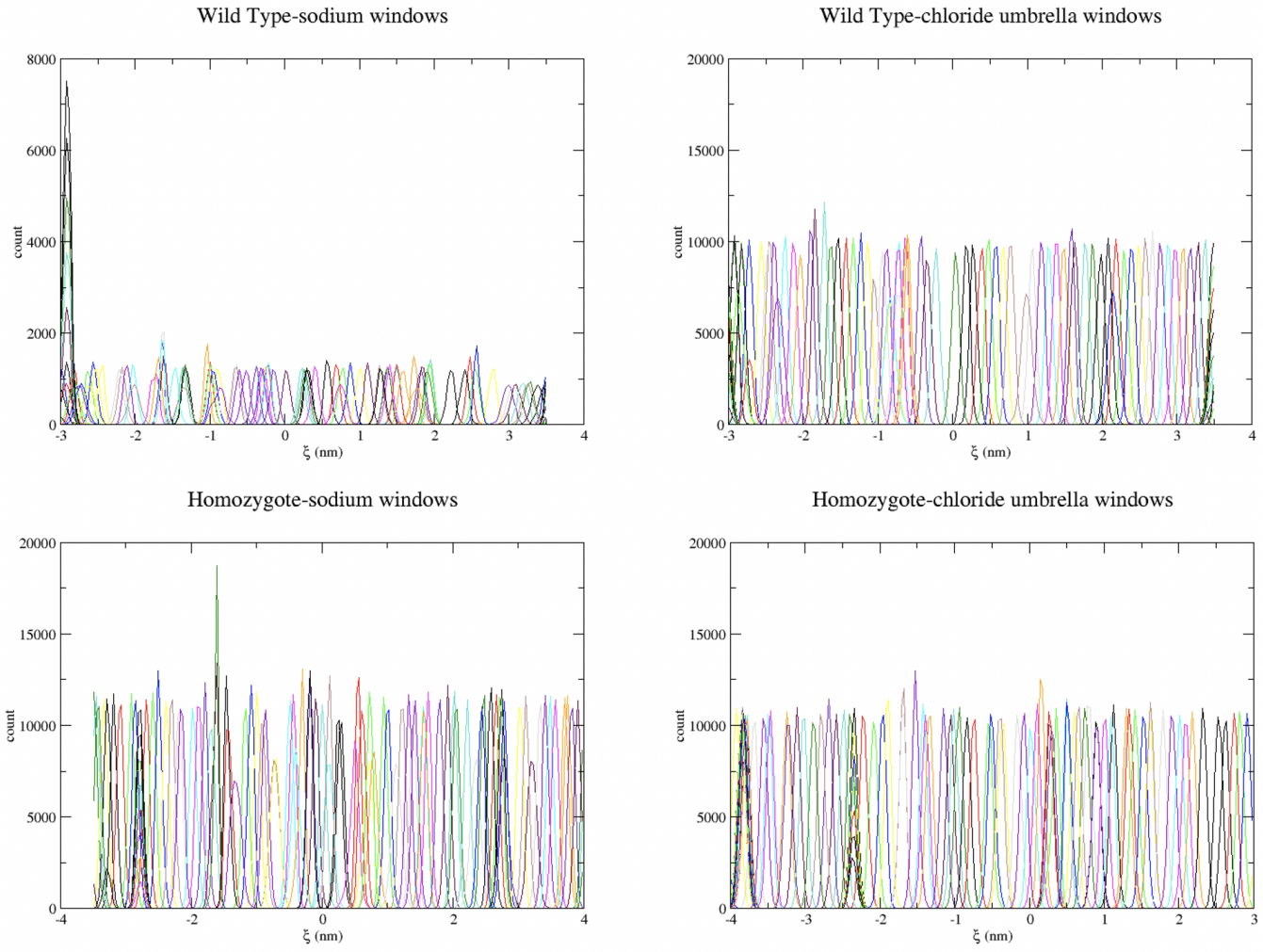

Figure C.1: Individual histograms for each umbrella sampling window used in the calculation of WT and homozygous PMFs for Na^+ and Cl^- ions.

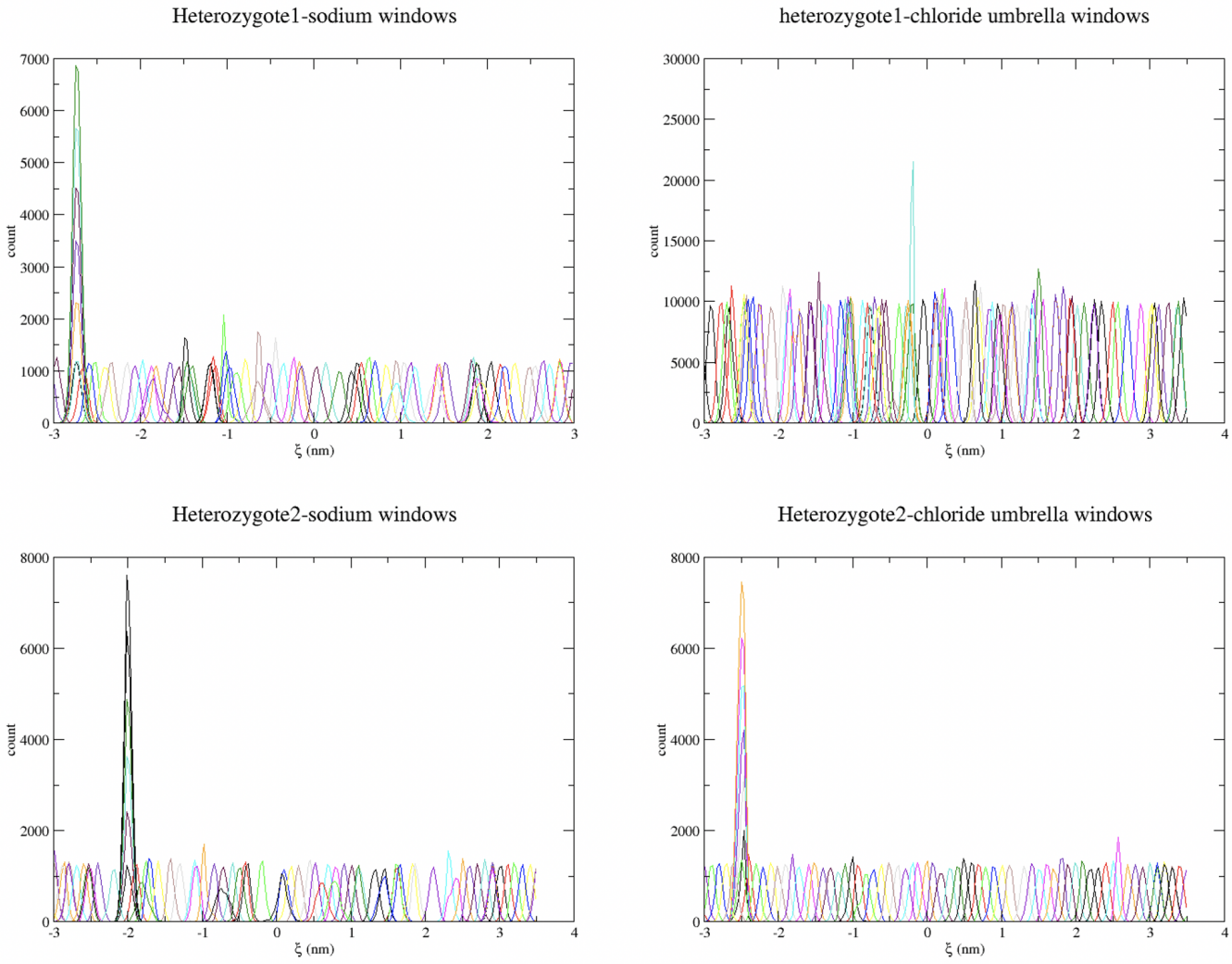

Figure C.2: Individual histograms for each umbrella sampling window used in the calculation of heterozygous PMFs for Na^+ and Cl^- ions.

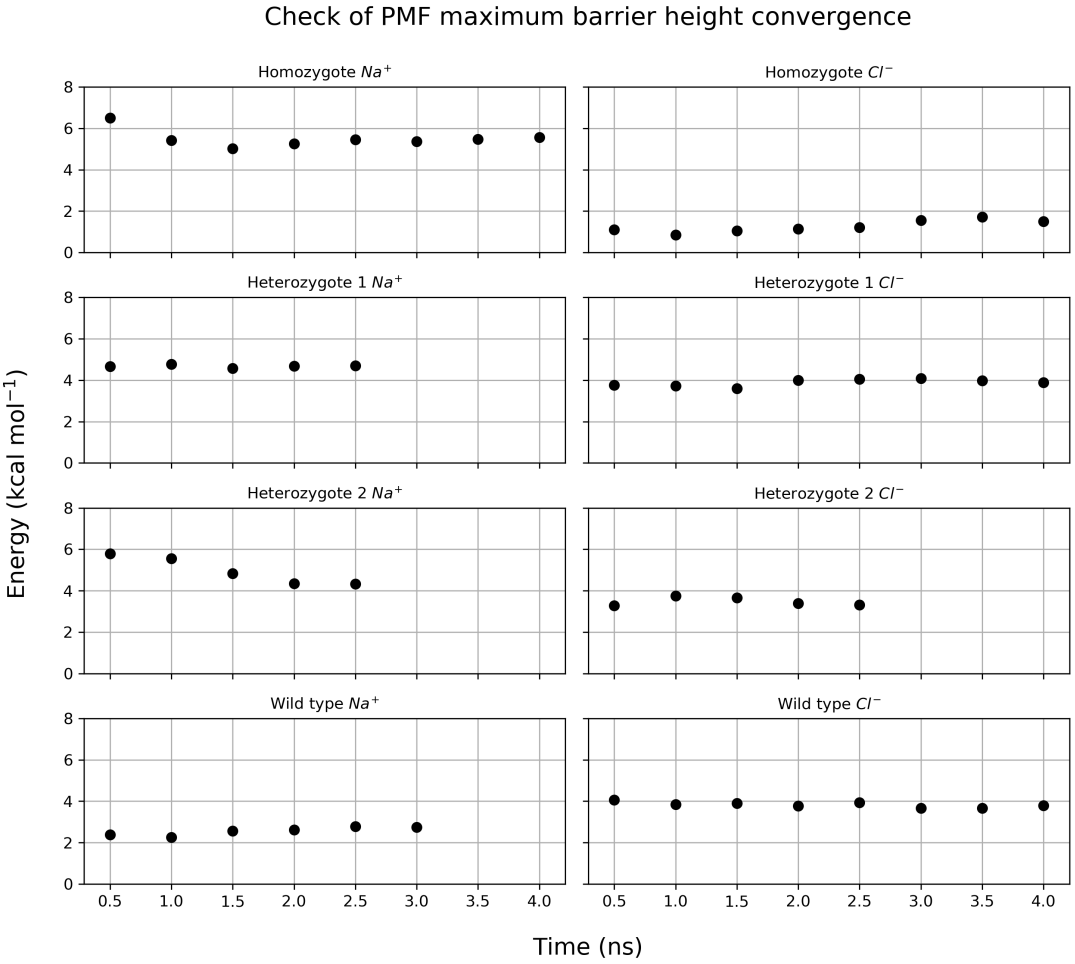

Figure C.3: Block analysis of all systems show fast convergence of barrier height values.

D
Publications

Muscle acetylcholine receptor conversion into chloride conductance at positive potentials by a single mutation

Hakan Cetin[a,b], Max Epstein[c], Wei W. Liu[a], Susan Maxwell[a], Pedro M. Rodriguez Cruz[a], Judith Cossins[a], Angela Vincent[a], Richard Webster[a], Philip C. Biggin[c], and David Beeson[a,1]

[a]Nuffield Department of Clinical Neurosciences, University of Oxford, Oxford OX3 9DS, United Kingdom; [b]Department of Neurology, Medical University of Vienna, 1090 Vienna, Austria; and [c]Structural Bioinformatics and Computational Biochemistry, Department of Biochemistry, University of Oxford, Oxford OX1 3QU, United Kingdom

Edited by Richard L. Huganir, The Johns Hopkins University School of Medicine, Baltimore, MD, and approved September 11, 2019 (received for review May 15, 2019)

Charge selectivity forms the basis of cellular excitation or inhibition by Cys-loop ligand-gated ion channels (LGICs), and is essential for physiological receptor function. There are no reports of naturally occurring mutations in LGICs associated with the conversion of charge selectivity. Here, we report on a CHRNA1 mutation (α1Leu251Arg) in a patient with congenital myasthenic syndrome associated with transformation of the muscle acetylcholine receptor (AChR) into an inhibitory channel. Performing patch-clamp experiments, the AChR was found to be converted into chloride conductance at positive potentials, whereas whole-cell currents at negative potentials, although markedly reduced, were still carried by sodium. Umbrella sampling molecular dynamics simulations revealed constriction of the channel pore radius to 2.4 Å as a result of the mutation, which required partial desolvation of the ions in order to permeate the pore. Ion desolvation was associated with an energetic penalty that was compensated for by the favorable electrostatic interaction of the positively charged arginines with chloride. These findings reveal a mechanism for the transformation of the muscle AChR into an inhibitory channel in a clinical context.

myasthenia | acetylcholine receptor | charge selectivity

The nicotinic acetylcholine receptor (AChR) in muscle is a member of the Cys-loop ligand-gated ion channel (LGIC) superfamily. It mediates electrical signal transmission from nerve to muscle via the opening/closing of a transmembrane cation conductive pore. The AChR is found at high density on the postsynaptic membrane of the neuromuscular junction, where it generates the endplate potential (EPP) in response to acetylcholine (ACh) released from the nerve terminal into the synaptic cleft. The EPP usually exceeds the threshold potential required for the activation of voltage-gated sodium channels that initiate an action potential in the muscle fiber and trigger muscle contraction. Various congenital myasthenic syndromes (CMSs) have been attributed to a malfunction of AChRs. The mutations reported to date affect different receptor properties such as ligand binding, conductance, gating, or desensitization (1, 2), but none have been shown to change ion selectivity.

The AChR channel pore selects for cations according to size (3) and is formed by the second transmembrane (M2) helix of each of the 5 receptor subunits (4). Cation selectivity is determined by the charge distribution along the ion permeation pathway. The intracellular and extracellular vestibules of the receptor adjacent to the transmembrane pore are electronegative and provide an environment to stabilize cations and increase their local concentration (5, 6). The upper portion of the pore is lined with hydrophobic residues restricting water occupancy and, as a result, prevents the passage of ions in the closed state (i.e., the hydrophobic gating mechanism) (7, 8). Upon receptor activation, the pore widens due to a displacement of the M2 helices, which relieves the hydrophobic gate and allows the hydration of the pore and the conduction of ions (9, 10). Within the pore, ions are further stabilized by interactions with ionized side chains in the first turn of the M2 α-helices (11). At the bottom of the transmembrane pore, negatively charged residues also facilitate cation entry (8, 12).

Charge selectivity is essential for physiological receptor function and forms the basis for excitatory and inhibitory LGICs. Mutations associated with reversed charge selectivity would give rise to transmembrane potentials that are physiologically detrimental. The first evidence for a transformation of a cation-selective into an anion-selective LGIC derived from experiments on chimeric α7-neuronal AChRs with substituted homologous residues from the glycine receptor (13). A minimum number of 2 substitutions (E237A and V251T) and the insertion of a proline residue between positions G236 and E237 were necessary for a successful transformation. The introduction of the same 3 mutations into 5-hydroxytryptamine$_3$ receptors again resulted in a cation-to-anion transformation of selectivity (14). Similar effects were observed in the glycine receptor after the introduction of the 3 inverse mutations from the α7-neuronal AChR, by which selectivity was switched from anionic into cationic (15). Together, these experimental constructs reveal that the substitution of a number of key residues in the M2 helix of LGICs is sufficient to mediate the conversion of charge selectivity, which, however, has not been reported in association with naturally occurring mutations and disease.

Here, we present functional and structural data on a CHRNA1 mutation (p.Leu251Arg) identified in a patient with CMS. The

Significance

We report on a single mutation in the α1-subunit M2 helix (p.α1Leu251Arg) of the muscle acetylcholine receptor (AChR) found in a patient with congenital myasthenic syndrome (CMS) that is shown to convert the AChR into chloride conductance at positive potentials. Constriction of the channel pore with partial desolvation and stabilization of the permeating chloride ions by the arginine residues is revealed as the underlying mechanism. This article is of general interest because it describes a mechanism for the transformation of the muscle AChR into an inhibitory channel, and presents a report of charge selectivity conversion in association with a naturally occurring single mutation. Our findings might also give explanation to a pathomechanism in CMS.

Author contributions: H.C., A.V., R.W., P.C.B., and D.B. designed research; H.C., M.E., W.W.L., S.M., P.M.R.C., J.C., and R.W. performed research; H.C. and M.E. analyzed data; H.C. and M.E. wrote the paper; P.M.R.C. and D.B. obtained clinical data; A.V., R.W., and D.B. provided supervision; and P.C.B. supervised umbrella sampling molecular dynamics simulations.

The authors declare no competing interest.

This article is a PNAS Direct Submission.

[1]To whom correspondence may be addressed. Email: david.beeson@ndcn.ox.ac.uk.

This article contains supporting information online at www.pnas.org/lookup/suppl/doi:10.1073/pnas.1908284116/-/DCSupplemental.

First published September 30, 2019.

mutation is located within the highly conserved M2 transmembrane helix, which lines the channel pore. This study provides evidence for a voltage-dependent conversion of ion selectivity from cationic to anionic and, consequently, the transformation of the muscle AChR from an excitatory into an inhibitory channel caused by a single amino acid substitution.

Results

Clinical Features of the Patient with Congenital Myasthenic Syndrome. The patient, now 14 y old, is female. Onset of symptoms was in infancy with feeding difficulties, dribbling, and reduced facial expression, delay in motor milestones, clear bilateral fatigable ptosis, limited ocular movement, and marked restriction in upgaze. Muscle MRI was normal. A muscle biopsy was nondiagnostic, with no mitochondrial abnormality evident and respiratory chain enzyme analysis normal, but it did show some type II fiber atrophy. Electromyography showed decrement and jitter, suggesting a disorder of neuromuscular transmission. On recent examination the fatigable ptosis and restriction of eye movements were present, along with neck flexor and mild facial weakness. There was no obvious weakness in upper and lower limbs, though muscle weakness was reported after sustained walking or toward the end of the day.

The clinical features and electromyography results suggested a diagnosis of myasthenia. Assays for anti-AChR antibodies, including for clustered AChRs (16) and anti-MuSK antibodies were negative, and so screening of genes for mutations that could cause CMS was undertaken. Mutations were excluded in most CMS genes (including CHRNB1, CHRNE, CHRND, DOK7, RAPSN, DPAGT1, and GFPT1) but a single heterozygous de novo variant predicted to be pathogenic was identified in CHRNA1 (c.812T > G, p.Leu271Arg) (transcript numbering according to ENST00000348749.9, which does not harbor the P3A exon, but contains the 20 amino acid signal sequence; thus the mutation is at position Leu251Arg excluding the signal sequence). For ease of reference with the many previous reports on defining the function of residues within the

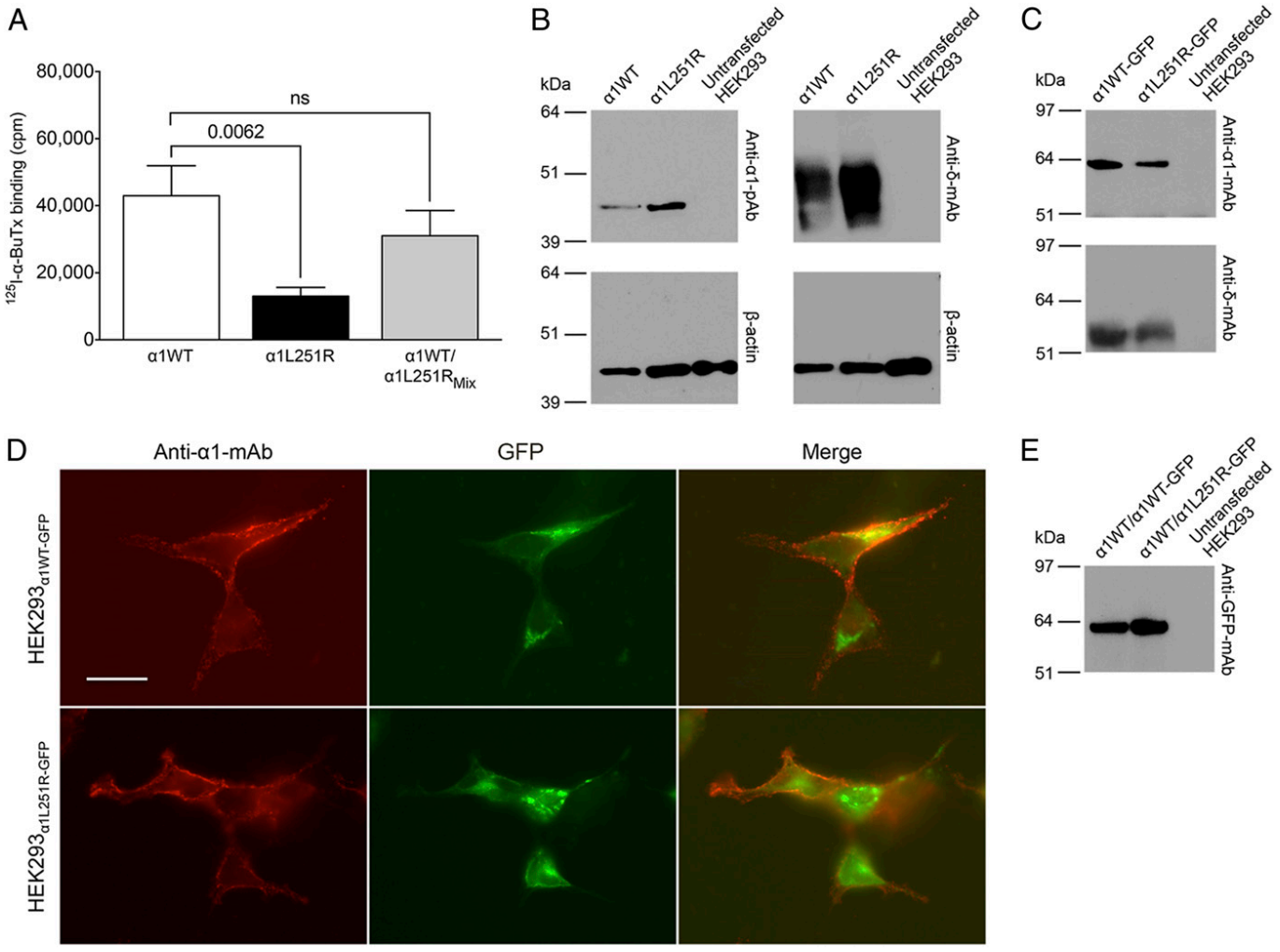

Fig. 1. The influence of the α1L251R mutation on AChR surface expression. (*A*) The bars show final results of ^{125}I-α-BuTx surface binding with the background level of radioactivity already subtracted from the cell-surface ^{125}I-α-BuTx activity in transfected cells ($n = 8$ experiments). Data are mean ± SEM. (*B*) Western blots of whole-cell extracts from HEK293$_{α1WT}$, HEK293$_{α1L251R}$, and untransfected HEK293 cells probed with either a rabbit anti-human α1-polyclonal antibody (pAb) (*Left*) or a mouse anti-human δ- monoclonal antibody (mAb) (*Right*). β-Actin probed with a monoclonal antibody was used as a loading control. (*C*) Western blots of immunoprecipitated surface AChRs using a mouse anti-human α1-monoclonal antibody (*Top*) and a mouse anti-human δ-monoclonal antibody (*Bottom*), respectively. HEK293 cells were transfected with a 2:1:1:1 ratio of α1WT-GFP-, β1-, δ-, ε-subunits (*Left* lane) or with a 2:1:1:1 ratio of α1L251R-GFP-, β1-, δ-, ε-subunits (*Middle* lane). (*D*) Immunofluorescence images of HEK293 cells transfected with a 2:1:1:1 ratio of α1WT-GFP-, β1-, δ-, ε-subunits (*Top*) or with a 2:1:1:1 ratio of α1L251R-GFP-, β1-, δ-, ε-subunits (*Bottom*). (Scale bar, 20 μm.) (*E*) Western blots of immunoprecipitated surface AChRs using a mouse anti-GFP monoclonal antibody. HEK293 cells were transfected with a 1:1:1:1:1 ratio of α1WT-, α1WT-GFP, β1-, δ-, ε-subunits and a 1:1:1:1:1 ratio of α1WT-, α1L251R-GFP, β1-, δ-, ε-subunits. ns, not significant.

AChR M2 helix, we will use the amino acid numbering according to the mature α1-subunit polypeptide and thus, from here, term this variant α1L251R. The CHRNA1 variant c.812T > G, p.L271R is not present on the exome variant server (https://evs.gs.washington.edu/EVS/) or in Ensembl genome browser 94 [(EMBL-EBI, Cambridge, UK (URL: https://www.ensembl.org)]. Screening of family DNA showed that this variant was not present in either parent, suggesting it arose de novo.

The p.α1L251 residue lies within the M2 helix of the AChR α1-subunit at the 9′ position corresponding to the consensus numbering system of Miller (17), in which position 1′ refers to the cytoplasmic end of the M2 helix. The consensus numbering system by Miller is used for comparison between different LGICs. The p.α1L251 residue is highly conserved across species and paralogues (18).

Surface Expression of $AChR_{α1L251R}$ Is Reduced. The impact of the α1L251R mutation on receptor surface expression was tested by transfection of cDNAs encoding the corresponding AChR subunits into HEK293 cells and counting AChR binding of radioactive ^{125}I-α-bungarotoxin (^{125}I-α-BuTx). Surface expression of $AChR_{α1L251R}$ was reduced to ∼30.3% of $AChR_{α1WT}$ ($t_{(14)} = 3.2$, $P = 0.0062$) (Fig. 1*A*). Detection of ^{125}I-α-BuTx binding on the surface of the cells indicates that $AChR_{α1L251R}$ is expressed on the cell surface, but for confirmation of this we used a monoclonal antibody to the extracellular main immunogenic region located on the AChR α1-subunit both for extracellular fluorescent labeling of AChRs (*SI Appendix*, Fig. S1) and in pull-down assays. The $AChR_{α1L251R}$ is efficiently expressed in the cell lysate (Fig. 1*B* and *SI Appendix*, Fig. S2 *A* and *B*) but less well assembled and transported to the cell surface (Fig. 1 *C* and *D* and *SI Appendix*, Fig. S2*C*), explaining the reduction of ^{125}I-α-BuTx binding to ∼30.3% of $AChR_{α1WT}$. However, the $AChR_{α1L251R}$ pentamer subunit composition appeared not to be altered as shown for the α1L251R-/δ-subunit ratio, which was similar to the α1WT-/δ-subunit ratio (Fig. 1*C* and *SI Appendix*, Fig. S2*D*). The ^{125}I-α-BuTx binding to the surface of $HEK293_{α1WT/α1L251R\_Mix}$ cells transfected with a mixture of $AChR_{α1WT}$ and $AChR_{α1L251R}$ was not significantly different compared to $HEK293_{α1WT}$ cells transfected with $AChR_{α1WT}$ alone (Fig. 1*A*), with significant surface expression levels of the α1L251R subunit in the presence of the α1WT subunit (Fig. 1*E*).

Whole-Cell Current Amplitude, Desensitization, and Deactivation Are Altered in Mutant AChRs. The functional consequences of the α1L251R mutation were first assessed by the analysis of burst duration of mutant channels transiently expressed in HEK293 cells. Performing recordings at low (100 nM) and high (30 μM) ACh concentrations and at various holding potentials ranging between −100 mV and +80 mV, no channel activity could be detected (5 transfections and 50 patches tested). Although surface expression levels of $AChR_{α1L251R}$ were reduced, the lack of any channel activity was unusual. To further evaluate the functional consequences of the α1L251R mutation, we then performed whole-cell patch-clamp experiments. In $AChR_{α1WT}$, current traces displayed a fast rise and a peak followed by an exponential current decay with almost complete desensitization after a 3-s pulse of 1 mM ACh (Fig. 2*A*). In $AChR_{α1L251R}$, current shape was changed in many aspects (Fig. 2*B*). Current amplitude was significantly reduced (by 96.7%) in $AChR_{α1L251R}$ ($n = 18$) compared to $AChR_{α1WT}$ ($n = 18$) (mean current amplitude of −12.1 ± 2.2 nA in $AChR_{α1WT}$ and −0.4 ± 0.1 nA in $AChR_{α1L251R}$, $t_{(34)} = 5.3$, $P < 0.0001$) (Fig. 3*A*), and desensitization was markedly reduced (mean fractional current decay of 95.4 ± 1.0% in $AChR_{α1WT}$ and 15.3 ± 1.7% in $AChR_{α1L251R}$, $t_{(34)} = 40.3$, $P < 0.0001$) (Fig. 3*B*). Receptor deactivation, defined as current decay during ACh washout at the end of receptor stimulation when remaining open receptors return to the closed state, was slower in $AChR_{α1L251R}$ compared to $AChR_{α1WT}$ (mean deactivation time constant of 76 ± 13 ms in $AChR_{α1WT}$ and 2,169 ± 256 ms in $AChR_{α1L251R}$, $t_{(34)} = 8.0$, $P < 0.0001$) (Fig. 3*C*).

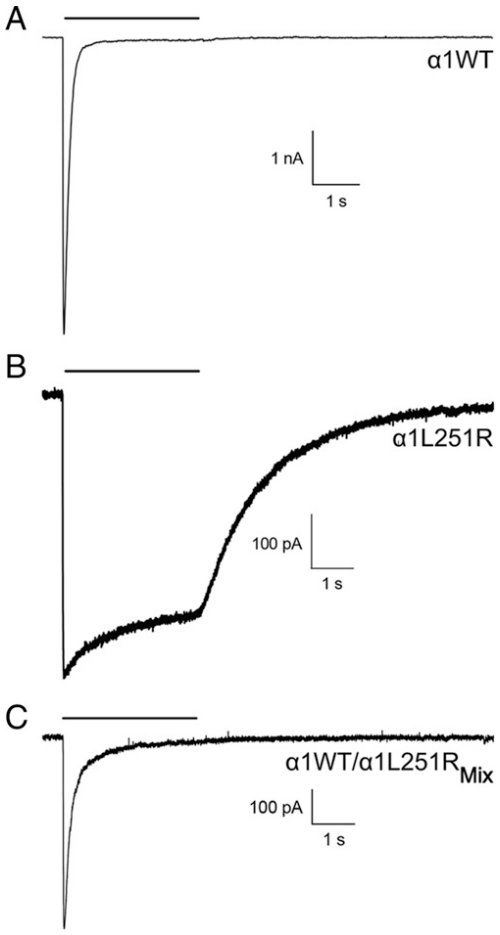

Fig. 2. Current recordings of wild-type and mutant AChRs expressed in HEK293 cells. Compared to $HEK293_{α1WT}$ (*A*), current amplitudes were lower in $HEK293_{α1L251R}$ (*B*) and $HEK293_{α1WT/α1L251R\_Mix}$ (*C*). Desensitization and deactivation were markedly slower in $HEK293_{α1L251R}$ compared to $HEK293_{α1WT}$ and $HEK293_{α1WT/α1L251R\_Mix}$.

In $HEK293_{α1WT/α1L251R\_Mix}$ cells expressing AChRs with a mixed range of subunit stoichiometries, current amplitude was significantly reduced compared to $HEK293_{α1WT}$ (−12.1 ± 2.2 nA in $HEK293_{α1WT}$ and −4.4 ± 1.4 nA in $HEK293_{α1WT/α1L251R\_Mix}$, $t_{(34)} = 2.9$, $P = 0.0060$) (Fig. 3*A*). Current decay was similar comparing $HEK293_{α1WT/α1L251R\_Mix}$ with $HEK293_{α1WT}$ (mean fractional current decay of 95.4 ± 1.0% in $HEK293_{α1WT}$ and 90.8 ± 2.9% in $HEK293_{α1WT/α1L251R\_Mix}$, $t_{(34)} = 1.5$, $P = 0.1512$) (Fig. 3*B*) but deactivation was significantly slower (mean deactivation time constant of 76 ± 13 ms $HEK293_{α1WT}$ and 148 ± 23 ms in $HEK293_{α1WT/α1L251R\_Mix}$, $t_{(34)} = 2.7$, $P = 0.0097$) (Fig. 3*C*).

The comparison of the current–voltage (I–V) relationship between $HEK293_{α1WT}$, $HEK293_{α1L251R}$, and $HEK293_{α1WT/α1L251R\_Mix}$ revealed further functional aspects of the mutation. Whereas the I–V relationship was linear in $HEK293_{α1WT}$ and $HEK293_{α1WT/α1L251R\_Mix}$ with a rectification index (RI) close to 1, there was a strong outward rectification observed at positive potentials in $HEK293_{α1L251R}$ with an increasing RI of up to 4.7 ± 0.7 at ±100 mV (Fig. 3 *D* and *E*). There was no shift of the reversal potential.

The αL251R Mutation Is Associated with a Conversion from Cationic to Anionic Selectivity. Electrophysiological experiments were performed at different AChR surface expression levels in

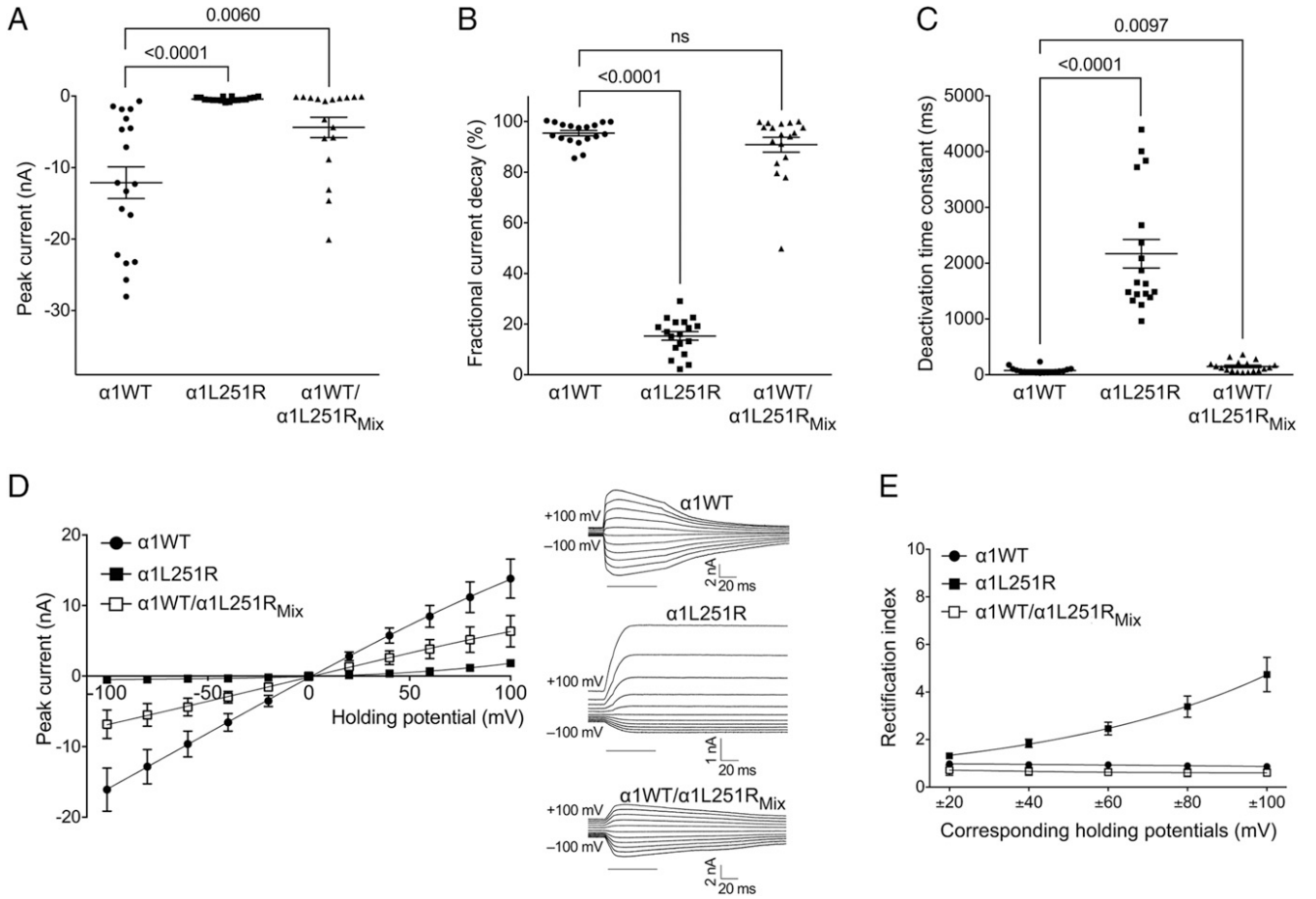

Fig. 3. Functional characterization of wild-type and mutant AChRs expressed in HEK293 cells. The α1L251R mutation was associated with reduced peak currents (*A*), slower desensitization (*B*) and deactivation (*C*) and with a change of the linear I–V relationship into outward rectification in HEK293$_{α1L251R}$ (*D*) and a RI > 1 at several holding potentials (*E*). HEK293$_{α1WT}$: n = 16, HEK293$_{α1L251R}$: n = 17, HEK293$_{α1WT/α1L251R_Mix}$: n = 15. Data are mean ± SEM. ns, not significant.

HEK293$_{α1WT}$ and HEK293$_{α1L251R}$. However, the whole-cell current reduction in AChR$_{α1L251R}$ to 3.3% of AChR$_{α1WT}$ in HEK293 cells was not explained by the surface expression, which was reduced to 30.3% in AChR$_{α1L251R}$ compared to AChR$_{α1WT}$. A functional defect of mutant AChRs, therefore, was a theory also supported by the altered whole-cell current kinetics in

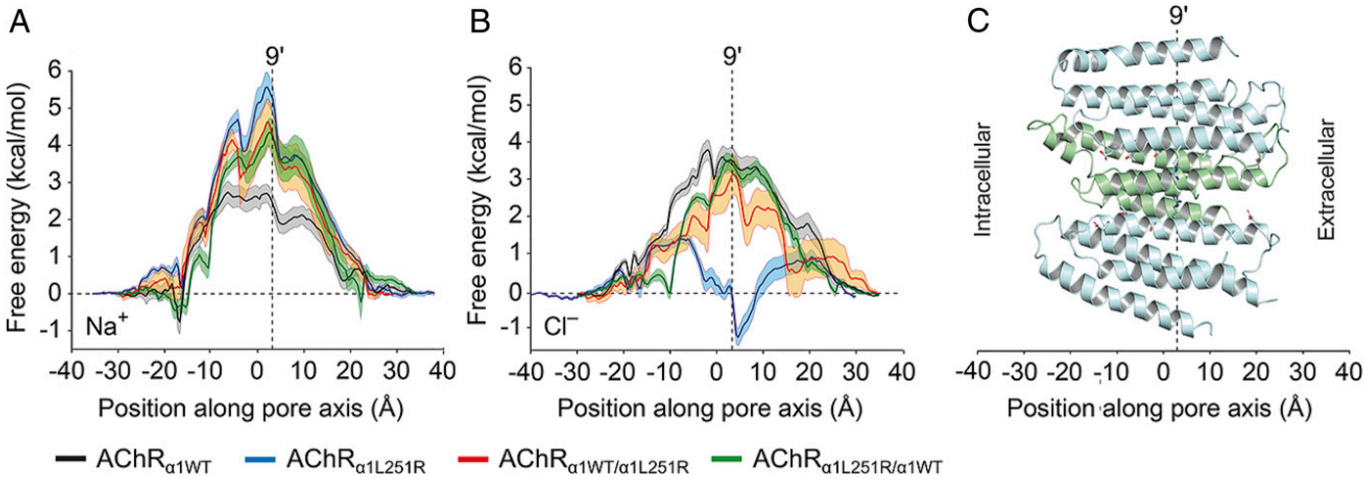

Fig. 4. Analysis of Na^+ and Cl^- passage through the transmembrane pore in wild-type and mutant AChRs by PMF calculations. PMF profiles for Na^+ (*A*) and Cl^- (*B*) ions in AChR$_{α1WT}$ (black), AChR$_{α1L251R}$ (blue), AChR$_{α1WT/α1L251R}$ (red), and AChR$_{α1L251R/α1WT}$ (green). (*C*) View on side of AChR$_{α1L251R}$ model within the same coordinate space as the PMF profiles in *A* and *B*. Residues at key positions are indicated in stick representation. The β1- and δ-subunits have been removed for clarity. At AChR$_{α1L251R}$, the reduction of the chloride barrier height to 1.5 kcal/mol around −8 Å as well as the introduction of an energetic well of −1.15 kcal/mol around 5 Å (together with the increase in barrier height to 5.57 kcal/mol for sodium) is indicative of strong chloride selective permeation. Error bars are 1 SD of the mean.

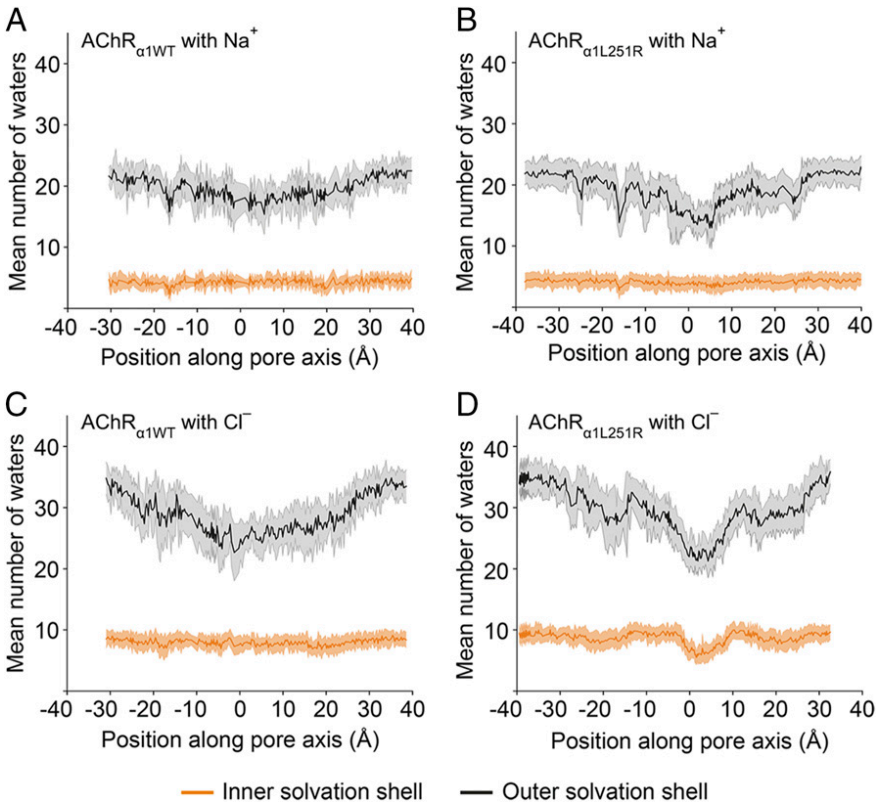

Fig. 5. Solvation shells of Na^+ and Cl^- ions as a function of their position along the reaction coordinate. Sodium is never desolvated from its inner solvation shell and only minor perturbations are observed in the outer solvation shell in both AChR$_{\alpha1WT}$ and AChR$_{\alpha1L251R}$ (*A* and *B*). Thus, the lack of Na^+ permeation observed reflects repulsion of the solvated Na^+. By contrast, Cl^- is observed to be desolvated around the L251R residue (around 3 Å in the reaction coordinate) in AChR$_{\alpha1L251R}$ (*D*) but not in AChR$_{\alpha1WT}$ (*C*). Error bars represent 1 SD.

HEK293$_{\alpha1L251R}$ and the significantly reduced whole-cell current amplitudes to 36.4% in HEK293$_{\alpha1WT/\alpha1L251R_Mix}$, in which AChR surface expression was not statistically different compared to HEK293$_{\alpha1WT}$ (Fig. 1*A*). We performed umbrella sampling molecular dynamics (USMD) simulations of wild-type and mutant AChRs to investigate the influence of the mutation on sodium and chloride passage through the transmembrane pore. First, potentials of mean force (PMFs) for AChR$_{\alpha1WT}$ were computed for both sodium and chloride ions (Fig. 4 *A*–*C*). The computed PMFs for AChR$_{\alpha1WT}$ indeed demonstrated selectivity for sodium, as expected. All barrier heights for sodium at mutant channels were higher than for chloride at AChR$_{\alpha1WT}$, indicative of reduced sodium permeability, and both AChR$_{\alpha1WT/\alpha1L251R}$ and AChR$_{\alpha1L251R/\alpha1WT}$ possessed similar (within error) PMF profiles.

Chloride barrier heights at AChR$_{\alpha1WT/\alpha1L251R}$/AChR$_{\alpha1L251R/\alpha1WT}$ were greater than that for sodium at AChR$_{\alpha1WT}$ but lower than that for chloride at AChR$_{\alpha1WT}$. Taken together with the experimental results above, it is likely that these values represent nonconductive states. It is worth noting that there was some

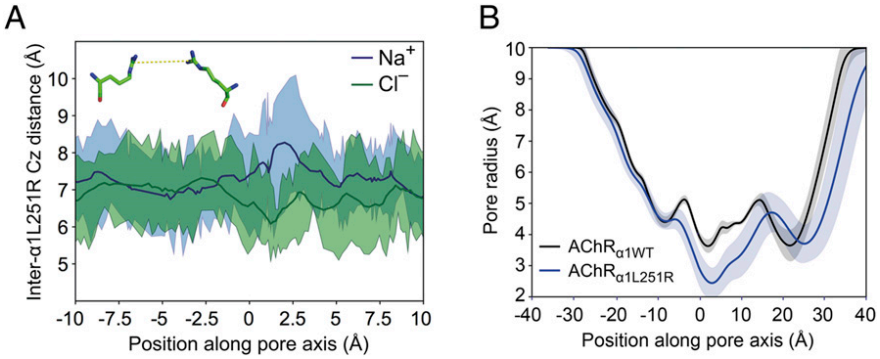

Fig. 6. Comparison of AChR$_{\alpha1L251R}$ guanidinium carbon internuclear distances with respect to either Na^+ or Cl^- permeation, and pore radii comparison between AChR$_{\alpha1WT}$ and AChR$_{\alpha1L251R}$. (*A*) Internuclear distances between central guanidinium carbons of both α1L251R residues show that Cl^- pulls the residues closer together at ∼1.25 Å along the reaction coordinate, with Na^+ exhibiting an opposing effect. Carbon is denoted by the forcefield atom type notation "*Cz*." (*B*) The narrow 2.4-Å pore radius of α1L251R near 2.5 Å in the reaction coordinate provides further evidence of tight coordination of Cl^- with α1L251R residues. Indeed, Fig. 5*D* demonstrates the partial dewetting that would need to occur in order to accommodate a permeating ion through a channel of this diameter. Error bars represent 1 SD.

discernible difference between the overall shapes of the PMF energy landscapes at $AChR_{\alpha1WT/\alpha1L251R}$/$AChR_{\alpha1L251R/\alpha1WT}$, likely arising from the pseudosymmetrical arrangement of subunit stoichiometries. However, this is unlikely to result in meaningful physiological differences between these channels.

The most pronounced effect occurred for chloride in $AChR_{\alpha1L251R}$, revealing a reduction in barrier height to 1.5 kcal/mol (around −8 Å) as well as the introduction of an energetic well around $z = 5$ Å of −1.15 kcal/mol. This, together with the increase in barrier height to 5.57 kcal/mol for sodium is indicative of strongly chloride selective permeation. Analyses of the first and second solvation shells (Fig. 5) of chloride at $AChR_{\alpha1L251R}$ showed that desolvation of these shells occurs around position $z = 3$ Å in the reaction coordinate, concordant with the reduction in channel radius at this location. The energetic penalty incurred through this desolvation is accounted for by the favorable electrostatic interactions of both arginine residues with chloride, in which they act as surrogate water molecules chelating the probe ion (Fig. 6*A*). An energetic well in the permeation pathway would be expected to slow down passage of ions and may contribute to a lower conductance than would be predicted on the basis of diameter alone.

Both chloride and sodium possess ion-O internuclear distances within their first solvation shell (19) (Fig. 6*A*) that would be incompatible for conduction through a pore of the size seen in $AChR_{\alpha1L251R}$ (radius of ∼2 Å) (Fig. 6*B*). In trajectories from the PMF profiles, sodium was never desolvated from its first solvation shell (Fig. 5 *A* and *B*) and only minor perturbations were observed in the second solvation shell in both $AChR_{\alpha1WT}$ and $AChR_{\alpha1L251R}$. Thus, the lack of permeation observed reflects repulsion of the solvated sodium ion. By contrast, chloride was observed to be desolvated (with a more substantial deformation of the second solvation shell) around the L251R residues (9′ position) in $AChR_{\alpha1L251R}$ but not in $AChR_{\alpha1WT}$ (Fig. 5 *C* and *D*).

The Conversion from Cationic to Anionic Selectivity Is Voltage Dependent. USMD simulations were complemented by whole-cell patch-clamp experiments with altered Cl^- and NaCl concentrations, respectively, in order to elucidate current rectification and the conversion of ion selectivity associated with the α1L251R mutation. The I–V relationship was analyzed after substitution of intra- or extracellular Cl^- by SO_4^{2-} to a residual Cl^- concentration of 10 mM. In $AChR_{\alpha1WT}$, Cl^- substitution had no appreciable effect on current rectification and reversal potential (Fig. 7 *A* and *B*). In $AChR_{\alpha1L251R}$, by contrast, the reduction of intracellular Cl^- concentration was associated with increased current amplitudes at positive potentials with the RI increasing to 8.0 ± 1.1 at ±100 mV (Fig. 7 *C* and *D*). Correspondingly, the reduction of extracellular Cl^- concentration reduced current amplitudes at positive potentials with a RI of 2.6 ± 0.4 at ±100 mV. Reversal potential was not shifted and AChR kinetics not affected by either condition in $AChR_{\alpha1L251R}$, suggesting no significant Cl^- permeability at negative potentials up to 0 mV.

To explore a voltage-dependent conversion of ion selectivity in $AChR_{\alpha1L251R}$ further, we performed experiments in which extracellular NaCl was substituted by glucose to a residual concentration of 20 mM. This resulted in a shift of the reversal potential toward negative voltages in $AChR_{\alpha1L251R}$ following the equilibrium potential of potassium (reversal potential of −28.3 ± 4.8 mV at 20 mM extracellular NaCl [$n = 10$] compared to 4.3 ± 3.7 mV at 150 mM extracellular NaCl [$n = 16$], $t_{(24)} = 5.4$, $P < 0.0001$), and was very similar to the shift observed in $AChR_{\alpha1WT}$ (reversal potential of −28.3 ± 4.8 mV in $AChR_{\alpha1L251R}$ at 20 mM NaCl [$n = 10$] compared to −32.0 ± 1.3 mV in $AChR_{\alpha1WT}$ at 20 mM NaCl [$n = 10$], $t_{(18)} = 0.7$, $P = 0.4649$) (Fig. 8 *A* and *B*). This is indicative of negligible chloride permeability at negative membrane potentials in $AChR_{\alpha1L251R}$. Together, these findings provide evidence for a significant contribution of chloride ions to $AChR_{\alpha1L251R}$ currents at positive potentials only.

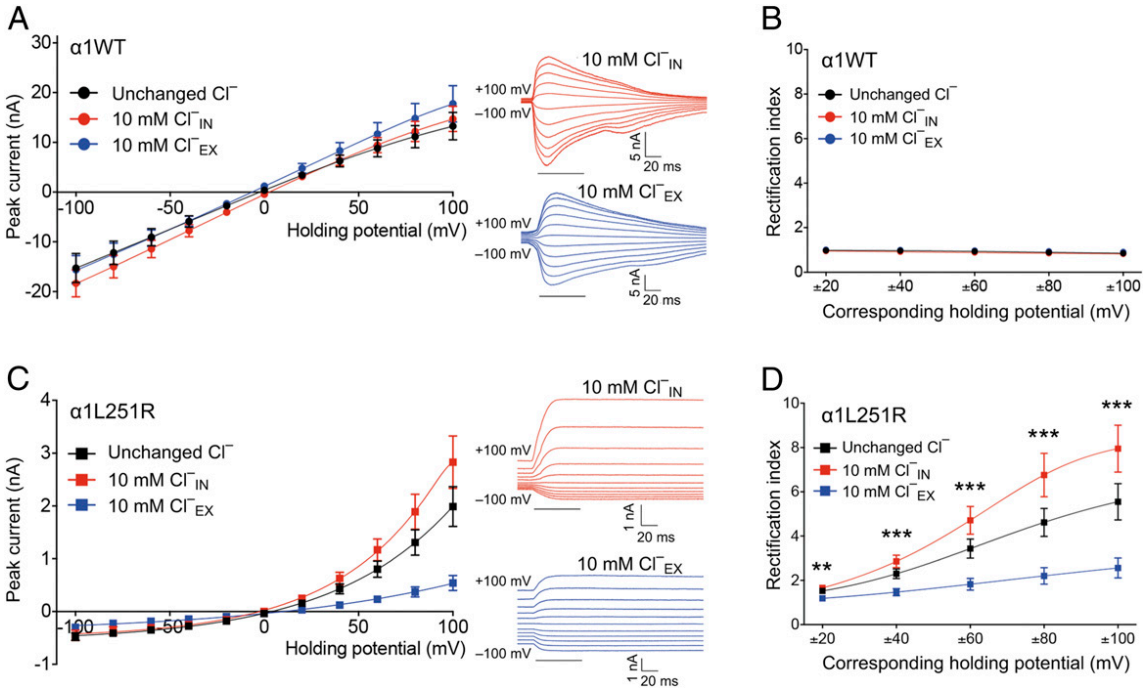

Fig. 7. The I–V relationship in $AChR_{\alpha1WT}$ and $AChR_{\alpha1L251R}$ in dependence of the intracellular ($_{IN}$) and extracellular ($_{EX}$) Cl^- concentration. In $AChR_{\alpha1WT}$, the I–V relationship was independent of the intra- or extracellular Cl^- concentration (*A*), with a RI around 1 in all groups with different Cl^- gradients (*B*), suggesting insignificant Cl^- conductance (unchanged Cl^-: black, $n = 17$; 10 mM Cl^-_{IN}: red, $n = 11$; 10 mM Cl^-_{EX}: blue, $n = 10$). In $AChR_{\alpha1L251R}$, the I–V relationship was independent of the intra- or extracellular Cl^- concentration at negative holding potentials, but was strongly chloride dependent at positive holding potentials (*C*), when current amplitudes increased at a reduced intracellular Cl^- concentration and decreased at a reduced extracellular Cl^- concentration, indicating a significant Cl^- conductance in $AChR_{\alpha1L251R}$ at positive holding potentials only (unchanged Cl^-: black, $n = 16$; 10 mM Cl^-_{IN}: red, $n = 11$; 10 mM Cl^-_{EX}: blue, n =12). The RI displayed a sigmoidal relationship in all groups with differing Cl^- gradients (*D*). Data are mean ± SEM. $^{**}P < 0.01$; $^{***}P < 0.001$ one-way ANOVA with Tukey's post hoc correction to test for a difference between 10 mM Cl^-_{IN} and 10 mM Cl^-_{EX}.

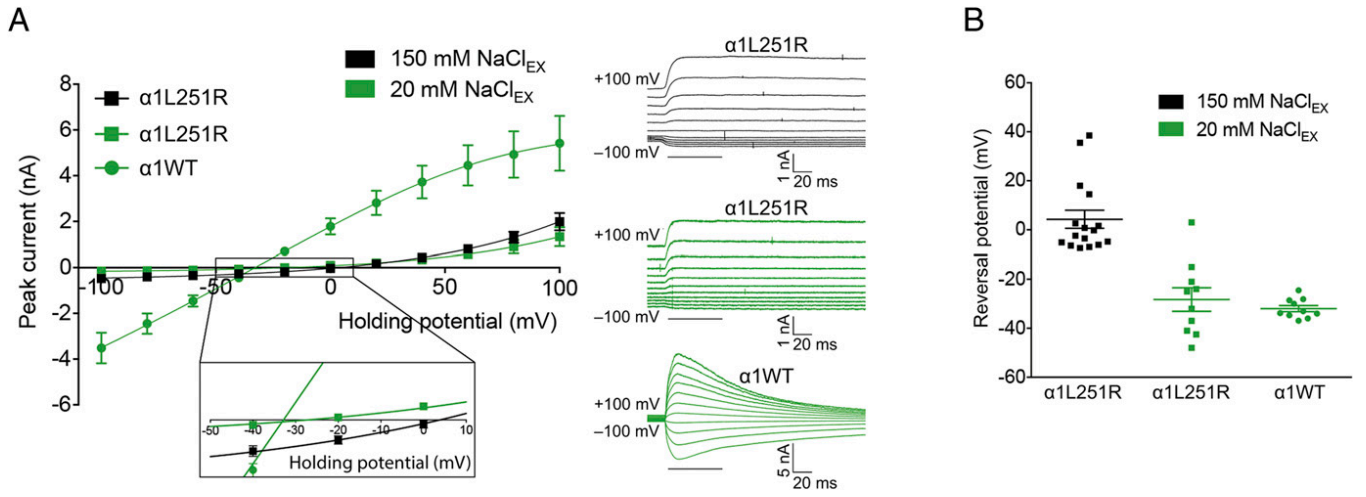

Fig. 8. The I–V relationship in AChR$_{α1WT}$ and AChR$_{α1L251R}$ in dependence of the extracellular NaCl concentration. The substitution of extracellular NaCl by glucose to a residual concentration of 20 mM resulted in a shift of the reversal potential toward negative voltages following the equilibrium potential of potassium in AChR$_{α1WT}$ (*A*). In AChR$_{α1L251R}$, the shift of the reversal potential upon substitution of extracellular NaCl by glucose followed the equilibrium potential of potassium toward negative voltages (*A*), with no significant difference of the reversal potential between AChR$_{α1L251R}$ and AChR$_{α1WT}$ (*B*). Data are mean ± SEM.

Discussion

The present study describes the effects of a mutation, α1L251R, found in a patient with CMS on AChR function. We demonstrate a profound reduction of whole-cell current amplitudes and prolongation of desensitization and deactivation time constants. Performing extensive functional analyses and computational modeling, we reveal decreased sodium permeability as the underlying mechanism for reduced current amplitudes in mutant AChRs. The most intriguing finding in this study, however, is the voltage-dependent conversion of ion selectivity from cationic to anionic, resulting from a single amino acid substitution. Although severely impaired, ion selectivity for sodium prevails at negative membrane potentials, whereas at positive membrane potentials, mutant AChRs become increasingly permeable for chloride.

The L251 lies at the approximate midpoint of the M2 transmembrane helix (the 9′ position, L9′) (17) and occupies a kink in each of the 5 AChR subunits pointing into the closed channel (4). Upon receptor activation, the M2 transmembrane helices rotate so that the L9′ residues no longer occlude the conduction pathway (9). In α7-neuronal AChRs, the substitution of L9′ by both polar and hydrophobic amino acids was shown to result in slower desensitization kinetics and increased sensitivity to agonist, but only substitutions with polar amino acids were associated with a change of inward rectification, which is characteristic for neuronal AChRs, into a linear I–V relationship (20). These findings are supported by studies on muscle AChRs, reporting that substitutions of L9′ by the hydrophilic amino acids serine (21) or threonine (22) in each of the 5 subunits slow desensitization and independently increase sensitivity to ACh. The substitution of L9′ by charged amino acids has not been examined so far.

In our study, the substitution of L9′ by the positively charged amino acid arginine in the α1-subunit altered AChR function in many aspects. The prolongation of desensitization and deactivation time constants is consistent with former studies (20–22). Although deactivation was not examined in those studies, its prolongation in the present study could have resulted from increased affinity of the mutant AChR for ACh as reported before (20–22). Whole-cell current amplitude was profoundly reduced, and our failure to detect single-channel currents was likely to result from single-channel amplitudes below detection level. The I–V relationship was changed into outward rectification, which was found to derive from a voltage-dependent conversion of ion selectivity from cationic to anionic. Conversion of ion selectivity was previously reported in α7-neuronal AChRs (12, 13), in 5-hydroxytryptamine$_3$ receptors (14), and in glycine receptors (15), but those studies found at least 3 mutations to be necessary for successful transformation. In α7-neuronal AChRs, the conversion of ion selectivity required the insertion of proline at the cytoplasmic end of the M2 helix (between G–3′ and E–2′) along with E–2′A and V13′T (12, 13) or L9′T (12). The insertion of proline, either alone or together with E–2′A or V13′T, however, yielded nonfunctional receptors. And in the absence of the proline insertion, the E–2′ and V13′T mutations were fully compatible with cationic receptors, either when introduced alone or together (12, 13). It was hypothesized that conversion of ion selectivity in α7-neuronal AChRs is not based on alterations of the M2 helix configuration, but rather due to a local structural reorganization in the vicinity of the proline insertion (12). Data presented here provide evidence that conversion of ion selectivity does not exclusively depend on the insertion of proline between G–3′ and E–2′ but can also be induced by the substitution of L9′ by a positively charged residue. The application of USMD simulations in our study enabled us to determine the underlying mechanism of ion selectivity conversion as well as obtain an energetic description of this process. The substitution of L9′ by arginine in both α1-subunits leads to a constriction of the channel pore radius from 3.6 Å in the AChR$_{α1WT}$ to 2.4 Å in the AChR$_{α1L251R}$ as measured by the minimum time-averaged pore radius. This represents a 33% reduction in minimum pore diameter, requiring that ions partially desolvate in order to permeate the AChR$_{α1L251R}$ pore (Fig. 5*D*). Ion desolvation is associated with an energetic penalty that is compensated for by the favorable electrostatic interaction of both arginines with chloride. At positive membrane potentials, when AChR$_{α1L251R}$ conductance for chloride is high, current amplitudes are still reduced compared to AChR$_{α1WT}$. This might be due to the strong interaction between chloride and both arginines resulting in an energetic reward for chloride with increasing dwell times at the position of both arginines translating to a reduction in conductance for chloride.

As the exact nature of the open state in Cys-loop receptors is still unclear, precisely how permeation occurs is unknown. Nevertheless, while the absolute values in the PMFs may show some variation, depending on the precise treatment of the model, the relative values are likely to be robust.

Among nicotinic acetylcholine receptors, only muscle AChRs display a linear I–V relationship (23), while neuronal AChRs are characterized by inward rectification (24). Mechanisms postulated

to underlie inward rectification in neuronal AChRs include a combination of block by intracellular magnesium or polyamines and voltage-dependent mechanisms intrinsic to the receptor (25–27). In our study, outward rectification derived from an asymmetry of $AChR_{\alpha1L251R}$ conductance for chloride, which was high at positive membrane potentials but declined progressively as the membrane was hyperpolarized. Instead, whole-cell currents, although markedly reduced, were found to be carried by sodium at negative membrane potentials. As an underlying mechanism, the membrane potential could have influenced the relative conformation of the charged arginine residues within the channel pore, and, consequently, desolvation and the permeability of chloride.

With the $AChR_{\alpha1L251R}$, $AChR_{\alpha1WT/\alpha1L251R}$, and $AChR_{\alpha1L251R/\alpha1WT}$ representing receptors with negligible sodium conductance, only $AChR_{\alpha1WT}$ (accounting for around 25% of normal AChR numbers) remains to be functionally active in our patient with CMS. Thus the major pathogenic mechanism for CMS in this case is not a reduction in AChR number on the cell surface, but a reduction in the number of functional AChRs on the cell surface (with 75% of the cell surface receptors not allowing sodium ions to contribute to membrane depolarization). One would thus expect the phenotype to have similar characteristics to a mild AChR deficiency syndrome, and this is precisely what we find for this patient. A reduction of the surface expression of functional AChRs to around 25% of normal is found to be on the cusp with respect to compromising the safety margin for neuromuscular transmission (28) and is compatible with the relatively mild phenotype of the patient. A precedent for a similar effect of a heterozygous mutation in CHRNA1 has previously been demonstrated for a severe fast channel mutation (28). The conversion of ion selectivity from cationic to anionic in $AChR_{\alpha1L251R}$ could add a detrimental impact on endplate potentials or action potentials at the neuromuscular junction. Upon activation by ACh, the inhibitory current carried by chloride influx in $AChR_{\alpha1L251R}$ could antagonize the endplate potential during depolarization mediated by the remaining $AChR_{\alpha1WT}$. The threshold potential necessary for the generation of an action potential in muscle cells, however, ranges around −50 mV (29), which is far below the membrane potential when $AChR_{\alpha1L251R}$ becomes permeable for chloride. In situations of increased (compensatory) vesicle release (30–32) or high input resistance, it could be possible that the postsynaptic membrane is depolarized close to a potential region at which chloride may be able to pass through $AChR_{\alpha1L251R}$. Action potentials also cause depolarizations up to +30 to 40 mV (29) and may therefore induce inhibitory currents in $AChR_{\alpha1L251R}$, which could accelerate the decline phase and contribute to early termination of action potentials limiting their propagation.

In conclusion, the present study elucidates a mechanism for the conversion of ion selectivity from cationic to anionic, resulting from a single amino acid substitution in muscle AChRs, and is relevant for patients with CMS, as the transformation from an excitatory to an inhibitory channel might also provide a pathomechanism not linked to CMS so far.

Methods

AChR surface expression was measured using the ^{125}I-α-BuTx binding assay. Electrophysiological recordings were performed on transiently transfected HEK293 cells. USMD simulations were based on the cryogenic-electron microscopy structure of the α1 glycine receptor in an open state that was used as the template structure to generate a comparative model of the adult muscle AChR. Consent for the study on congenital myasthenic syndromes in the United Kingdom was approved by Oxfordshire Research Ethics Committee (REC) B: 04.OXB.017 and Oxfordshire REC C: 09/H0606/74, and informed consent was given by the patient in this study. Full materials and methods are available in *SI Appendix, Materials and Methods*.

ACKNOWLEDGMENTS. We thank Prof. L. Sivilotti (University College London [UCL], London, UK) and Dr. R. Lape (UCL, London, UK) for helpful discussions. We are grateful for financial support offered by the following funding agencies: H.C. was funded by an Erwin Schrödinger Fellowship (J3589), by the Austrian Science Fund, and by a grant from the Nuffield Department of Clinical Neurosciences, University of Oxford. M.E. is supported by an Engineering and Physical Sciences Research Council (EPSRC) Industrial Cooperative Awards in Science & Engineering (iCASE) studentship with Defence Science and Technology Laboratory (DSTL). D.B. holds a Medical Research Council Program Grant (MR/M006824/1), which funds R.W.

1. A. G. Engel, X. M. Shen, D. Selcen, S. M. Sine, Congenital myasthenic syndromes: Pathogenesis, diagnosis, and treatment. *Lancet Neurol.* **14**, 461 (2015).
2. R. Webster *et al.*, A novel congenital myasthenic syndrome due to decreased acetylcholine receptor ion-channel conductance. *Brain* **135**, 1070–1080 (2012).
3. D. J. Adams, T. M. Dwyer, B. Hille, The permeability of endplate channels to monovalent and divalent metal cations. *J. Gen. Physiol.* **75**, 493–510 (1980).
4. N. Unwin, Acetylcholine receptor channel imaged in the open state. *Nature* **373**, 37–43 (1995).
5. N. Unwin, Refined structure of the nicotinic acetylcholine receptor at 4A resolution. *J. Mol. Biol.* **346**, 967–989 (2005).
6. I. Ivanov, X. Cheng, S. M. Sine, J. A. McCammon, Barriers to ion translocation in cationic and anionic receptors from the Cys-loop family. *J. Am. Chem. Soc.* **129**, 8217–8224 (2007).
7. O. Beckstein, P. C. Biggin, M. S. P. Sansom, A hydrophobic gating mechanism for nanopores. *J. Phys. Chem. B* **105**, 12902–12905 (2001).
8. C. Song, B. Corry, Role of acetylcholine receptor domains in ion selectivity. *Biochim. Biophys. Acta* **1788**, 1466–1473 (2009).
9. A. Miyazawa, Y. Fujiyoshi, N. Unwin, Structure and gating mechanism of the acetylcholine receptor pore. *Nature* **423**, 949–955 (2003).
10. N. Unwin, Y. Fujiyoshi, Gating movement of acetylcholine receptor caught by plunge-freezing. *J. Mol. Biol.* **422**, 617–634 (2012).
11. G. D. Cymes, C. Grosman, Identifying the elusive link between amino acid sequence and charge selectivity in pentameric ligand-gated ion channels. *Proc. Natl. Acad. Sci. U.S.A.* **113**, E7106–E7115 (2016).
12. P. J. Corringer *et al.*, Mutational analysis of the charge selectivity filter of the alpha7 nicotinic acetylcholine receptor. *Neuron* **22**, 831–843 (1999).
13. J. L. Galzi *et al.*, Mutations in the channel domain of a neuronal nicotinic receptor convert ion selectivity from cationic to anionic. *Nature* **359**, 500–505 (1992).
14. M. J. Gunthorpe, S. C. Lummis, Conversion of the ion selectivity of the 5-HT(3a) receptor from cationic to anionic reveals a conserved feature of the ligand-gated ion channel superfamily. *J. Biol. Chem.* **276**, 10977–10983 (2001).
15. A. Keramidas, A. J. Moorhouse, C. R. French, P. R. Schofield, P. H. Barry, M2 pore mutations convert the glycine receptor channel from being anion- to cation-selective. *Biophys. J.* **79**, 247–259 (2000).
16. M. I. Leite *et al.*, IgG1 antibodies to acetylcholine receptors in 'seronegative' myasthenia gravis. *Brain* **131**, 1940–1952 (2008).
17. C. Miller, Genetic manipulation of ion channels: A new approach to structure and mechanism. *Neuron* **2**, 1195–1205 (1989).
18. H. A. Lester, The permeation pathway of neurotransmitter-gated ion channels. *Annu. Rev. Biophys. Biomol. Struct.* **21**, 267–292 (1992).
19. Y. Marcus, Ionic radii in aqueous solutions. *Chem. Rev.* **88**, 1475–1498 (1988).
20. F. Revah *et al.*, Mutations in the channel domain alter desensitization of a neuronal nicotinic receptor. *Nature* **353**, 846–849 (1991).
21. C. Labarca *et al.*, Channel gating governed symmetrically by conserved leucine residues in the M2 domain of nicotinic receptors. *Nature* **376**, 514–516 (1995).
22. G. N. Filatov, M. M. White, The role of conserved leucines in the M2 domain of the acetylcholine receptor in channel gating. *Mol. Pharmacol.* **48**, 379–384 (1995).
23. K. Imoto *et al.*, Rings of negatively charged amino acids determine the acetylcholine receptor channel conductance. *Nature* **335**, 645–648 (1988).
24. I. Forster, D. Bertrand, Inward rectification of neuronal nicotinic acetylcholine receptors investigated by using the homomeric alpha 7 receptor. *Proc. Biol. Sci.* **260**, 139–148 (1995).
25. A. Mathie, D. Colquhoun, S. G. Cull-Candy, Rectification of currents activated by nicotinic acetylcholine receptors in rat sympathetic ganglion neurones. *J. Physiol.* **427**, 625–655 (1990).
26. S. B. Sands, M. E. Barish, Neuronal nicotinic acetylcholine receptor currents in phaeochromocytoma (PC12) cells: Dual mechanisms of rectification. *J. Physiol.* **447**, 467–487 (1992).
27. A. P. Haghighi, E. Cooper, Neuronal nicotinic acetylcholine receptors are blocked by intracellular spermine in a voltage-dependent manner. *J. Neurosci.* **18**, 4050–4062 (1998).
28. R. Webster *et al.*, Mutation in the AChR ion channel gate underlies a fast channel congenital myasthenic syndrome. *Neurology* **62**, 1090–1096 (2004).
29. S. J. Wood, C. R. Slater, Action potential generation in rat slow- and fast-twitch muscles. *J. Physiol.* **486**, 401–410 (1995).
30. S. G. Cull-Candy, R. Miledi, A. Trautmann, O. D. Uchitel, On the release of transmitter at normal, myasthenia gravis and myasthenic syndrome affected human end-plates. *J. Physiol.* **299**, 621–638 (1980).
31. P. C. Molenaar *et al.*, Acetylcholine in intercostal muscle from myasthenia gravis patients and in rat diaphragm after blockade of acetylcholine receptors. *Prog. Brain Res.* **49**, 449–458 (1979).
32. J. J. Plomp *et al.*, Acetylcholine release in myasthenia gravis: Regulation at single endplate level. *Ann. Neurol.* **37**, 627–636 (1995).

Structural correlates of human muscle nicotinic acetylcholine receptor subunit assembly mediated by δ(+) interface residues

Max Epstein[a], Susan Maxwell[b], Thomas J. Piggot[c], David Beeson[b], Isabel Bermudez[d] and Philip C. Biggin[a*]

[a]Department of Biochemistry, Structural Bioinformatics and Computational Biochemistry, University of Oxford, Oxford, UK

[b]Nuffield Department of Clinical Neurosciences, University of Oxford, Oxford OX3 9DS, United Kingdom

[c]Chemical, Biological and Radiological Sciences, Defense Science and Technology Laboratory, Porton Down, Salisbury, Wiltshire, UK

[d]Department of Biological and Medical Sciences, Faculty of Health and Life Sciences, Oxford Brookes University, Oxford, UK

To whom correspondence should be addressed.

Philip.biggin@bioch.ox.ac.uk

Keywords: muscle, nicotinic acetylcholine receptor, molecular dynamics, simulation, allosteric, assembly, α-BuTx, electrophysiology.

Abstract

Muscle nicotinic acetylcholine receptors are a class of heteropentameric ligand-gated cation channels with constituent subunits adopting a fixed stoichiometric arrangement. The specific amino acid residues that govern subunit ordering are however, only partially understood. By integrating all-atom molecular dynamics simulations, bioinformatics, two-electrode voltage clamp electrophysiology and ^{125}I-α-bungarotoxin assays of chimeric nAChR subunits, we identify residues across the extracellular, transmembrane and extended M4 helix of the δ subunit that make structural signatures that contribute to intransigent assembly rules. Furthermore, functional differences observed in $\alpha_2\delta_2\beta$ receptors can be rationalized by changes in dynamical behavior that manifest themselves at the agonist binding site.

Introduction

Nicotinic acetylcholine receptors (nAChRs) are a class of pentameric ligand-gated ion channel (pLGIC) that come in a number of different combinations given their particular subunit composition. This composition effects overall biophysical characteristics and pharmacology, with different stoichiometries appearing preferentially in different tissue types [1]. NAChRs are comprised of one to four different subunits selected from an overall repertoire of 17 possible subunits in vertebrates [1]. End-plate nAChRs consist of α, β, δ and ε subunits in the case of adult muscle and α, β, δ and ɣ for foetal or denervated muscle, arranged in a specific order (**Fig. 1a**), that was first established by the work on Unwin and more recently confirmed by Hibbs and colleagues [2]. In the wild-type adult muscle nAChR, the orthosteric binding sites are located at α/δ and α/ε interfaces. The α subunit is typically referred to as the principal subunit (indicated by "+"), whilst the partner subunit is referred to as the complementary subunit ("-").

The invariant stoichiometry and large overall subunit repertoire implies a high degree of allostery that can be attributed to the requirement of individual subunits to be at defined locations with respect to the overall quaternary structure. Indeed, the nAChR has been shown to act as a so-called 'allosteric machine' [3]. The effect of any given subunit on muscle nAChR function can therefore be thought of as context dependent [4] and that if complementary orthosteric subunit faces (i.e δ and ε) were exchanged, whilst preserving all other structural aspects of the receptor, the overall receptor biophysics would differ from wild type. To what extent this is the case however is not understood and in order to answer this question, the full set of molecular determinants for specific stoichiometric assembly needs to be elucidated first.

Studies in GlyRs [5,6], $GABA_AR$s [7], $5HT_3$Rs [8] and nAChRs [9-16] provide clues as to the individual amino acid residues responsible for governing receptor assembly, expression efficiency, and the underlying mechanisms for oligomerization. However, not all of the molecular determinants that control subunit order in the human nicotinic acetylcholine receptor have yet been found. In previous work [15], mouse β/γ chimeras were used to determine the location of β(-) face residues important for assembly. Additionally, the molecular determinants for the mouse γ subunit at α(-) and α(+) interfaces were shown to reside at the extracellular domain (ECD). What δ(+) residues are responsible for forming the apparently exclusive interface with the β(-) face have yet to be specifically determined.

Previous studies of non-human muscle nAChR subunits in heterologous expression systems [17-19] and *in vivo* [20] have shown a certain degree of flexibility for the arrangement of muscle subunits that is limited predominantly to the so-called 'double-δ' stoichiometry but with evidence of a larger number of arrangements in mice [21] and rat [22] as well as inter-species variation with regards to expression efficiency [23]. There is currently a lack of evidence for variant stoichiometries for human subtypes.

By examining the propensity for variant muscle nAChR stoichiometries of heterologously expressed human cDNA subunits, we have elucidated permitted interfaces. The inability to express $\alpha_2\varepsilon_2\beta$ and $\alpha_2\gamma_2\beta$ stoichiometries in contrast to $\alpha_2\delta_2\beta$ alluded to the presence of molecular determinants responsible for WT arrangements arising from the δ(+)β(-) interface.

Supplementation of this initial electrophysiological assessment of permitted interfaces with extensive all-atom molecular dynamics simulations and bioinformatic analysis by way of a

multiple-sequence alignment allowed a more detailed description of the specific molecular determinants responsible for this invariant interface. This was then validated by ^{125}I-α-BuTx binding to chimeric subunits transiently transfected in HEK293 cells.

Furthermore, we sought to characterise the biophysical properties of the human αδβ nAChR that we obtained under experimental conditions and determine a structural explanation for its differing behaviour to WT by comparing simulations of apo and acetylcholine (ACh) bound states of human adult muscle nAChR. The simulations suggested little change in the ACh binding modes as expected. However, we also observed a distinct increased mobility of loop-C at the αδ interface in the apo state, compared to the $\alpha\varepsilon$ interface. Taking the large (18.75 fold) reduction in EC_{50} for the $\alpha_2\delta_2\beta$ receptor compared to WT with the observations from simulation, we hypothesise that increased C-loop motility at the agonist binding site could allow for a less occluded binding site and would facilitate the recognition of ACh during the initial diffusive stage of agonist binding.

Methods

Homology modelling

Full length sequences of adult human end-plate nAChR subunits were aligned with the target sequences of α_3 and β_4 nAChR subunits which correspond to the subunits present in the template model (6PV7) [24]. Additional phylogenetically related subunits were included to improve confidence in the multiple sequence alignment, which was then performed using MUSCLE [25] before manual editing to obtain the final alignments (**SI Fig. 1**). In the first instance a single model was generated. This model was further refined by generating 10 additional models for three different non-conserved loop regions sequentially. Modeller [26]

was used to build the models. Specifically, this included residues 562-572, 969-977 and 1768-1776 situated on δ, β and ε subunits respectively and numbered according to sequential .pdb residue numbering. At each step of the loop refinement procedure, models were carried forward for additional loop refinement based on the best molpdf score. In total, 31 models were generated before arriving at the final template structure. The intracellular domain was not included as it was not resolved in the template structure.

Docking

ACh was docked using a grid box spacing of 1.0 Å with the docking box centered on the aromatic box for both orthosteric interfaces. Exhaustiveness was set to 8 and docking calculations performed in Vina 1.1.2 [27]. For all ligands, Gasteiger charges [28] where added and non-polar H atoms merged using Autodock 1.5.6 [29]. Docked poses were selected based on the proximity of the choline moiety to the centre of the aromatic box.

MD simulations

The homology model was embedded in a 100% POPC bilayer using inflategro.pl [30] before being solvated using a TIP3P water model [31]. Na^+ and Cl^- ions were added to neutralise the system before additional ions to make the system up to a final concentration of 0.15 M. This system was then energy minimised via the steepest descent algorithm (step size 0.01 nm, max number of steps = 50000). Electrostatics where calculated using the Particle mesh Ewald algorithm [32] with electrostatic cut off set to 10 Å, a cubic interpolation and fourier spacing of 10 Å. A 10 Å cutoff for the Van der Waals interactions was implemented. H-bonds were constrained using LINCS [33] to allow for a 2 fs time-step. Amber ff99SB-ILDN was used as the protein forcefield [34] and lipids were modelled using Slipids [35] . Each system was equilibrated in the NPT ensemble for 1 ns using semi-isotropic Berendsen pressure coupling [36] (tau = 1.0) and temperature coupling with V-

rescale [37] (tau = 0.1) at 310 K. Backbone atoms were restrained with 1000 kj/mol/A^2 force constant in order to allow for solvent and lipid molecules to equilibrate around the protein. Due to significant expansions in the z-axis after this short equilibration step, all water molecules were removed and periodic boundary conditions reduced along this axis before re-solvating and re-ionising the resulting system to decrease excessive buffer and improve overall sampling. The resulting system was then equilibrated for a further 5 ns in the same thermodynamic ensemble with holonomic constraints applied to h-bonds using the LINCS algorithm and position restraints removed to allow proper equilibration of the protein. Production runs were carried out with the Nosé-Hoover [38] (tau t=0.5) and Parrinello-Rahman (tau p=1.0) thermostat and barostat for 100 ns each. All simulations were performed using gromacs [39].

Multiple Sequence Alignment and Contact Matrix analysis

For the identification of potential residues involved in arrangement- an MSA of mammalian δ, ε and γ subunits was generated (**SI Fig. 2**). Candidate positions were selected based on whether at a specific point in the alignment, both γ and ε residues were conserved whilst δ residues differed. A pair-wise protein-protein Cβ atom contact prediction with a cut-off distance of 8 Å was selected according to the CASP criteria [40] and generated using MDanalysis [41]. Specific residues are numbered according to order of appearance in respective uniprot fasta files whilst disregarding signal peptide sequence. All residue numbers are labeled according to the mature peptide sequence herein.

Molecular Biology

Wild type human muscle cDNA subunits {Beeson, 1993 #9554} were subcloned into pcDNA3.1 (Invitrogen). The δ-ε-ε chimera was generated by PCR with overlap extension

[42] (**SI Table 1**). Additional chimeric constructs were synthesised by GeneArt (Regensburg, Germany). Full-length sequences of mutant subunit cDNAs were verified by sequencing (Eurofins-MWG, Germany). Specifically, δ/ε domain swaps occurred betweenδ residue numbers 231 for the ECD-TMD boundary, 320 for M3-MX & ICD boundary and 418 for the ICD-M4 boundary with the corresponding aligned residues according to **SI Fig. 1.**

^{125}I-α-BuTx binding assay, cell culture and transfections

^{125}I-α-BuTx binding assay, cell culture and transfections were carried out according to the protocol outlined in previous work [43] in which 2:2:1 ratios of α, chimeric and β subunits and α, δεɣ and β subunits were transfected into HEK293 cells for chimeric and double-'δεɣ' stoichiometries. 2:1:1:1 ratios of α, δ, β, ε and α, δ, β, ɣ were transfected into HEK293 cells for WT stoichiometries. ^{125}I-α-BuTx binding assays were done 2 days post-transfection with each assay performed in triplicate wells to ensure reproducibility. Results were normalized according to WT counts performed on the same day and seeded from the same original batch of HEK293 cells.

Expression of nAChRs in Xenopus Oocytes

Xenopus laevis oocytes were purchased from Xenopus One (Michigan USA). Toad ovary dissection was done according to regulations set out by the UK Home Office. Xenopus oocytes were prepared as described by previous methods [44]. Wild type human nAChR $\alpha_1\beta_1\delta\varepsilon$ subunit cDNAs were co-injected into the nuclei of oocytes at a 1:1:1:1 ratio and volume of 50.6 nl/oocyte, using a Nanoject Automatic Oocyte Injector (Drummond, Broomall, PA, USA). $2\alpha_1 2\delta\beta_1$, $2\alpha_1 2\varepsilon\beta_1$, $2\alpha_1 2\gamma\beta_1$ stoichiometries were injected at a radio of 2:2:1. 2 ng of cDNA was injected per oocyte. Post injection, oocytes were incubated for 2-5 days at 18

°C in modified Barth's solution containing1 mM KCl, 2.4 mM NaHCO3, 88 mM NaCl, 0.3 mM Ca(NO3)2, 0.82 mM MgSO4, 0.41 mM CaCl2, 15 mM HEPES and 5 mg/l neomycin (pH 7.6).

Electrophysiology and concentration response curves

All recordings were performed within 2 to 5 days after injection. Oocytes were placed in a recording chamber of 0.1 ml and perfused at 15 ml/min with Ringer's solution of composition: KCl 2.8 mM, NaCl 150 mM, $CaCl_2$ 1.8 mM, HEPES 10 mM ; pH 7.4 adjusted with NaOH and NaCl to obtain the desired pH. The two-electrode voltage-clamp (TEVC) configuration was used to obtain current responses, using a holding potential of -60 mV. The automated HiClamp setup (Multi Channel Systems) was used to obtain electrophysiological recordings. 3 M KCl was used as the electrode solution with a small aliquot of mineral oil at the entrance of each electrode to prevent evaporation and the formation of salt crystals. All experiments were performed with electrodes that had resistances of less than 1 MΩ. Serial dilutions of ACh in Ringer's solution was done on the day of use from frozen stock of 10 mM. Experiments were performed at room temperature. For all experiments, a 6 to 8 point log concentration-response curve (CRC) was obtained. Currents were normalised relative to ACh EC_{100} (1mM). Washes between ACh applications were 3 minutes long. Stabilisation of oocytes with ACh EC_{100} was done at the start of each experiment and intermittently after every two ACh applications in order eliminate run-up or run-down of responses from being included in subsequent data analyses.

Data analysis

All CRCs were fit with to a non-linear regression, mono-phasic four-parameter Hill equation

using Prism 5 software (Graph Pad, CA, USA). Individual EC_{50} values for electrophysiology experiments were plotted and analyzed by way of unpaired two-tailed t-test. A p value of less than 0.05 was deemed to be significantly different. ^{125}I-α-BuTx binding assays were analysed by one-way ANOVA with Tukey's post hoc test to control for multiple comparisons.

Results

The expression of $\alpha_2\delta_2\beta$ nAChRs and lack of $\alpha_2\varepsilon_2\beta$ or $\alpha_2\gamma_2\beta$ nAChRs implies exclusive contacts at the δ(+)β(-) interface

2:2:1 ratios of αδβ, αεβ or αγβ nAChR subunit cDNAs were injected into Xenepous oocytes to assess whether these variable stoichiometries could express competent receptors. As no currents could be detected for αεβ and αγβ injections,1:2:1 ratios were also attempted - again with no detection of currents. $\alpha_2\delta_2\beta$ receptors exhibited a statistically significant difference to WT EC_{50}, with a resulting decrease in EC_{50} from 17.58 μM (upper 95% CI = 32.66 uM, lower 95% CI = 9.46 μM) (n=9) to 0.938μM (upper 95% CI= 1.73 μM, lower 95% CI = 0.51 μM) (n=17) (**Fig. 1**). In order to rule out the possibility of cell surface expression of non-functional receptors, ^{125}I-α-BuTx binding assays were performed on these subunit ratios with no detectible expression on the cell surface. As $\alpha_2\gamma_2\beta$ and $\alpha_2\varepsilon_2\beta$ stoichiometries could not form functional pentamers, this indicated that either the δ subunit was somehow adapted to form an exclusive interface with the β(-) face and or that the β(-) interface prevents formation with γ and ε subunits.

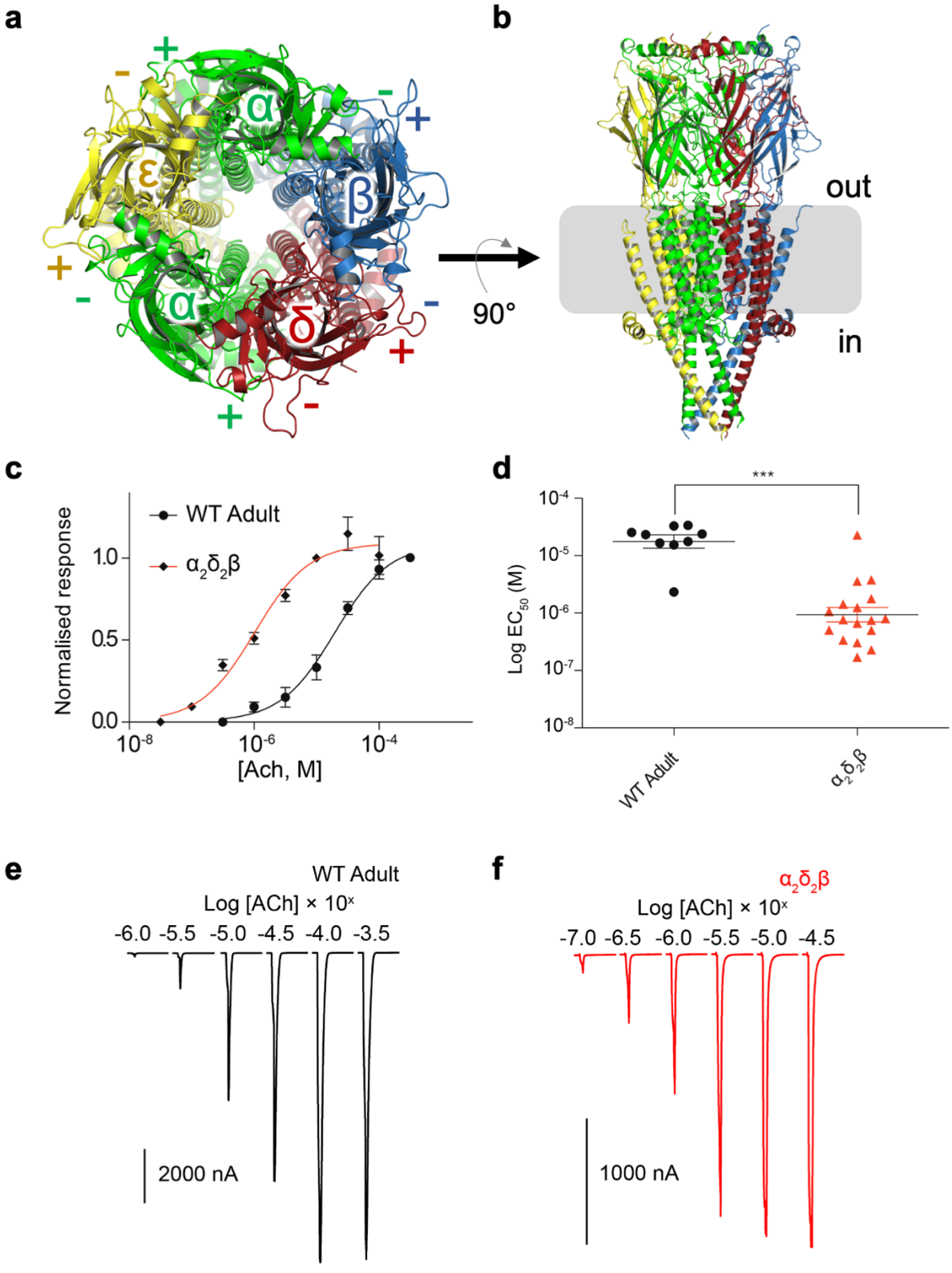

Fig. 1 Electrophysiological measurements on WT and $\alpha_2\delta_2\beta$ receptors. **a** Homology model showing arrangement of α, β, δ, and ε subunits coloured green, blue, red and yellow respectively, in the human muscle adult nAChR viewed from the synapse. **b** Model rotated 90° with the approximate location of the membrane indicated by a grey rectangle. **c** Normalized log concentration (in M) response curve of ACh at WT and $\alpha_2\delta_2\beta$ stoichiometry nAChRs. **d** Spread of EC_{50} values from ACh concentration response curves with mean and 95% confidence intervals shown and $p < 0.0001$ denoted by asterisks. **e** Representative current traces of WT (black) and **f** $\alpha_2\delta_2\beta$ receptor (red).

MD simulations and MSA integration point to specific residues on ECD, TMD and M4 extended helix of the δ subunit as important in forming exclusive contacts with β(-)

To obtain a more precise estimate of which residues in the δ(+) subunit contribute to the uniqueness of the δ(+)β(-) interface, we ran 10 x 100 ns all-atom molecular dynamics simulations of the adult human muscle nAChR. A pairwise contact matrix was employed to analyse each individual residues Cβ carbon atom distances between δ and β subunits (**Fig. 2**). A cutoff distance of 8 Å was selected according to the CASP criteria for protein-protein interaction distances. Residues that fell within this criteria for over 70% of aggregate simulation time (**Fig. 2b**) were then projected on to a snapshot from one of these simulations as shown in **Fig. 2a**. When 60% of aggregate simulation time is used to determine contacts, there was negligible change, with only δ H335 interactions no longer being detected.

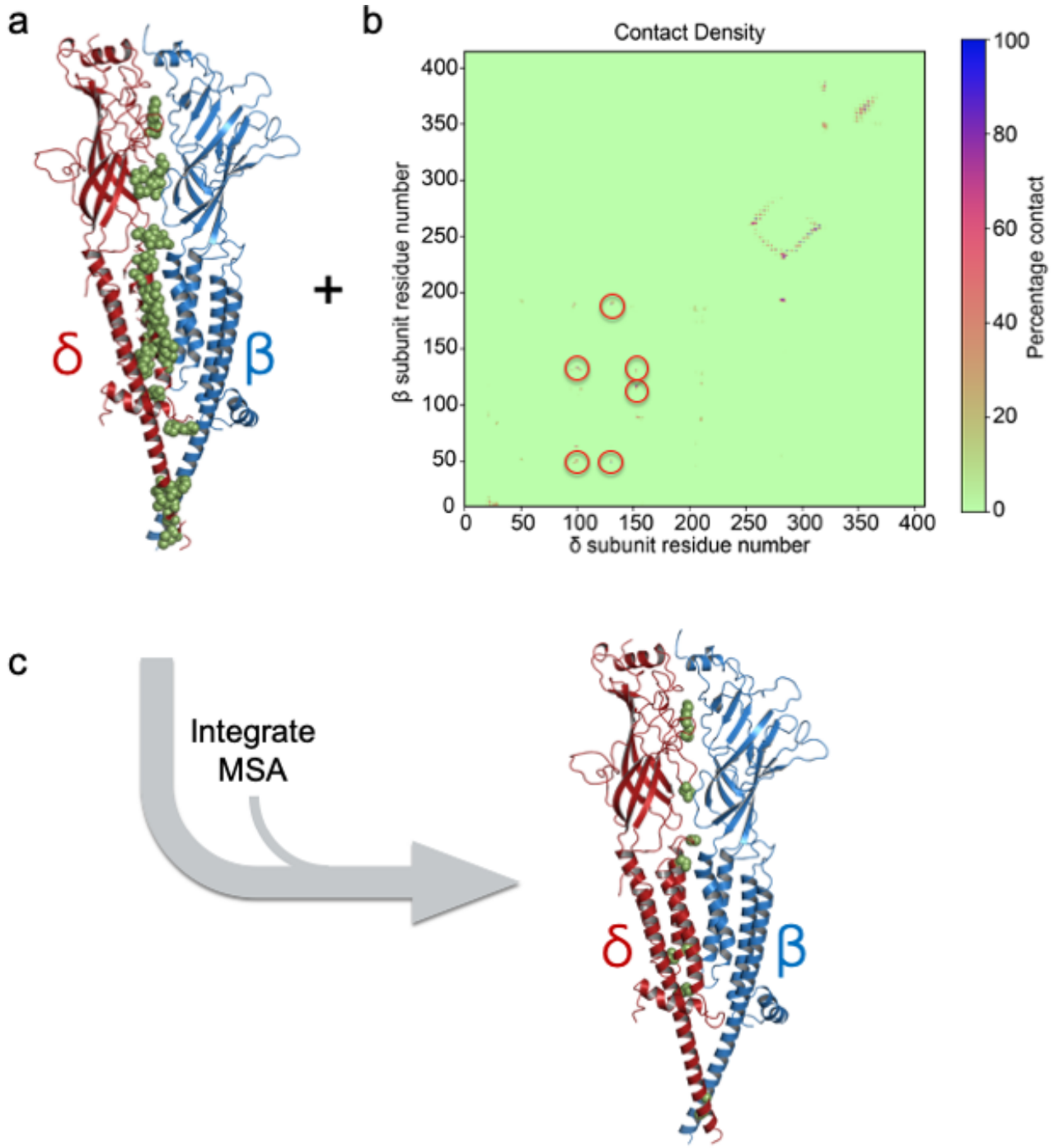

Fig. 2 Identification of important contacts. **a** Representative snapshot from apo simulations. δ and β subunits shown in red and blue respectively. Green sphere representation denotes all δ subunit residues who's Cβ atoms or Cα for glycine came within 8 Å of the β subunit over 70% of aggregate simulation time. α and ε subunits have been removed for clarity. **b** Pairwise residue contact matrix with red circles used to clarify single contact points in the ECD. **c** Remaining residues (green spheres) after filtering the contact matrix by MSA criteria (see main text for definition).

In order to filter out spurious residues that reside at the δ(+)β(-) interface but are not important in determining the interface, an MSA of all uniprot approved sequences of

mammalian δ, ε and ɣ subunit sequences was performed (**SI Fig. 2**). As ε and ɣ subunits occupy the same position in the global receptor WT topology it can be inferred that the residues that permit their particular positions are conserved with respect to one another and that corresponding δ subunit residues should also be conserved but not when compared to ε and ɣ. Residues that fit this evolutionary criteria and that were also detected by the contact matrix distance analysis were identified and mapped to the structure (**Fig. 2c**). Whilst intracellular domain residues were detected in the MSA that fulfilled this evolutionary criteria, the lack of structural template of which to model this domain on meant that they could not be detected in the contact analysis. Percentage contact time for each specific residue identified from the contact analysis and MSA integration was calculated (**SI Table 2**) to help manually check the data.

^{125}I-α-BuTx assays on chimeric subunits confirm that δ(+)β(-) specific interface determinants occur across domains.

In order to experimentally confirm that residues important for forming the δ(+)β(-) interface occur across domains, a series of chimeric δ/ε subunit constructs were made ($\delta_{chimera}$) (**Fig. 3a**) and injected in 2:2:1 ratios to investigate the role of three domains of the δ subunit were necessary for functional expression. The resulting chimeric receptors in transfected HEK293 cells and their cell surface expression were measured by ^{125}I-α-BuTx binding to surface expressed chimeras (**Fig. 3**). A receptor comprised of purely WT δ subunits (ie a receptor with the following composition: $\alpha_2\delta_2\beta$) shows a reduced surface expression (**Fig. 3b**) with respect to WT (ie $\alpha_2\delta\varepsilon\beta$), but surface expression is still robust and can be explained by the loss of favourable contacts between δ(+) and α(-). It should be noted that as both δ and ε subunits are tolerated between α subunits, the use of double chimeras will not preclude the analysis of δ(+)β(-) interface. However, it may result in reduced overall surface expression. The δ subunit chimera constructs δεε, δεδ and εδε show little to no surface

expression (**Fig. 3b**) and are not statistically significantly different from one another (**Table 1**). Receptors with the δδε chimera however, are capable of reaching the surface of the cell (**Fig. 3b**) and are statistically significantly different from δεε, δεδ and εδε containing constructs (**Table 1**). The δδε construct containing receptors are also statistically significantly different from the αδβ nAChR ($\alpha_2\delta_2\beta$) indicating that the intracellular domain is not critical in forming δ(+)β(-) interfaces, but does however promote increased cell surface expression efficiency. Overall, the expression of receptor with the δδε construct and the lack thereof for the receptors containing the δεδ and εδε and δεε constructs, indicates that both extracellular and transmembrane domains contain the molecular signatures for enabling δ(+)β(-) interface formation.

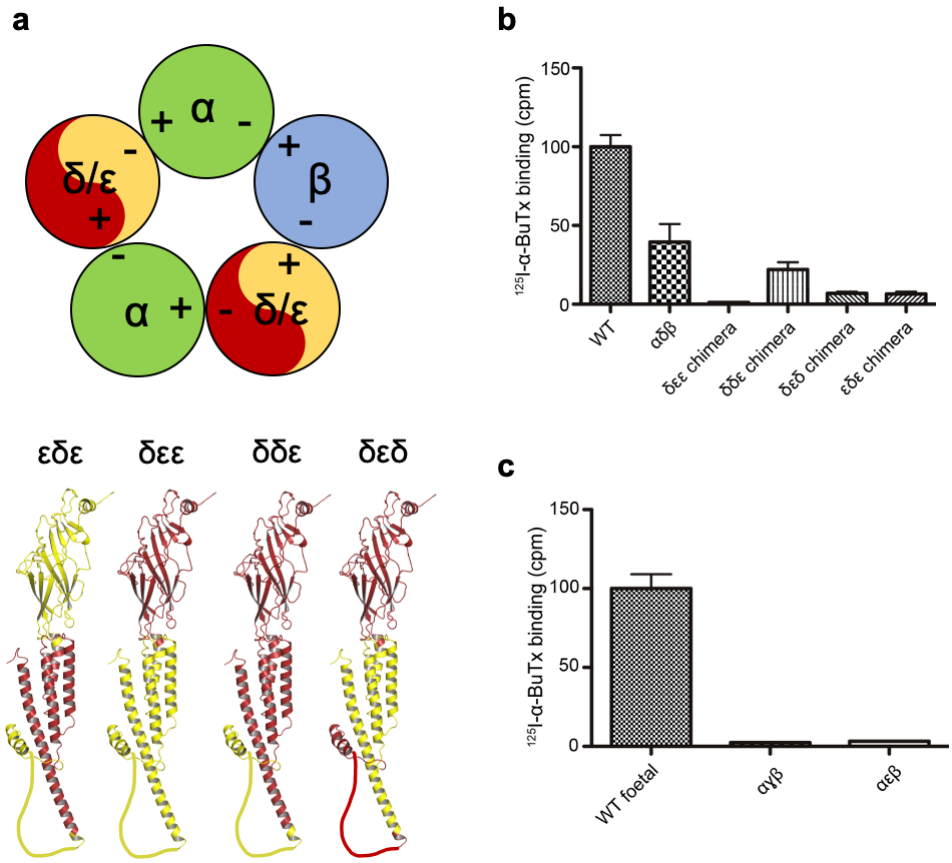

Fig. 3 Chimeric construct strategy. **a** Schematic of constructs used for ^{125}I-α-BuTx assay and associated models of each chimeric subunit, with ε segments in yellow and δ in red. **b** ^{125}I-α-BuTx assay means (normalised to WT counts) with associated 95% confidence interval. WT n=12, αδβ n=6, δεε n = 6, δδε n = 6, δεδ n=6, εδε n=5. **c** ^{125}I-α-BuTx data for αγβ (n=3) and αεβ (n=3) normalised to WT foetal receptor (n=2).

Table 1. ANOVA with Tukey's multiple comparison test for the surface expression of different δ subunit chimeras.

Construct	Significance
WT vs αδβ	***
WT vs δεε	***
WT vs δδε	***
WT vs δεδ	***
WT vs εδε	***
αδβ vs δεε	***
αδβ vs δδε	***
αδβ vs δεδ	***
αδβ vs εδε	***
δεε vs δδε	***
δεε vs δεδ	ns
δεε vs εδε	ns
δδε vs δεδ	*
δδε vs εδε	*
δεδ vs εδε	ns

*** < 0.0001, * < 0.05, ns = not significant

δK173, δN119 and δS297 participate in interface contacts via hydrogen bonding with βS134, βQ62 and βN251 respectively

MD analysis of specific residues highlighted from the integrated contact matrix analysis showed that δK173 is capable of participating in hydrogen bonding interactions with the proximal β face residue S134, with a peak observed at around 5 Å (**Fig. 4a**). There exists an additional peak at around 7 Å that would be indicative of non-interacting residues. Indeed, the overall span of this histogram indicates a high degree of flexibility for these residues. The ability of δN119 was also further assessed to form hydrogen bonds with neighbouring β subunit residue Q62 as both residues Cβ atoms were within 8 Å of each other as determined from the contact matrix analysis. As both residues contain hydrogen bond donor and acceptor atoms, density histograms for each pair was plotted (**Fig. 4b**). Major residue-residue interactions are mediated via the δN119 carbonyl group and βQ62 amino group. While δN119 amino - βQ62 carbonyl interactions are possible, they represent a minority of the hydrogen bond interactions between this residue pair. A further interaction is found between at the top of the TMD between the sidechain OH atom of δS297 and the sidechain oxygen of βN251 (**Fig. 3c**).

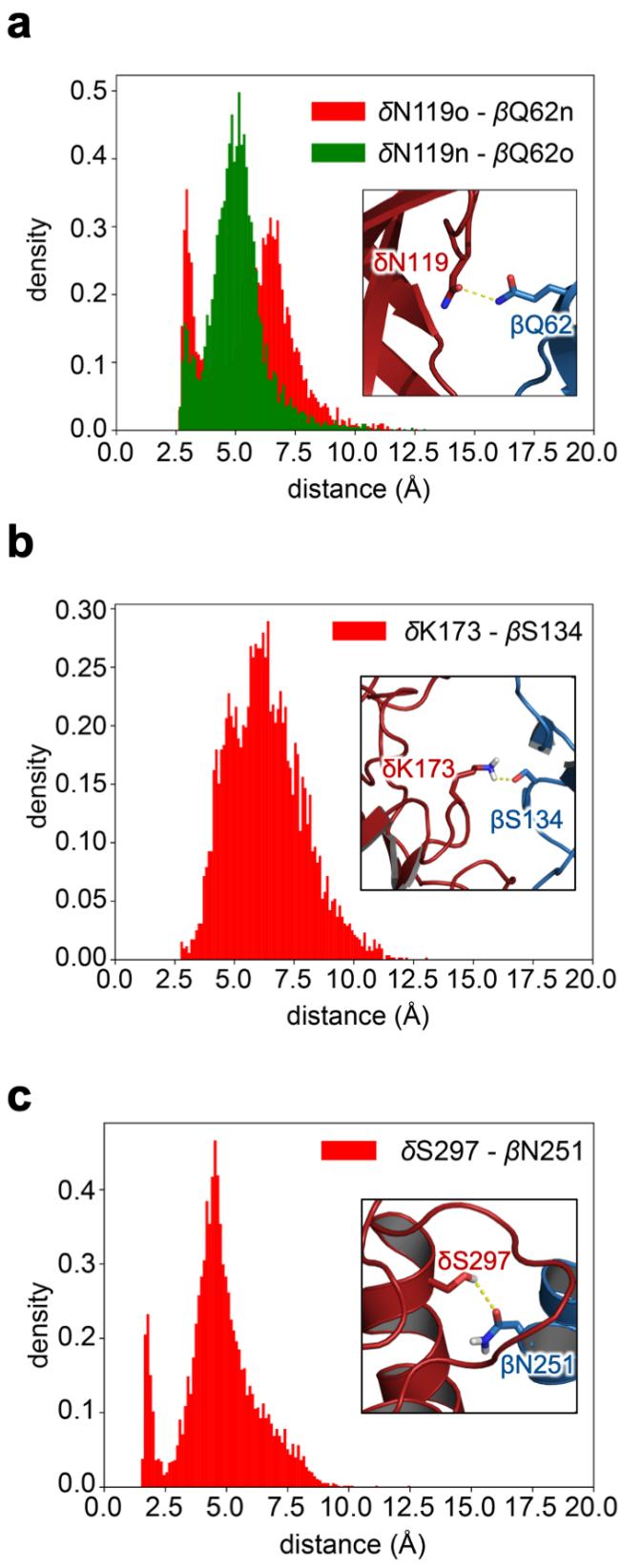

Fig. 4 Density histograms of ECD δ(+)β(-) contacts. **a** Distance between each nitrogen and oxygen atom pair between δN119 and βQ62. **b** Distance between δK173 and βS134 nitrogen and oxygen atoms. **c** Distance between δS297 and βN251 nitrogen and oxygen atoms. Inserts are representative snapshots from simulations with δ in 'fire-brick' red cartoon representation and β in 'sky-blue' cartoon representation. Amino acids of interest are shown in the stick representation, with their oxygen and nitrogen atoms coloured red and blue respectively.

C-loop dynamics are not equivalent at respective agonist-binding interfaces

Simulations were also used to further understand the shift in the EC_{50} that arises from a double δ receptor (**Fig. 1**). 10 additional 100 ns MD simulations were performed with ACh docked into both agonist binding sites and C-loop motions in apo and ACh-bound states compared. Comparison of the binding mode of ACh at both interfaces revealed no differences (**Fig. 5a**) in terms of the interaction of ACh with the binding pocket and is consistent with previous simulation reports of ACh dynamics in nAChRs [45]. The overall mode of interaction (**Fig. 5b**) is also preserved throughout all simulations. When ACh is bound, the C-loop mobility, as assessed by the variation of distance between the C-loop vicinal cysteines (Cys237 and Cys238) and the benzene ring of Trp194, does not differ appreciably between interfaces, although a negligible peak can be observed near 17.5 Å for the αδ interface. However, for the apo state, the mean position of the C-loop at the αδ interface is slightly shifted towards larger values, at around 11 Å, compared to approximately 10 Å for the αε interface. This is also coupled with a pronounced additional peak, observed at around 15 Å, suggesting that the C-loop can adopt a new, more open, state at the αδ interface.

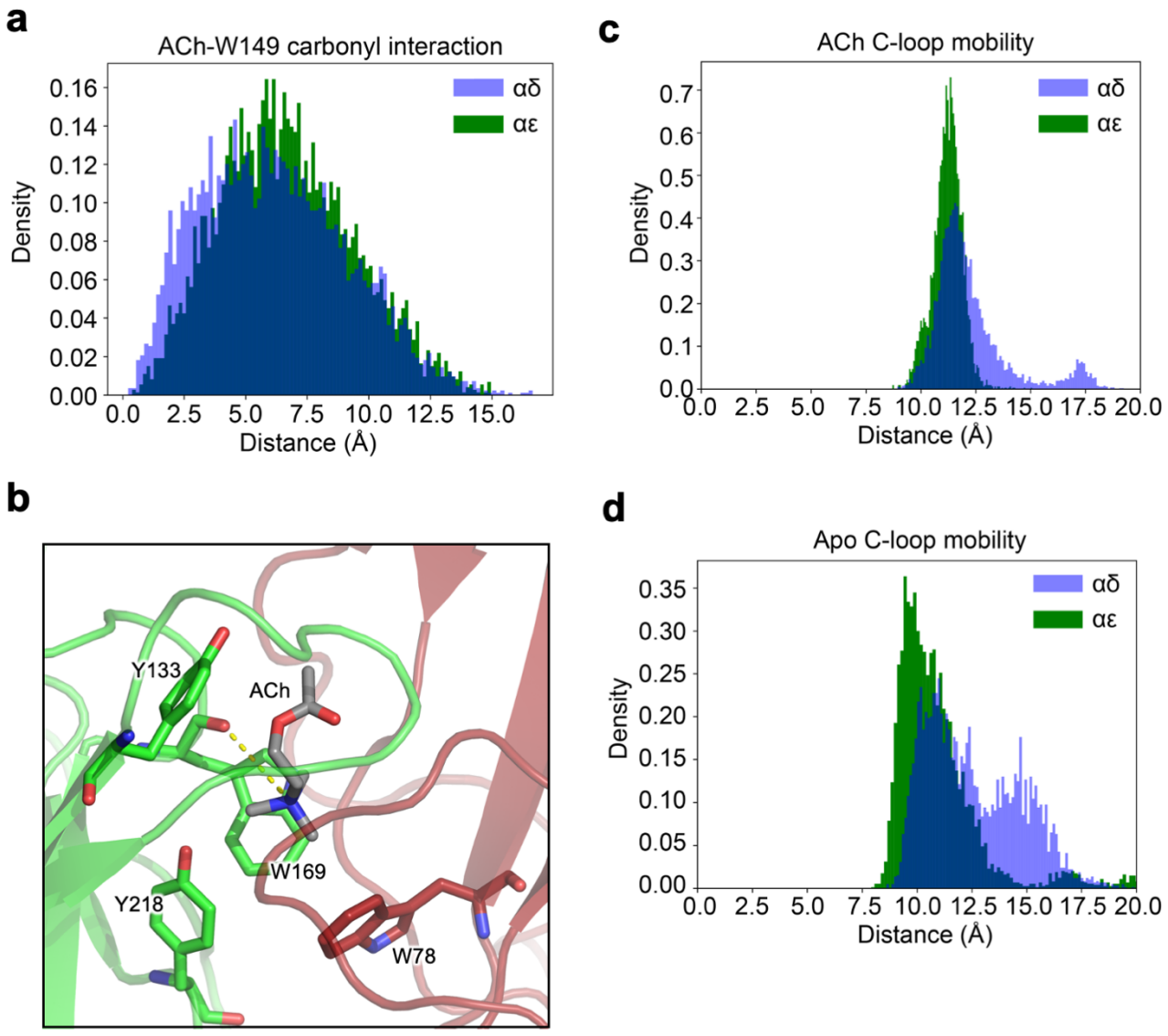

Fig. 5 C-loop dynamics. **a** Density histogram of ACh ammonium nitrogen and W149 carbonyl oxygen at αδ and αε interfaces as exemplified by the snapshot in **b** with the distance between W149 carbonyl and ACh ammonium nitrogen displayed as a dashed yellow line. **c** Density histograms between centre of geometry of C-loop disulphide sulphur atoms and centre of geometry of benzene moiety of W149 α subunit at both ACh and (D) apo state nAChR.

Discussion

The ability of nAChR subunits to assemble in variable stoichiometries expands the already large functional diversity of this receptor family. The muscle nAChR subtype is especially interesting in this regard, not only on account of the developmental switch that occurs during

neuromuscular maturation [46,47], but also from the apparent intransigence of subunit ordering. It appears that ε/ɣ and δ subunits have evolved to occupy a fixed position in the global receptor topology despite the fact that if swapped for one another - both agonist binding sites would be preserved. This implies that the pseudo-symmetrical architecture of the receptor can allosterically effect each orthosteric site in unique ways and that the overall contributions to overall receptor biophysics arising from individual subunit interfaces depends on their context with regards to all other subunit positions. In order to obtain experimental evidence of this however, the molecular determinants at the δ subunit responsible for forming an interface with the β subunit must be first be elucidated. As all previous studies focus on non-human subtypes and given the large inter-species diversity commonly observed between specific nAChR stoichiometries [23] - and especially demonstrated by differences in response to ACh [48-51] this provided further justification for the study outlined herein. Additionally, while regions on both α inter-subunit interfaces that govern assembly have been identified for mouse muscle nAChRs [15]. How δ is adapted to exclusively form interfacial contacts with the β subunit in the context of a pentamer in human subtypes has not been shown. While attempts to delineate interfacial components have been addressed via cryo-EM structures of *Torpedo* ACh receptors [2,52], this does not precisely pinpoint assembly specific residues. Retrospective evaluation of the recently published *Torpedo* structure [53], 6UWZ, also shows species specific variation at assembly identified positions (**SI Fig. 3**).

Injection of 2:2:1 ratios of respective subunits for $\alpha_2\varepsilon_2\beta$, $\alpha_2\delta_2\beta$ and $\alpha_2\gamma_2\beta$ stoichiometries only yielded currents for $\alpha_2\delta_2\beta$. This pointed to residues on δ(+)β(-) face as the determinants for stoichiometric invariance. Furthermore, $\alpha_2\delta_2\beta$ shows a large shift in EC_{50} for ACh in agreement with previous results for bovine muscle receptors [18]. Given this and previous data, a subunit order of αδαδβ (clockwise viewed from the synapse) is completely

consistent. However, we cannot at this stage, completely rule out other alternatives. That would require the use of concatemers [54, Mazzaferro, 2014 #6892], a technique that has recently been used to show that loose subunits can lead to heterogenous receptor populations, although this was for α4β2α5 receptors [55]. Nevertheless, due to the robust currents recorded, no change in hill slope compared to WT and the requirement of a β subunit for cell surface expression [17,19], a reasonable and parsimonious assumption is that this receptor adopts a αδαδβ ordering.

Given that pLGIC ICDs can assemble independently of the rest of the receptor [8] and that functional channels can be obtained without intracellular domains [56], it is unsurprising that our δδε chimeric subunit can still form functional pentamers. The ICD is also known to participate in interactions with cytoskeletal proteins and in the case of the δ subunit, is predicted to be mostly unfolded [57]. This makes it very unlikely to participate in determining subunit ordering to any extent. The δδε chimeric construct also leads to decreased expression with respect to WT and $\alpha_2\delta_2\beta$, therefore, the ICD is important for expression efficiency but not for forming specific arrangements. Furthermore, mutation to δεε, causes complete ablation in expression. Comparing this with δδε indicates that δ transmembrane domain (TMD) residues are involved in some capacity for forming specific arrangements.

It would appear however that from the lack of expression for the εδε chimeric construct that residues identified on the δ ECD are also important in forming specific arrangements. This demonstrates that the molecular determinants for forming the exclusive δ(+)β(-) interface are not confined to a single domain and is particularly interesting given that previous determinants of assembly have been show to reside at ECD 'assembly boxes' [58,5].

From the MD simulations, hydrogen bond interactions between δN119 and βQ62 were observed, with well-defined peaks (**Fig. 4a**). Hydrogen bond donor and acceptor moieties for both residues do not seem to interact simultaneously which would theoretically increase the strength of this part of the interface, however the definition of peaks would be indicative of stable interactions overall for these residues. Hydrogen bonding was also observed between residues δK173- βS134 (Fig. 4B) with a broad overall histogram indicative of high residue flexibility. An identifiable peak at 5 Å probably corresponds to hydrogen bonding interactions, whilst the major peak occurred closer to 7 Å. The proximity of these residues to the solvent exposed region of the ECD funnel as well as the high level of flexibility would indicate sub-optimal interactions despite δK173 residing at the same position as conserved ɣ residues shown to be essential for forming ɣ(+)α(-) interactions in mice nAChRs [15]. It should also be noted that as well as the favourable interactions mediated by δ(+) interface residues responsible for allowing WT stoichiometry to occur, unfavourable interactions between homologous residues of the ε(+) face and β(-) face may also prevent ε(+)β(-) interfaces from occurring. δK173 and δN119 are replaced by threonine and isoleucine in the ε subunit and would represent the loss of potential hydrogen bond interactions (**SI Fig. 4**). To this end, homologous δ(+) and ε(+) residues could work in tandem with favourable and unfavourable interactions respectively to enable the fixed stoichiometry of WT human muscle nAChRs.

Residues δS297 and δA302 in the M2-M3 loop of the δ subunit show hydrogen bonding and hydrophobic interactions respectively with residues on the β subunit **(Fig. 4c and SI Fig 5a**). It is well established that the M2-M3 linker acts as a key structural motif in coupling agonist binding to gating [59,60]. Although mutations to ε and β subunits have been demonstrated to change the open time constant, no such change could be observed for homologous residues at the δ subunit [61]. Given this and from the data described herein, it is likely that

part of this region could serve an alternative function and could be important in forming an optimal interface with the β(-) faces. While residues δE277 in the -1' position and δT279 in the 1' position of the M1-M2 loop were highlighted from the contact matrix analysis, the conservation of δE277 with β and α subunits, as well as its well-known role in determining ion selectivity [62] make it highly unlikely that it is involved in forming the δ(+)β(-) interface. Despite this, δT279 is positioned within the inter-helical bundles of both subunits and is not conserved widely across muscle subunits (**SI Fig. 5b).** The importance of inter-helical interactions in shaping overall receptor stoichiometry arising from intra-helical aromatic interactions has been previously eluded to [6]. H335 was also identified from the contact analysis, although with a significantly reduced overall percentage contact with the β-face compared to other residues (**SI Table 2**). Uncertainty around the protonation state of this residue also makes it difficult to determine its role, if any, in the δ (+)β(-) interface and results from the simulation for this residue should be taken with caution. Residues δP439 and δG442 were identified from the contact matrix analysis and reside toward the intracellular end of the extended M4 helix (**SI Fig. 5c)**. Given their physicochemical properties and solvent exposure, it is likely that they form highly favourable hydrophobic interactions with β subunit residues.

As a precursor to assessing the effect of δ and ε subunit position on receptor function and response to ACh, we wanted to first determine the extent of differences intrinsic to both $\alpha\delta$ and $\alpha\varepsilon$ interfaces. To do this, we performed additional MD simulations with ACh docked into both orthosteric sites of the WT adult nAChR and compared interfaces in the apo and ACh bound states. Whilst the binding mode of ACh was comparable between interfaces (**Fig. 5a**), loop-C dynamics was markedly changed when comparing between apo and ACh bound states (**Fig 5c, d**). The shifted density observed for the αδ interface in the apo state compared to the αε interface as well as an additional peak at around 15 Å indicates a non-

occluded agonist binding site. This would translate mechanistically to a decreased k_{on} for ACh and could explain the shift in EC_{50} observed (**Fig. 1**). While this would manifest in differing K_d values for ACh at both binding sites, previous work in mouse muscle nAChRs has shown both interfaces to be functionally equivalent [45]. Despite this, there exist large variations in overall nAChR sensitivity to ACh across species [50,51,49]. In addition, the close proximity of the non-conserved δ loop-F to loop-C (**SI Fig. 6**) could feasibly cause changes in the response to ACh as it has been postulated that signal propagation post ACh binding occurs from the C-loop to the M2-M3 loop via the F-loop [63]. Differences in the contributions from both interfaces to gating have also been previously demonstrated [64] and given the 46.3% sequence identity between human δ and ε subunits, there are many structural opportunities for changes in ACh sensitivity.

Conclusions

Using a combination of electrophysiology, bioinformatics and MD simulations, we have identified residues across the extracellular, transmembrane and extended M4 helix of the human nAChR δ subunit that contribute to the intransigent assembly of WT muscle nAChRs. This aligns with previous studies on the assembly of pLGICs and offers a new insight into the strict rules governing the specific arrangement of end-plate nAChRs. Additionally, we have shown that differences in EC_{50}s between WT and $\alpha_2\delta_2\beta$ nAChRs can be rationalised by the altered dynamics of the C-loop observed in MD simulations and which may influence ACh binding kinetics.

Acknowledgements

We thank Dr Richard Webster and Dr Judith Cossins for useful discussions. M.E. is supported by an Engineering and Physical Sciences Research Council (EPSRC) Industrial

Cooperative Awards in Science & Engineering (iCASE) studentship (voucher number 15220076) with the Defence Science and Technology Laboratory (DSTL). PCB thanks the BBSRC for funding (BB/S001247/1). This project made use of computation time on JADE (EP/P020275/1) via HECBioSim (http://www.hecbiosim.ac.uk), supported by EPSRC (grant no. EP/R029407/1). We thank Advanced Research Computing (Oxford) for additional computer time.

Author contributions

P.C.B and M.E. conceived the study. M.E planned the simulation protocol, performed and analyzed the MD simulations. M.E. performed and analyzed the electrophysiology and I.B. supervised the electrophysiology. M.E. and S.M. performed the ^{125}I-α-BuTx assays and M.E. analyzed the data. D.B. supervised the ^{125}I-α-BuTx assays. P.C.B., T.J.P and M.E. interpreted the results. P.C.B and M.E. wrote the paper.

Compliance with ethical standards

Dissection of *Xenopus laevis* was done in accordance with UK Home office regulations.

Conflict of interest

The authors declare no competing interests.

References

1. Albuquerque EX, Pereira EFR, Alkondon M, Rogers SW (2009) Mammalian nicotinic acetylcholine receptors: from structure to function. Physiol Rev 89 (1):73-120. doi:10.1152/physrev.00015.2008

2. Rahman MM, Teng J, Worrell BT, Noviello CM, Lee M, Karlin A, Stowell MHB, Hibbs RE (2020) Structure of the native muscle-type nicotinic receptor and inhibition by snake venom toxins. Neuron. doi:https://doi.org/10.1016/j.neuron.2020.03.012

3. Changeux J-P (2018) The nicotinic acetylcholine receptor: a typical 'allosteric machine'. Philos Trans R Soc Lond 373 (1749):20170174. doi:10.1098/rstb.2017.0174

4. Gharpure A, Noviello CM, Hibbs RE (2020) Progress in nicotinic receptor structural biology. Neuropharmacology 171:108086. doi:https://doi.org/10.1016/j.neuropharm.2020.108086

5. Griffon N, Büttner C, Nicke A, Kuhse J, Schmalzing G, Betz H (1999) Molecular determinants of glycine receptor subunit assembly. The EMBO journal 18 (17):4711-4721. doi:10.1093/emboj/18.17.4711

6. Haeger S, Kuzmin D, Detro-Dassen S, Lang N, Kilb M, Tsetlin V, Betz H, Laube B, Schmalzing G (2010) An intramembrane aromatic network determines pentameric assembly of Cys-loop receptors. Nat Struct Mol Biol 17 (1):90-98. doi:10.1038/nsmb.1721

7. Wong L-W, Tae H-S, Cromer BA (2014) Role of the ρ1 GABAC receptor n-terminus in assembly, trafficking and function. ACS Chem Neurosci 5 (12):1266-1277. doi:10.1021/cn500220t

8. Pandhare A, Pirayesh E, Stuebler AG, Jansen M (2019) Triple arginines as molecular determinants for pentameric assembly of the intracellular domain of 5-HT3A receptors. J Gen Physiol 151 (9):1135-1145. doi:10.1085/jgp.201912421

9. Yu X-M, Hall ZW (1991) Extracellular domains mediating ε subunit interactions of muscle acetylcholine receptor. Nature 352 (6330):64-67. doi:10.1038/352064a0

10. Green WN, Claudio T (1993) Acetylcholine receptor assembly: Subunit folding and oligomerization occur sequentially. Cell 74 (1):57-69. doi:10.1016/0092-8674(93)90294-Z

11. Blount P, Merlie JP (1990) Mutational analysis of muscle nicotinic acetylcholine receptor subunit assembly. J Cell Biol 111 (6):2613-2622. doi:10.1083/jcb.111.6.2613

12. Merlie JP, Lindstrom J (1983) Assembly in vivo of mouse muscle acetylcholine receptor: Identification of an α1-subunit species that may be an assembly intermediate. Cell 34 (3):747-757. doi:10.1016/0092-8674(83)90531-7

13. Saedi MS, Conroy WG, Lindstrom J (1991) Assembly of Torpedo acetylcholine receptors in Xenopus oocytes. J Cell Biol 112 (5):1007-1015. doi:10.1083/jcb.112.5.1007

14. Gu Y, Forsayeth JR, Verrall S, Yu XM, Hall ZW (1991) Assembly of the mammalian muscle acetylcholine receptor in transfected COS cells. J Cell Biol 114 (4):799-807. doi:10.1083/jcb.114.4.799

15. Kreienkamp H-J, Maeda RK, Sine SM, Taylor P (1995) Intersubunit contacts governing assembly of the mammalian nicotinic acetylcholine receptor. Neuron 14:635-644

16. Blount P, Smith MM, Merlie JP (1990) Assembly intermediates of the mouse muscle nicotinic acetylcholine receptor in stably transfected fibroblasts. J Cell Biol 111 (6):2601-2611. doi:10.1083/jcb.111.6.2601

17. Charnet P, Labarca C, Lester HA (1992) Structure of the gamma-less nicotinic acetylcholine receptor: learning from omission. Mol Pharmacol 41 (4):708

18. Jackson MB, Imoto K Fau - Mishina M, Mishina M Fau - Konno T, Konno T Fau - Numa S, Numa S Fau - Sakmann B, Sakmann B (1990) Spontaneous and agonist-induced openings of an acetylcholine receptor channel composed of bovine muscle alpha-, beta- and delta-subunits. Euro J Physiol 417 (0031-6768 (Print)):129-135

19. Kullberg R, Owens JL, Camacho P, Mandel G, Brehm P (1990) Multiple conductance classes of mouse nicotinic acetylcholine receptors expressed in Xenopus oocytes. Proc Natl Acad Sci USA 87 (6):2067-2071. doi:10.1073/pnas.87.6.2067

20. Park J-Y, Mott M, Williams T, Ikeda H, Wen H, Linhoff M, Ono F (2014) A single mutation in the acetylcholine receptor δ-subunit causes distinct effects in two types of neuromuscular synapses. J Neurosci 34 (31):10211-10218. doi:10.1523/JNEUROSCI.0426-14.2014

21. Liu Y, Brehm P (1993) Expression of subunit-omitted mouse nicotinic acetylcholine receptors in Xenopus laevis oocytes. J Physiol 470 (1):349-363. doi:10.1113/jphysiol.1993.sp019862

22. Nicke A, Rettinger J, Mutschler E, Schmalzing G (1999) Blue native page as a useful method for the analysis of the assembly of distinct combinations of nicotinic acetylcholine receptor subunits. J Recept SigTransduct 19 (1-4):493-507. doi:10.3109/10799899909036667

23. Gu Y, Camacho P, Gardner P, Hall ZW (1991) Identification of two amino acid residues in the ϵ subunit that promote mammalian muscle acetylcholine receptor assembly in COS cells. Neuron 6 (6):879-887. doi:https://doi.org/10.1016/0896-6273(91)90228-R

24. Gharpure A, Teng J, Zhuang Y, Noviello CM, Walsh RM, Cabuco R, Howard RJ, Zaveri NT, Lindahl E, Hibbs RE (2019) Agonist selectivity and ion permeation in the α3β4 ganglionic nicotinic receptor. Neuron 104 (3):501-511.e506. doi:https://doi.org/10.1016/j.neuron.2019.07.030

25. Edgar RC (2004) MUSCLE: Multiple sequence alignment with high accuracy and high throughput. Nucleic Acids Research 32 (5):1792-1797

26. Webb B, Sali A (2014) Comparative protein structure modeling using modeller. Curr Prot Bioinf 5:5.61-65.66.32

27. Trott O, Olson AJ (2010) AutoDock Vina: improving the speed and accuracy of docking with a new scoring function, efficient optimization, and multithreading. J Comput Chem 31 (2):455-461. doi:10.1002/jcc.21334

28. Gasteiger J, Marsili M (1978) New model for calculating atomic charges in molecules. Tetrahedron Lett 19 (34):3181-3184

29. Goodsell DS, Olson AJ (1990) Automated docking of substrates to proteins by simulated annealing. Proteins: Struct Function Bioinf 8 (3):195-202. doi:10.1002/prot.340080302

30. Kandt C, Ash WL, Peter Tieleman D (2007) Setting up and running molecular dynamics simulations of membrane proteins. Methods 41 (4):475-488. doi:https://doi.org/10.1016/j.ymeth.2006.08.006

31. Jorgensen WL, Chandresekhar J, Madura JD, Impey RW, Klein ML (1983) Comparison of simple potential functions for simulating liquid water. J Chem Phys 79:926-935

32. Darden T, York D, Pedersen L (1993) Particle mesh Ewald - an N.log(N) method for Ewald sums in large systems. J Chem Phys 98 (12):10089-10092

33. Hess B (2008) P-lincs: A parallel linear constraint solver for molecular simulation. J Chem Theor Comput 4 (1):116-122. doi:10.1021/ct700200b

34. Lindorff-Larsen K, Piana S, Palmo K, Maragakis P, Klepeis J, Dror R, Shaw D (2010) Improved side-chain torsion potentials for the Amber ff99SB protein force field. Proteins: Struc Func Genet 78:1950-1958

35. Jämbeck JPM, Lyubartsev AP (2012) Derivation and systematic validation of a refined all-atom force field for phosphatidylcholine lipids. J Phys Chem B 116 (10):3164-3179. doi:10.1021/jp212503e

36. Berendsen HJC, Postma JPM, van Gunsteren WF, DiNola A, Haak JR (1984) Molecular dynamics with coupling to an external bath. J Chem Phys 81:3684-3690

37. Bussi G, Donadio D, Parrinello M (2007) Canonical sampling through velocity rescaling. J Chem Phys 126

38. Evans DJ, Holian BL (1985) The Nose–Hoover thermostat. J Chem Phys 83 (8):4069-4074. doi:10.1063/1.449071

39. Abraham MJ, Murtola T, Schulz R, Páll S, Smith JC, Hess B, Lindahl E (2015) GROMACS: High performance molecular simulations through multi-level parallelism from laptops to supercomputers. SoftwareX 1–2:19-25. doi:http://dx.doi.org/10.1016/j.softx.2015.06.001

40. Monastyrskyy B, D'Andrea D, Fidelis K, Tramontano A, Kryshtafovych A (2016) New encouraging developments in contact prediction: Assessment of the CASP11 results. Proteins: Struct Func Bioinf 84 (S1):131-144. doi:10.1002/prot.24943

41. Gowers RJ, Linke M, Barnoud J, Reddy TJE, Melo MN, Seyler SL, Dotson DL, Domanski J, Buchoux S, Kenney IM, Beckstein O MDAnalysis: A Python package for the rapid analysis of molecular dynamics simulations. In: Benthall S, Rostrup S (eds) Python in Science, Austin, Tx., 2016.

42. Heckman KL, Pease LR (2007) Gene splicing and mutagenesis by PCR-driven overlap extension. Nature Protocols 2 (4):924-932. doi:10.1038/nprot.2007.132

43. Cetin H, Epstein M, Liu WW, Maxwell S, Rodriguez Cruz PM, Cossins J, Vincent A, Webster R, Biggin PC, Beeson D (2019) Muscle acetylcholine receptor conversion into chloride conductance at positive potentials by a single mutation. Proc Nat Acad Sci 116:21228-21235. doi:10.1073/pnas.1908284116

44. Moroni M, Vijayan R, Carbone A, Zwart R, Biggin PC, Bermudez I (2008) Non-agonist-binding subunit interfaces confer distinct functional signatures to the alternate stoichiometries of the {alpha}4{beta}2 nicotinic receptor: An {alpha}4-{alpha}4 interface is required for Zn^{2+} potentiation. J Neurosci 28 (27):6884-6894

45. Nayak TK, Bruhova I, Chakraborty S, Gupta S, Zheng W, Auerbach A (2014) Functional differences between neurotransmitter binding sites of muscle acetylcholine receptors. Proc Natl Acad Sci USA

46. Hall ZW, Sanes JR (1993) Synaptic structure and development: The neuromuscular junction. Cell 72:99-121. doi:10.1016/S0092-8674(05)80031-5

47. Brehm P, Henderson L (1988) Regulation of acetylcholine receptor channel function during development of skeletal muscle. Devel Biol 129 (1):1-11. doi:https://doi.org/10.1016/0012-1606(88)90156-X

48. Galzi J-L, Changeux J-P (1994) Neurotransmitter-gated ion channels as unconventional allosteric proteins. Curr Opin Struct Biol 4 (4):554-565. doi:https://doi.org/10.1016/S0959-440X(94)90218-6

49. Gross A, Ballivet M, Rungger D, Bertrand D (1991) Neuronal nicotinic acetylcholine receptors expressed in Xenopus oocytes: role of the α subunit in agonist sensitivity and desensitization. Pflügers Archiv 419 (5):545-551. doi:10.1007/BF00370805

50. Couturier S, Erkman L, Valera S, Rungger D, Bertrand S, Boulter J, Ballivet M, Bertrand D (1990) Alpha 5, alpha 3, and non-alpha 3. Three clustered avian genes encoding neuronal nicotinic acetylcholine receptor-related subunits. J Biol Chem 265 (29):17560-17567

51. Chavez-Noriega LE, Crona JH, Washburn MS, Urrutia A, Elliott KJ, Johnson EC (1997) Pharmacological characterization of recombinant human neuronal nicotinic acetylcholine receptors hα2β2, hα2β4, hα3β2, hα3β4, hα4β2, hα4β4 and hα7 expressed in Xenopus oocytes. J Pharm Exp Thera 280 (1):346

52. Unwin N (2005) Refined Structure of the Nicotinic Acetylcholine Receptor at 4Å Resolution. J Mol Biol 346:967-989

53. Rahman MM, Teng J, Worrell BT, Noviello CM, Lee M, Karlin A, Stowell MHB, Hibbs RE (2020) Structure of the native muscle-type nicotinic receptor and inhibition by snake venom toxins. Neuron:in press. doi:10.1016/j.neuron.2020.03.012

54. Mazzaferro S, Benallegue N, Carbone A, Gasparri F, Vijayan R, Biggin PC, Moroni M, Bermudez I (2011) An additional ACh binding site at the α4/α4 interface of the (α4β2)2α4 nicotinic acetylcholine receptor confers stoichiometry-specific properties. J Biol Chem 286:31043-31054

55. Prevost MS, Bouchenaki H, Barilone N, Gielen M, Corringer P-J (2020) Concatemers to re-investigate the role of α5 in α4β2 nicotinic receptors. Cell Mol Life Sci:in press. doi:10.1007/s00018-020-03558-z

56. Jansen M, Bali M, Akabas MH (2008) Modular design of cys-loop ligand-gated ion channels: Functional 5-HT3 and GABA ρ1 receptors lacking the large cytoplasmic M3M4 loop. J Gen Physiol 131 (2):137-146. doi:10.1085/jgp.200709896

57. Kukhtina V, Kottwitz D, Strauss H, Heise B, Chebotareva N, Tsetlin V, Hucho F (2006) Intracellular domain of nicotinic acetylcholine receptor: the importance of being unfolded. J Neurochemistry 97 (s1):63-67. doi:10.1111/j.1471-4159.2005.03468.x

58. Kuhse J, Laube B, Magalei D, Betz H (1993) Assembly of the inhibitory glycine receptor: Identification of amino acid sequence motifs governing subunit stoichiometry. Neuron 11 (6):1049-1056. doi:https://doi.org/10.1016/0896-6273(93)90218-G

59. Jha A, Cadugan DJ, Purohit P, Auerbach A (2007) Acetylcholine receptor gating at extracellular transmembrane domain interface: the cys-loop and M2-M3 linker. J Gen Physiol 130 (6):547-558. doi:10.1085/jgp.200709856

60. Lee WY, Sine SM (2005) Principal pathway coupling agonist binding to channel gating in nicotinic receptors. Nature 438 (7065):243-247. doi:10.1038/nature04156

61. Grosman C, Salamone FN, Sine SM, Auerbach A (2000) The extracellular linker of muscle acetylcholine receptor channels is a gating control element. J Gen Physiol 116 (3):327-340. doi:10.1085/jgp.116.3.327

62. Jensen ML, Schousboe A, Ahring PK (2005) Charge selectivity of the Cys-loop family of ligand-gated ion channels. J Neurochemistry 92 (2):217-225. doi:10.1111/j.1471-4159.2004.02883.x

63. Oliveira ASF, Edsall CJ, Woods CJ, Bates P, Nunez GV, Wonnacott S, Bermudez I, Ciccotti G, Gallagher T, Sessions RB, Mulholland AJ (2019) A general mechanism for signal propagation in the nicotinic acetylcholine receptor family. J Am Chem Soc 141 (51):19953-19958. doi:10.1021/jacs.9b09055

64. Akk G, Sine S, Auerbach A (1996) Binding sites contribute unequally to the gating of mouse nicotinic alpha D200N acetylcholine receptors. J Physiol 496 (Pt 1) (Pt 1):185-196. doi:10.1113/jphysiol.1996.sp021676

Bibliography

1. Maehle, A. H. "Receptive Substances": John Newport Langley (1852-1925) and his Path to a Receptor Theory of Drug Action. *Medical History* **48,** 153–174 (2004).
2. Katz, B. Y. B. & Miledi, R. The Statistical Nature of The Acetylcholine Potential and Its Molecular Components. *J. Physiol* **224,** 665–699 (1972).
3. Katz, B. & Miledi, R. The binding of acetylcholine to receptors and its removal from the synaptic cleft. *The Journal of Physiology* **231,** 549–574 (1973).
4. Boulter, J. *et al.* Isolation of a clone coding for the alpha-subunit of a mouse acetylcholine receptor. *Journal of Neuroscience* **5,** 2545–2552 (1985).
5. Numa, S. *et al.* Molecular structure of the nicotinic acetylcholine receptor. *Cold Spring Harbor symposia on quantitative biology* **48 Pt 1,** 57–69 (1983).
6. Millar, N. S. A review of experimental techniques used for the heterologous expression of nicotinic acetylcholine receptors. *Biochemical Pharmacology* **78,** 766–776 (2009).
7. Sigworth, F. The Variance of Sodium Current Fluctuations at The Node of Ranvier. *The Journal of physiology,* 97–129 (1980).
8. Neher, E. & Sakmann, B. Single-channel currents recorded from membrane of denervated frog muscle fibres. *Nature* **260,** 799–802 (1976).
9. Changeux, J.-P. Allostery and the Monod-Wyman-Changeux Model After 50 Years. *Annual Review of Biophysics* **41,** 103–133 (2012).
10. Henderson, R. From Electron Crystallography to Single Particle CryoEM (Nobel Lecture). *Angewandte Chemie - International Edition* **57,** 10804–10825 (2018).
11. Unwin, N. *et al.* Arrangement of the acetylcholine receptor subunits in the resting and desensitized states, determined by cryoelectron microscopy of crystallized Torpedo postsynaptic membranes. *The Journal of cell biology* **107,** 1123–1138 (1988).
12. Nakane, T. *et al.* Single-particle cryo-EM at atomic resolution. *BioRxiv* (2020).
13. Lev, B. *et al.* String method solution of the gating pathways for a pentameric ligand-gated ion channel. *Proceedings of the National Academy of Sciences of the United States of America* **114,** E4158–E4167 (2017).

14. Changeux, J. P. Protein dynamics and the allosteric transitions of pentameric receptor channels. *Biophysical Reviews* **6,** 311–321 (2014).

15. Changeux, J. P. & Christopoulos, A. Allosteric Modulation as a Unifying Mechanism for Receptor Function and Regulation. *Cell* **166,** 1084–1102 (2016).

16. Cetin, H. *et al.* Muscle acetylcholine receptor conversion into chloride conductance at positive potentials by a single mutation. *Proceedings of the National Academy of Sciences of the United States of America* **116,** 21228–21235 (2019).

17. Engel, A. G. *et al.* Congenital myasthenic syndromes: Pathogenesis, diagnosis, and treatment. *The Lancet Neurology* **14,** 420–434 (2015).

18. Engel, A. G. *et al.* The spectrum of congenital myasthenic syndromes. *Molecular Neurobiology* **26,** 347–367 (2002).

19. Timperley, C. M. *et al.* Advice on assistance and protection provided by the Scientific Advisory Board of the Organisation for the Prohibition of Chemical Weapons: Part 1. On medical care and treatment of injuries from nerve agents. *Toxicology* **415,** 56–69 (2019).

20. Sine, S. M. & Engel, A. G. Recent advances in Cys-loop receptor structure and function. *Nature* **440** (2006).

21. Nys, M. *et al.* Structural insights into Cys-loop receptor function and ligand recognition. *Biochemical Pharmacology* **86,** 1042–1053 (2013).

22. Putrenko, I. *et al.* A family of acetylcholine-gated chloride channel subunits in Caenorhabditis elegans. *Journal of Biological Chemistry* **280,** 6392–6398 (2005).

23. Pirri, J. K. *et al.* A Tyramine-Gated Chloride Channel Coordinates Distinct Motor Programs of a Caenorhabditis elegans Escape Response. *Neuron* **62,** 526–538 (2009).

24. Zheng, Y. *et al.* Identification of two novel Drosophila melanogaster histamine-gated chloride channel subunits expressed in the eye. *Journal of Biological Chemistry* **277,** 2000–2005 (2002).

25. Cannard, K. The acute treatment of nerve agent exposure. *Journal of the Neurological Sciences* **249,** 86–94 (2006).

26. Chatterjee, S. & Bartlett, S. Neuronal Nicotinic Acetylcholine Receptors as Pharmacotherapeutic Targets for the Treatment of Alcohol Use Disorders. *CNS & Neurological Disorders - Drug Targets* **9,** 60–76 (2012).

27. Wouda, J. A. *et al.* Varenicline attenuates cue-induced relapse to alcohol, but not nicotine seeking, while reducing inhibitory response control. *Psychopharmacology* **216,** 267–277 (2011).

28. Gilles, C. & Luthringer, R. Pharmacological models in healthy volunteers: Their use in the clinical development of psychotropic drugs. *Journal of Psychopharmacology* **21,** 272–282 (2007).

29. Hone, A. J. & McIntosh, J. M. Nicotinic acetylcholine receptors in neuropathic and inflammatory pain. *FEBS Letters* **592,** 1045–1062 (2018).

30. Zdanowski, R. *et al.* Role of $\alpha 7$ nicotinic receptor in the immune system and intracellular signaling pathways. *Central European Journal of Immunology* **40,** 373–379 (2015).

31. Trimmer, J. S. *et al.* Primary structure and functional expression of a mammalian skeletal muscle sodium channel. *Neuron* **3,** 33–49 (1989).

32. Flucher, B. E. & Daniels, M. P. Distribution of Na+ channels and ankyrin in neuromuscular junctions is complementary to that of acetylcholine receptors and the 43 kd protein. *Neuron* **3,** 163–175 (1989).

33. Martyn, J. A. J. *et al.* Basic principles of neuromuscular transmission. *Anaesthesia* **64 Suppl 1,** 1–9 (2009).

34. Wu, J. & Lukas, R. J. Naturally-expressed nicotinic acetylcholine receptor subtypes. *Biochemical Pharmacology* **82,** 800–807 (2011).

35. Gharpure, A. *et al.* Agonist Selectivity and Ion Permeation in the $\alpha 3\beta 4$ Ganglionic Nicotinic Receptor. *Neuron* **104,** 501–511.e6 (2019).

36. Dellisanti, C. D. *et al.* Crystal structure of the extracellular domain of nAChR $\alpha 1$ bound to α-bungarotoxin at 1.94 Å resolution. *Nature Neuroscience* **10,** 953–962 (2007).

37. Tsouloufis, T. Reconstitution of conformationally dependent epitopes on the N-terminal extracellular domain of the human muscle acetylcholine receptor alpha subunit expressed in Escherichia coli: implications for myasthenia gravis therapeutic approaches. *International Immunology* **12,** 1255–1265 (2000).

38. Luo, J. *et al.* Main immunogenic region structure promotes binding of conformation- dependent myasthenia gravis autoantibodies, nicotinic acetylcholine receptor conformation maturation, and agonist sensitivity. *Journal of Neuroscience* **29,** 13898–13908 (2009).

39. Rahman, M. M. *et al.* Structure of the Native Muscle-type Nicotinic Receptor and Inhibition by Snake Venom Toxins. *Neuron* **106,** 952–962.e5 (2020).

40. Shimomura, M. *et al.* Roles of loop C and the loop B-C interval of the nicotinic receptor α subunit in its selective interactions with imidacloprid in insects. *Neuroscience Letters* **363,** 195–198 (2004).

41. Albuquerque, E. X. *et al.* Mammalian nicotinic acetylcholine receptors: From structure to function. *Physiological Reviews* **89,** 73–120 (2009).

42. Le Novère, N. & Changeux, J. P. The ligand gated ion channel database. *Nucleic Acids Research* **27,** 340–342 (1999).

43. Blount, P. & Merlie, J. P. Mutational analysis of muscle nicotinic acetylcholine receptor subunit assembly. *Journal of Cell Biology* **111,** 2613–2622 (1990).

44. Unwin, N. *et al.* Activation of the nicotinic acetylcholine receptor involves a switch in conformation of the α subunits. *Journal of Molecular Biology* **319,** 1165–1176 (2002).

45. Unwin, N. Acetylcholine receptor channel imaged. *Nature* **373,** 37–43 (1995).

46. Czajkowski, C. *et al.* Negatively charged amino acid residues in the nicotinic receptor delta subunit that contribute to the binding of acetylcholine. *Proceedings of the National Academy of Sciences of the United States of America* **90,** 6285–6289 (1993).

47. Corringer, P.-J. *et al.* Identification of a New Component of the Agonist Binding Site of the Nicotinic alpha7 Homooligomeric Receptor. *The Journal of Biological Chemistry* **270,** 11749–11752 (1995).

48. Lester, H. A. *et al.* Cys-loop receptors: New twists and turns. *Trends in Neurosciences* **27,** 329–336 (2004).

49. Olsen, J. A. *et al.* Molecular recognition of the neurotransmitter acetylcholine by an acetylcholine binding protein reveals determinants of binding to nicotinic acetylcholine receptors. *PLoS ONE* **9,** 1–8 (2014).

50. Sixma, T. K. & Smit, A. B. Acetylcholine binding protein (AChBP): A secreted glial protein that provides a high-resolution model for the extracellular domain of pentameric ligand-gated ion channels. *Annual Review of Biophysics and Biomolecular Structure* **32,** 311–334 (2003).

51. Zhong, W. *et al.* From ab initio quantum mechanics to molecular neurobiology: A cation-π binding site in the nicotinic receptor. *Proceedings of the National Academy of Sciences of the United States of America* **95,** 12088–12093 (1998).

52. Nayak, T. K. *et al.* Functional differences between neurotransmitter binding sites of muscle acetylcholine receptors. *Proceedings of the National Academy of Sciences of the United States of America* **111,** 17660–17665 (2014).

53. Miyazawa, A. *et al.* Structure and gating mechanism of the acetylcholine receptor pore. *Nature* **423,** 949–955 (2003).

54. Dämgen, M. A. & Biggin, P. C. A Refined Open State of the Glycine Receptor Obtained via Molecular Dynamics Simulations. *Structure* **28,** 130–139.e2 (2020).

55. Carswell, C. L. *et al.* Role of the Fourth Transmembrane a Helix in the Article Role of the Fourth Transmembrane a Helix in the Allosteric Modulation of Pentameric Ligand-Gated Ion Channels. *Structure* **23,** 1655–1664 (2015).

56. Hosie, A. M. *et al.* Endogenous neurosteroids regulate GABAA receptors through two discrete transmembrane sites. *Nature* **444,** 486–489 (2006).

57. Dacosta, C. J. *et al.* A distinct mechanism for activating uncoupled nicotinic acetylcholine receptors. *Nature Chemical Biology* **9,** 701–707 (2013).

58. Sunshine, C. & McNamee, M. G. Lipid modulation of nicotinic acetylcholine receptor function: the role of membrane lipid composition and fluidity. *BBA - Biomembranes* **1191,** 59–64 (1994).

59. Thompson, M. J. *et al.* The functional role of the αM4 transmembrane helix in the muscle nicotinic acetylcholine receptor probed through mutagenesis and co-evolutionary analyses. *Journal of Biological Chemistry* **295,** 11056–11067 (2020).

60. Baier, C. J. *et al.* Disclosure of cholesterol recognition motifs in transmembrane domains of the human nicotinic acetylcholine receptor. *Scientific Reports* **1** (2011).

61. Lester, H. A. The permeation pathway of neurotransmitter-gated ion channels. *Annual Review of Biophysics and Biomolecular Structure* **21,** 267–292 (1992).

62. Rudell, J. C. *et al.* The MX-Helix of Muscle nAChR Subunits Regulates Receptor Assembly and Surface Trafficking. *Frontiers in Molecular Neuroscience* **13,** 1–13 (2020).

63. Croxen, R. End-plate gamma- and varepsilon-subunit mRNA levels in AChR deficiency syndrome due to varepsilon-subunit null mutations. *Brain* **124,** 1362–1372 (2001).

64. Ealing, J. Mutations in congenital myasthenic syndromes reveal an varepsilon subunit C-terminal cysteine, C470, crucial for maturation and surface expression of adult AChR. *Human Molecular Genetics* **11,** 3087–3096 (2002).

65. Wang, J. M. *et al.* A transmembrane motif governs the surface trafficking of nicotinic acetylcholine receptors. *Nature Neuroscience* **5,** 963–970 (2002).

66. Imoto, K. *et al.* Rings of negatively charged amino acids determine the acetylcholine receptor channel conductance. *Nature* **335,** 645–648 (1988).

67. Galzi *et al.* Mutations in the Channel Domain of a Neuronal Nicotinic Receptor Convert Ion Selectivity from Cationic to Anionic. *Nature* **359,** 500–505 (1992).

68. Althoff, T. *et al.* X-ray structures of GluCl in apo states reveal a gating mechanism of Cys-loop receptors. *Nature* **512,** 333–337 (2014).

69. Ivanov, I. *et al.* Barriers to ion translocation in cationic and anionic receptors from the cys-loop family. *Journal of the American Chemical Society* **129,** 8217–8224 (2007).

70. Gharpure, A. *et al.* Agonist Selectivity and Ion Permeation in the $\alpha 3\beta 4$ Ganglionic Nicotinic Receptor. *Neuron* **104,** 501–511.e6 (2019).

71. Beckstein, O. & Sansom, M. S. A hydrophobic gate in an ion channel: The closed state of the nicotinic acetylcholine receptor. *Physical Biology* **3,** 147–159 (2006).

72. Monod, J. *et al.* On the nature of allosteric transitions: A plausible model. *Journal of Molecular Biology* **12,** 88–118 (1965).

73. Sakmann, B. *et al.* Single acetylcholine-activated channels show burst-kinetics in presence of desensitizing concentrations of agonist. *Nature* **286,** 71–73 (1980).

74. Lape, R. *et al.* On the nature of partial agonism in the nicotinic receptor superfamily. *Nature* **454,** 722–727 (2008).

75. Mukhtasimova, N. *et al.* Detection and trapping of intermediate states priming nicotinic receptor channel opening. *Nature* **459,** 451–454 (2009).

76. Harpole, T. J. & Delemotte, L. Conformational landscapes of membrane proteins delineated by enhanced sampling molecular dynamics simulations. *Biochimica et Biophysica Acta - Biomembranes* **1860,** 909–926 (2018).

77. Kumar, A. *et al.* Mechanisms of activation and desensitization of full-length glycine receptor in membranes. *BioRxiv* (2019).

78. Sauguet, L. *et al.* Crystal structures of a pentameric ligand-gated ion channel provide a mechanism for activation. *Proceedings of the National Academy of Sciences of the United States of America* **111,** 966–971 (2014).

79. Ma, Q. *et al.* Exploring the Relationship between Nicotinic Acetylcholine Receptor Ligand Size, Efficiency, Efficacy, and C-Loop Opening. *Journal of Chemical Information and Modeling* **57,** 1947–1956 (2017).

80. Del Castillo, J. & Katz, B. Interaction at end-plate receptors between different choline derivatives. *Proceedings of the Royal Society of London. Series B, Containing papers of a Biological character. Royal Society (Great Britain)* **146,** 369–381 (1957).

81. Gao, F. *et al.* Agonist-mediated conformational changes in acetylcholine-binding protein revealed by simulation and intrinsic tryptophan fluorescence. *Journal of Biological Chemistry* **280,** 8443–8451 (2005).

82. Celie, P. H. *et al.* Nicotine and carbamylcholine binding to nicotinic acetylcholine receptors as studied in AChBP crystal structures. *Neuron* **41,** 907–914 (2004).

83. Venkatachalan, S. P. & Czajkowski, C. A conserved salt bridge critical for GABAA receptor function and loop C dynamics. *Proceedings of the National Academy of Sciences of the United States of America* **105,** 13604–13609 (2008).

84. Gupta, S. *et al.* A mechanism for acetylcholine receptor gating based on structure, coupling, phi, and flip. *Journal of General Physiology* **149,** 85–103 (2016).

85. Taly, A. *et al.* Implications of the quaternary twist allosteric model for the physiology and pathology of nicotinic acetylcholine receptors. *Proceedings of the National Academy of Sciences of the United States of America* **103,** 16965–16970 (2006).

86. Taly, A. *et al.* Normal mode analysis suggests a quaternary twist model for the nicotinic receptor gating mechanism. *Biophysical Journal* **88,** 3954–3965 (2005).

87. Oliveira, A. S. F. *et al.* A General Mechanism for Signal Propagation in the Nicotinic Acetylcholine Receptor Family. *Journal of the American Chemical Society* **141,** 19953–19958 (2019).

88. Rovsnik, U. *et al.* Characterization of the dynamic resting state of a pentameric ligand-gated ion channel by cryo-electron microscopy and simulations. *BioRxiv* **1,** 1–476. arXiv: `arXiv:1011.1669v3` (2020).

89. Chakrapani, S. & Auerbach, A. A speed limit for conformational change of an allosteric membrane protein. *Proceedings of the National Academy of Sciences of the United States of America* **102,** 87–92 (2005).

90. Lee, W. Y. & Sine, S. M. Principal pathway coupling agonist binding to channel gating in nicotinic receptors. *Nature* **438,** 243–247 (2005).

91. Vaughan, C. K. *et al.* A structural double-mutant cycle: Estimating the strength of a buried salt bridge in barnase. *Acta Crystallographica Section D: Biological Crystallography* **58,** 591–600 (2002).

92. Jha, A. *et al.* Acetylcholine receptor gating at extracellular transmembrane domain interface: The Cys-Loop and M2-M3 linker. *Journal of General Physiology* **130,** 547–558 (2007).

93. Nelson, M. E. *et al.* Alternate Stoichiometries of alpha4 beta2 Nicotinic Acetylcholine Receptors. **63,** 332–341 (2003).

94. Mazzaferro, S. *et al.* Additional Acetylcholine (ACh) binding site at $\alpha4/\alpha4$ interface of $(\alpha4\beta2)$ $2\alpha4$ nicotinic receptor influences agonist sensitivity. *Journal of Biological Chemistry* **286,** 31043–31054 (2011).

95. Bren, N. & Sine, S. M. Identification of Residues in the Adult Nicotinic Acetylcholine Receptor That Confer Selectivity for Curariform Antagonists. **272,** 30793–30798 (1997).

96. Sine, S. M. Molecular dissection of subunit interfaces in the acetylcholine receptor : Identification of residues that determine curare selectivity. **90,** 9436–9440 (1993).

97. Baumann, S. W. *et al.* Individual Properties of the Two Functional Agonist Sites in GABA A Receptors. **23,** 11158–11166 (2003).

98. Young, G. T. *et al.* Potentiation of $\alpha7$ nicotinic acetylcholine receptors via an allosteric transmembrane site. *Proceedings of the National Academy of Sciences of the United States of America* **105,** 14686–14691 (2008).

99. Gill, J. K. *et al.* Agonist activation of $\alpha7$ nicotinic acetylcholine receptors via an allosteric transmembrane site. *Proceedings of the National Academy of Sciences of the United States of America* **108,** 5867–5872 (2011).

100. John Mihic, S. *et al.* Sites of alcohol and volatile anaesthetic action on GABA(A) and glycine receptors. *Nature* **389,** 385–389 (1997).

101. Laverty, D. *et al.* Crystal structures of a GABA A -receptor chimera reveal new endogenous neurosteroid-binding sites. *Nature Structural and Molecular Biology* **24,** 977–985 (2017).

102. Hamouda, A. K. *et al.* Physostigmine and galanthamine bind in the presence of agonist at the canonical and noncanonical subunit interfaces of a nicotinic acetylcholine receptor. *Journal of Neuroscience* **33,** 485–494 (2013).

103. Chiara, D. C. *et al.* Identification of amino acids in the nicotinic acetylcholine receptor agonist binding site and ion channel photolabeled by 4-[(3-trifluoromethyl)-3H-diazirin-3-yl] benzoylcholine, a novel photoaffinity antagonist. *Biochemistry* **42,** 271–283 (2003).

104. Chiara, D. C. *et al.* [3H]chlorpromazine photolabeling of the Torpedo nicotinic acetylcholine receptor identifies two state-dependent binding sites in the ion channel. *Biochemistry* **48,** 10066–10077 (2009).

105. Kapur, A. *et al.* Tryptophan 86 of the alpha subunit in the Torpedo nicotinic acetylcholine receptor is important for channel activation by the bisquaternary ligand suberyldicholine. *Biochemistry* **45,** 10337–10343 (2006).

106. Husain, S. S. *et al.* P-trifluoromethyldiazirinyl-etomidate: A potent photoreactive general anesthetic derivative of etomidate that is selective for ligand-gated cationic ion channels. *Journal of Medicinal Chemistry* **53,** 6432–6444 (2010).

107. Hamouda, A. K. *et al.* Multiple transmembrane binding sites for p-trifluoromethyldiazirinyl-etomidate, a photoreactive Torpedo nicotinic acetylcholine receptor allosteric inhibitor. *Journal of Biological Chemistry* **286,** 20466–20477 (2011).

108. Tapper, A. R. *et al.* Nicotine Activation of alpha4* Receptors: Sufficient for Reward, Tolerance, and Sensitization. *Science* **306,** 1029–1032 (2004).

109. Henderson, B. J. *et al.* Structure-activity relationship studies of sulfonylpiperazine analogues as novel negative allosteric modulators of human neuronal nicotinic receptors. *Journal of Medicinal Chemistry* **54,** 8681–8692 (2011).

110. Henderson, B. J. *et al.* Defining the putative inhibitory site for a selective negative allosteric modulator of human $\alpha4\beta2$ neuronal nicotinic receptors. *ACS Chemical Neuroscience* **3,** 682–692 (2012).

111. Henderson, B. J. *et al.* Negative allosteric modulators that target human $\alpha4\beta2$ neuronal nicotinic receptors. *Journal of Pharmacology and Experimental Therapeutics* **334,** 761–774 (2010).

112. Rego Campello, H. *et al.* Unlocking Nicotinic Selectivity via Direct C-H Functionalization of (-)-Cytisine. *Chem* **4,** 1710–1725 (2018).

113. Jahn, K. *et al.* Deactivation and desensitization of mouse embryonic- and adult-type nicotinic receptor channel currents. *Neuroscience Letters* **307,** 89–92 (2001).

114. Winegar, B. D. Potency of agonists and competitive antagonists on adult- and fetal-type nicotinic acetylcholine receptors. *Cellular and Molecular Neurobiology* **17,** 35–50 (1997).

115. Villarroel, A. & Sakmann, B. Calcium permeability increase of endplate channels in rat muscle during postnatal development. *Journal of Physiology* **496,** 331–338 (1996).

116. Haeger, S. *et al.* An intramembrane aromatic network determines pentameric assembly of Cys-loop receptors. *Nature Structural and Molecular Biology* **17,** 90–99 (2010).

117. Kreienkamp, H. J. *et al.* Intersubunit contacts governing assembly of the mammalian nicotinic acetylcholine receptor. *Neuron* **14,** 635–644 (1995).

118. Kuhse, J. *et al.* Assembly of the inhibitory glycine receptor: Identification of amino acid sequence motifs governing subunit stoichiometry. *Neuron* **11,** 1049–1056 (1993).

119. Greger, I. H. *et al.* Molecular determinants of glycine receptor subunit assembly. *The EMBO Journal* **18,** 4711–4721 (1999).

120. Beeson, D. Congenital myasthenic syndromes: Recent advances. *Current Opinion in Neurology* **29,** 565–571 (2016).

121. Engel, A. G. *Rosenberg's Molecular and Genetic Basis of Neurological and Psychiatric Disease* **2,** 539–555 (2020).

122. Cossins, J. *et al.* A mouse model of AChR deficiency syndrome with a phenotype reflecting the human condition. *Human Molecular Genetics* **13,** 2947–2957 (2004).

123. Shen, X. M. *et al.* Highly fatal fast-channel syndrome caused by AChR ϵ subunit mutation at the agonist binding site. *Neurology* **79,** 449–454 (2012).

124. Croxen, R. *et al.* Recessive inheritance and variable penetrance of slow-channel congenital myasthenic syndromes. *Neurology* **59,** 162–168 (2002).

125. Engel, A. G. *et al.* New mutations in acetylcholine receptor subunit genes reveal heterogeneity in the slow-channel congenital myasthenic syndrome. *Human Molecular Genetics* **5,** 1217–1227 (1996).

126. Wang, H. L. *et al.* Mutation in the M1 domain of the acetylcholine receptor α subunit decreases the rate of agonist dissociation. *Journal of General Physiology* **109,** 757–766 (1997).

127. Milone, M. *et al.* Slow-channel myasthenie syndrome caused by enhanced activation and agonist binding affinity due to mutation in the M2 domain of the ACHR α subunit. *Italian Journal of Neurological Sciences* **18,** 24 (1997).

128. Navedo, M. F. *et al.* Novel beta subunit mutation causes a slow-channel syndrome by enhancing activation and decreasing the rate of agonist dissociation. *Mol Cell Neurosci.* **32,** 82–90 (2006).

129. Gomez, C. M. *et al.* Novel Delta Subunit Mutation in Slow-Channel Syndrome Causes Severe Weakness by Novel Mechanisms HHS Public Access Author manuscript. *Ann Neurol* **51,** 102–112 (2002).

130. Ohno, K. *et al.* Congenital myasthenic syndrome caused by decreased agonist binding affinity due to a mutation in the acetylcholine receptor ϵ subunit. *Neuron* **17,** 157–170 (1996).

131. Brownlow, S. *et al.* Acetylcholine receptor δ subunit mutations underlie a fast-channel myasthenic syndrome and arthrogryposis multiplex congenita. *Journal of Clinical Investigation* **108,** 125–130 (2001).

132. Shen, X. M. *et al.* Mutation causing severe myasthenia reveals functional asymmetry of AChR signature cystine loops in agonist binding and gating. *Journal of Clinical Investigation* **111,** 497–505 (2003).

133. Webster, R. *et al.* Mutation in the AChR ion channel gate underlies a fast channel congenital myasthenic syndrome. *Neurology* **62,** 1090–1096 (2004).

134. Milone, M. *et al.* Mode switching kinetics produced by a naturally occurring mutation in the cytoplasmic loop of the human acetylcholine receptor ϵ subunit. *Neuron* **20,** 575–588 (1998).

135. Wang, H. L. *et al.* Fundamental gating mechanism of nicotinic receptor channel revealed by mutation causing a congenital myasthenic syndrome. *Journal of General Physiology* **116,** 449–460 (2000).

136. Müller, J. S. *et al.* CHRND mutation causes a congenital myasthenic syndrome by impairing co-clustering of the acetylcholine receptor with rapsyn. *Brain* **129,** 2784–2793 (2006).

137. Abicht, A. *et al.* A common mutation (epsilon1267delG) in congenital myasthenic patients of Gypsy ethnic origin. *Neurology* **53,** 1564–1569 (1999).

138. Ohno, K. *et al.* Congenital myasthenic syndromes due to heteroallelic nonsense/missense mutations in the acetylcholine receptor ϵ subunit gene: Identification and functional characterization of six new mutations. *Human Molecular Genetics* **6,** 753–766 (1997).

139. Eddleston, M. Poisoning by pesticides. *Medicine (United Kingdom)* **48,** 214–217 (2020).

140. Wood, S. J. & R. Slater, C. Safety factor at the neuromuscular junction. *Progress in Neurobiology* **64,** 393–429 (2001).

141. Sussman, J. L. & Silman, I. Acetylcholinesterase: structure and use as a model for specific cation-protein interactions. *Current Opinion in Structural Biology* **2,** 721–729 (1992).

142. Hörnberg, A. *et al.* Crystal structures of acetylcholinesterase in complex with organophosphorus compounds suggest that the acyl pocket modulates the aging reaction by precluding the formation of the trigonal bipyramidal transition state. *Biochemistry* **46,** 4815–4825 (2007).

143. Millard, C. B. *et al.* Crystal structures of aged phosphonylated acetylcholinesterase: Nerve agent reaction products at the atomic level. *Biochemistry* **38,** 7032–7039 (1999).

144. Shafferman, A. *et al.* Mutagenesis of human acetylcholinesterase. Identification of residues involved in catalytic activity and in polypeptide folding. *Journal of Biological Chemistry* **267,** 17640–17648 (1992).

145. Sussman, J. L. *et al.* Atomic structure of acetylcholinesterase from Torpedo californica: A prototypic acetylcholine-binding protein. *Science* **253,** 872–879 (1991).

146. Quinn, D. M. *et al.* Delineation and decomposition of energies involved in quaternary ammonium binding in the active site of acetylcholinesterase. *Journal of the American Chemical Society* **122,** 2975–2980 (2000).

147. Bazelyansky, M. *et al.* Fractional Diffusion-Limited Component of Reactions Catalyzed by Acetylcholinesterase. *Biochemistry* **25,** 125–130 (1986).

148. Sirin, G. S. & Zhang, Y. How is acetylcholinesterase phosphonylated by Soman? An ab initio QM/MM molecular dynamics study. *Journal of Physical Chemistry A* **118,** 9132–9139 (2014).

149. Love, A. H. *et al.* Investigating the affinities and persistence of VX nerve agent in environmental matrices. *Chemosphere* **57,** 1257–1264 (2004).

150. Nagao, M. *et al.* Definitive evidence for the acute sarin poisoning diagnosis in the Tokyo subway. *Toxicology and Applied Pharmacology* **144,** 198–203 (1997).

151. Nozaki, H. *et al.* A case of VX poisoning and the difference from sarin. *The Lancet* **346,** 698–699 (1995).

152. Okudera, H. Clinical features on nerve gas terrorism in Matsumoto. *Journal of Clinical Neuroscience* **9,** 17–21 (2002).

153. Macilwain, C. Study proves iraq used nerve gas. *Nature* **363,** 3 (1993).

154. Newmark, J. The birth of nerve agent warfare: Lessons from Syed Abbas Foroutan. *Neurology* **62,** 1590–1596 (2004).

155. Nakagawa, T. & Tu, A. T. Murders with VX: Aum Shinrikyo in Japan and the assassination of Kim Jong-Nam in Malaysia. *Forensic Toxicology* **36,** 542–544 (2018).

156. Vale, J. A. *et al.* Novichok: a murderous nerve agent attack in the UK. *Clinical Toxicology* **56,** 1093–1097 (2018).

157. Maxwell, D. M. *et al.* A structure-activity analysis of the variation in oxime efficacy against nerve agents. *Toxicology and Applied Pharmacology* **231,** 157–164 (2008).

158. Heilbronn, E. In vitro reactivation and "ageing" of Tabun-inhibited blood cholinesterases. **12,** 25–36 (1963).

159. Worek, F. *et al.* Kinetic analysis of interactions between human acetylcholinesterase, structurally different organophosphorus compunds and oximes. *Biochemical Pharmacology* **68,** 2237–2248 (2004).

160. Masson, P. *et al.* Structural approach to the aging of phosphylated cholinesterases. *Chemico-Biological Interactions* **187,** 157–162 (2010).

161. Shafferman, A. *et al.* Aging of phosphylated human acetylcholinesterase: Catalytic processes mediated by aromatic and polar residues of the active centre. *Biochemical Journal* **318,** 833–840 (1996).

162. Barak, D. *et al.* Carbocation-mediated processes in biocatalysts. Contribution of aromatic moieties. *Journal of the American Chemical Society* **119,** 3157–3158 (1997).

163. Shafferman, A. *et al.* Aging of phosphylated human acetylcholinesterase: Catalytic processes mediated by aromatic and polar residues of the active centre. *Biochemical Journal* **318,** 833–840 (1996).

164. Masson, P. & Nachon, F. Cholinesterase reactivators and bioscavengers for pre- and post-exposure treatments of organophosphorus poisoning. *Journal of Neurochemistry* **142,** 26–40 (2017).

165. Wilson, I. B. & Ginsburg, S. A powerful reactivator of alkylphosphate-inhibited acetylcholinesterase. *BBA - Biochimica et Biophysica Acta* **18,** 168–170 (1955).

166. Worek, F. *et al.* Recent advances in evaluation of oxime efficacy in nerve agent poisoning by in vitro analysis. *Toxicology and Applied Pharmacology* **219,** 226–234 (2007).

167. Wilson, I. B. & Ginsburg, S. Reactivation of alkylphosphate inhibited acetylcholinesterase by bis quaternary derivatives of 2-PAM and 4-PAM. *Biochemical Pharmacology* **1,** 200–206 (1959).

168. Ekström, F. J. *et al.* Novel nerve-agent antidote design based on crystallographic and mass spectrometric analyses of tabun-conjugated acetylcholinesterase in complex with antidotes. *Clinical Pharmacology and Therapeutics* **82,** 282–293 (2007).

169. Hörnberg, A. *et al.* Crystal structures of oxime-bound fenamiphos-acetylcholinesterases: Reactivation involving flipping of the His447 ring to form a reactive Glu334-His447-oxime triad. *Biochemical Pharmacology* **79,** 507–515 (2010).

170. Giacoppo, J. O. *et al.* Molecular modeling and in vitro reactivation study between the oxime BI-6 and acetylcholinesterase inhibited by different nerve agents. *Journal of Biomolecular Structure and Dynamics* **33,** 2048–2058 (2015).

171. Cabal, J. *et al.* Specification of the structure of oximes able to reactivate tabun-inhibited acetylcholinesterase. *Basic and Clinical Pharmacology and Toxicology* **95,** 81–86 (2004).

172. Shih, T. M. *et al.* Control of nerve agent-induced seizures is critical for neuroprotection and survival. *Toxicology and Applied Pharmacology* **188,** 69–80 (2003).

173. Shih, T. M. *et al.* Anticonvulsants for nerve agent-induced seizures: The influence of the therapeutic dose of atropine. *Journal of Pharmacology and Experimental Therapeutics* **320,** 154–161 (2007).

174. Capacio, B. R. & Shih, T. Anticonvulsant Actions of Anticholinergic Drugs in Soman Poisoning. *Epilepsia* **32,** 604–615 (1991).

175. Maxwell, D. M. The specificity of carboxylesterase protection against the toxicity of organophosphorus compounds. *Toxicology and Applied Pharmacology* **114,** 306–312 (1992).

176. Zapolski. Differential sensitivity of plasma carboxylesterase-null mice to parathion, chlorpyrifos and chlorpyrifos oxon, but not to diazinon, dichlorvos, diisopropylfluorophosphate, cresyl saligenin phosphate, cyclosarin thiocholine, tabun thiocholine, and carbofu. *Bone* **23,** 1–7. arXiv: `NIHMS150003` (2008).

177. Grob, B. D. & Harvey, J. C. Effects in man of the anticholinesterase compound sarin (isopropyl methyl phophonofluoridate). *J Clin Invest* **37,** 350–368 (1957).

178. Lockridge, O. *et al.* Naturally Occurring Genetic Variants of Human Acetylcholinesterase and Butyrylcholinesterase and Their Potential Impact on the Risk of Toxicity from Cholinesterase Inhibitors. *Chemical Research in Toxicology* **29,** 1381–1392 (2016).

179. Saxena, A. *et al.* Prophylaxis with human serum butyrylcholinesterase protects guinea pigs exposed to multiple lethal doses of soman or VX. *Biochemical Pharmacology* **81,** 164–169 (2011).

180. Clark, M. G. *et al.* Effects of physostigmine and human butyrylcholinesterase on acoustic startle reflex and prepulse inhibition in C57BL/6J mice. *Pharmacology Biochemistry and Behavior* **81,** 497–505 (2005).

181. Novikov, B. N. *et al.* Improved pharmacokinetics and immunogenicity profile of organophosphorus hydrolase by chemical modification with polyethylene glycol. *Journal of Controlled Release* **146,** 318–325 (2010).

182. Trovaslet-Leroy, M. *et al.* Organophosphate hydrolases as catalytic bioscavengers of organophosphorus nerve agents. *Toxicology Letters* **206,** 14–23 (2011).

183. Wales, M. E. & Reeves, T. E. Organophosphorus hydrolase as an in vivo catalytic nerve agent bioscavenger. *Drug Testing and Analysis* **4,** 271–281 (2012).

184. Tattersall, J. E. Ion channel blockade by oximes and recovery of diaphragm muscle from soman poisoning in vitro. *British Journal of Pharmacology* **108,** 1006–1015 (1993).

185. Seeger, T. *et al.* Restoration of soman-blocked neuromuscular transmission in human and rat muscle by the bispyridinium non-oxime MB327 in vitro. *Toxicology* **294,** 80–84 (2012).

186. Kassa, J. *et al.* Evaluation of the benefit of the bispyridinium compound MB327 for the antidotal treatment of nerve agent-poisoned mice. *Toxicology Mechanisms and Methods* **26,** 334–339 (2016).

187. Niessen, K. V. *et al.* In vitro pharmacological characterization of the bispyridinium non-oxime compound MB327 and its 2- and 3-regioisomers. *Toxicology Letters* **293,** 190–197 (2018).

188. Scheffel, C. *et al.* Counteracting desensitization of human α7-nicotinic acetylcholine receptors with bispyridinium compounds as an approach against organophosphorus poisoning. *Toxicology Letters* **293,** 149–156 (2018).

189. Königer, C. *et al.* Effect of MB327 and oximes on rat intestinal smooth muscle function. *Chemico-Biological Interactions* **204,** 1–5 (2013).

190. Turner, S. R. *et al.* Protection against nerve agent poisoning by a noncompetitive nicotinic antagonist. *Toxicology Letters* **206,** 105–111 (2011).

191. Timperley, C. M. *et al.* 1,1'-(Propane-1,3-diyl)bis(4-tert-butylpyridinium) di(methanesulfonate) protects guinea pigs from soman poisoning when used as part of a combined therapy. *MedChemComm* **3,** 352–356 (2012).

192. Kassa, J. *et al.* Some benefit from non-oximes MB408, MB442 and MB444 in combination with the oximes HI-6 or obidoxime and atropine in antidoting sarin or cyclosarin poisoned mice. *Toxicology* **408,** 95–100 (2018).

193. Niessen, K. V. *et al.* Affinities of bispyridinium non-oxime compounds to [3H] epibatidine binding sites of Torpedo californica nicotinic acetylcholine receptors depend on linker length. *Chemico-Biological Interactions* **206,** 545–554 (2013).

194. Niessen, K. V. *et al.* Interaction of bispyridinium compounds with the orthosteric binding site of human $\alpha 7$ and Torpedo californica nicotinic acetylcholine receptors (nAChRs). *Toxicology Letters* **206,** 100–104 (2011).

195. Ring, A. *et al.* Bispyridinium compounds inhibit both muscle and neuronal nicotinic acetylcholine receptors in human cell lines. *PLoS ONE* **10** (2015).

196. Wein, T. *et al.* Searching for putative binding sites of the bispyridinium compound MB327 in the nicotinic acetylcholine receptor. *Toxicology Letters* **293,** 184–189 (2018).

197. Kontoyianni, M. *et al.* Evaluation of Docking Performance: Comparative Data on Docking Algorithms. *Journal of Medicinal Chemistry* **47,** 558–565 (2004).

198. Mnatsakanyan, N. & Jansen, M. Experimental determination of the vertical alignment between the second and third transmembrane segments of muscle nicotinic acetylcholine receptors. *Journal of Neurochemistry* **125,** 843–854 (2013).

199. Sheridan, R. D. *et al.* Nicotinic antagonists in the treatment of nerve agent intoxication. *Journal of the Royal Society of Medicine* **98,** 114–115 (2005).

200. Price, M. E. *et al.* Pharmacokinetic profile and quantitation of protection against soman poisoning by the antinicotinic compound MB327 in the guinea-pig. *Toxicology Letters* **244,** 154–160 (2016).

201. Leach, A. R. *Molecular modelling: principles and applications* 2nd Editio (Pearson Education Limited, 2001).

202. Bayly, C. I. *et al.* A Second Generation Force Field for the Simulation of Proteins, Nucleic Acids, and Organic Molecules. *Journal of the American Chemical Society* **117,** 5179–5197 (1995).

203. MacKerell, A. D. *et al.* All-atom empirical potential for molecular modeling and dynamics studies of proteins. *Journal of Physical Chemistry B* **102,** 3586–3616 (1998).

204. Kaminski, G. A. *et al.* Evaluation and reparametrization of the OPLS-AA force field for proteins via comparison with accurate quantum chemical calculations on peptides. *Journal of Physical Chemistry B* **105,** 6474–6487 (2001).

205. Lindorff-Larsen, K. *et al.* Systematic validation of protein force fields against experimental data. *PLoS ONE* **7,** 1–6 (2012).

206. Jämbeck, J. P. & Lyubartsev, A. P. Derivation and systematic validation of a refined all-atom force field for phosphatidylcholine lipids. *Journal of Physical Chemistry B* **116,** 3164–3179 (2012).

207. Wang, J. M. *et al.* Development and testing of a general amber force field. *J. Comput. Chem.* **25,** 1157–1174. arXiv: z0024 (2004).

208. Jämbeck, J. P. & Lyubartsev, A. P. An extension and further validation of an all-atomistic force field for biological membranes. *Journal of Chemical Theory and Computation* **8,** 2938–2948 (2012).

209. Hess, B. P-LINCS: A parallel linear constraint solver for molecular simulation. *Journal of Chemical Theory and Computation* **4,** 116–122 (2008).

210. Darden, T. *et al.* Particle mesh Ewald: An N · log(N) method for Ewald sums in large systems. *The Journal of Chemical Physics* **98,** 10089–10092 (1993).

211. Nosé, S. A molecular dynamics method for simulations in the canonical ensemble. *Molecular Physics* **52,** 255–268 (1984).

212. Hoover, W. G. Canonical dynamics: Equilibrium phase-space distributions. *Physical Review A* **31,** 1695–1697 (1985).

213. Bussi, G. *et al.* Canonical sampling through velocity rescaling. *Journal of Chemical Physics* **126** (2007).

214. Parrinello, M. & Rahman, A. Polymorphic transitions in single crystals: A new molecular dynamics method. *Journal of Applied Physics* **52,** 7182–7190 (1981).

215. Berendsen, H. J. *et al.* Molecular dynamics with coupling to an external bath. *The Journal of Chemical Physics* **81,** 3684–3690 (1984).

216. Rost, B. Twilight zone of protein sequence alignments. *Protein Engineering* **12,** 85–94 (1999).

217. Sali, A. & Blundell, T. Sali, A. & Blundell, T. L. Comparative modelling by satisfaction of spatial restraints. J. Mol. Biol. 234, 779-815. *Journal of molecular biology* **234,** 779–815 (1994).

218. Fiser, A. & Sali, A. Modeling of loops in protein structures. *Protein Science* **9,** 1753–1773 (2000).

219. Trott, O. & J. Olson, A. Autodock vina: improving the speed and accuracy of docking. *Journal of Computational Chemistry* **31,** 455–461 (2010).

220. Gasteiger, J. & Marsili, M. A new model for calculating atomic charges in molecules. *Tetrahedron Letters* **19,** 3181–3184 (1978).

221. Goodsell, D. S. & Olson, A. J. Automated docking of substrates to proteins by simulated annealing. *Proteins: Structure, Function, and Bioinformatics* **8,** 195–202 (1990).

222. Salomon-Ferrer, R. *et al.* An overview of the Amber biomolecular simulation package. *Wiley Interdisciplinary Reviews: Computational Molecular Science* **3,** 198–210 (2013).

223. Wang, J. *et al.* Automatic atom type and bond type perception in molecular mechanical calculations. *Journal of Molecular Graphics and Modelling* **25,** 247–260 (2006).

224. Sousa Da Silva, A. W. & Vranken, W. F. ACPYPE - AnteChamber PYthon Parser interfacE. *BMC Research Notes* **5,** 1–8 (2012).

225. M, T. G. & Valleau, J. Nonphysical Sampling Distributions in Monte Carlo Free-Energy Estimation: Umbrella Sampling. *J. Comput. Phys.* **23,** 187 (1977).

226. Roux, B. The calculation of the potential of mean force using computer simulations. *Computer Physics Communications* **91,** 275–282 (1995).

227. Kumar, S. *et al.* The weighted histogram analysis method for free-energy calculations on biomolecules. *Journal of Computational Chemistry* **13,** 1011–1021 (1992).

228. Heckman, K. L. & Pease, L. R. Gene splicing and mutagenesis by PCR-driven overlap extension. *Nature Protocols* **2,** 924–932 (2007).

229. Costanzi, S. *et al.* Nerve Agents: What They Are, How They Work, How to Counter Them. *ACS Chemical Neuroscience* **9,** 873–885 (2018).

230. Sirin, G. S. & Zhang, Y. How is acetylcholinesterase phosphonylated by Soman? An ab initio QM/MM molecular dynamics study. *Journal of Physical Chemistry A* **118,** 9132–9139 (2014).

231. Chandar, N. B. & Ganguly, B. A first principles investigation of aging processes in soman conjugated AChE. *Chemico-Biological Interactions* **204,** 185–190 (2013).

232. Massoulié, J. *et al.* Molecular and cellular biology of cholinesterases. *Progress in Neurobiology* **41,** 31–91 (1993).

233. Hulse, E. J. *et al.* Respiratory complications of organophosphorus nerve agent and insecticide poisoning: Implications for respiratory and critical care. *American Journal of Respiratory and Critical Care Medicine* **190,** 1342–1354 (2014).

234. Harrison, P. K. *et al.* A guinea pig hippocampal slice model of organophosphate-induced seizure activity. *Journal of Pharmacology and Experimental Therapeutics* **310,** 678–686 (2004).

235. Marrs, T. C. The role of diazepam in the treatment of nerve agent poisoning in a civilian population. *Toxicological Reviews* **23,** 145–157 (2004).

236. Tang, X. *et al.* Reaction pathway for reactivation and aging of paraoxon-inhibited-acetylcholinesterase: A QM/MM study. *Computational and Theoretical Chemistry* **1035,** 44–50 (2014).

237. Carletti, E. *et al.* Structural evidence that human acetylcholinesterase inhibited by tabun ages through O-dealkylation. *Journal of Medicinal Chemistry* **53,** 4002–4008 (2010).

238. Sirin, G. S. *et al.* Aging mechanism of soman inhibited acetylcholinesterase. *Journal of Physical Chemistry B* **116,** 12199–12207 (2012).

239. Sanson, B. *et al.* Crystallographic snapshots of nonaged and aged conjugates of soman with acetylcholinesterase, and of a ternary complex of the aged conjugate with pralidoxime. *Journal of Medicinal Chemistry* **52,** 7593–7603 (2009).

240. Bajgar, J. *et al.* Treatment of Organophosphate Intoxication Using Cholinesterase Reactivators:Facts and Fiction. *Mini-Reviews in Medicinal Chemistry* **7,** 461–466 (2007).

241. Tattersall, J. E. Ion channel blockade by oximes and recovery of diaphragm muscle from soman poisoning in vitro. *British Journal of Pharmacology* **108,** 1006–1015 (1993).

242. Niessen, K. V. *et al.* Affinities of bispyridinium non-oxime compounds to [3H] epibatidine binding sites of Torpedo californica nicotinic acetylcholine receptors depend on linker length. *Chemico-Biological Interactions* **206,** 545–554 (2013).

243. Lynagh, T. & Pless, S. A. Principles of agonist recognition in Cys-loop receptors. *Frontiers in Physiology* **5,** 1–12 (2014).

244. Zhong, W. *et al.* From ab initio quantum mechanics to molecular neurobiology: A cation-π binding site in the nicotinic receptor. *Proceedings of the National Academy of Sciences of the United States of America* **95,** 12088–12093 (1998).

245. Beene, D. L. *et al.* Cation-π interactions in ligand recognition by serotonergic (5-HT3A) and nicotinic acetylcholine receptors: The anomalous binding properties of nicotine. *Biochemistry* **41,** 10262–10269 (2002).

246. Pless, S. A. *et al.* A cation-π interaction at a phenylalanine residue in the glycine receptor binding site is conserved for different agonists. *Molecular Pharmacology* **79,** 742–748 (2011).

247. Gharpure, A. *et al.* Agonist Selectivity and Ion Permeation in the $\alpha 3\beta 4$ Ganglionic Nicotinic Receptor. *Neuron* **104,** 501–511.e6 (2019).

248. Ma, Q. *et al.* Exploring the Relationship between Nicotinic Acetylcholine Receptor Ligand Size, Efficiency, Efficacy, and C-Loop Opening. *Journal of Chemical Information and Modeling* **57,** 1947–1956 (2017).

249. Webb, B. & Sali, A. Comparative protein structure modeling using MODELLER. *Current Protocols in Bioinformatics* **2014,** 5.6.1–5.6.32 (2014).

250. Morris, G. & Huey, R. AutoDock4 and AutoDockTools4: Automated docking with selective receptor flexibility. *Journal of ...* **30,** 2785–2791 (2009).

251. Kandt, C. *et al.* Setting up and running molecular dynamics simulations of membrane proteins. *Methods* **41,** 475–488 (2007).

252. Jorgensen, W. L. *et al.* Comparison of simple potential functions for simulating liquid water. *The Journal of Chemical Physics* **79,** 926–935 (1983).

253. Darden, T. *et al.* Particle mesh Ewald: An N · log(N) method for Ewald sums in large systems. *The Journal of Chemical Physics* **98,** 10089–10092 (1993).

254. Hess, B. P-LINCS: A parallel linear constraint solver for molecular simulation. *Journal of Chemical Theory and Computation* **4,** 116–122 (2008).

255. Lindorff-Larsen, K. *et al.* Improved side-chain torsion potentials for the Amber ff99SB protein force field. *Proteins: Structure, Function and Bioinformatics* **78,** 1950–1958 (2010).

256. Berendsen, H. J. *et al.* Molecular dynamics with coupling to an external bath. *The Journal of Chemical Physics* **81,** 3684–3690 (1984).

257. You, A. *et al.* The Nose–Hoover thermostat. *Journal of Chemical Physics* **4069** (2007).

258. Parrinello, M. & Rahman, A. Polymorphic transitions in single crystals: A new molecular dynamics method. *Journal of Applied Physics* **52,** 7182–7190 (1981).

259. Mallipeddi, P. L. *et al.* Interactions of acetylcholine binding site residues contributing to nicotinic acetylcholine receptor gating: Role of residues Y93, Y190, K145 and D200. *Journal of Molecular Graphics and Modelling* **44,** 145–154 (2013).

260. Morales-Perez, C. L. *et al.* X-ray structure of the human $\alpha4\beta2$ nicotinic receptor. *Nature* **538,** 411–415 (2016).

261. Ma, Q. *et al.* Exploring the Relationship between Nicotinic Acetylcholine Receptor Ligand Size, Efficiency, Efficacy, and C-Loop Opening. *Journal of Chemical Information and Modeling* **57,** 1947–1956 (2017).

262. Taly, A. *et al.* Discrimination of agonists versus antagonists of nicotinic ligands based on docking onto AChBP structures. *Journal of Molecular Graphics and Modelling* **30,** 100–109 (2011).

263. Blaber, L. C. & Bowman, W. C. Studies on the Repetitive Discharges Evoked in Motor Nerve and Skeletal Muscle After Injection of Anticholinesterase Drugs. *British Journal of Pharmacology and Chemotherapy* **20,** 326–344 (1963).

264. Timperley, C. M. & Tattersall, J. *Best Synthetic Methods: Organophosphorus (V) Chemistry* **V,** 1–89 (Elsevier Ltd, 2014).

265. Khan, H. M. *et al.* Improving the Force Field Description of Tyrosine-Choline Cation-π Interactions: QM Investigation of Phenol-N(Me)4+ Interactions. *Journal of Chemical Theory and Computation* **12,** 5585–5595 (2016).

266. Rupakheti, C. R. *et al.* Modeling induction phenomena in amino acid cation–π interactions. *Theoretical Chemistry Accounts* **137,** 1–6 (2018).

267. Gupta, S. *et al.* A mechanism for acetylcholine receptor gating based on structure, coupling, phi, and flip. *Journal of General Physiology* **149,** 85–103 (2016).

268. Purohit, P. & Auerbach, A. Unliganded gating of acetylcholine receptor channels. *Proceedings of the National Academy of Sciences of the United States of America* **106,** 115–120 (2009).

269. Ohkawara, B. *et al.* Congenital myasthenic syndrome–associated agrin variants affect clustering of acetylcholine receptors in a domain-specific manner. *JCI Insight* **5** (2020).

270. Webster, R. *et al.* A novel congenital myasthenic syndrome due to decreased acetylcholine receptor ion-channel conductance. *Brain* **135,** 1070–1080 (2012).

271. Engel, A. G. *et al.* A newly recognized congenital myasthenic syndrome attributed to a prolonged open time of the acetylcholine-induced ion channel. *Annals of Neurology* **11,** 553–569 (1982).

272. Unwin, N. & Fujiyoshi, Y. Gating movement of acetylcholine receptor caught by plunge-freezing. *Journal of Molecular Biology* **422,** 617–634 (2012).

273. Beckstein, O. *et al.* A hydrophobic gating mechanism for nanopores. *Journal of Physical Chemistry B* **105,** 12902–12905 (2001).

274. Miller, C. Genetic manipulation of ion channels: A new approach to structure and mechanism. *Neuron* **2,** 1195–1205 (1989).

275. Adams, D. J. *et al.* The permeability of endplate channels to monovalent and divalent metal cations. *Journal of General Physiology* **75,** 493–510 (1980).

276. Cymesa, G. D. & Grosman, C. Identifying the elusive link between amino acid sequence and charge selectivity in pentameric ligand-gated ion channels. *Proceedings of the National Academy of Sciences of the United States of America* **113,** 7106–7115 (2016).

277. Harpole, T. J. & Grosman, C. A Crucial Role for Side-Chain Conformation in the Versatile Charge Selectivity of Cys-Loop Receptors. *Biophysical Journal* **116,** 1667–1681 (2019).

278. Ivanov, I. *et al.* Barriers to ion translocation in cationic and anionic receptors from the cys-loop family. *Journal of the American Chemical Society* **129,** 8217–8224 (2007).

279. Corringer, P. J. *et al.* Mutational analysis of the charge selectivity filter of the α7 nicotinic acetylcholine receptor. *Neuron* **22,** 831–843 (1999).

280. Gunthorpe, M. J. & Lummis, S. C. Conversion of the Ion Selectivity of the 5-HT3A Receptor from Cationic to Anionic Reveals a Conserved Feature of the Ligand-gated Ion Channel Superfamily. *Journal of Biological Chemistry* **276,** 10977–10983 (2001).

281. Keramidas, A. *et al.* M2 pore mutations convert the glycine receptor channel from being anion- to cation-selective. *Biophysical Journal* **79,** 247–259 (2000).

282. Leite, M. I. *et al.* IgG1 antibodies to acetylcholine receptors in 'seronegative' myasthenia gravis. *Brain* **131,** 1940–1952 (2008).

283. Du, J. *et al.* Glycine receptor mechanism elucidated by electron cryo-microscopy. *Nature* **526,** 224–229 (2015).

284. Klesse, G. *et al.* CHAP: A Versatile Tool for the Structural and Functional Annotation of Ion Channel Pores. *Journal of Molecular Biology* **431,** 3353–3365 (2019).

285. Beckstein, O. & Sansom, M. S. The influence of geometry, surface character, and flexibility on the permeation of ions and water through biological pores. *Physical Biology* **1,** 42–52 (2004).

286. Aryal, P. *et al.* Hydrophobic gating in ion channels. *Journal of Molecular Biology* **427,** 121–130 (2015).

287. Trick, J. L. *et al.* Designing a hydrophobic barrier within biomimetic nanopores. *ACS Nano* **8,** 11268–11279 (2014).

288. Revah, F. *et al.* Mutations in the channel domain alter desensitization of a neuronal nicotinic receptor. *Nature* **353,** 846–849 (1991).

289. Labarca, C. *et al.* Channel gating governed symmetrically by conserved leucine residues in the M2 domain of nicotinic receptors. *Nature* **376,** 514–516 (1995).

290. Filatov, G. N. & White, M. M. The role of conserved leucines in the M2 domain of the acetylcholine receptor in channel gating. *Molecular Pharmacology* **48,** 379–384 (1995).

291. Forster, I. *et al.* Inward Rectification of Neuronal Nicotinic Acetylcholine Receptors Investigated by Using the Homomeric α 7 Receptor Stable. **260,** 139–148 (1995).

292. Mathie, A. *et al.* Rectification of currents activated by nicotinic acetylcholine receptors in rat sympathetic ganglion neurones. *The Journal of Physiology* **427,** 625–655 (1990).

293. Steven, B. Y. *et al.* Neuronal Nicotinic Acetylcholine Receptor Currents in Phaeochromocytome (PC12) Cells: Dual Mechanisms of Rectification. **447,** 467–487 (1992).

294. Haghighi, A. P. & Cooper, E. Neuronal nicotinic acetylcholine receptors are blocked by intracellular spermine in a voltage-dependent manner. *Journal of Neuroscience* **18,** 4050–4062 (1998).

295. Webster, R. *et al.* Mutation in the AChR ion channel gate underlies a fast channel congenital myasthenic syndrome. *Neurology* **62,** 1090–1096 (2004).

296. Wood, S. J. & Slater, C. R. Action potential generation in rat slow- and fast-twitch muscles. *The Journal of Physiology* **486,** 401–410 (1995).

297. Cull-Candy, S. G. *et al.* On the release of transmitter at normal, myasthenia gravis and myasthenic syndrome affected human end-plates. *The Journal of Physiology* **299,** 621–638 (1980).

298. Molenaar, P. C. *et al.* Effect of ephedrine on muscle weakness in a model of myasthenia gravis in rats. *Neuropharmacology* **32,** 373–376 (1993).

299. Plomp, J. J. *et al.* Acetylcholine release in myasthenia gravis: Regulation at single end-plate level. *Annals of Neurology* **37,** 627–636 (1995).

300. Albuquerque, E. X. *et al.* Mammalian nicotinic acetylcholine receptors: From structure to function. *Physiological Reviews* **89,** 73–120 (2009).

301. Grudzinska, J. *et al.* The β subunit determines the ligand binding properties of synaptic glycine receptors. *Neuron* **45,** 727–739 (2005).

302. Zhong, W. From ab initio quantum mechanics to molecular neurobiology : A cation – pi binding site in the nicotinic receptor. *Proceedings of the National Academy of Sciences* **95,** 12088–12093 (1998).

303. Changeux, J. P. The nicotinic acetylcholine receptor: A typical 'allosteric machine'. *Philosophical Transactions of the Royal Society B: Biological Sciences* **373** (2018).

304. Wong, L. W. *et al.* Role of the ρ1 GABAC receptor N-terminus in assembly, trafficking and function. *ACS Chemical Neuroscience* **5,** 1266–1277 (2014).

305. Pandhare, A. *et al.* Triple arginines as molecular determinants for pentameric assembly of the intracellular domain of 5-HT3A receptors. *The Journal of general physiology* **151,** 1135–1145 (2019).

306. Blount, P. *et al.* Assembly intermediates of the mouse muscle nicotinic acetylcholine receptor in stably transfected fibroblasts. *Journal of Cell Biology* **111,** 2601–2611 (1990).

307. Gu, Y. *et al.* Identification of two amino acid residues in the epsilon subunit that promote mammalian muscle acetylcholine receptor assembly in COS cells. *Neuron* **6,** 879–887 (1991).

308. Saedi, M. S. *et al.* Assembly of Torpedo acetylcholine receptors in Xenopus oocytes. *Journal of Cell Biology* **112,** 1007–1015 (1991).

309. Merlie, J. P. & Lindstrom, J. Assembly in vivo of mouse muscle acetylcholine receptor: Identification of an α subunit species that may be an assembly intermediate. *Cell* **34,** 747–757 (1983).

310. Blount, P. & Merlie, J. P. Mutational analysis of muscle nicotinic acetylcholine receptor subunit assembly. *Journal of Cell Biology* **111,** 2613–2622 (1990).

311. Green, W. N. & Claudio, T. Acetylcholine receptor assembly: Subunit folding and oligomerization occur sequentially. *Cell* **74,** 57–69 (1993).

312. Yu, X.-m. & Hall, Z. W. Extracellular domains mediating epsilon subunit interactions of muscle acetylcholine receptor. **352,** 64–67 (1991).

313. Kullberg, R. & Owens, J. L. Multiple conductance classes of mouse nicotinic acetylcholine receptors in Xenopus oocytes. **87,** 2067–2071 (1990).

314. Jackson, M. B. *et al.* Spontaneous and agonist-induced openings of an acetylcholine receptor channel composed of bovine muscle α-, β and δ-subunits. *Pflügers Archiv European Journal of Physiology* **417,** 129–135 (1990).

315. Charnet, P. *et al.* Structure of the gamma-less nicotinic acetylcholine receptor: Learning from omission. *Molecular Pharmacology* **41,** 708–717 (1992).

316. Park, J. Y. *et al.* A single mutation in the acetylcholine receptor δ-subunit causes distinct effects in two types of neuromuscular synapses. *Journal of Neuroscience* **34,** 10211–10218 (2014).

317. Nicke, A. *et al.* Blue native page as a useful method for the analysis of the assembly of distinct combinations of nicotinic acetylcholine receptor subunits. *Journal of Receptor and Signal Transduction Research* **19,** 493–507 (1999).

318. Liu, B. Y. Y. & Brehm, P. Expression of Subunit-Omitted Mouse Nicotinic Acetylcholine Receptors in Xenopus Laevis Oocytes. *Journal of Physiology* **470,** 349–363 (1993).

319. Edgar, R. C. MUSCLE: Multiple sequence alignment with high accuracy and high throughput. *Nucleic Acids Research* **32,** 1792–1797 (2004).

320. Jorgensen, W. L. *et al.* Comparison of simple potential functions for simulating liquid water. *The Journal of Chemical Physics* **79,** 926–935 (1983).

321. Darden, T. *et al.* Particle mesh Ewald: An N $\cdot$ log(N) method for Ewald sums in large systems. *The Journal of Chemical Physics* **98,** 10089–10092 (1993).

322. Hess, B. P-LINCS: A parallel linear constraint solver for molecular simulation. *Journal of Chemical Theory and Computation* **4,** 116–122 (2008).

323. Jämbeck, J. P. M. & Lyubartsev, A. P. Derivation and systematic validation of a refined all-atom force field for phosphatidylcholine lipids. *Journal of Physical Chemistry B* **116,** 3164–3179 (2012).

324. Jämbeck, J. P. & Lyubartsev, A. P. Another piece of the membrane puzzle: Extending slipids further. *Journal of Chemical Theory and Computation* **9,** 774–784 (2013).

325. Jämbeck, J. P. & Lyubartsev, A. P. An extension and further validation of an all-atomistic force field for biological membranes. *Journal of Chemical Theory and Computation* **8,** 2938–2948 (2012).

326. Lindorff-Larsen, K. *et al.* Improved side-chain torsion potentials for the Amber ff99SB protein force field. *Proteins: Structure, Function and Bioinformatics* **78,** 1950–1958 (2010).

327. Berendsen, H. J. C. *et al.* Molecular dynamics with coupling to an external bath. *The Journal of Chemical Physics* **81,** 3684–3690 (1984).

328. Bussi, G. *et al.* Canonical sampling through velocity rescaling. *Journal of Chemical Physics* **126** (2007).

329. Parrinello, M. & Rahman, A. Polymorphic transitions in single crystals: A new molecular dynamics method. *Journal of Applied Physics* **52,** 7182–7190 (1981).

330. Monastyrskyy, B. *et al.* New encouraging developments in contact prediction: Assessment of the CASP11 results. *Proteins: Structure, Function and Bioinformatics* **84,** 131–144 (2015).

331. Naveen Michaud-Agrawal *et al.* Software News and Updates MDAnalysis: A Toolkit for the Analysis of Molecular Dynamics Simulations. *Journal of computational chemistry* **32,** 2319–2327 (2011).

332. Gowers, R. *et al.* MDAnalysis: A Python Package for the Rapid Analysis of Molecular Dynamics Simulations. *Proceedings of the 15th Python in Science Conference,* 98–105 (2016).

333. Terejko, K. *et al.* The C loop at the orthosteric binding site is critically involved in GABAA receptor gating. *Neuropharmacology* **166,** 107903 (2020).

334. Gleitsman, K. R. *et al.* An intersubunit hydrogen bond in the nicotinic acetylcholine receptor that contributes to channel gating. *Journal of Biological Chemistry* **283,** 35638–35643 (2008).

335. Griffon, N. *et al.* Molecular determinants of glycine receptor subunit assembly. *EMBO Journal* **18,** 4711–4721 (1999).

336. Brehm, P. & Henderson, L. Regulation of acetylcholine receptor channel function during development of skeletal muscle. *Developmental Biology* **129,** 1–11 (1988).

337. Hall, Z. W. & Sanes, J. R. Synaptic structure and development: The neuromuscular junction. *Cell* **72,** 99–121 (1993).

338. Chavez-Noriega, L. E. *et al.* Pharmacological characterization of recombinant human neuronal nicotinic acetylcholine receptors hα2β2, hα2β4, hα3β2, hα3β4, hα4β2, hα4β4 and hα7 expressed in xenopus oocytes. *Journal of Pharmacology and Experimental Therapeutics* **280,** 346–356 (1997).

339. Couturier, S. *et al.* alpha5, alpha3 and Non-alpha3: Three Clustered Avian Genes Encoding Neuronal Nicotinic Acetylcholine Receptor-Related Subunits. **265,** 17560–17567 (1990).

340. Gross, A. *et al.* Neuronal nicotinic acetylcholine receptors expressed in. *Journal of neurochemistry* **419,** 545–551 (1991).

341. Galzi, J. L. & Changeux, J. P. Neurotransmitter-gated ion channels as unconventional allosteric proteins. *Current Opinion in Structural Biology* **4,** 554–565 (1994).

342. Unwin, N. Refined structure of the nicotinic acetylcholine receptor at 4 Å resolution. *Journal of Molecular Biology* **346,** 967–989 (2005).

343. Rahman, M. M. *et al.* Structure of the Native Muscle-type Nicotinic Receptor and Inhibition by Snake Venom Toxins. *Neuron,* 1–11 (2020).

344. Le Novère, N. *et al.* The diversity of subunit composition in nAChRs: Evolutionary origins, physiologic and pharmacologic consequences. *Journal of Neurobiology* **53,** 447–456 (2002).

345. Kullberg, R. & Owens, J. L. Multiple conductance classes of mouse nicotinic acetylcholine receptors in Xenopus oocytes. **87,** 2067–2071 (1990).

346. Jansen, M. *et al.* Modular design of cys-loop ligand-gated ion channels: Functional 5-HT 3 and GABA ρ1 receptors lacking the large cytoplasmic M3M4 loop. *Journal of General Physiology* **131,** 137–146 (2008).

347. Kukhtina, V. *et al.* Intracellular domain of nicotinic acetylcholine receptor: the importance of being unfolded. *Journal of neurochemistry* **97,** 63–67 (2006).

348. Jha, A. *et al.* Acetylcholine receptor gating at extracellular transmembrane domain interface: The Cys-Loop and M2-M3 linker. *Journal of General Physiology* **130,** 547–558 (2007).

349. Grosman, C. *et al.* The extracellular linker of muscle acetylcholine receptor channels is a gating control element. *Journal of General Physiology* **116,** 327–339 (2000).

350. Jensen, M. L. *et al.* Charge selectivity of the Cys-loop family of ligand-gated ion channels. *Journal of Neurochemistry* **92,** 217–225 (2005).

351. Nayak, T. K. *et al.* Functional differences between neurotransmitter binding sites of muscle acetylcholine receptors. *Proceedings of the National Academy of Sciences* **111,** 17660–17665 (2014).

352. Oliveira, A. S. F. *et al.* A General Mechanism for Signal Propagation in the Nicotinic Acetylcholine Receptor Family. *Journal of the American Chemical Society* **141,** 19953–19958 (2019).

353. Hajduk, P. J. *et al.* Predicting protein druggability REVIEWS. Drug Discov. Today, 10,1675–1682. *Drug Discovery Today* **10,** 1675–1682 (2005).

354. Miller, E. B. *et al.* A Reliable and Accurate Solution to the Induced Fit Docking Problem for Protein-Ligand Binding. *ChemRxiv* (2020).

355. Klesse, G. *et al.* Induced Polarization in Molecular Dynamics Simulations of the 5-HT3Receptor Channel. *Journal of the American Chemical Society* **142,** 9415–9427 (2020).

356. Cymesa, G. D. & Grosman, C. Identifying the elusive link between amino acid sequence and charge selectivity in pentameric ligand-gated ion channels. *Proceedings of the National Academy of Sciences of the United States of America* **113,** 7106–7115 (2016).

357. Dämgen, M. A. *et al.* Comment on "On the Functional Annotation of Open-Channel Structures in the Glycine Receptor". *Structure* **28,** 601–603 (2020).

358. Beckstein, O. & Sansom, M. S. A hydrophobic gate in an ion channel: The closed state of the nicotinic acetylcholine receptor. *Physical Biology* **3,** 147–159 (2006).

359. Kutzner, C. *et al.* Computational electrophysiology: The molecular dynamics of ion channel permeation and selectivity in atomistic detail. *Biophysical Journal* **101,** 809–817 (2011).

360. Langley, J. N. On the reaction of cells and of nerve-endings to certain poisons, chiefly as regards the reaction of striated muscle to nicotine and to curari. *The Journal of Physiology* **33,** 374–413 (1905).

361. Chatzidaki, A. & Millar, N. S. Allosteric modulation of nicotinic acetylcholine receptors. *Biochemical Pharmacology* **97,** 408–417 (2015).

362. Pedersens, S. E. *et al.* Structure of the Noncompetitive Antagonist-binding Site of the. *Biochemistry* **267,** 10489–10499 (1992).

363. Middleton, R. E. *et al.* Photoaffinity labeling the Torpedo nicotinic acetylcholine receptor with [3H]Tetracaine, a nondesensitizing noncompetitive antagonist. *Molecular Pharmacology* **56,** 290–299 (1999).

364. Chiara, D. C. *et al.* Identification of Nicotinic Acetylcholine Receptor Amino Acids Photolabeled by the Volatile Anesthetic Halothane. *Biochemistry* **42,** 13457–13467 (2003).

365. Ziebell, M. R. *et al.* Identification of Binding Sites in the Nicotinic Acetylcholine Receptor for [3H]Azietomidate, a Photoactivatable General Anesthetic. *Journal of Biological Chemistry* **279,** 17640–17649 (2004).

366. Nirthanan, S. *et al.* Identification of binding sites in the nicotinic acetylcholine receptor for TDBzl-etomidate, a photoreactive positive allosteric effector. *Journal of Biological Chemistry* **283,** 22051–22062 (2008).

367. Gharpure, A. *et al.* Progress in nicotinic receptor structural biology. *Neuropharmacology* **171** (2020).